Forschungsbericht 2020-28

Assessment of scale resolving turbulence models in the TAU code for canonical shock-turbulence interaction

Jimmy-John Hoste

Deutsches Zentrum für Luft- und Raumfahrt
Institut für Aerodynamik und Strömungstechnik
Göttingen

Deutsches Zentrum
DLR für Luft- und Raumfahrt

Forschungsbericht 2020-28

Assessment of scale resolving turbulence models in the TAU code for canonical shock-turbulence interaction

Jimmy-John Hoste

Deutsches Zentrum für Luft- und Raumfahrt
Institut für Aerodynamik und Strömungstechnik
Göttingen

169 Seiten
117 Bilder
34 Tabellen
126 Literaturstellen

Deutsches Zentrum
DLR für Luft- und Raumfahrt

Herausgeber:

Deutsches Zentrum
für Luft- und Raumfahrt e. V.
Wissenschaftliche Information
Linder Höhe
D-51147 Köln

ISSN 1434-8454
ISRN DLR-FB-2020-28
Erscheinungsjahr 2023

DOI: https://doi.org/10.57676/tq7r-en64

CFD, Überschallströmung, Stoßwellen, LES, skalenauflösende Turbulenzmodellierung

Jimmy-John HOSTE
DLR, Institut für Aerodynamik und Strömungstechnik, Göttingen

Bewertung von skalenauflösenden Turbulenzmodellen im TAU-Code für die Behandlung kanonischer Stoß-Turbulenz-Wechselwirkung

Dieser Bericht beschreibt Ergebnisse einer Studie zur numerischen Modellierung der kanonischen Stoß-Turbulenz-Wechselwirkung (STI). Dabei wurde der TAU-CFD-Löser des DLR angewendet. Bisherige Grundlagenuntersuchungen, wurden typischerweise mit Forschungscodes und hochgenauen numerischen Verfahren höherer Ordnung für Raum- und Zeitdiskretisierungen durchgeführt. TAU, als ein Code der für industrielle Anwendungen mit komplexen Konfigurationen konzipiert ist, basiert im Wesentlichen auf Schemata zweiter Ordnung. Der vorliegende Bericht analysiert typische Fehler eines solchen Verfahrens bei der Behandlung von Stoß-Turbulenz-Wechselwirkungsphänomenen. Die Wesentliche Herausforderung besteht darin, die numerische Dissipation weitgehend zu reduzieren um un-physikalische Dämpfung zu vermeiden und im Umfeld der Stoßwelle soweit zu erhöhen um numerische Instabilitäten zu verhindern. Zu diesem Zweck wurden skalenauflösende Turbulenzmodelle in TAU für mehrere Wechselwirkungsszenarien systematisch untersucht. Die hier vorgestellten Studien wurden zwischen 2018 und 2020 in der Abteilung Raumfahrzeuge des DLR-Instituts für Aerodynamik und Strömungstechnik im Rahmen des DAAD-DLR Austauschprogramms durchgeführt.

CFD, supersonic flow, shock waves, LES, scale resolving turbulence models

(Published in English)

Jimmy-John HOSTE
German Aerospace Center (DLR), Institute of Aerodynamics and Flow Technology, Göttingen

Assessment of scale resolving turbulence models in the TAU code for canonical shock-turbulence interaction

This report contains the detailed description of the study of the canonical shock-turbulence interaction (STI) problem performed with the DLR's TAU CFD solver. STI studies reported in the literature are typically performed with high-order (> 2nd) accurate numerical schemes for space- and time discretizations. Instead, TAU, being a code used for both industrial and academic purposes, contains second-order accurate numerics. The motivation of this work is to understand how such a solver copes with the canonical STI setup which requires low dissipation to describe the turbulence accurately while higher dissipation is needed to avoid numerical issues in the shock capturing process. To this end, the scale-resolving capability of TAU has been carefully investigated for several STI's where turbulence has been described with a Large Eddy Simulations (LES) method.

The studies presented herein have been performed between 2018 and 2020 at the Spacecraft Department of the DLR's Institute of Aerodynamics and Flow Technology (Gottingen, Germany), supported by the DAAD-DLR scholarship.

Document properties

Title	Assessment of scale resolving turbulence models in the TAU code for canonical shock-turbulence-interaction
Subject	turbulence, LES, shock waves
Institute	Institute of Aerodynamics and Flow Technology, Spacecraft Department
Compiled by	Dr. ir. Jimmy-John O.E. Hoste
Participants	Dr. ir. Jimmy-John O.E. Hoste
Checked by	Dr. Tim Horchler, Dr.-Ing. Sebastian Karl
Release by	Deutsches Zentrum für Luft- und Raumfahrt
Date	January 2, 2023
Report number	DLR-FB-2020-28

Contents

Abstract

This report contains the detailed description of the study of the canonical shock-turbulence interaction (STI) problem performed with the DLR's TAU CFD solver. STI studies reported in the literature are typically performed with high-order ($>$ 2nd) accurate numerical schemes for space- and time discretizations. Instead, TAU, being a code used for both industrial and academic purposes, contains second-order accurate numerics. The motivation of this work is to understand how such a solver copes with the canonical STI setup which requires low dissipation to describe the turbulence accurately while higher dissipation is needed to avoid numerical issues in the shock capturing process. To this end, the scale-resolving capability of TAU has been carefully investigated for several STI's where turbulence has been described with a Large Eddy Simulations (LES) method.

The studies presented herein have been performed between 2018 and 2020 at the Spacecraft Department of the DLR's Institute of Aerodynamics and Flow Technology (Göttingen, Germany), supported by the DAAD-DLR scholarship.

Acknowledgements

I wish to acknowledge the many discussions with Jan-Erik Schumann throughout the realisation of this work as well as the continuous support provided by Sebastian Karl, especially in the idea of compiling this work in the form of a report. I'm also very grateful to Johan Larsson and Yogesh Prasaad Madras Sethuraman for their availibility in answering diverse thoughts and questions during the realization of this work. The input on the extended literature chapter from Diego Donzis is highly appreciated. Many thanks to Tim Horchler, Daniela François and Axel Probst for the (synthetic) turbulence and numerically related guidance. Thank you to the late Klaus Hannemann for providing the opportunity to work on this exciting subject. I'm grateful for the many interactions in numerical and experimental topics at the Spacecraft Department of DLR. Finally, thank you to Katarzyna Kurkowiak for providing the motivation in finalizing this long overdue report.

1. Current Status of the Canonical Shock-Turbulence Interaction Problem

In a first part (1.1), the numerical work on the presently considered subject will be detailed in a chronological manner. The focus will be on the numerical work relying on Computational Fluid Dynamics (CFD). The herein referred literature can be consulted for further details about associated experimental or analytical work. A brief summary is then provided with some outlooks on the topic. Finally, the motivations for the present work will be detailed (1.2).

1.1. Literature Study

The numerical study of the canonical shock-turbulence interaction (STI) has been subject to many investigations since the early 1990's pioneering three-dimensional work of Lee et al. [61, 59, 54]. Canonical STI represents a simplification of the type of interactions between turbulence and shock waves that occur, for instance, in supersonic air-breathing propulsion flow paths (inlet, isolator, combustor and nozzle). The simplification entails realistic isotropic turbulence convected through a normal shock wave, as depicted in Figure 1-1 . It enables furthering our understanding of the mechanisms driving the interaction as well as the requirements for the numerical choices to adequately study and predict the problem (turbulence description, discretization schemes and order, shock capturing schemes, grids).

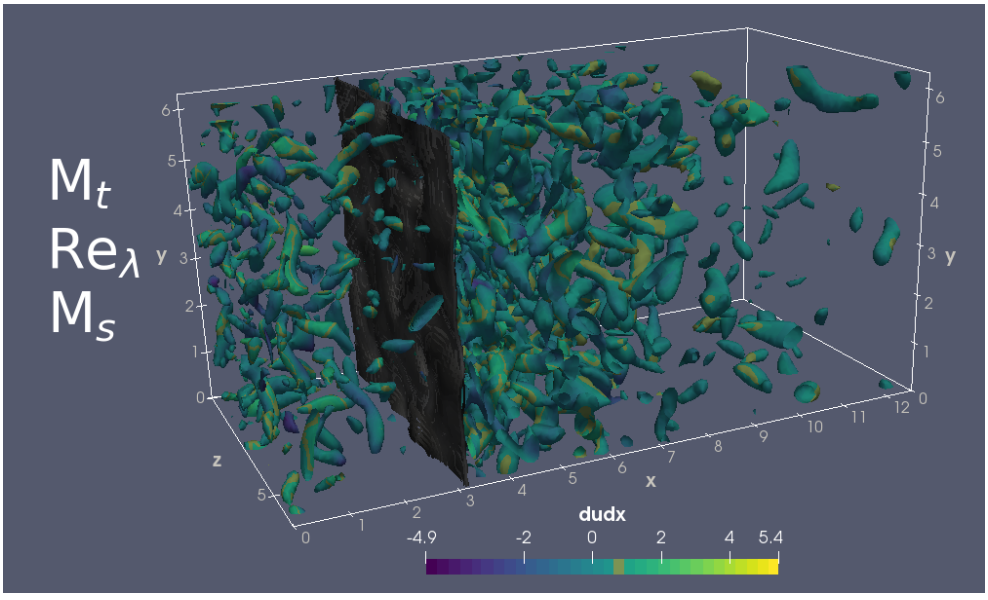

1-1 Illustration of the canonical STI problem. Visualised turbulent structures are identified by the Lambda-2 criterion (between -48 and -10 for pre-shock, -2 for post-shock) and colored by the instantaneous streamwise dilatation. The shock front is identified by negative values for the latter parameter.

Given the low shock Mach number (weak shocks with $M = M_s \in [1.05,1.20]$) considered in the

early Direct Numerical Simulation (DNS) study by Lee et al. [59], the shock could be resolved by the Navier-Stokes equations on the selected grids. A quasi-incompressible free-stream turbulence, of solenoidal nature, was convected through the shock wave. The incoming levels of turbulence fluctuations are characterized by the turbulent Mach number, M_t, which has different definitions throughout the literature. The most common definition being:

$$M_t = \frac{\sqrt{R_{kk}}}{\tilde{a}} = \frac{\sqrt{2TKE}}{\tilde{a}} = \frac{\sqrt{3}u_{rms}}{\tilde{a}} \tag{1-1}$$

where the quantities are the trace of the Reynolds stress tensor (R_{kk}), the Favre-averaged speed of sound ($\tilde{a}$), the turbulent kinetic energy (TKE) and the root mean square velocity fluctuations (u_{rms}). The higher the value of M_t for a given shock strength, the stronger the incoming fluctuations.

On top of M_t, another dimensionless quantity is required to completely characterize the turbulence. This would usually be the Taylor microscale Reynolds number and is defined as

$$Re_{\lambda_\alpha} = \frac{\bar{\rho} u_{\mathrm{rms}} L_{\lambda_\alpha}}{\bar{\mu}} \tag{1-2}$$

where we have, the time-averaged - density ($\bar{\rho}$) and dynamic viscosity ($\bar{\mu}$), as well as the Taylor microscale defined as

$$L_{\lambda_\alpha} = \lambda_\alpha = \frac{\sqrt{\overline{u_\alpha'^{\,2}}}}{\sqrt{\overline{u_{\alpha,\alpha}'^{\,2}}}} \tag{1-3}$$

with the velocity fluctuations (u_α') in the direction α. Einstein notation is adopted where a derivative of a variable "a" with respect to a spatial direction (α in this case) is written as $a_{,\alpha}$.

Three different Taylor microscales and Taylor Reynolds numbers can be defined associated to each flow direction. It reduces to a single value in the case of isotropic turbulence which is why the following discussion will only use singular references to them. In accordance to every Reynolds number definition, the lower the Re_λ value, the more viscous the flow. It is also possible to use an integral scale Reynolds number, Re_L (or Re_T) instead, which typically relies on the dissipation length scale (L_ϵ). The latter length scale has also different definitions throughout the literature but does commonly relate to R_{kk} (or TKE) and the dissipation of TKE (ϵ).

Compressible turbulence can be considered as an interaction between three types of modes (or waves): sound-wave (also known as acoustic) , vorticity (also known as solenoidal) and entropy modes. This classification follows from the work of Kovasznay [49] which performed a linearized analysis of the Navier-Stokes equations in terms of small perturbations (with respect to the mean). Several linearly independent solutions, and the equations describing them, were obtained and re-grouped into the three above categories. The interaction of any of these waves with a shock wave leads to the generation of all three modes through non-linear processes. The linear independence

(first order approximation) between the different modes is also the basis of what is known as Linear Interaction Analysis (LIA) which was introduced by Ribner [91, 92] and Moore [77]. LIA has become an ad hoc tool in the different analysis of canonical STI as it provides rapid estimations to which DNS or other numerical results can be compared too. It can also be used in a predictive manner but due to the underlying assumptions, its validity to the desired interaction (turbulence type and shock strength) must be carefully evaluated at first. That is [59]

- the upstream Mach number variations should be small with respect to the mean incoming Mach number;
- the time for the turbulence to pass through the shock should be small compared to turbulence time scale ($\sim TKE/\epsilon$).

The first requirement is equivalent to small perturbations (and relates therefore to M_t). The second relates to the nature of the turbulence itself and ensures that the redistribution of turbulent energy (which is highly nonlinear) does not happen quickly enough so that the turbulence has not considerably changed in the shock region. Also noteworthy is the adoption of Rapid Distortion Theory (RDT) to study the STI problem analytically [62], however its assumptions are more restrictive than LIA [53, 52]. Note that in the following discussions, if the type of incoming turbulence is not mentioned, it implies that it is of (quasi-) purely vortical nature.

The work of Lee et al. [59] is no exception in the use of LIA to discuss their predictions for $M_t \in$ [0.05,0.11] and $Re_\lambda \in$ [16,20]. The authors studied the mechanism of turbulence amplification through the shock in terms of TKE (or diagonal components of Reynolds stress tensor, $R_{\alpha\alpha}$) and vorticity fluctuations variances ($\overline{\omega_\alpha'^2}$). Both of these parameters demonstrate that the initially isotropic turbulence becomes axi-symmetric through the interaction. DNS shows an increase in streamwise (R_{11}) and transverse (R_{22}) velocity fluctuations across the shock wave, from which LIA only predicts the latter. A monotone decrease in R_{11} is observed through LIA. Through an analysis of the budget of TKE, the mechanism responsible for the rapid evolution (increase followed by decrease) in TKE is identified. Just downstream the shock wave, the pressure work is dominant while the viscous dissipation takes over further downstream. The pressure work can be divided in contributions from the pressure-dilatation and the pressure-transport from which the latter is dominant (especially in shock-normal direction), hence explaining the rapid TKE evolution following from an acoustic transient (acoustic wave propagation generated through the interaction). The pressure-dilatation is responsible for the conversion of mean internal energy into TKE.

The vorticity fluctuation variance has an important impact on the dissipation of TKE. LIA predicts an amplification solely for the transverse components ($\overline{\omega_2'^2}$, $\overline{\omega_3'^2}$) and no change in streamwise component ($\overline{\omega_1'^2}$). The amplification increases with shock strength and appears to reach an asymptotic value. DNS confirm this transverse amplification trend. However, further downstream the shock, a Reynolds dependency is observed on the streamwise and transverse components' evolution:

- a higher Re_λ (Re_T) results in a slow increase of $\overline{\omega_1'^2}$ and a slower decay of $\overline{\omega_2'^2}$
- a lower Re_λ (Re_T) results in a monotone decrease of $\overline{\omega_1'^2}$ and a more rapid decay of $\overline{\omega_2'^2}$

This observations are further studied through the budget of vorticity fluctuations variances. Inside

the shock, the vorticity compression is responsible for the $\overline{\omega_2'^2}$ amplification while it is balanced by vortex stretching for $\overline{\omega_1'^2}$, hence explaining the negligible influence on the latter component. Downstream, a balance between the viscous and vortex stretching terms is observed for $\overline{\omega_2'^2}$ and is responsible for the monotone decay. The same is true for $\overline{\omega_1'^2}$ at low Reynolds numbers. At higher Reynolds number, the turbulent vortex stretching is sufficiently amplified to overtake the viscous dissipation, explaining the slow increase in $\overline{\omega_1'^2}$. The transverse vorticity components amplification mechanism are observed to be primarily linear for low turbulence levels, defined as a function of M_t and the Mach number. Specifically, for

$$K_{Lee} = \frac{M_t}{(M^2 - 1)} < 0.1 \tag{1-4}$$

LIA predictions agree relatively well with the DNS.

Lee et al. [59] also looked at the turbulent length scales , thermodynamic fluctuation and instantaneous shock structure. The former parameter decreases across the shock which is also observed through LIA. Thermodynamic fluctuations remain isentropic throughout the interaction and demonstrates the invalidity of the strong Reynolds analogy (RSA) in STI. The RSA relates density fluctuations to entropy (temperature) fluctuations with a correlation coefficient of -1 (Morkovin's hypothesis), an hypothesis which proves to be valid in compressible turbulent boundary layers up to the hypersonic speeds [96]. The isentropic character of the thermodynamic fluctuations is also satisfied instantaneously. A budget of the density fluctuation variance shows that its amplification is due to mean flow compression. In terms of the instantaneous shock structure, for M_t / $(M^2 - 1) < 0.1$, a clear shock front could be observed. General discrepancies between LIA and DNS results are stronger with an increase of M_t / $(M^2 - 1)$.

The work of Lee et al. [59] did "benchmark" the aspects of STI subsequent studies partially or fully considered which are diagonal Reynolds stress components (or TKE), vorticity fluctuations variances, turbulent length scales, thermodynamic fluctuations and shock structure. In order to extend the reach of numerical tools for STI study at conditions deemed more realistic, i.e. higher Reynolds numbers, further developments are required which involve the use of Large Eddy Simulation (LES). E.g. isotropic turbulence is considered fully developed for $Re_\lambda > 100$ [68]. The study of stronger shocks would require to move away from shock resolving towards shock-capturing or shock-fitting techniques as the cost of resolving the shock increases with Mach number (thinner shocks [60]) and the Navier-Stokes become invalid inside shock waves for $M > 2$ [59]. Moreover, realistic conditions could involve different types of upstream turbulence. The above aspects have been the topics of canonical STI studies to date which is discussed below.

Lee [54] formulated an LES framework which could be used for future studies of STI and which was tested on decaying compressible isotropic turbulence. It is concluded that further studies are required before application to STI. Another focus of this work was the development of a shock-capturing scheme. Several numerical studies were performed with DNS to evaluate the most suitable application of shock-capturing. Among these studies was the canonical STI for one of the conditions of Lee et al. [59] enabling a direct comparison with shock-resolved results. Good agree-

ment was observed for the quantities compared and the most suitable numerical setup is found to be the application of the shock-capturing scheme solely in the shock-normal direction for the convective fluxes and in a pre-defined region near the shock wave.

The shock-capturing framework developed in [59] was subsequently applied to three-dimensional canonical STI studies for strong shocks ($\geq$ 1.5) by Lee et al. [56, 60]. The importance of the streamwise grid resolution in shock-capturing was discussed in Lee et al. [60] as a poor resolution could not enable the reproduction of transverse velocity and entropy fluctuations from the shock resolved simulations. It is argued that shock front corrugation has a significant effect on the transverse velocity fluctuations and should be adequately resolved. The grid refinement is also crucial for the thermodynamic fluctuations and does depend on the dissipative character of the shock-capturing scheme. Vortical turbulence within a similar range of M_t and Re_λ as in [59] were considered yielding lower levels of upstream turbulence (see lower M_t / (M^2-1)). The same mechanism responsible for the rapid evolution of TKE behind the shock is observed. An improved use of LIA was made resulting in comparable trends to DNS in the amplification of velocity fluctuations. It was done through compensation of post-shock viscous decay (larger for transverse components) by extrapolating CFD results back to the mean shock location. The boundaries of the shock oscillations are obtained by evaluating

$$\frac{d\bar{u}_1}{dx} = 0 \tag{1-5}$$

Specifically, regions where the mean dilatation is zero. Consequently the mean shock position can be inferred. Inside the shock, $d\bar{u}/dx$ is negative (compression) and outside the shock it is mostly zero (both dilatation and compression). Comparable trends between LIA and DNS indicate a mainly linear process to be responsible for the rapid evolution of TKE: an anti-correlation between acoustic and vortical velocity fluctuations exist just behind the shock. This was confirmed through analysis of the linear acoustic energy balance (neglecting the effect of entropy fluctuations): energy is transferred from acoustic potential energy (pressure or density fluctuations) to turbulent kinetic energy.

Similarly to the weak shock observations in [59], Taylor (and transverse density) microscales decrease through the interaction which is more pronounced for higher Mach numbers. For the stronger shocks considered in their work (M = 2, 3), Lee et al. [56] show that the dissipation length scale (L_ϵ) also decreases across the shock. LIA predictions agree well with DNS for both the microscales and L_ϵ. Moreover, regarding the latter, LIA suggests that, for $M < 1.65$, L_ϵ increases slightly through the interaction which can be explained by the fact that the TKE and ϵ get similarly amplified for weak shocks. With increased shock strength the TKE amplification saturates faster than the vorticity fluctuations variance (main contributor to ϵ) leading to the observed reduction in L_ϵ. The thermodynamic fluctuations are observed (LIA and DNS) to be non-isentropic after the interaction which is due to the increased effect of entropy fluctuations. From M = 1.65, LIA predicts that the entropy fluctuations become more dominant than acoustic fluctuations. Recall that for weak shocks ($M <$ 1.2) it was previously shown [59] that the thermodynamic fluctuations remain isentropic through the interaction.

Around the same time as the above studies of Lee et al. [59, 54, 56, 60] an interest in the effect

of the nature (vortical, acoustic, entropy) of the upstream turbulence was investigated by several authors [33, 34, 72, 41].

Hannappel et al. [33, 34] investigated with DNS the impact of compressibility, i.e. vortical and acoustic upstream turbulence, on the three-dimensional canonical STI setup for a strong shock wave (M = 2). The authors considered a very low pre-shock $Re_\lambda \approx 4$ as well as low levels of upstream fluctuations (M_t / $(M^2 - 1) << 0.1$). The level of compressibility of the inflow turbulence is defined through a parameter χ which is the ratio of compressible (or irrotational) TKE to total TKE. Simulations with a value of χ = 0.5 were compared to the incompressible case (purely vortical turbulence) with χ = 0. The compressibility is shown to increase the transverse vorticity fluctuations. In contrast, its effect on the transverse velocity fluctuations (R_{22}) is a decreased amplification. It is explained by a reduction of the pressure-transport (or pressure-diffusion) term within the pressure-work which is responsible for the rapid post-shock evolution of TKE. No apparent influence of the compressibility on R_{11} is reported. The transverse Taylor microscales get less significantly reduced through the interaction for χ = 0.5 and the thermodynamic fluctuations less amplified (an order of magnitude).

Mahesh et al. [72] investigated the effect of entropy fluctuations on the canonical STI with DNS for shock strengths of 1.29 and 1.8. Entropy fluctuations are introduced through the density fluctuations by applying the weak form (in rms) of Morkovin's hypothesis (negatively correlated velocity-temperature fluctuations). Shown by mean flow profiles, the presence of entropy fluctuations increase the mean shock thickness, i.e. an increase in shock motion, with respect to the purely vortical upstream turbulence. For a given shock strength, entropy fluctuations increase the velocity fluctuations amplification with a stronger effect on the streamwise component. A higher Mach number results in stronger amplification levels considering upstream entropy fluctuations. LIA predicts similar trends with higher amplifications than the DNS and shows an increased influence of entropy fluctuations (stronger amplification) with increasing Mach number. In case of positively correlated velocity and temperature fluctuations, LIA shows a supression of the amplification.

Similar DNS observations as for the velocity fluctuations are observed for the vorticity fluctuations: upstream entropy fluctuations increase the amplification of the transverse components. However, an additional influence is shown on the downstream evolution of the streamwise component $\overline{\omega_1'^2}$, i.e. an increase which is more pronounced for higher Mach number. Recall that in the case of purely vortical turbulence, Lee et al. [59] demonstrated a Reynolds number dependency on the same $\overline{\omega_1'^2}$ evolution. Also notewhorthy is a return to isotropy within the considered computational domain of the vorticity fluctuations for the stronger shock case (M = 1.8). A linearized analysis yielding the governing equations for vorticity fluctuations explains the above observations. The latter equation shows that changes in vorticity fluctuations can happen as a result of bulk compression and a baroclinic term. The former has a postive contribution which increases with shock strength and thus enhances fluctuations. The vorticity fluctuations amplification due to incident entropy waves occurs through the baroclinic contribution. An enhancement requires a negative correlation between upstream velocity and temperature fluctuations while the opposite would result in a supression.

With regard to the impact of entropy fluctuations on the thermodynamic quantities, for the lower Mach number case (M = 1.29), Morkovin's hypothesis (in its weak form, i.e. rms sense) is shown to be invalid just downstream the interaction but smaller deviations from this hypothesis are seen

further downstrean. In the near field behind the shock, acoustic (pressure) fluctuations are important but decay very quickly. At the higher Mach number (M = 1.8), similar trends are seen but a stronger decay in temperature and density fluctuations are present. Their levels become similar to the pressure fluctuations with increased downstream distance. Linear analysis shows that only the first part of Morkovin's hypothesis (weak form) holds which relates density to temperature fluctuations. A linear analysis of stagnation temperature fluctuations showed a significant influence of shock front oscillations, which increases with Mach number, resulting in the invalidity of the last part of Morkovin's hypothesis relating temperature and velocity fluctuations.

Jamme et al. [41] provided a combined study of three types of upstream fluctuations (vortical, vortical and solenoidal, vortical and acoustic) with similar inflow turbulence in terms of M_t and Re_λ. The authors wanted to ascertain previous observations from the literature. A major difference between the work of Jamme et al. [41] and all of the previously discussed work, as well as the majority of the subsequent work, is the use of a second-order accurate discretization scheme for space and time. In contrast, other work considered high-order accurate (> 2) spatio-temporal discretization schemes. Their findings confirmed previous DNS observations as well as LIA predictions.

Around the same time as the work of Jamme et al. [41], some authors [20, 25, 19] focused on the application of LES to the canonical STI problem with vortical upstream turbulence.

Ducros et al. [20] devised, and extensively tested through separate problems, a numerical framework which could be used to study shock turbulence interaction with LES. They considered a second-order accurate central scheme with sufficient dissipation to capture the shock discontinuity and as less as possible dissipation in order to adequately predict the evolution of the turbulence away from the shock. The canonical STI was studied in an inviscid setting motivated by the primarily aim of their work in understanding the most appropriate combination of the numerical settings (artificial dissipation, shock sensor).

The work of Garnier et al. [25] looked at the performance of four different subgrid scale (SGS) models among which two are of the dynamic type. A priori DNS simulations are first performed and compared to reference DNS [59, 60] with similar predictive capability in terms of velocity and vorticity fluctuations amplification. The DNS results are then filtered to enable comparison of the velocity fluctuations with the different LES predictions. The different SGS models are the Smagorinsky, the mixed scale (MSM), they dynamic Smagorinsky (DSM) and dynamic mixed scale (DMM). On grids refined with the aim of correctly account for shock front corrugation effects (see also 3.1), the different SGS models give similar results for streamwise and transverse velocity fluctuations. The dynamic models perform somewhat better and the Smagorinsky model is shown to be the most dissipative with stronger deviations from the filtered DNS. A strong influence of different grid refinements on the predictions are observed and linked to the loss of shock corrugation instead of poor performance of the SGS models.

While Garnier et al. [25] looked at eddy viscosity models for the SGS in LES, Dubois et al. [19] considered a subgrid-scale estimation model instead. The authors compared the results with a dynamic

SGS model [76] for two different Reynolds numbers and inflow turbulence levels (not explicitly communicated). Both SGS models are only applied in the transverse directions (not in the shock-normal direction). For the lower Reynols number case (also lower level of inflow turbulence), a comparison with the filtered DNS of the SGS stress tensor, SGS heat flux and SGS dissipation shows a general superiority of the SGS estimation method on the finest grid considered. Post-shock TKE levels as well as streamwise vorticity fluctuations are overestimated by the dynamic SGS. Moreover, a decrease in streamwise grid resolution affects the latter model much more than the SGS estimation model. Similar transverse vorticity fluctuations amplifications are predicted by both models. For the higher Reynolds number case, both SGS models are in better agreement on the finest grid resolution considered than in the lower Reynolds number case. Regarding the thermodynamic fluctuations, density and pressure fluctuations are in closer agreement with filtered DNS for the estimation model while the dynamic model performs better for the temperature. The study concludes that the estimation model is at least as good as the dynamic model.

Still considering vortical upstream turbulence, Sesterhenn et al. [98], Rawat et al. [88, 89] and Wang et al. [123, 124] focused on the application of shock-fitting methods and applied it to the DNS of the canonical STI problem with strong shocks. Sesterhenn et al. [98] demonstrate that their shock-fitting method is capable of reproducing previous trends in velocity fluctuations and vorticity fluctutions amplifications as well as the reduction of Taylor microscales for shock Mach numbers of 2 and 3. They authors suggest that shock-fitting might be more suitable when evolving towards higher Mach numbers (thinner shocks) given the fact that the shock is treated as a discontinuity. Instead, shock-capturing methods would require finer meshes at higher Mach numbers in order to capture shock front corrugations which scale with the upstream turbulence intensity (u_{rms} / u_1) [60].

Rawat et al. [88] exploit further the previously mentioned advantage of shock-fitting methods by studying shock Mach numbers up to 10 at very low upstream turbulence levels and Reynolds number (Re_λ). Note that the same inflow turbulence was used for each Mach number, hence decreasing the incoming turbulence intensity with increase in Mach number. The DNS results confirm LIA predictions of TKE amplification which reaches an asymptotic value for higher Mach numbers. Evolution of transverse vorticity amplification levels with Mach number are in close agreement with LIA. The higher the Mach number, the stronger the post-shock anisotropy as shown by the vorticity fluctuations. In terms of transverse Taylor microscale just behind the shock, agreement between the shock-fitting and LIA improves with increase in Mach number.

In a later work, Rawat et al. [89] considered a broader range of incoming turbulent Mach numbers (0.121 - 0.376) as well as Reynolds numbers (6.2-40.5) and Mach numbers (2-20). Strong interconnections between the considered parameters were observed and many results discussed. Similar observations on the effect of Mach number as in [88] are showns for similar turbulent inflow conditions (Re_λ = 6.2, M_t=0.121). However, a general conclusion of their work is a strong deviation from LIA (as no other DNS data is available) for higher Mach numbers. E.g. shock front distortions were similarly predicted to LIA for Mach numbers below 8 where the phenomenon can be linearly related to the turbulence intensity. Beyond Mach 8, strong deviations are observed where LIA underpredicts the distortions with respect to the DNS. Regarding the Reynolds stresses, for a given combination of

Re_λ and M_t, the streamwise component's (R_{11}) amplification decreases with increase in Mach up till a value of ≈ 8. Beyond this "treshold" an increase in amplification is however observed. It must be noted that an increase in Mach number implies a decrease in upstream turbulence intensity as M_t is kept constant. R_{22} gets amplified with an increase in Mach number but so does its subsequent decay rate. In a comparison with LIA, for lower Mach numbers (below 6,7 or 8 depending on the quantity of interest) the agreement is quite good for R_{11}, R_{22} and the TKE amplifications but strong deviations are seen for further increases in Mach. For a fixed value of M_t at a given Mach number, an increase in Re_λ increases the amplification of R_{11}. investigating the vorticity variance fluctuations show a return to isotropy for specific combinations of Mach, M_t and Re_λ. Some trends on the effect of the latter two parameters are discussed. The Re_λ dependency of the streamwise vorticity fluctuations variance documented by Lee et al. [59] is as well observed by the authors: $\overline{\omega_1'^2}$ increases behind the shock for higher Re_λ. However, increasing the Mach number results in a smaller increase which eventually transforms in a decrease, $\approx$ above Mach 10, for the higher Re_λ cases. This strongly influences the return to isotropy. The transverse component's amplification ($\overline{\omega_2'^2}$) generally increases with Mach number which is coupled with a sharper subsequent decay.

Wang et al. [123, 124] extended the above code's [88, 89] capability to include chemical and thermal nonequilibrium effects. They applied this shock-fitting solver, for a perfect gas setting, to the canonical STI problem with Mach numbers ranging from 2 to 30 and for inflow turbulence with M_t and Re_λ ranging between 0.083 and 0.143 and 18.9 and 52.4, respectively. The study provides addition DNS data which are in line with previous findings [88, 89].

Around the same time as the previously discussed shock-fitting work [88, 89, 123, 124], within a shock-capturing DNS framework, several authors [53, 63, 30, 12, 31, 52] increased the range (upper limit) of Re_λ and M_t compared to prior investigations. Stronger shocks were also considered.

Larsson et al. [53] (see also [63]) demonstrated the need for refining the grids in all directions to adequately resolve the post-shock turbulence. The different results discussed (for Mach < 2) suggest that previous DNS of Lee et al. [56, 60] was under-resolved. Finer grids are needed to capture the return to isotropy in vorticity fluctuations downstream the shock which occured for all cases shown. Another discrepancy with previous DNS, as well as with LIA, is that the R_{11} amplification remains larger than R_{22} for all shock Mach numbers considered. This in turn influences the levels of anisotropy in velocity fluctuations. Moreover, with regard to the Taylor microscales, λ_1 becomes rapidly larger than λ_2 at some distance from the shock while LIA predicts $\lambda_1 < \lambda_2$ and varying results where obtained in previous works. The authors also studied instantaneous shock structures introducing the classifications "wrinkled" and "broken" shock regimes. Building further on the parameter M_t / $(M^2 - 1)$ (Equation 1-4), introduced by Lee et al. [59], a broken shock could be identified for M_t / $(M^2 - 1) \geq 0.06$ (based on the selected conditions up to Mach 6). Recall that Lee et al. [59] identified a clear shock structure, which would be equivalent to a wrinkled shock, for M_t / $(M^2 - 1) < 0.1$ instead.

Grube et al. [30] performed DNS of the canonical STI problem with a highly compressible inflow

($M_t \approx 0.89$, $Re_\lambda \approx 20$) where eddy shocklets can occur. A compressibility ratio (χ) of ≈ 29 % is documented. A strong shock (M = 5) was considered so that in terms of turbulence intensity (u_{rms} / U) the selected condition yields levels similar or smaller than the ones selected by Larsson et al. [53]. Their observations are in line with what was previously seen by the latter authors regarding TKE, vorticity amplification and length scale reductions. The shock front distortion is observed to be much stronger than previous studies and results in increased upstream influence on the collected statistics (farther upstream). In a subsequent study, Grube et al. [31], provided further simulation data for similar Re_λ (≈ 20), at different shock and turbulent Mach numbers (still highly compressible). Stronger deviations from the laminar Rankine-Hugoniot jump conditions are observed for increased M_t (keeping fixed M) and a decrease in amplification of TKE and Reynolds stresses. The similarity parameter related to the STI amplification proposed by Donzis [16] was shown to hold only for one out of the three cases.

The work of Crespo [12] focused on the interaction between a shock and a turbulent shear layer. As part of their investigation, the canonical STI was considered as a point of comparison but was not their primary focus. Turbulent inflow conditions (with relatively low turbulent intensity) already considered in the literature were selected to interact with a Mach 1.5 and Mach 3 shock. Canonical STI results are in line with what had already been reported in the literature for TKE, vorticity, length scales and thermodynamic fluctuations.

Larsson et al. [52] build further upon the work of Larsson et al. [53] ($Re_\lambda \approx 40$) and considers additional simulations including higher Reynolds numbers ($Re_\lambda \approx 70$). A comparison of several methods to obtain post-shock TKE amplification from DNS data demonstrated that LIA is able to provide reasonable predictions of this quantity. A return to isotropy of vorticity fluctuations (and thus the small scales) occur after a very short distance (≈ 10 convected Kolmogorov time scales). This observation renders the prediction of vorticity amplifications through the interaction as not very important for realistic conditions , i.e. it suffices to consider the vorticity isotropic after the interaction in practical applications. An improved criterion, with respect to Larsson et al. [53], for the identification of the broken shock regime is provided

$$K = \frac{M_t}{M-1} > 0.6 \tag{1-6}$$

which coincides with a separate study from Donzis [18].

Motivated by a lack of agreement in amplification factors between LIA and simulations, Donzis [17], considered the shock thickness as an important parameter from a theoretical perspective. This lead to an improved similarity parameter K which is related to the ratio of laminar shock thickness (δ_l) and the Kolmogorov length scale (η) as follow:

$$\frac{\delta_l}{\eta} \approx K \equiv \frac{M_t}{Re^{0.5}(M-1)} \tag{1-7}$$

Around the same period, the role of the shock thickness in the STI was confirmed by Ryu and

Livescu [97] with shock-resolved DNS. The authors demonstrated a reconciliation between LIA and DNS, i.e. DNS converges towards LIA for lower turbulence levels (M_t) as well as for more viscous flows (lower values of Re_λ). A broad parameter space was used with $M_s \in$ [1.1, 2.2] , and $Re_\lambda \in$ [10,45] and $M_t \in$ [0.02,0.31]. The latter two parameters are taken just before the shock. When evolving toward smaller turbulence levels, it is important to ensure large enough scale separation between the shock width (δ) and the small scale fluctuations of the incoming turbulence (η). In turn, this ensures that viscous and nonlinear effects remain small during the interaction itself which is one of the assumption of LIA. An estimate for this scale separation was derived by Moin et al. [75] yielding

$$\frac{\delta}{\eta} \approx \frac{7.69 M_t}{Re_\lambda^{0.5}(M_s - 1)} \tag{1-8}$$

In this formula, δ represents the laminar shock thickness, an assumption following from the fact that turbulent fluctuations do not significantly alter the upstream Mach number. The small scale fluctuations of the turbulence are represented by the Kolmogorov length scale η in Equation 1-8, similarly to Equation 1-7. Note that the scale separation plays an important role in grids requirements for shock capturing [75] schemes.

The scale separation, i.e. ratio of δ/η was actively controlled (changing M_t for fixed other quantities) by Ryu and Livescu [97]. As M_t (the scale separation) becomes smaller convergence of DNS toward LIA is shown in terms of Reynolds stress and vorticity variance amplifications. The authors took a step further by relying on LIA to generate a post-shock turbulence state. This state was subsequently analysed in detail for M_s = 2.2 and 6 as well as compared to DNS at M_s = 2.2. It is pointed out that such LIA approach is particularily useful to overcome provlems associated with higher Mach numbers where DNS becomes too costly to resolve the shock structure, the Navier-Stokes Equations can't be relied on to resolve the shock wave region (invalid for $M_s > 2$, see Sherman [103]), and grid requirements can become to restrictive to describe the post-shock turbulence (even with shock capturing).

Interest in LES of the canonical STI had also started to re-emerge around the same time as the previously discussed shock-capturing [53, 30, 31, 12, 52] and shock-resolving [97] DNS.

Genin et al. [27, 28] considered a compressible extension of the Localized Dynamic k_{sgs} Model (LDKM) with a hybrid shock capturing scheme. Shock Mach numbers of 1.29, 2 and 3, and an inflow Re_λ and M_t of 39.5 and 0.22, respectively, were selected for study. An a priori DNS study was performed demonstrating the inedequacy of upwind-type discretization schemes with issues being mostly observed in the post-shock decay. The DNS data is subsequently used (filtering on LES grids) to evaluate the LDKM and comparison with the DSM which prove to perform well in other fundamental turbulence studies (see also Garnier et al. [25] for canonical STI). Generally, a good correlation between the LDKM SGS terms and the exact terms is shown in this a priori study. Moreover, the importance of the diffusion of TKE_{sgs} (= k_{sgs}) due to pressure fluctuations is demonstrated by the budget of TKE_{sgs}. The authors mention that this terms' contribution is often neglected in modeling of the TKE_{sgs}' governing equation which is not the case for the LDKM. The LES study of the STI were performed without SGS model, with LDKM and with DSM in conjunction with a

dynamic Pr_t evaluation. The R_{11} amplification is generally well predicted by the LDKM, except for the Mach 3 case with possible cause the loss of corrugation associated with the use of coarser grids (for LES).The R_{22} amplifications are under predicted by all models.

Bermejo-Moreno et al. [5] presented an extensive study of the effect of SGS models (previously discussed in [3]) on the canonical STI. Models of two families were considered, mixed eddy-diffusivity models and structural based models. Shock Mach numbers of 1.5 and 3.5 with inflow Re_λ = 75 and M_t were considered. Two LES grids were selected, one isotropic and one with stretched cells in the streamwise direction. Filtered DNS results were used for reference. In addition, the order of the discretization schemes, its directional application and the conditional use of SGS (not used in region based on a shock sensor) were defining the test space. A multitude of observations are discussed. It was shown that deactivating the SGS model in the shock region, which adds dissipation, improved the results. The stretched grid mainly affected the transverse Reynolds stresses with generally better predictive capability.

Hickel et al. [35] studied a Mach 1.5 canonical STI case, with the same inflow turbulence as Bermejo-Moreno et al. [5], considering an implicit LES (ILES) framework: the Adaptive Local Deconvolution Method. Comparative predictive capability to other explicit LES predictions (DSM) were shown. It must be noted that the grid sizes in this comparison were rather coarse, especially in the post-shock region, however the main point of interest was the adequacy of the ILES formulation. Subsequently, a detailed grid sensitivity of the ILES was shown which confirmed previous observations about the importance of streamwise grid spacing on the R_{22} amplification (see e.g. [5]).

The canonical STI setup has shown to remain relevant, as in the past 5 years a multitude of approaches where considered (LES, DNS, LIA+DNS) for its study. A general trend is the aim to evolving towards more realistic application conditions.

Livescu et al. [68, 67] took the work of Ryu et al. [97] by relying on LIA to generate post-shock turbulence for detailed analysis. A Re_λ of 180 is selected which would be extremely costly for a classical DNS study of the canonical STI. Moroever, the motivation for such a high value is that isotropic turbulence is only considered fully developed (large enough to have a separation between the energy containing - and dissipative scales) for $Re_\lambda > 100$ (see also Dimotakis [15]). Livescu et al. [68] consider Mach numbers up to 10 ($\delta/\eta = 0.0003$). An important result from the post-shock turbulence study is that its nature is not fully three-dimensional any more but two-dimensional axi-symmetric and is more pronounced at higher M_s. This in turn will affects the post-shock decay behavior. Livescu et al. [67] uses the post-shock LIA generated turbulence to study the phenomenon of backscatter with relevance to the SGS modelling in LES. Backscatter is typically not modeled in LES as it can render simulations unstable (acting as a source term). It is shown that backscatter increases when comparing pre- and post-shock states with dependence on M_s.

Several studies took the canonical STI problem further by considering aspects relevant to mixing of fluids; for instance relevant in supersonic combustors.

Tian et al. [116, 115] studied the effect of a variable density (multi-fluid) in the canonical STI prob-

lem. In a single-fluid situation, which was studied up till this point, density fluctuations are only induced by thermodynamic or acoustic fluctuations. A multi-fluid case would additionaly have composition variations affecting the density. Comparison between the multi-fluid and single-fluid STI cases was enabled by solving an additional transport equation for a passive scalar in the latter case. The shock-LIA methodology (generating post-shock turbulence state through LIA) used by Ryu et al. [97] and Livescu et al. [68, 67] can not be relied on in a variable density STI. This follows from nonlinearities arising during the interaction with the shock, which LIA assumes to be absent. Moreover, shock-LIA does not allow for post-shock decay studies. Full DNS simulations must therefore be considered. Due to the prohibitive computational cost and Mach number limitations of a shock resolving strategy, a shock capturing method was considered instead. As the dissipative character of a shock capturing scheme can impact the STI, a first investigation consisted of an evaluation of convergence toward LIA based on the scale separation (Equation 1-8) for the single fluid case. Some differences in behavior with respect to shock resolving DNS were brought to light. The convergence to LIA requires a minimum value of $Re_\lambda \approx 45$. Consequently, their present study looked at the latter value with $M_t = 0.09$ and $M_s = 2$. The simulations demonstrate a stronger amplification of TKE and transverse vorticity fluctuation variance in a multi-fluid setting. A stronger reduction in Taylor microscale and Kolmogorov scale is also observed. Investigation of the scalar variance show enhanced scalar mixing with respect to the single-fluid case. Post-shock transients do also differ; the multi-fluid case reveals a more rapid return of isotropy of the small scales. Moroever, there is a difference in the influence of the shock on the post-shock evolution between the Batchelor scale, λ_b, (smallest scalar scales, computed from the scalar dissipation) and Taylor microscales (intermediate size in comparison to λ_b). A mixing asymmetry is also observed. An additional comprehensive discussion on the subject of variable density physics in the context of shock waves is provided by Livescu [66] and a follow up work on multi-fluid density effects on the post-shock state's flow topology is covered in [117].

Boukharfane et al. [6] focused on the scalar dissipation changes through the STI. In a first set of investigations, confidence in their numerical setup was build through comparison of the different amplifications with the literature. Subsequently, an in depth study of the different components present in the governing equations describing the vorticity evolution is detailed. It comprises discussions on the nature of the turbulence with similar observations as Ryu et al. [97]. Finally, the authors discuss the evolution of a passive scalar through the shock. Specific attention is brought to the scalar dissipation rate (SDR) of this scalar, a quantity with high relevance to the field of turbulent combustion, specifically mixing. Comparisons are made in the presence and absence of the shock wave. The variance of the passive scaler is shown to decrease through the interaction with the shock, which is in line with the single-fluid observations of Tian et al. [116], and scalar mixing is intensified.

Still in the context of passive scalar canonical STI, Gao et al. [24, 23] considered a broader parameter space to further the current understanding with shock capturing DNS; $M_s \in [1.28,5]$, $M_t \in [0.09,0.42]$ and $Re_\lambda \in [37,74]$ as well as Schmidt numbers (Sc) $\in [0.5,2]$. The study of flow topologies and alignment of scalar gradients can have great benefit to the development of turbulent models , for instance, in structured-based subgrid scale models for LES.

Sethuraman et al. [102, 99, 100] focused on the thermodynamic fluctuations in the "standard" (single fluid) canonical STI setup. Their work was motivated by a limited number of studies up to date on the subject as most work was concerned by the velocity fluctuations dynamics throug the shock. Thermodynamic fluctuations do, however, play an important role in, for instance, the turbulence mass and heat flux, and their study could lead to improved turbulence modeling. Moreover, the scarce studies on the topic were limited in parameter space (low M_s and M_t), a gap which the authors aim to close. Sethuraman et al. [102] considered values of Mach numbers $\in$ [1.23,3.5] for M_t = 0.15 and Re_λ = 33. A detailed investigation on the grid refinement demonstrate that the parameters used as a reference for adequate grids by Tian et al. [116] ($\eta_u \approx$ 1.4 the numerical shock thickness δ_n) and by Boukharfane et al. [6] ($\eta_u \approx$ 4-8 δ_x) are not universal and do depend on the adopted numerics. The estimated ratio of η_d/η_u provided by Larsson et al. [52], which relies on the laminar jump conditions, appears to be sufficient. The authors also mention the invalidity of Equation 1-8 for Mach numbers above 2. A suggestion of a different approach to obtain statistics in the shock region which is not influenced by the oscillating shock motion is made. In terms of the STI, higher shock strength (M_s) result in higher post-shock pressure variances which monotonically increase. Similar observations are made for the post-shock entropy variances except that the monotonic increase demonstrates a saturating behavior. Temperature and density fluctuations evolution show some similarities to the pressure variances. Finally, the budget of thermodynamic fluctuations are analysed and the results can be relied on to develop "corrections/additions‚Äù for turbulence models based on the STI physics.

In a follow up work, Sethuraman et al. [100] consider $M_t \in$ [0.05,0.4] to study its effect on the thermodynamic fluctuations. The same Mach number range as in [102] is selected and Re_λ is kept between 30 and 33. For a given M_s, an increase in M_t is paired with an increase in post-shock thermodynamic variances which is somewhat different than the velocity fluctuations behavior. It is also shown that for higher values of M_t, the presence of all three wave types (acoustic, entropy and vortical) are required in the prediction with LIA in order to agree with DNS results. The generated DNS database from [102, 100] is subsequently used in conjunction with LIA to generate predictive models for thermodynamic field variables [101].

In a similar manner as Sethuraman et al. [101], with relevance to shock dominated applications, other authors have developed and improved models relying on knowledge acquired from scale-resolving CFD studies and LIA [106, 86, 87, 46, 119, 94, 7, 95, 120, 50]

Chen and Donzis [10] applied shock resolved DNS to the canonical STI study in conditions where M_s $\in$ [1.07,1.4], $M_t \in$ [0.02,0.51] and $Re_\lambda \in$ [5,65]. Their work was motivated by the scarce number of studies considering higher incoming turbulence levels (M_t) which also plays a role in the formation of shock holes (see [52]) and therefore further quantifying the classification of STI types. Simulations shows that for increased M_t, at a given combination of M_s and Re_λ, the streamwise Reynolds stress amplification (in average) cannot be identified any more, which the authors denote by a "vanished" state. This vanishing is not observed, for instance, in the averaged pressure jump. The states at

which this occurs coincide with values for the similarity parameter K, with definition below, close to 1.

$$K = \frac{M_t}{Re^{0.5}(M_s - 1)} \tag{1-9}$$

Equation 1-9 (see also Equation 1-7) is closely related to the scale separation formulation of Equation 1-8. Several theoretical considerations are discussed in order to suggest scaling parameters. Another point of interest by the authors is the possible anisotropic character of the incoming turbulence, a topic which was briefly studied by Jamme et al. [42] who did not observe fundamentally new mechanism compared to the isotropic case. It was shown to not impact significantly the mean jumps in quantities.

Finally, Braun et al. [9] studied the canonical STI with LES and an improved stretched vortex model (SVM) dubbed the hybrid-SVM (HSVM), a structured-based SGS model. The work is motivated by the use of LES in a predictive sense, instead of focusing on the reproduction of existing DNS results. Therefore, the range of Re_λ values was considerably increased ($\in$ [20,2500]) to study conditions outside the grasp of current DNS. $M_s \in$ [1.2,3] and $M_t \in$ [0.06,0.18] were selected. In order to avoid excessive dissipation in the shock region, the SGS model is deactivated in that region. Adaptive mesh refinement is adopted with careful considerations of the application of the SGS model and a mesh refinement study is presented which suggests that the ratio of coarsest mesh spacing Δx_c to the numerical shock thicknes (δ_s) could be sufficient to evaluate adequate meshes. Comparison with DNS and LIA at different M_s shows similarities in Reynolds stress amplifications. In terms of post-shock dissipation (vorticity amplifications), the comparison with LIA is good below M_s of 2.2.

The LES confirms that for fixed M_s (=1.5) R_{11} amplification first increases with Re_λ (20-40), then decreases (70-100) and remains approximately leveled (> 100). It also confirms that entropy modes become dominant in the density fluctuations behind the shock at higher M_s. Moreover, the mass weighted velocity fluctuations return to isotropy at some point downstream the shock (unlike the Reynolds stresses). Finally, the SGS Reynolds stresses take longer to return to isotropy (in comparison to the SGS vorticity or vorticity).

1.1.1. Summary and Outlook

The literature overview has shown a multitude of numerical studies tackling the canonical STI setup. They encompass a broad range of conditions (M_s, M_t, Re_λ) and even different types of incoming turbulence, in the sense of Kovasznay's analysis. DNS has furthered our fundamental understanding of the topic identifying the different underlying mechanisms, at first through shock resolving and subsequently through shock capturing approaches. In this process, it has been used hand in hand with LIA which has proven to be a powerful tool to study the canonical STI problem, in spite of some discrepancies with the CFD. The reconciliation of DNS with LIA for lower turbulence levels has been an important milestone. By increasing the reliability of LIA over the years, the possibility of its use to generate a post-shock turbulence state without the need to perform full DNS simulations (dubbed the shock-LIA approach), has allowed to overcome computational limitations of DNS in furthering the understanding of the turbulence nature after the interaction with a shock. The shock-LIA ap-

proach will certainly have a role in the continued pursuit toward the comprehension of turbulence mechanisms. With the underlying aim of allowing the study of conditions deemed more realistic, and out of reach for DNS, LES has been considered and SGS models carefully evaluated against existing DNS reference data. A handful of LES studies of the canonical STI setup have subsequently been performed at conditions with higher relevance to real world applications. Henceforward, it will unavoidably be relied upon in the latter context. Over the past few years, an emerging interest in mixing phenomena in the canonical STI was shown and has opened up a whole new path of study with interest for supersonic combustion applications.

1.2. Present Considerations

The present work is motivated by somewhat different considerations than the ones covered in the above literature study. Instead of aiming for the detailed study and understanding of the mechanisms present in the canonical STI problem, the goal is to evaluate the capability of the TAU CFD solver, developed at DLR, in reproducing well documented behaviors. Except for the work of Jamme et al. [41, 42] (with DNS) and Ducros et al. [20] (invisid LES), all DNS and LES related studies of the canonical STI problem adopted high-order accurate ($>$ 2th order) spatial discretization schemes. The majority also relied on third - or higher order time-discretization, with some exception which used second-order accurate approaches. While high-order schemes are unquestionably required to investigate the detailed turbulence and shock wave physics in such an academic problem, they are not considered the norm for industrial type applications where lower-order numerics ($<$ 3th order) are more widespread. In addition, DNS remains out of reach for the study of large scale geometries due to its high associated computational cost. Scale-resolving simulations in such cases must be performed with LES or Detached Eddy Simulations (DES). TAU was mainly developed with the purpose of performing large-scale industrial aerodynamics computations, and in a lesser sense to the in-depth study of canonical problems. Its numerics are, therefore, up to second-order in space and time. In terms of scale-resolving capability, both LES and DES are available. A pertinent question that arises is whether such numerical approaches can still be relied upon to study shock dominated flow problems. Can we recover the expected turbulence amplifications? What about the post-shock decay behavior? This work aims at answering these questions through the study of the canonical STI problem with the scale-resolving LES capability of the TAU CFD solver.

2. The Turbulence Generation

A first step toward the canonical STI study consists of generating turbulence which is convected through the shock. The generated turbulence is not purely random as we seek given characteristics: level of isotropy, type of turbulence (vortical, acoustic, entropy) and combination of M_t and Re_λ. Several methods have been considered in the literature with two main approaches: a spatial and a temporal way. Presently, the temporal approach was preferred, however, both will be detailed up to some level.

2.1. In a spatial manner

The methodology consists of generating fluctuations at the inflow plane and is described, for instance, by Lee et al. [58]. The fluctuations for a variable (e.g. streamwise velocity component) are artificially generated by following a target energy spectrum where the phases have a randomized temporal dependence and changed as to avoid periodic behavior. The resulting signal, in frequency domain, is transformed back into the physical space and superimposed on the mean of the quantity of interest. The fluctuations generated at the inflow plane are convected through and the turbulence starts to develop, i.e. higher order correlations start to form, and evolves towards a realistic state (see 2.2.2 for more details on this). The methodology was, for instance, adopted in the STI studies by Lee et al. [59] as well as by Garnier et al. [25]. However, as pointed out by the latter authors, the streamwise length required to obtain a realistic turbulence state increases with the Mach number (M_s). Computational cost considerations of adopting longer domains can become a limiting factor in which case a temporal turbulence generation approach (see 2.2) would be preferred. However, the generated turbulence in a temporal manner relies on Taylor's hypothesis which is limited in M_t.

2.1.1. High turbulent Mach numbers

When M_t starts to become higher, shock-like structures called eddy shocklets [55] can occur in turbulent flows and the incoming turbulence is not of incompressible nature any more (also referred to as solenoidal or vortical or divergence free turbulence). In a comparative study between spatially and temporally evolving turbulence, Lee et al. [58] demonstrated that Taylor's hypothesis remains valid when $u_{rms}/U_s \approx 0.15$. This in turn implies that M_t should remain below ≈ 0.38. Note that it is not possible to set a hard limit on these numbers given the Reynolds number dependency on the occurrence of eddy shocklets [55]. The invalidity of Taylor's hypothesis implies for the canonical STI that temporally generated turbulence cannot be used as an inflow.

Another approach that was considered to overcome the above limitation, and avoiding the need to rely on a fully spatial method, which is still limited by the downstream distance to obtain a realistic turbulent state, is the use of forced isotropic turbulence. The methodology was adopted by Grube et

al. [31] and consists of forcing a target spectrum as described by, e.g. Overholt and Pope [79]. The target spectrum is obtained through a temporal turbulent decay and is characterised by a desired combination of M_t and Re_λ. Grube et al. [31] investigated M_t levels above 0.52. Note, however, that the equivalent ratios of u_{rms}/U_s were below 0.15 due to the high incoming Mach numbers ($M_s > 3.5$). Other authors [97, 68, 67, 9] did also opt for a forced isotropic turbulent inflow in their STI studies, in spite of the lower M_t levels where Taylor's hypothesis could still be applied.

2.1.2. Other synthetic turbulence methods: STG, SEM

Another possibility could be to generate the turbulence through methodologies popular in hybrid RANS / LES studies. Such an approach would be especially of interest for large scale computations where scale-resolving turbulence methods (LES / DES) will only be applied in specific regions (see e.g. [108]). A multitude of approaches have been proposed in the literature [104, 125] of which two have been implementd in TAU : a synthetic turbulence generator (STG) [22] and a synthetic eddy method (SEM) [84, 105]. The STG is based on the work of Adamian and Travin [1] and the SEM based on the work of Jarrin et al. [43]. These approaches could be of interest in boundary free flows such as the canonical STI setup. Their possible use was therefore explored within the latter context as part of this work.

2.1.2.1. The STG (SEM) setup

The idea consists of having a computational domain which is divided in three zones as depicted in Figure 2-1: one RANS zone, one STG zone, and one LES zone. Note that LES is also activated in the STG zone, the difference being that additional source terms are activated in the latter to initiate the turbulent fluctuations.

A uniform supersonic inflow is prescribed with given turbulent conditions (turbulence intensity and ratio of turbulent to laminar viscosity) and a supersonic outflow where values are extrapolated from the interior of the domain. Periodic boundaries are prescribed for the transverse directions. Inviscid fluxes are treated with the AUSMDV upwind scheme [122, 65]. The same setup is valid for the SEM.

In brief, the STG generates fluctuations by sampling a reference spectrum. This reference spectrum is defined based on an integral length scale (TKE^3/ϵ) and its integrated area equals the TKE. Further specifics are given in, e.g. [104]. The TKE and ϵ values are obtained from reference points of the RANS region. In order to account for the double periodic character of our setup, a correction should be added to the STG methodology. The procedure follows the work by Morsbach and Franke [78] and has been implemented in the TAU code as part of this work. Details can be found in Appendix B.

In order to exert a level of control on the desired fully developed turbulent state that we wish to obtain (combination of M_t and Re_λ) in the LES zone, the free decay turbulence equations can be relied on. The methodology is discussed in Appendix A.1 but in summary:
A synthetic turbulence method will force fluctuations based on a reference state, presently the RANS region. It then takes some time, or better space in this setup, before a fully developed turbulent

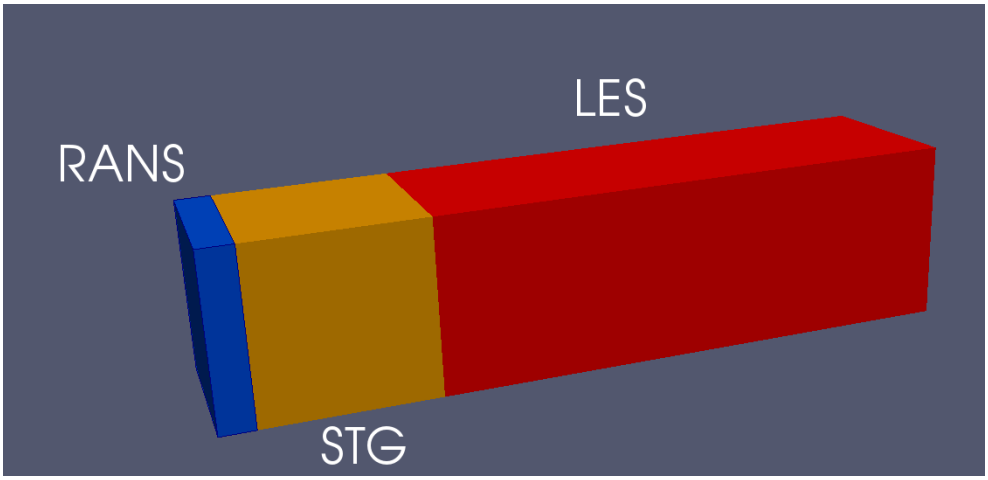

2-1 Illustration of the STG (or SEM) setup.

state is achieved. This goes hand in hand with a spatial decay. If the reference RANS state coincides with our targeted turbulence state we will not obtain the same state in our LES zone, at least not with fully developed turbulence. It is therefore adviced to rely on a different reference state, in which case the free decay equations can be used to get upstream turbulence conditions which should, in theory, result in the desired state at some point. The STG / SEM methdology normally ensures a rapid transition to a fully developed turbulent state.

2.1.2.2. Results of the STG simulations

Diverse conditions, grids and parameter tests were performed and only a small portion of the results will be discussed to provide a view of the essential experience gathered.

Results for a fairly incompressible condition, given in Table 2-1, are presented. It corresponds to one of the pre-shock turbulent states studied by Larsson *et al.* [52] with a relatively low incoming Mach number of 1.05. $x_{singular}$ refers to the singularity given by Equation A.8 in the free spatial decay and sets a limit for the maximum allowed upstream distance that can be considered for a given target. The free-stream dissipation rate grows very quickly with the upstream distance (see also ω/ω_{FS} in Table 1 in Spalart and Rumsey [109]) and reaches unrealistic (infinite) values. In terms of the decay itself, the singularity implies an upper limit for the turbulence intensity that can be achieved for a given setup. In the STG studies corresponding to Figure 2-1, dimensional domains and quantities were considered.

Relying on the free decay Equations (see A.1), turbulence conditions at an 8 mm upstream state, i.e. at the free-stream inflow, are obtained and listed in Table 2-2.

Simulations, with the inflow conditions of Table 2-2, were performed on two different grids. The coarser grid had a uniform grid spacing Δx of 5.55e-5 m while the finer grid had one of 3.70e-5 m. Those quantities were obtained as $2\pi L_{\epsilon,s}/32$ and $2\pi L_{\epsilon,s}/48$, respectively, where $2\pi L_{\epsilon,s}$ is set as the domains' transverse dimensions size. Given the fact that results did not differ much between both

2-1 Target conditions selected for the STG corresponding to the first pre-shock condition listed by Larsson *et al.* [52]

p (Pa)	**T (K)**	γ	**R (J/(mole K))**	ρ **(kg/**m^3**)**
1e5	300	1.4	287.1	1.161
a (m/s)	**M**$_s$	**M**$_t$	**Re**$_\lambda$	**Re**$_L$
347.25	1.05	0.05	39	180
L_ϵ **(m)**	L_λ (m)	L_η **(m)**	L_ϵ/L_η	
2.8262e-4	6.123e-5	4.94e-6	58	
I **or** T_u	μ_t/μ	**TKE (**m^2/s^2**)**	ω **(1/s)**	**x**$_{singular}$**(m)**
0.027493	19.84	150.73	482674.53	0.009123

2-2 Free-stream conditions (8 mm pre-spatial decay) selected for the STG corresponding to the condition of Table 2-1

p (Pa)	**T (K)**	γ	**R (J/(mole K))**	ρ **(kg/**m^3**)**
1e5	300	1.4	287.1	1.161
a (m/s)	**M**$_s$	**M**$_t$	**Re**$_\lambda$	**Re**$_L$
347.25	1.05	0.156	42	216
L_ϵ **(m)**	L_λ (m)	L_η **(m)**	L_ϵ/L_η	
1.09e-4	2.11e-5	1.66e-6	66	
I **or** T_u	μ_t/μ	**TKE (**m^2/s^2**)**	ω **(1/s)**	
0.0858	23.8	1468.92	3920615.69	

cell spacings, the coarser grid analysis is mostly discussed. The cell spacing is on the higher side being larger than $L_{\lambda,\infty}$ but remaining smaller than $L_{\lambda,s}$. The total cell size was $(5+32\times5)\times32\times32$, using 5 cells between the inflow and STG box and 4 equivalent STG box sizes in downstream region. The domain definition is such that the STG box is isotropic in size and cell numbers. In physical coordinates this yields $9.213e-3m\times1.776e-3m\times1.776e-3$ m. In terms of $L_{\epsilon,s}$ we have $(6\times6\times32)$ $L_{\epsilon,s}$. The free stream eddy turnover time τ_t is computed as 6.75e-7 s.

A RANS simulation, that converged to a steady-state, with the k-ω SST, is used to prescribe the initial flow field for the STG. The resulting RANS decay is shown in Figure 2-2. Following the initialization, the simulation is run for approximatively 3 flow through times to get rid of initial transients. One flow through time is equal to 2.53e-5 s. Subsequently, statistics are collected for 19 flow through times. A dual time-stepping scheme with fixed time step of 2e-8s was adopted.

Figure 2-3 shows the resulting TKE decay. The black curve (full line) represents the total TKE, the blue curve (dotted) the resolved portion and the green curve (dash dotted) the subgrid-scale part. The target condition from Table 2-1 is indicated by the horizontal line. After an initial decay in

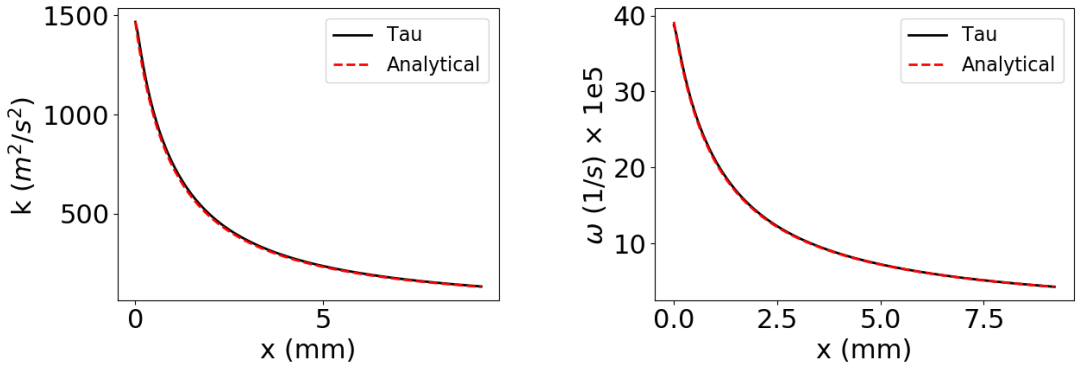

2-2 RANS decay of TKE (left) and ω (right) with inflow conditions set according to Table 2-2.

the RANS region, the synthetic turbulenc amplification is clearly visible. However, as soon we exit the STG region, a strong damping of the turbulent fluctuations (see resolved portion) is occuring, followed by a rapid decay. The strong damping is confirmed by the ratio of resolved to total TKE in the same Figure. Such a damping is however not expected, giving rise to many more investigations as to why this is present in our simulations. Only the most pertinent will now be discussed.

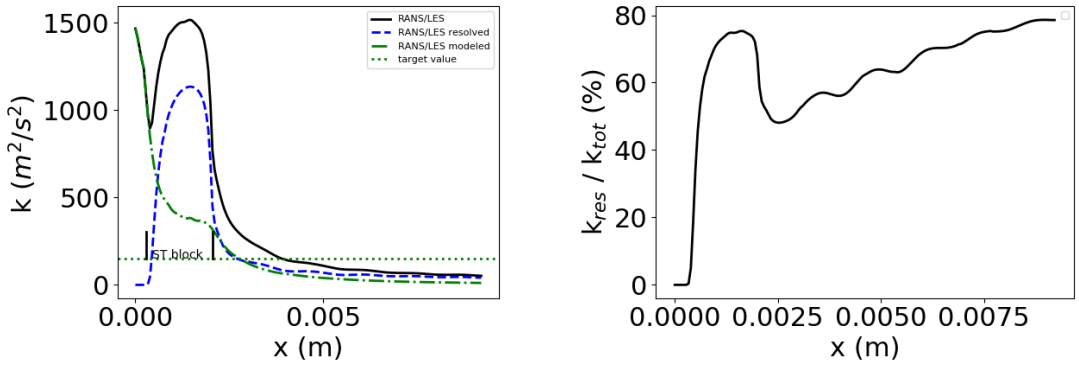

2-3 STG evolution of TKE (left) and portion of resolved TKE (right) with grid 1 (Δx = 5.55e-5m).

A first (logical) check was the adequateness of the grid size. The finer grid did demonstrate a slightly less strong damping (Figure 2-4) of the resolved TKE but still not within expectations. The SEM did also show a similar issue.

Another investigation, to understand the possible cause for damping, was dedicated to the influence of the blending function within the STG formulation. The setup of Figure 2-1 has two interfaces where the definition of the governing equations differ. To ensure smooth transition towards and from the STG zone, it is possible to rely on a blending function which gradually applies the forcing of fluctuations. The blending functions available in TAU are shown in Figure 2-5 and are defined based on a spatial direction, presently the streamwise direction. The influence of blending types 1, 3 and 4 on the post STG-zone damping was evaluated. It did, however, show to not be the

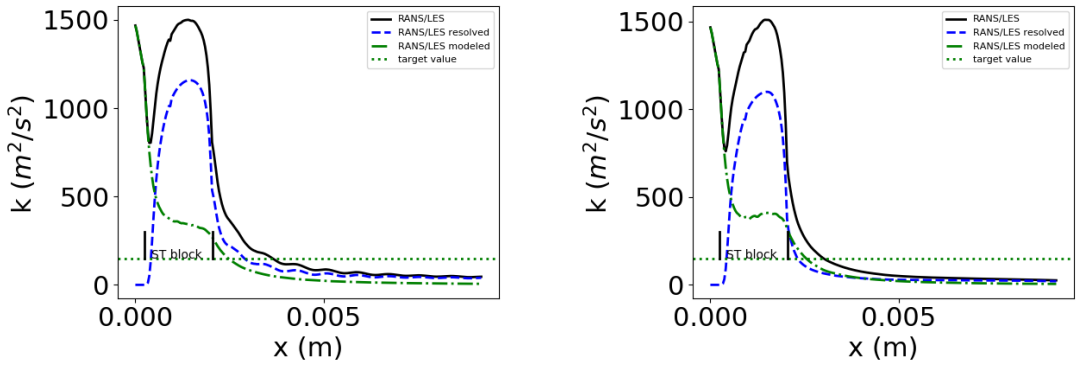

2-4 STG (left) and SEM (right) evolution of TKE with grid 2 (Δx = 3.70e-5 m).

cause for the latter observation.

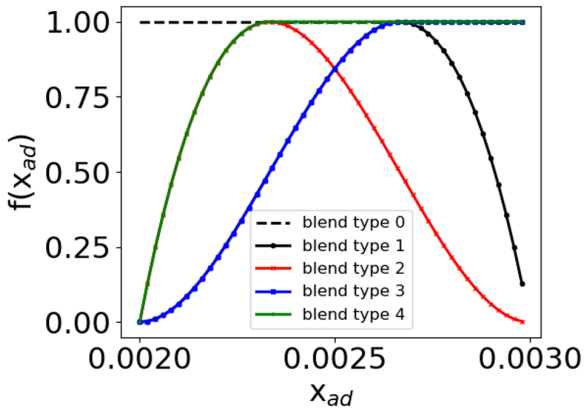

2-5 Blending functions available for use with the STG.

The cause for damping has ultimately been found by considering a different flux treatment: a central discretization scheme, the LD2 (see 4.1). The resulting decay is shown in Figure 2-6. Unlike the upwind scheme (Figure 2-4), the levels of turbulent fluctuations remain high, and the subsequent decay more gradual. The red (dashed) curve indicates the RANS decay behavior. Visualising the instantaneous streamwise velocity component within a slice, Figure 2-7, gives further information on what is happening. The small scale fluctuations seem to have dissapeared in the upwind case while they are present for the central scheme. The underlying reason has been found in conjunction with other studies in 4.1. It is related to Thornber's [114] low Mach number modification's implementation in TAU which depends on the local Mach number. Due to the supersonic convective speed, the modification won't apply in the present case, yielding a highly dissipated turbulence field. A possibility would have been to continue fine tuning the STG methodology in conjunction with the central scheme. However, other hurdles (see also 2.1.2.3), both central scheme and STG related, have been encountered which have led to consider a temporal method to generate a desired turbulence state instead.

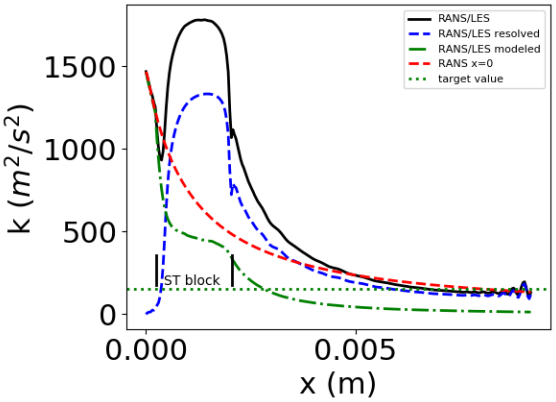

2-6 STG evolution of TKE with a central scheme and grid 2 (Δx = 3.70e-5 m).

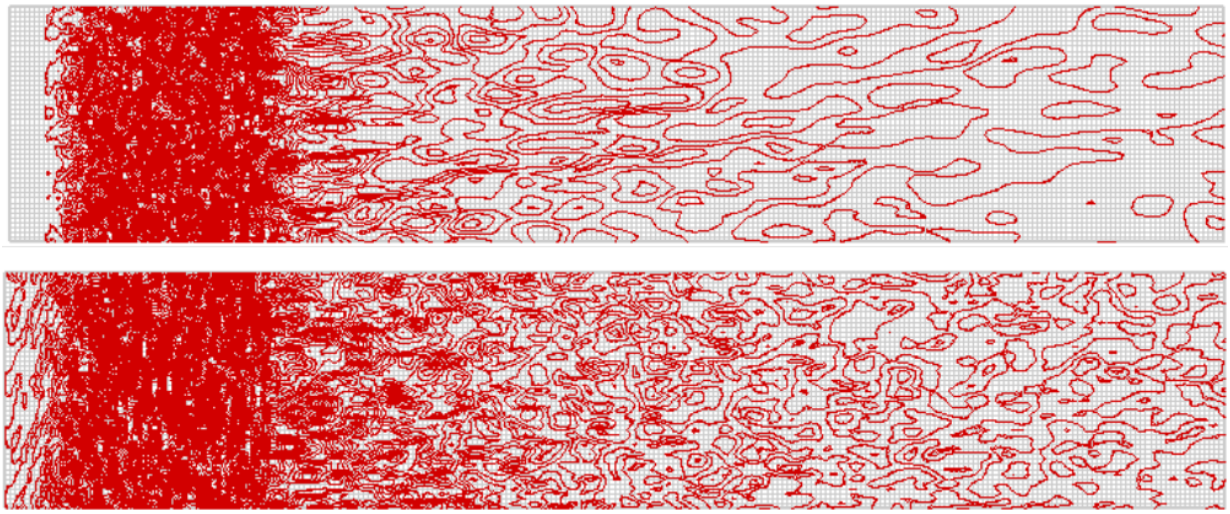

2-7 Instantaneous streamwise velocity-component obtained with upwind (upper) and central (lower) schemes on grid 2 (Δx = 3.70e-5 m).

2.1.2.3. Lessons learned on the STG

The STG and SEM are approaches which could be very useful in practical shock dominated flow applications where scale resolving turbulence descriptions must be locally considered. In such a hybryd RANS/ LES (or DES) framework, turbulent fluctuations could be introduced by relying on RANS zones. Their use toward the study of a canonical application has, however, shown to be very difficult, specifically in generating a desired turbulence state. Most of the present investigations were dedicated to the STG, but some of the issues would remain relevant to the SEM. Some of the observations and concerns are now listed.

- The STG's blending function (Figure 2-5) is problematic in controlling our type of injected turbulence. A divergent free STG flow field would not keep this characteristic when injected in the domain.
- It is possible to not consider a blending function, but would result in sharp / uncontrolled tran-

sitions between the different zones (RANS, STG, LES). It is especially problematic for the central scheme where disturbances would move upstream toward the RANS zone.

- The central scheme induces upstream fluctuations in conjunction with the STG, although a blending function is applied, when the convective speed is not high enough. The issue is shown for a Mach 1.05 case in Figure 2-7.
- The current implementation of the central scheme demonstrate some instabilities near the supersonic outflow (see Figure 2-6) which are expected to amplify with an increased inflow Mach number.
- Several of the central scheme's related issues mentioned previously (upstream disturbances, outflow) could be resolved by the use of geometrical zones where different settings (coefficients) could be applied. More dissipative zones could therefore be introduced. The downside could, however, be that the spatial turbulent decay occurs too rapidly (too dissipative) and hence non-physical.
- The upwind scheme, in its current implementation, cannot be relied on for use with the STG. An overly dissipative behavior has been observed and linked to Thornber's low Mach number modification to not be active due to supersonic local Mach numbers.
- The STG, even though divergence-free by construction, does not generate consistent divergence-free turbulence. The underlying reasons have not been found.
- The application of the STG is undeniably linked to the shock strength. For a given desired level of turbulence, stronger shocks will require longer spatial evolution to achieve realistic turbulence. It's window of application is therefore restricted.
- It has yet to be shown if it is possible to exert a level of control on the STG as to obtain a desired downstream turbulence state: realistic, isotropic, divergence-free, desired M_t and Re_λ. The main level of control is the upstream RANS region with a combination of TKE, and ω (or ϵ). The whole assumption in why the methodology would work is that the expected decay rate will resume after the introduction of the synthetic fluctuations. The STG will definitely provide a fully developed turbulence state, but will it be the one we expect or desire?
- An unexplored aspect of the STG, in this work, is the generation of the thermodynamic fluctuations. For low levels of M_t, its influence would be expected to be limited and uniform pressure and density fields could be used. This would not be true any more when the level of compressibility of the turbulence increases.

2.2. In a temporal manner

The method of choice, like many other authors in the literature, is to generate a desired turbulence state from a temporally decaying homogeneous isotropic turbulence (DHIT) simulation. The field is then convected through the STI's computational domain (Figure 1-1) by Relying on Taylor's hypothesis [111]. We start with an initial turbulence field (see 2.2.1) and let it decay up to a point where our turbulence has become realistic (see 2.2.2) and aim a certain turbulence state (see 2.2.3). The author is grateful to Johan Larsson (University of Maryland, US) and Yogesh Prasaad Madras Sethuraman (International Centre for Theoretical Sciences, India) for their guidance in this task.

2.2.1. The methodology

Many authors rely on the description of Passot and Pouquet [80] as well as Erlebacher *et al.* [21] to generate the initial turbulence field. It is based on a spectral representation of turbulence and does therefore require an inverse Fourier transform to obtain the fluctuations in physical space.

The idea consists of prescribing fluctuations of a quantity by sampling a given reference energy spectrum. The most relied upon spectrum is of Gaussian type defined as a function of the wavenumber *k* as

$$E(k) \sim k^4 e^{-2\left(\frac{k}{k_0}\right)^2} \tag{2-1}$$

where k_0 is the wavenumber associated with the peak in energy which will be referred to as peak wavenumber. Equation 2-1 represents a noisy large scale instability [80] which is illustrated in Figure 2-8 as the "Gaussian model". This model is adequate for low Reynolds number turbulence but at higher values a von Karman like spectrum is more appropriate:

$$E(k) \sim k^4 \left[1 + \left(\frac{k}{k_0}\right)^2\right]^{-17/6} \tag{2-2}$$

The spectrum is illustrated as the "von Karman model" in Figure 2-8.

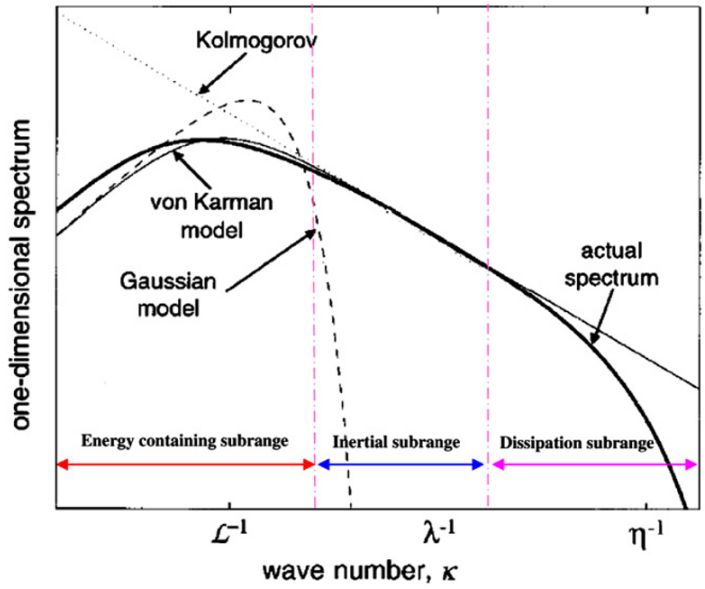

2-8 Initial turbulence spectra types (Figure 1 of [38]) [1]

Equation 2-1 or 2-2 are usually relied on to generate velocity fluctuations. The divergence-free (or solenoidal or vortical) character of the velocity field can be ensured through an Helmoltz decompo-

[1] Reprinted from the Journal of Wind Engineering and Industrial Aerodynamics, 98, S.H. Huang,Q.S. Li,J.R. Wu, A general inflow turbulence generator for large eddy simulation, p 600 - 617, Copyright (2010), with permission from Elsevier.

sition as explained in [21]. Note that through the latter method, a desired level of compressibility can be introduced. In addition, to avoid aliasing errors, a sharp cut-off filter should be considered with cut-off frequency, the Nyquist frequency.

A last aspect to consider are the thermodynamic fluctuations. In a compressible flow, a coupling between the latter and the velocity field exist and therefore, fluctuations of density and pressure (or temperature) must be consistently introduced. Multiple approaches to do so exist including the work of Pirozolli and Grasso [81] and that of Ristorcelli and Blaisdell [93]. Towards the incompressible limit, hence low M_t, it is possible to rely on uniform fields for the thermodynamic quantities. An acoustic transient will then be observed but has a limited strength. This approach was considered by Lee *et al.* [59], Ducros *et al.* [20] and Jamme *et al.* [41], for instance.

The different initial fluctuations are finally introduced on a cubic domain, typically of non-dimensional size $(2\pi)^3$ which results in wavenumbers ranging from 1 up to what the chosen number of grid cells allows, discretized by uniform (isotropic) grids. A triple periodic boundary condition is applied and the flow is allowed to decay in time with a scale-resolving numerical approach (DNS, LES, DES).

In the present work, first attempts in generating initial fluctuations were made following the work of Davidson and Billson [14]. Unlike other approaches, there is no Fourier or inverse Fourier transform required in the methodology. Moreover, it relies on a modified von Karman spectrum : the von Karman Pao spectrum. As the framework does not implicitly contain ways to prescribe thermodynamic fluctuations, other options were sought. Ultimately, the toolbox to generate turbulence for the Hybrid CFD code [4] used in the STI work by Larsson *et al.* [53, 52] has been adopted. Herein, the thermodynamic fluctuations are generated following the methodology of Ristorcelli and Blaisdell [93]. I would like to extend my gratitude to Johan Larsson from the University of Maryland for providing the code to do so.

2.2.2. Realistic Turbulence

An important aspect is that the turbulent field to be used for interacting with the shock should be realistic, i.e. fully developed. The initialisation process is based on sampling a reference spectrum (see Figure 2-8). Therefore, (higher order) correlations between the turbulent structures, characterized by wavenumber, have not yet been formed. These are important to dissipate energy as indicated by Tavoularis *et al.* [44] (Chapter 3: homgeonous flows).

The velocity derivative skewness, defined in Equation 2-3, is an indicator of non-linear interactions and can thus be relied on to evaluate if turbulence is fully developed. Its non-Gaussian nature in a turbulent flow is what determines the dissipation rate [113]. Note that the skewness of any quantity can be defined, and that another velocity component could've been considered but as the turbulence should be isotropic, the final result would be the same. The value should settle between -0.4 and -0.5 for $Re_\lambda \approx 50$ as indicated by Lee *et al.* [57]. In a temporal decay, the velocity derivative skewness, defined as in Equation 2-3, is characterised by a sharp decrease followed by a

slow increase to finally settle around a certain value.

$$S_{u_{,x}} = \frac{\overline{(u_{,x})^3}}{\overline{(u_{,x})^2}^{3/2}} \tag{2-3}$$

The velocity derivative skewness is a parameter related to small scales [52]. The limiting factor in obtaining realistic turbulence is, however, the development of larger scales which occur more slowly. This is especially true for higher Re_λ. For this reason, Larsson *et al.* ensured that the dissipation length scale, L_ϵ (Equation A.18), started growing in time before selecting a desired turbulence state.

A final check is the shape of the energy spectrum, which can indicate possible issues as discussed in [121]. A common problem would be an energy pile up at small scales due to a lack of dissipation which could be linked to the numerics or initialization.

2.2.3. Desired Turbulence

Ultimately, we desire to obtain a targeted turbulence prior to the shock wave. This means, that for a given M_s, a turbulence state should be selected from the temporal decay accounting for the spatial decay length before reaching the shock wave in the actual STI simulation of Figure 1-1. Therefore, $t_{select} = t_{target} - \Delta t_{inlet,shock} = t_{target} - \Delta x_{inlet,shock} / u_s$.

The other important factor is to obtain a given combination of M_t and Re_λ just before the shock. It leads to the question of how this can be achieved, and how these values can be controlled based on the initial conditions. In a DHIT simulation, we will typically set a value of Prandtl number (0.7 or 0.75 in literature) and specify the ratio of heat capacities γ to 1.4. The turbulence generator of Larsson (see 2.2.1) provides an initial velocity field with total turbulent kinetic energy (integration of E(k) over all wavenumbers that can be represented on the chosen grid) equal to 1.5 which is equivalent to rms velocity components equal to 1 (U_{rms}). Mean density and temperature fields are set to ≈ 1. With this information, the only way to control M_t is by setting the gas constant R.

$$R_{target} = \frac{2TKE/M_{t_{target}}}{\gamma \bar{T}} \tag{2-4}$$

In turn, the different choices lead to the pressure field being defined by the gas constant : $p = R_{target}$.

Regarding Re_λ, the only free parameter left to control is the viscosity:

$$\mu_{target} = \frac{\bar{\rho} U_{rms} L_\lambda}{Re_{\lambda_{target}}} \tag{2-5}$$

where L_λ is the spatially averaged Taylor microscale and is set by the initial fluctuating velocity field (average of L_λ in every grid point). Presently, the streamwise Taylor microscale (see Equation 1-3) is

selected. An eddy turnover time can subsequently be defined as

$$\tau_{eddy} = \frac{L_\lambda}{U_{rms}} \approx L_\lambda \tag{2-6}$$

and is used as a guidance for the time step selection in the simulations.

As to which combination of M_t and Re_λ should be initially specified to obtain a target combination at some point in the temporal decay is not known *a priori*. It is unfortunately a trial and error procedure as it strongly depends on the adopted numerics (see 4.1), turbulent flow treatment (DNS, LES, DES) and grids (see 3). This will be demonstrated in this work.

The type of turbulence is another characteristic we target in our pre-shock turbulent state. Presently, (quasi-) purely vortical turbulence is of interest. The turbulence generator ensures a divergence free initial velocity field. By considering its coupling to the thermodynamic quantities in the initialisation, the desired characteristic should be ensured. As mentioned previously, at low M_t, uniform density, temperature and pressure fields could be considered and have as well been used in some simulations.

Finally, the desired turbulence should be as isotropic as possible, with variations lower than 5 % deemed acceptable. While the method to generate an initial turbulent flow field is isotropic by construction, it is not a given to obtain an isotropic realistic turbulence state. One of the reasons is a finite number of grid points. A trial and error procedure had to be adopted. For instance, in the generation of the turbulent flow for the test case of Garnier (Subsection 5.2.2), out of 15 DHIT cases, 7 resulted in an isotropy within 5 %. Moreover, it was impossible, for the different conditions of interest, to obtain isotropic turbulence with a peak wavenumber of 4 for the initial spectrum. The reason for this has not been uncovered. Therefore, peak wavenumbers of 6 were considered instead.

2.3. Final comments on the turbulence generation

While originally a spatial method was considered for the task of obtaining a desired realistic pre-shock turbulence state (see 2.1.2), the approach had to be abandoned for different reasons (see 2.1.2.3) and a temporal approach (the DHIT) favored instead (see 2.2).

Througout this work, several hurdles regarding the turbulence generation with a DHIT case were encountered. These will be discussed at different locations of this report but a succinct overview is given in this section.

- As mentioned in 2.2.3, obtaining realistic isotropic turbulence has been a trial and error process. Depending on the random initial fluctuating fields, an isotropic state within 5 % after some decay in time could be obtained. No *a priori* indication of this success could be found except for the fact that when initial anisotropies in the velocity field where above 5%, an isotropic state could never be retrieved. For a given initial velocity field, the observations are the same whether or not

initial thermodynamic fluctuations are considered.

- In the present work, it was not possible to obtain isotropic turbulence with an initial peak wavenumber (k_0) of 4, except for the Wray test case (see A.2.2). This regardless of the type of initial spectrum: Gaussian (Equation 2-1) or von Karman (Equation 2-2). Both types resulted in the same initial spectrum shape, on the considered grids and low values of Re_λ, due to the application of a sharp cut-off filter in order to avoid aliasing errors. It appears that the large-scale instability peaking at k_0 = 4, is difficult to handle for the second-order accurate spatial discretization schemes adopted in this work. A possible cause for this could be their dissipative character, even though the observation did not change by considering a range of grids up to DNS-like size. It is noteworthy to mention that increasing the peak wavenumber implies more smaller turbulent scales and a reduction of the periodic boundary condition's influence on the simulation as pointed out by Vreman *et al.* [121].
- The whole motivation of LES (or DES) is to resolve only a portion of the turbulent kinetic energy which leads to the use of coarser grids compared to DNS. This advantage is especially of interest for practical applications. There is however a caveat: the size of the coarsest grid. While for some conditions presently selected (see Section 5.2) grid sizes of 32^3 and 48^3 cells for a $(2\pi)^3$ cube where appropriate from an LES point of view ($>$ 80 % TKE resolved guideline of Pope [83]), it was impossible to obtain turbulence with reasonable isotropy. The role of second-order accurate schemes is probably prominent in this result (see also 3.2).
- The velocity derivative skewness ($S_{u,x}$) is used as an indication for realistic turbulence (see 2.2.2). Values of $\approx$ -0.5 are reported by different authors [57, 52] for moderate $Re_\lambda < 50$ which have been observed from high resolution DNS DHIT studies (see also Appendix A.2 , Figure A.2.4 with inverse sign). As the quantity is an indication of the dissipation that is linked to correlations being formed between scales, its value will be affected by the order of the considered numerical schemes. Therefore, a second-order accurate solver will not obtain similar values as others that use higher-order schemes. This was also observed by Vreman *et al.* [121] whom adopt the strategy that the velocity derivative skewness should become and remain negative as an indication of a realistic turbulence state. The authors did additionally observe a dependence of the level of compressibility on its evolution with second-order accurate LES simulations. Garnier *et al.* [25] did also document different values than -0.5 in their high resolution LES work. In this work, $S_{u,x}$ values did also differ from the expected DNS levels . The selected grid size did also play a major role as shown in Section 3.2 (Table 3-1).
- The dissipation length scale is another parameter to be considered in the evaluation of realistic turbulence as pointed out by Larsson *et al.* [52] (see 2.2.2). Its definition, Equation A.18, is based on the knowledge of the dissipation rate of TKE: ϵ. The majority of this dissipation occurs at the smallest turbulence scales which are modeled in an LES. Therefore, to obtain $\epsilon \approx \epsilon_{sgs}$, an estimation must be used which in turn relies on the estimate of the TKE_{sgs}. The latter requires the specification of a coefficient with different values reported in the literature (see also 3.3). While this coefficient has a limited impact on the TKE_{sgs} estimation on fine enough grids, its influence is considerable on the ϵ estimation. Therefore, both values for the coefficient were considered and it was ensured that both L_ϵ values demonstrated an increasing behavior in time. Alternatively, it could be possible to compute ϵ from the time derivative of the total TKE (see Equation A.11) but as it would require many instantaneous solutions to be saved, it was not considered.

- The desired turbulence is characterised by a combination of M_t and Re_λ. The former is related to the TKE (Equation 1-1) and the latter on L_λ (Equation 1-2). In an LES, the total TKE consists of a resolved and a modeled portion from which the latter requires an estimate which is coefficient dependent. As the major contribution comes from the resolved part, M_t is relatively well estimated based on the TKE_{sgs}, that is, if grids are fine enough. The problem lies, however, in Re_λ, and more specifically L_λ . The latter relies on velocity derivatives which are strongly dependent on the grid size as discussed in Section 3.2. It is therefore extremely difficult, with LES grids, to make comparisons with a Re_λ value from other work reported in the literature.
- The premise of the DHIT approach to generate turbulence for the STI is the validity of Taylor's hypothesis. The validity is subject to the values of M_t and Re_λ [58] (see 4.1.2). For the conditions presently considered it could be relied on.
- Finally, the DHIT procedure to generate desired realistic turbulence (see 2.2.1) provides a single instantaneous flow field which can be converted (through convecting at a given speed) into a time signal with a limited length. This single instance does not suffice to study the canonical STI problem as statistics need to be collected over a given period of time. Moreover, the flow has to pass through some initial transients. Therefore, multiple flow fields should be considered for convection through the STI domain. These multiple flow fields must be generated through separate DHIT simulations and carefully "blended" in order to avoid numerical artifacts (see e.g. Xiong *et al.* [126]) and ensuring as realistic an inflow signal as possible. Another possibility would be to consider a single instantaneous flow field to be convected periodically (see 4.2.2.1). The impact of this simplifcation was demonstrated to be limited and therefore adopted in the present work.

3. Grids

The canonical STI problem has shown to be extremely dependent on the grid size and the cell spacing (see 3.1). The conditions of interest, in an LES or DES simulation, show a dependency on the grid size due to its direct relation to the filter width (see 3.2). Finally, the subgrid scale contribution must be modeled and as well considered in some of the statistics to be studied (see 3.3).

3.1. Size and Stretching

In a DNS, the smallest (dissipative) turbulent scales must be resolved, which sets a requirement on the smallest cell size. The Kolmogorov length scale (L_η) is used as a reference and the requirement translates practically into [53]

$$k_{max} L_\eta \geq 1.5 \tag{3-1}$$

where $k_{\max}$ is the maximum resolved wavenumber and is valid for isotropic turbulence. Early DNS of the canonical STI [59, 60] showed already that the energy spectrum is amplified at larger wavenumbers which results in a decrease of the smallest length scales (or increase in largest wavenumbers) across a shock wave. An estimate of the decrease in Kolmogorov length scale based on the Rankine-Hugoniot jump conditions is given by Larsson *et al.* [53]:

$$\frac{L_{\eta,d}}{L_{\eta,u}} \approx \left(\frac{T_d}{T_u}\right)^{3/8} \left(\frac{\rho_d}{\rho_u}\right)^{-1} \tag{3-2}$$

The decrease in L_η has implications on the grid sizes which does not solely involve the streamwise direction but the transverse as well. Note that the above definition is based on the Kolmogorov length scale which is obtained from Equation A.20 and is valid for locally isotropic turbulence. The problem is that the turbulence becomes anisotropic (axi-symmetric) when passing through a shock wave. The concept of a Kolmogorov length scale is therefore not valid any more. However, some distance downstream the shock wave ($k_0 x \geq 10$), the vorticity variances, which are associated to the smallest scales, are returning to isotropy. It could therefore be implied that a Kolmogorov length scale can be defined when that point is reached. Therefore, an estimate such as Equation 3-2 does still make sense. A grid refinement study by Larsson *et al.* [53] did show a strong variation of the vorticity variances. Their return to isotropy occurs faster on finer grids which does make sense given that vorticity is primarily associated with small scale motion. The results of Larsson *et al.* [53] suggests that the post-shock turbulence in the early DNS work of Lee *et al.* [59, 60] is under-resolved. The cell size requirement must therefore be carefully analysed.

The decrease in turbulent length scales across a shock does also have implications for a LES. In a well resolved LES, the contribution of the resolved scales to the total TKE (Equation 3-10) should be at least 80 % [83, 29]. Such a requirement is usually obtained when the minimum cell size is close to the Taylor microscale L_λ (= L_{λ_1} = L_{λ_2} = L_{λ_3} in isotropic turbulence). The decrease in turbulent length

scales across the shock does also apply to the Taylor microscales which was also shown by DNS (see e.g. [59, 53]). The decrease is very localised in the shock region and levels quickly reach higher values (lower than pre-shock) but remain anisotropic with $L_{\lambda_1} > L_{\lambda_2}$ [53]. The latter inequality was not consistently observed in the early (under-resolved) DNS of Lee *et al.* [59, 60]. The implication of a decrease in turbulent length scales in the case of LES is much less restrictive than in a DNS as the target remains the satisfaction of Equation 3-10. It must however be checked. Figure 3-1 presents the percentage of TKE resolved by a grid comprising $104 \times (64)^2$ cells for different conditions: Mach 1.5 of Jamme *et al.* [41] (M_t = 0.133, Re_λ = 5.5), Mach 1.2 of Garnier *et al.* [25] (M_t = 0.136, Re_λ = 11.9) and Mach 1.5 of Larsson *et al.* [53] (M_t = 0.160, Re_λ = 40.0). The SGS contribution to the total TKE is estimated with Equation 3-9 and C_k = 0.07 which is the most conservative option following the discussion in Subsection 3.3. Figure 3-1 shows that the LES resolution is sufficient in the pre-shock region for all cases. In the post-shock region, the higher Re_λ case (Larsson) is under-resolved in the region just behind the shock by this specific grid. This would have to be kept in mind in further analyses.

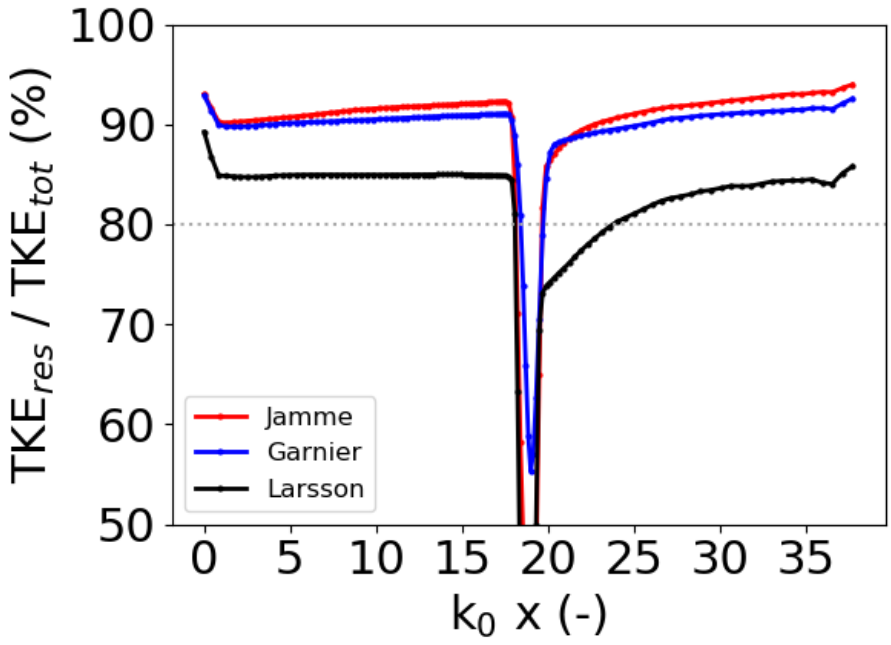

3-1 Percentage of resolved TKE for different conditions selected in present work. $(2\pi)^3$ box, $104 \times (64)^2$ cells. k_0 = 6.

Another important requirement relates to the streamwise cell spacing in the presence of a shock wave. In shock-resolving simulations, such as in [59, 41], the grid should be fine enough so that the shock front inclincation angles are adequately captured, and so is the shock front corrugation, which becomes a more stringent requirement at higher shock Mach numbers (thinner shocks). In a shock-resolving DNS, the latter translates to a shock-normal grid aspect ratio [60]

$$r_\Delta = \frac{\Delta x}{\Delta y} = O(i_t) \tag{3-3}$$

and scales with the turbulence intensity ($i_t = u_{\mathrm{rms}}/\bar{u}_1$). The shock front corrugation is shown to have a strong impact on the evolution of transverse velocity fluctuations through the interaction and should therefore be correctly resolved [60]. In a shock-capturing setting, the shock front corrugation is the important length scale and is of comparable size to the small turbulence length scales. Shock thickness becomes irrelevant. Nevertheless, the parameter r_Δ, remains a useful reference to describe the required shock-normal grid spacing which will be slightly less restrictive. Garnier *et al.* [25] did for instance consider shock front corrugation resolutions (r_Δ) according to Equations 3-4 and 3-5, for a Mach 1.2 and Mach 2 interaction, respectively.

$$r_\Delta = \frac{(\Delta x)_{min}}{\Delta y} = 2\sqrt{3} i_t \tag{3-4}$$

$$r_\Delta = \frac{(\Delta x)_{min}}{\Delta y} = \sqrt{3} i_t \tag{3-5}$$

The grid stretching does also have an impact on the scale separation between the smallest turbulence scales ($L_\eta = \eta$) and the (numerical) shock wave thickness (δ / δ_n). A large separation implies that the STI is mainly of linear nature and observations should be more comparable to LIA [97]. Such a characteristic is sought for as limiting the viscous effects, which are grid and solver (numerics) dependent, allow for a more universal discussion of the STI. Ryu *et al.* [97] propose to use the (inverse) ratio of (numerical) shock thickness to Kolmogorov length scale (Equation 1-8) as a parameter to control the scale separation. This scale separation was carefully investigated in the shock-capturing DNS of Tian *et al.* [116] which did show that a scale separation ratio $\eta/\delta_n > 1.4$ suffices for converged statistics. As the numerical shock thickness strongly depends on both the grid and the numerics, it is likely that a different solver has different requirements.

It must be noted that the streamwise grid stretching could possibly affect the SGS modeling in a LES. This would be the case for the standard Smagorinsky SGS model of Garnier *et al.* [25] which relies on the cell volume for the filter width. In this work, such impact is not present as the maximum cell edge length is used to define the filter width. Finally, it was observed that too high cell aspect ratios lead to instabilities with the central scheme. Such influence must be kept in mind when constructing a grid.

In present work, the grading was performed with the so-called Roberts cluster function which is detailed in [13] or [2]. An example of such spacing is shown in Figure 3-2 with resulting x-velocity flow field in Figure 3-3 where the shock front corrugation is visible. The xz plane at the center is shown.

To illustrate the effect of grid stretching, the Reynolds stress amplifications in the Mach 1.2 STI of Garnier (see also Subsection 5.2.2) is given in Figure 3-4. The inflow sampled DHIT box has Re_λ = 15.27 and $M_{t,\mathrm{res}}$ = 0.190. Selected grids contain 96×96^2 (uniform) and 138×96^2 (grading) cells. The grading in the latter grid is defined based on Equation 3-4 considering i_t = 0.05 which follows

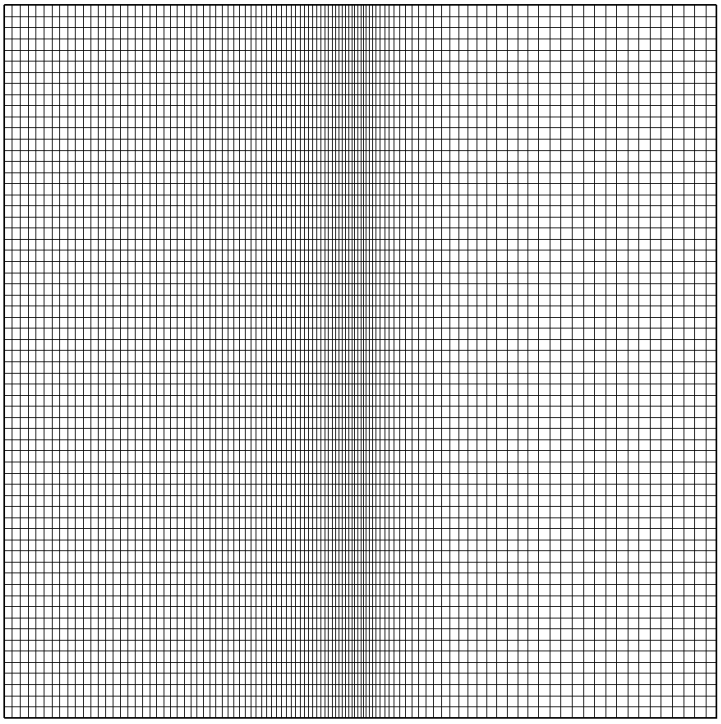

3-2 Example of streamwise grid spacing , $(2\pi)^3$ box, $104 \times (64)^2$ cells.

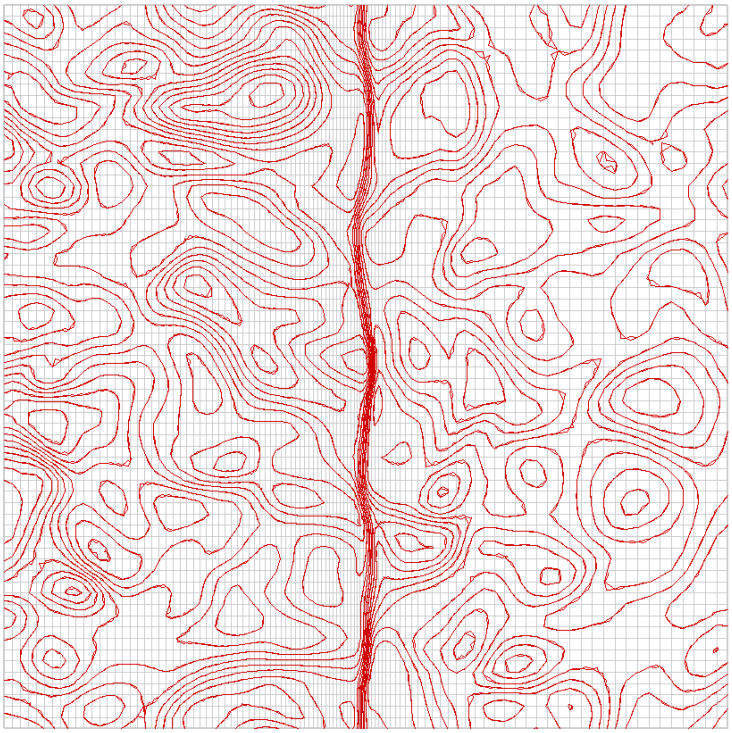

3-3 Example of shock front corrugation (x-velocity shown) in xz-plane. $(2\pi)^3$ box with $104 \times (64)^2$ cells.

from the work of Lee *et al.* [59] and is slightly more conservative than Garnier *et al.* [25] (i_t = 0.07).

The peak (resolved) R_{11} is 3.5 % higher with adequate grid stretching to capture the shock front corrugation. For the transverse component R_{22}, the post-shock region is mostly affected by the uniform grid spacing with a more rapid decay.

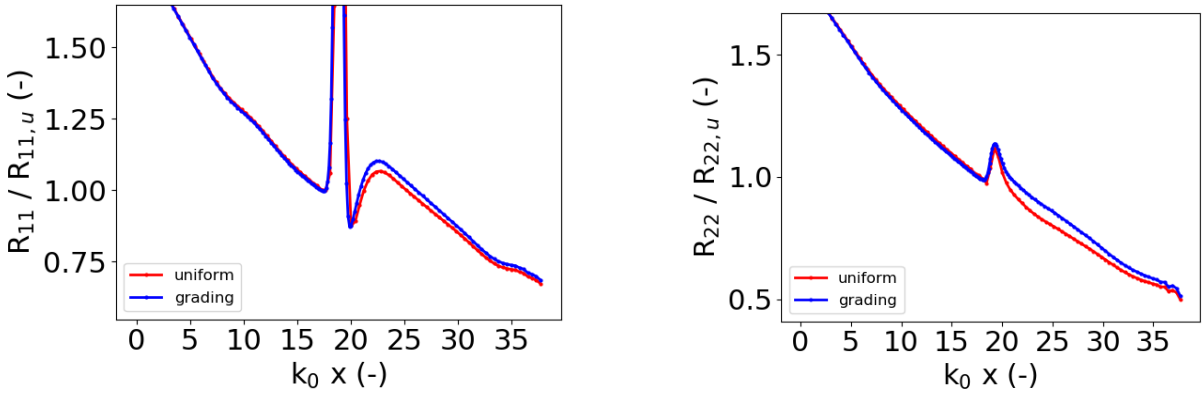

3-4 Effect of cell stretching on the amplifications for the Mach 1.2 STI of Garnier. uniform = 96×96^2 cells, grading = 138×96^2 cells, k_0 = 6.

3.2. Refinement and Coarsening

The desired pre-shock quantities are affected by the selected grid size. M_t is less affected given the main contribution from the large scales which are resolved on an adequate LES grid ($>$ 80 % of energy resolved). Re_λ (actually L_λ) is more of an issue with strong grid dependencies, at least with the second order accurate discretization schemes selected in this work. Such dependency can become problematic when operations involve different grids such as the filtering of a turbulent flow field. The latter is for instance commonly applied when LES of the canonical STI is performed with DNS generated inflow database (see e.g. Garnier *et al.* [25]). The procedure would however imply changes in Re_λ (L_λ) and M_t, both in the inflow database as well as in the pre-shock values due to changes in the decay rates. This is examplified with Figures 3-5 to 3-7.

The grids considered contain 96^3, 64^3 and 48^3 cells uniformly distributed on a domain size of $(2\pi)^3$. The inflow was generated on the finest grid and the DHIT solution (Re_λ = 14.02 and $M_{t,res}$ = 0.186) is convected at Mach 1.2. Filtering of this flow field on the other two grids is performed. No shock is considered in the setup. For the simulations, R (gas constant) and μ are kept the same as the finest grid, only the convective mean flow superimposed on the fields is adapted accordingly, as well as the time step size controlling the varying inflow BC. This would be equivalent to the procedure of Garnier *et al.* [25]. The characteristics of the filtered turbulence fields are given in Table 3-1. Re_λ as well as the velocity derivative skewness increases by coarsening the grid. Slightly surprising is the higher resolved M_t for the coarsest grid. The percentage of resolved TKE (Equation 3-10), also used in the computation of $M_{t,tot}$, relies on estimating the SGS TKE with Equation 3-9 and C_k = 0.07.

3-1 Filtering effect on different grid sizes for Garnier condition 1, i=240 turbulent box.

	96^3	**64^3**	**48^3**
$M_{t,res}$	0.186	0.182	0.186
$M_{t,tot}$	0.192	0.193	0.204
$Re_{\lambda,1}$	13.96	15.20	16.54
$Re_{\lambda,2}$	14.24	15.52	16.90
$Re_{\lambda,3}$	13.87	15.08	16.40
$\overline{Re_\lambda}$	14.02	15.27	16.62
$S_{u,x}$	-0.368	-0.324	-0.289
S_{mean}	-0.418	-0.375	-0.338
% tke resolved	94	89	83

As expected, a quicker spatial decay is observed for M_t (resolved part only) in Figure 3-5. The higher initial M_t on the coarsest grid seems to be relaxing to lower levels . The increase in L_λ (Figure 3-6) is responsible for the increase in Re_λ (Figure 3-5). The velocity derivative skewness (Figure 3-6) remain at the higher levels caused by the coarsening. The anisotropy in Reynolds stresses is given in Figure

3-7 and increases with coarsening the grid. On the coarsest grid, the levels are not within the 5 % range any more. The same increase in vorticity anisotropies is shown, that, for this initial field, has too high values on all grids. Nevertheless, the original temporal decay shows anisotropies within desired bounds. The cause for this increase could be found in the uniform spacing choice.

The take away from this investigation is that a separate temporal decay should be performed for the different grids. This would imply separate (initial) turbulence generation too. However, it seemed to be problematic to obtain isotropic turbulence on coarser grids (48^3 cells or less) with second order accurate spatio-temporal discretization methods for the turbulent conditions considered here. Such feature is not unheard off. In a DHIT study, Thornber *et al.* [113] mention that for their conditions, with ILES, at a grid size of 32^3 cells, the flow is significantly anisotropic. For the finer grids (above 64^3 cells) the anisotropy levels remain below 6 %. The study was performed with the Minmod limiter, which should be 2nd order accurate, as well as with a third-order accurate limiter. They state that the 32^3 cells grid does not allow for a realistic turbulent flow development and the velocity derivative statistics evolution are Gaussian (skewness and flatness), even for the third order limiter.

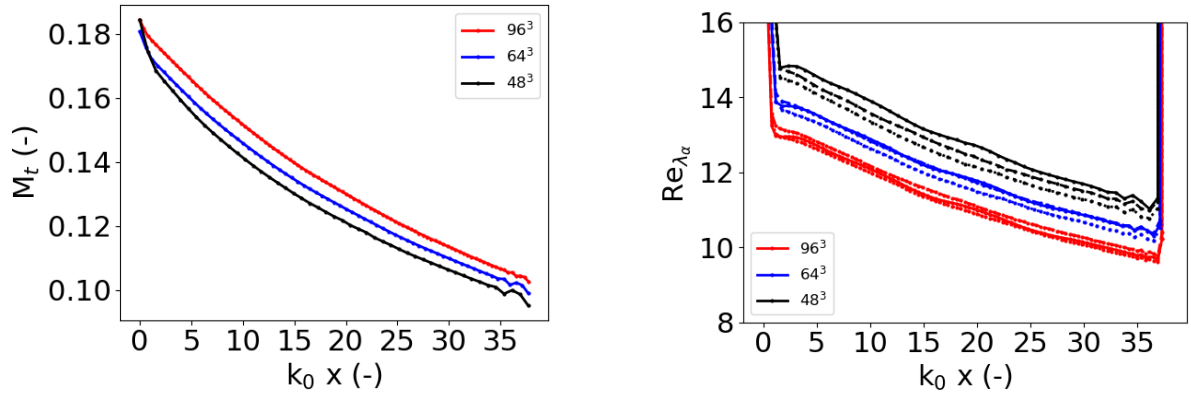

3-5 Effect of filtering on M_t (left) and Re_λ (right) without shock wave. k_0 = 6, full: $\alpha = 1$, dashed: $\alpha = 2$, dotted: $\alpha = 3$.

Note that the discontinuities present at the starting and end axial positions of some of the figures is purely an artefact of the computations of the derivatives.

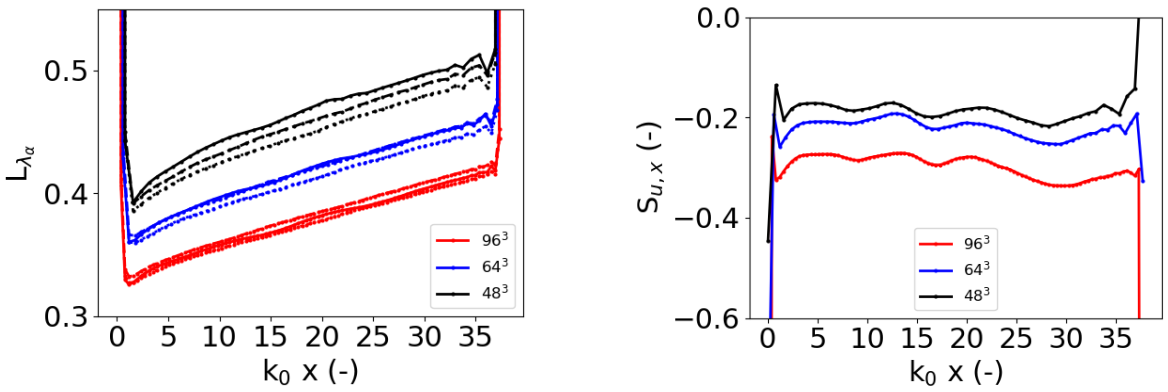

3-6 Effect of filtering on L_λ (left) and $S_{u,x}$ (right) without shock wave. k_0 = 6, full: $\alpha = 1$, dashed: $\alpha = 2$, dotted: $\alpha = 3$.

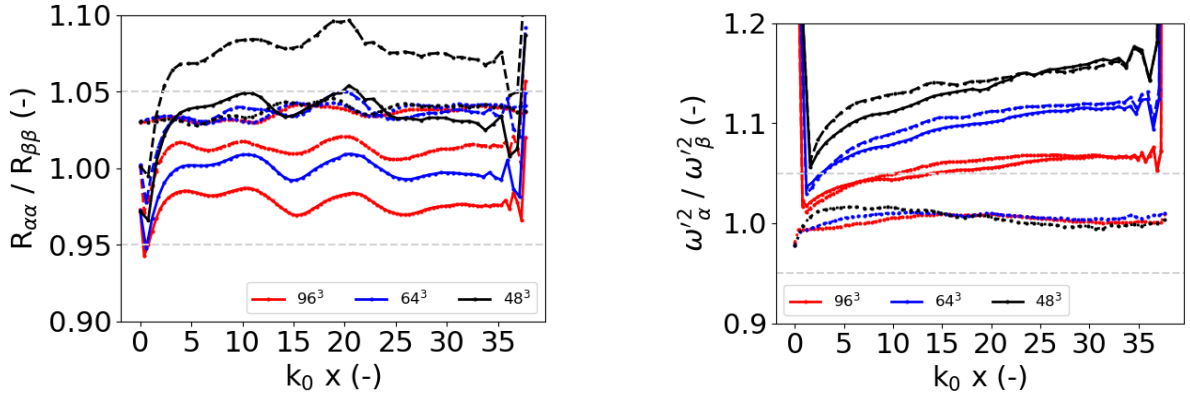

3-7 Effect of filtering on anisotropies of Reynolds stresses (left) and vorticity variances (right) without shock wave. k_0 = 6, full: $\alpha = 1$, $\beta = 2$, dashed: $\alpha = 1$, $\beta = 3$, dotted: $\alpha = 2$, $\beta = 3$.

3.3. Subgrid-scale contribution

In a LES simulation, only the large scales are resolved, and therefore the only fluctuating information readily available is from those scales. The smallest, unresolved / modeled scales are also contributing to the fluctuating flow field. When relying on a DNS simulation as a reference, the comparison with a LES result requires to account for the subgrid scale contribution to the parameter of interest. In the canonical STI problem, such a parameter could be the Reynolds stress amplifications for instance.

In TAU, Smagorinsky's eddy viscosity model is used for closure which assumes isotropy of the smallest (modeled) scales (see also the original work of Smagorinsky [107] and Lilly [64]).

$$\nu_t = (C_s\Delta)^2|\tilde{S}| = (C_s\Delta)^2(2\tilde{S}_{ij}\tilde{S}_{ij})^{1/2} \tag{3-6}$$

where C_s is set to 0.17 in TAU, following calibration with temporally DHIT studies. Δ is the filter width and can be defined several ways. The standard setting of TAU defines it as the maximum of the cell edge lengths (Equation 3-7).

$$\Delta = max(\Delta x, \Delta y, \Delta z) \tag{3-7}$$

The standard Smagorinsky's model has been considered in different STI studies (e.g. [25, 5]). In spite of its known excessive dissipative character in the canonical STI problem, it's simplicity with respect to dynamic models renders its use for industrial type applications attractive. Moreover, other aspects of the canonical STI setup (grid size and stretching, numerics) do play an important (or even more important) role in addition to the SGS model's choice.

The SGS contribution to the fluctuating field could be obtained, in analogy to RANS, through a TKE

$$TKE_{sgs} = \frac{1}{2}\left(\overline{u'^2_{sgs} + v'^2_{sgs} + w'^2_{sgs}}\right) = \frac{3}{2}\overline{u'^2_{sgs}} \tag{3-8}$$

where the last equality makes use of the isotropy assumption. In search of u'_{sgs}, the problem is now reduced into finding TKE_{sgs}. A common and simple estimate for this parameter is given by [90, 26, 29]

$$TKE_{sgs} = \left(\frac{\nu_t}{C_k\Delta}\right)^2 \tag{3-9}$$

The last step is the choice of the constant C_k. A logical choice would be $C_k = C_s = 0.17$ but different values for this parameter are reported in the literature, e.g. $C_k = 0.07$ [26, 29] (scramjet flow studies) or $C_k = 0.094$ [90, 47].

The difficulty in setting C_k lies in the fact that refining an LES grid will influence both the numerical and the SGS dissipation. This is especially problematic in evaluating whether a selected grid resolution is adequate. A commonly adopted parameter to establish the latter is the ratio of resolved to

total (resolved + SGS) TKE following Pope [83]

$$S = \frac{TKE_{res}}{TKE_{tot}} = \frac{TKE_{res}}{TKE_{res} + TKE_{sgs}} \tag{3-10}$$

Reuß *et al.* [90] investigated this ratio by comparing several methods to estimate the subgrid scale portion of the turbulent kinetic energy with varying complexity, among which Equation 3-9. A temporally DHIT test case is considered and confirmed the strong dependency of the estimation method on the grid size through comparison with experimental reference data: overestimating and underestimating S (Equation 3-10) on the coarsest and finest grid, respectively. No estimation method is shown to be superior over another and therefore, the additional cost of more elaborate approaches is not justifiable. In conclusion, estimating TKE_{SGS} through Equation 3-9 is acceptable. Nevertheless, the problem of selecting C_k remains.

In order to help in this selection process, the ratio of turbulent to molecular viscosities μ_t/μ was investigated in the canonical STI at Mach 1.2 targeting turbulence conditions of Garnier *et al.* [25]. The smaller this value, the closer the resolution is to the DNS. Recall that μ_t is provided in the LES by the subgrid-scale model. Figure 3-8 shows the resulting profiles for two different grids. They correspond to Grid 1 - Case 2 and Grid 2 - Case 2 of Table 5-2, respectively. The absolute μ_t/μ values are quite low (compare to Figure A.2.11) in both cases and the differences are approximatively a factor 2. It must be noted that the post-shock evolution of μ_t/μ is somewhat different to that shown for a Mach 2 STI study of Garnier *et al.* [25] (Figure 10, Smagorinsky). Table 3-2 summarizes the SGS contribution (in %) to the total TKE with Equation 3-9 considering two values for the constant C_k (0.07 and 0.17). In all cases the contributions of the SGS fluctuations is below 1.5 % and is consistent with the low μ_t/μ ratio in Figure 3-8. A C_k value of 0.07 is more conservative. The results confirm that the selected resolutions are close to a DNS. It is however, still not trivial to decide which value for C_k would be the most suitable.

3-2 SGS contribution to the R_{11} amplification in the Mach 1.2 canonical STI of Garnier *et al.* [25].

Case ID	δ/η **(res)**	R_{11} / $R_{11,u}$ **(res)**	R_{11} / $R_{11,u}$ **(tot C_k = 0.07)**	**% SGS (C_k = 0.07)**	R_{11} / $R_{11,u}$ **(tot C_k = 0.17)**	**% SGS (C_k = 0.17)**
104×64^2						
Grid1 - Case 2	1.50	1.115	1.129	1.2	1.120	0.5
138×96^2						
Grid2 - Case 2	1.44	1.113	1.122	0.8	1.116	0.2

The same ratio is plotted for two other canonical STI simulations in Figure 3-9: the Mach 1.5 of Jamme *et al.* [41] and the Mach 1.28 of Larsson *et al.* [51]. See Section 5.2 for further details on the cases. The results are shown for the coarser of the two grids ($104 \times (64)^2$ cells) considered in

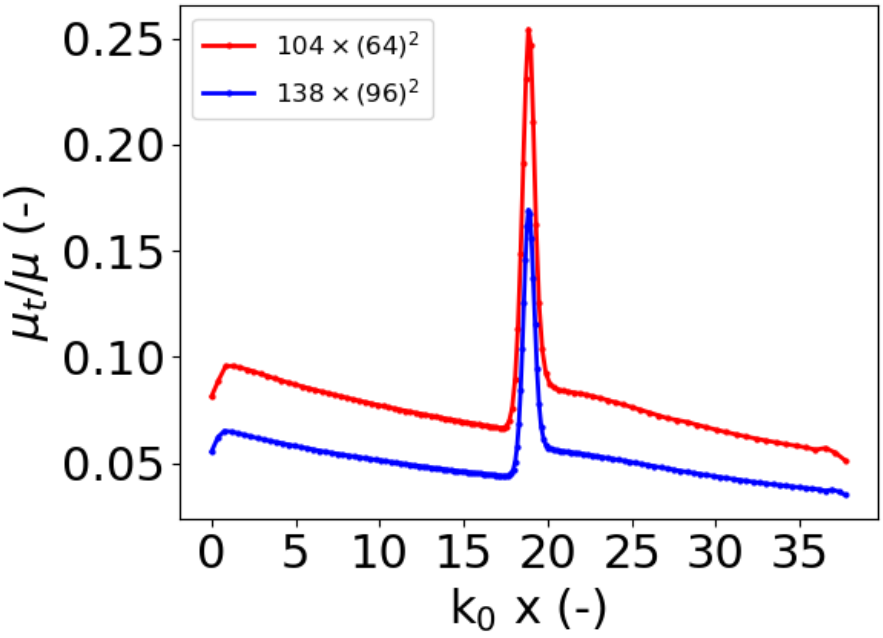

3-8 Ratio of μ_t/μ in the canonical STI conditions of Garnier *et al.* [25] at Mach 1.2. k_0 = 6. In this LES, μ_t is obtained from the subgrid-scale modeling.

the above discussion. The pre-shock turbulence (based on resolved flow field) is M_t = 0.138, Re_λ = 5.63 and M_t = 0.136, Re_λ = 38.86 for Jamme and Larsson, respectively. Pre-shock conditions in the simulation of Garnier are M_t = 0.131 and Re_λ = 11.32 (see Table 5-2: Grid1 - Case 2).

In the case of Jamme, where Re_λ is extremely low, μ_t/μ levels are similar to the finer grid of Figure 3-8. In the second-order accurate reference DNS [41], the grid convergence study in a temporal DHIT based on one-dimensional energy spectra indicated that $(64)^3$ points are not sufficient. A domain containing $(128)^3$ points did yield better agreement between predictions and theory. However, in the decay of TKE and ϵ for the same study, discrepancies between the different grids were extremely small and the $(64)^3$ could be judged fine enough. A simulation with $150 \times (96)^2$ cells was also performed and shows differences in μ_t/μ smaller than a factor $\approx$ 1.5 with respect to the coarser grid. In terms of SGS fluctuations contribution to the R_{11} amplification (Table 3-3), the differences between the two grids for this low Re_λ case are similar to Garnier in Table 3-2, regardless of the C_k value. The observation indicate a proximity to DNS resolution.

Regarding the results for Larsson, the levels of μ_t/μ are much higher than for Garnier and Jamme on the same grid which is expected given the higher Re_λ. Note that the DNS of Larsson [53] required $(384)^2$ points in the tranverse planes and is mainly set to account for the decrease in Kolmogorov length scale (higher wavenumber). Nevertheless, the presently selected grid size is far from a DNS resolution. In terms of SGS contribution to the R_{11} amplification, the difference between the C_k values is larger than 3 % while in all other cases discussed it was below 1 %. In terms of the

parameter S (Equation 3-10), C_k = 0.07 would yield a value of 85 % while C_k = 0.17 indicates that 97 % of the total TKE is resolved in the DHIT box sampled for the inflow. Considering the grid requirement for DNS used by Larsson, it would appear that C_k = 0.17 overestimates considerably the portion of resolved TKE, suggesting C_k = 0.07 to result in a more appropriate estimation of the SGS TKE through Equation 3-9. Nonetheless, looking at both values for C_k is useful as it sets bounds within which the expected SGS contribution would lie.

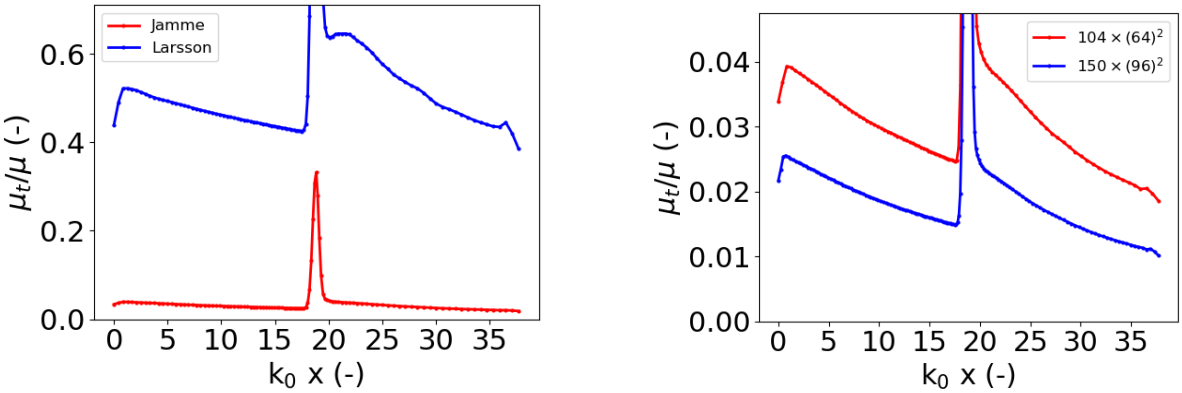

3-9 Ratio of μ_t/μ in the canonical STI.. Comparison between the conditions of Jamme *et al.* [41] and Larsson *et al.* [53] on grid with $104 \times (64)^2$ cells (left) and comparison between two grids for Jamme *et al.* [41] (right). k_0 = 6.

3-3 SGS contribution to the R_{11} amplification in the Mach 1.5 and Mach 1.28 canonical STI of Jamme *et al.* [41] and Larsson *et al.* [53].

Case ID	δ/η **(res)**	R_{11} / $R_{11,u}$ **(res)**	R_{11} / $R_{11,u}$ **(tot C_k = 0.07)**	**% SGS (C_k = 0.07)**	R_{11} / $R_{11,u}$ **(tot C_k = 0.17)**	**% SGS (C_k = 0.17)**
104×64^2						
Grid 1 - Jamme	0.89	1.195	1.208	1.1	1.199	0.4
Grid 1 - Larsson	0.60	1.315	1.376	4.6	1.328	1.3
150×96^2						
Grid 2 - Jamme	0.86	1.190	1.201	0.9	1.193	0.3

4. Numerics

The aim is to select the most appropriate spatio-temporal discretization settings in TAU to study the STI problem. On one hand we have the turbulence while on the other hand we have a shock wave. Appropriate description of the turbulence requires as low as possible numerical dissipation which could affect the decay rates. The presence of a discontinuity, such as a shock wave, requires numerical dissipation for stability considerations as well as some way to recognize its presence in the flow field which could be achieved through a "sensor". These requirements will mostly impact the spatial discretization and is the topic of Section 4.1. The temporal discretization is discussed in Section 4.2.

4.1. Spatial discretization

TAU allows for two main categories of spatial discretization schemes: upwind schemes (including AUSMDV [122, 65]) and the LD2 central scheme [70, 105]. Several comparison tests have been performed by multiple authors in TAU among which the temporally decaying turbulence is the most relevant to the STI scale resolving capability. In this section, the two aforementioned categories of spatial treatment will be assessed in the context of the final setup of this work: generating turbulence (see 4.1.1), convecting the generated turbulence (see 4.1.2), study the STI. The latter implies shock capturing capability and is the subject of 4.1.3.

4.1.1. Temporally Decaying Homogeneous Isotropic Turbulence (DHIT)

Temporal DHIT test cases are commonly used to calibrate coefficients of LES or DES models relating to the subgrid scale behavior. They are usually performed on $(2\pi)^3$ domains yielding wavenumbers starting from 1 ($k = 2\pi/L_x$). A popular test case is the one of Comté-Bellot and Corrsin [11] and has previously been studied with TAU by Knopp et al. [47]. Another possible DHIT reference is the unpublished DNS database of Wray (1997) [1]. More information on the different data is provided in Appendix A.2.1. The Wray test case was reproduced with the LES capability of TAU (A.2.2) in which the upwind (the AUSMDV) and central flux schemes are compared. Simulations were performed starting from an initial realistic DNS flow field as well as starting from a random initial turbulence field which has to develop into a realistic state with LES. The latter setting is relevant to this work's methodology in obtaining the desired pre-shock turbulence (see 2.2). The result of this study is summarized in Appendix A.2.2.

The comparison between the upwind (AUSMDV) and central scheme (LD2) was also made considering turbulent conditions of interest in the context of the STI from Garnier et al. [25]. The initial field is characterised by a Gaussian spectrum (Equation 2-1) with $M_{t,0}$ = 0.36, $Re_{\lambda,0}$ = 28 and k_0 = 6 and

[1] See `https://torroja.dmt.upm.es/turbdata/agard/chapter3/HOM02/CB512.f_t`

is allowed to decay on a $(2\pi)^3$ domain discretized by 64^3 cells. Uniform thermodynamic initial flow fields were prescribed which is acceptable given the low Reynolds number considered here [59, 25]. Note that $M_{t,0}$ is computed from the resolved part of the velocity fluctuations.

The ratio of turbulent to laminar eddy viscosity in Figure 4-1 indicate that the selected grid size (yielding a filter width of $2\pi/64$ = 0.0981747704) is quite close to a DNS resolution in comparison to Figure A.2.11. Note that Garnier et al. [25] used a 64^3 cells cube with their high-order accurate DNS. The velocity derivative skewness levels are around -0.38 and, similarly to Figure A.2.16, it is not evident to rely on it to evaluate whether the turbulence is realistic. It could however be inferred that initial transients occur before t/τ_t = 2 (where $\tau_t \approx 0.36$). L_ϵ, computed according to Equation A.18 and relying on Equation A.11, starts to increase around t = 2 τ_t and confirms that the turbulence is realistic around that time. Some differences between the upwind and central scheme are visible but remain small. Higher velocity derivative skewness levels indicate higher numerical dissipation which in this case is visible for the upwind scheme.

This increased dissipation is also visible in the decay of the turbulent Mach number (based on resolved TKE) and Re_λ in Figure 4-2. However, the differences with the central scheme are smaller than 2 %, from which it can be concluded that both schemes are adequate to simulate the temporal DHIT. This observation is valid for the grid considered here and might not hold at much coarser grids. Figure 4-3 shows the velocity fluctuations' (Reynolds stress) - and vorticity variances' anisotropies with small differences in their values. The horizontal (dashed) lines indicate the 5 % anisotropy levels. The turbulence demonstrate the desired levels of isotropy (within 5 %). The turbulence generated here will subsequently be used to interact with a shock wave in a spatial simulation and is described in Subsection 4.1.2.

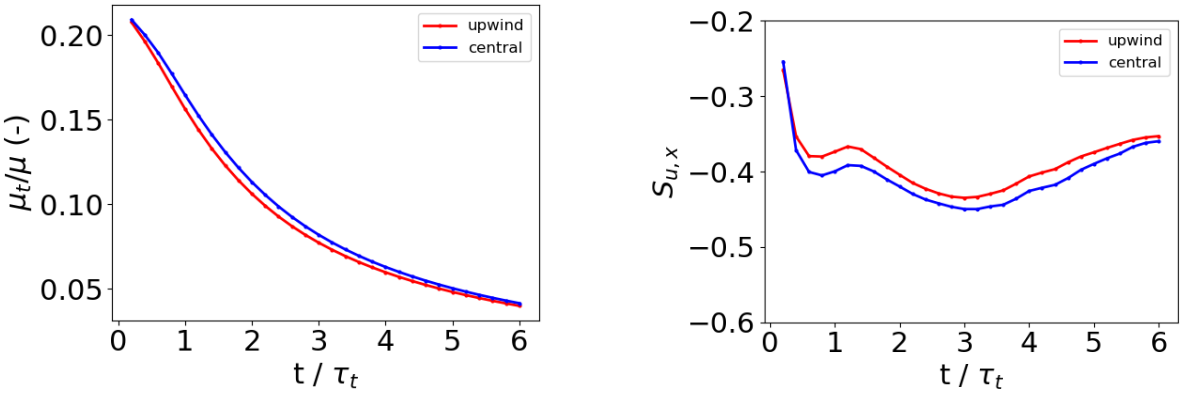

4-1 Effect of spatial discretization on the viscosity ratio (left) and velocity derivative skewness (right) in the DHIT case with $M_{t,0}$ = 0.36, $Re_{\lambda,0}$ = 28 and k_0 = 6. Grid with 64^3 cells, $\tau_t \approx 0.36$

4.1.2. Spatially Decaying Isotropic Turbulence: Taylor's hypothesis

In the majority of STI studies, a temporally generated turbulence flow field is convected through the domain by relying on Taylor's hypothesis. A detailed study between spatially and temporally generated turbulence by Lee et al. [58] demonstrated that the aforementioned hypothesis can be relied

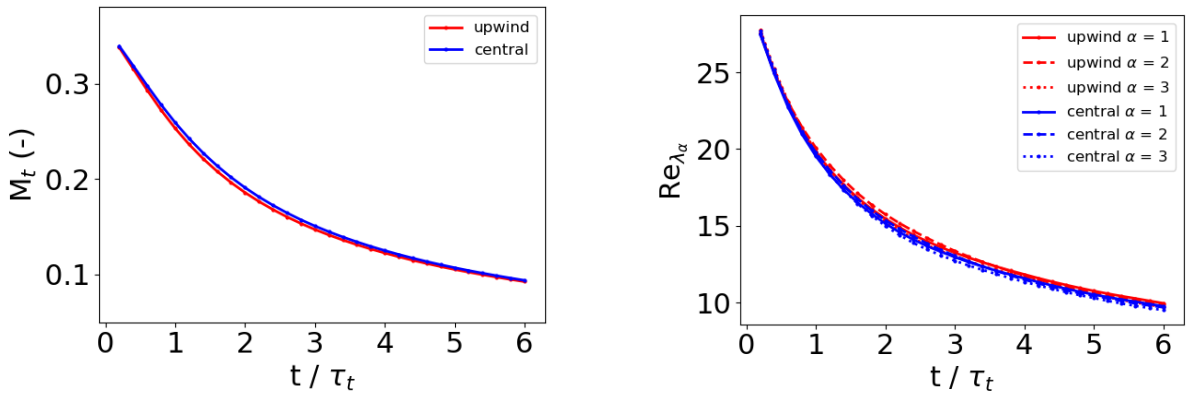

4-2 Effect of spatial discretization on $M_{t,res}$ (left) and Re_λ (right) in the DHIT case with $M_{t,0}$ = 0.36, $Re_{\lambda,0}$ = 28 and k_0 = 6. Grid with 64^3 cells, $\tau_t \approx 0.36$

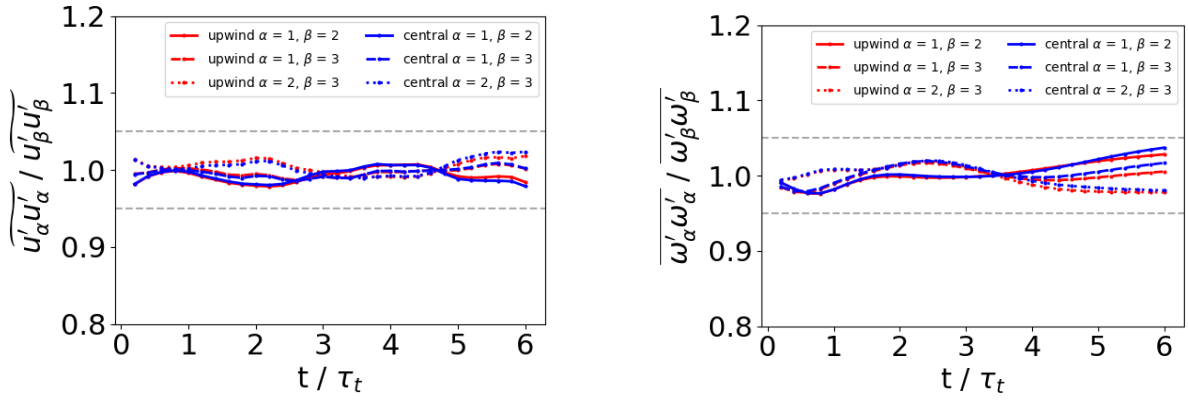

4-3 Effect of spatial discretization on anisotropies of Reynolds stresses (left) and vorticity variances (right) in the DHIT case with $M_{t,0}$ = 0.36, $Re_{\lambda,0}$ = 28 and k_0 = 6. Grid with 64^3 cells, $\tau_t \approx 0.36$

on, if the turbulence intensity (u_{rms}/u) remains below 0.15 [25]. This in turn implies that M_t should remain below ≈ 0.38. One of the reasons for such restriction is the occurrence of compressibility effects such eddy shocklets at higher M_t.

In a first step, the turbulence field obtained from the temporal DHIT is convected at supersonic speed through a domain of the same size and allows a simple comparison without any effect of a shock wave. The boundary conditions are, supersonic inflow and supersonic outflow in the streamwise direction, and periodic planes in the transverse directions. The turbulence flow field at time t/τ_t = 2.2 of the DHIT presented in Figures 4-1 to 4-3 is selected. The flow field is characterised by Re_λ = 15.15 (= mean($Re_{\lambda,1}$,$Re_{\lambda,2}$,$Re_{\lambda,3}$)) and $M_{t,res}$ = 0.176. A supersonic convective speed is superimposed in the streamwise direction of this flow field according to a shock Mach number (M_s) of 1.2. Following sensitivity studies similar to the one described in 4.2, the time step is set to 1/100th of the time to travel between two inflow planes at the uniformly superimposed convective speed. The implication off this time step reduction on the boundary condition has been investigated in

4.2.2.2 and has shown to have minimal influence. The low dispersion setting of the central scheme is not activated as it was shown to result in spurious oscillations in the presence of shocks (see 4.1.3).

Figure 4-4 shows the spatial evolution of the Reynolds stress anisotropies and turbulent Mach number for the part of the domain prior to where the shock will be located. A strong discrepancy in both flux treatments is shown which was not observed in the temporal DHIT case (see 4.1.1). The upwind scheme's prediction demonstrate a strong growth in anisotropy between the streamwise and spanwise directions from the start of the domain which is paired with an increased dissipation rate (see M_t). Not shown here are the individual Reynolds stress components where the streamwise component's decay rate is much quicker than the spanwise's ones.

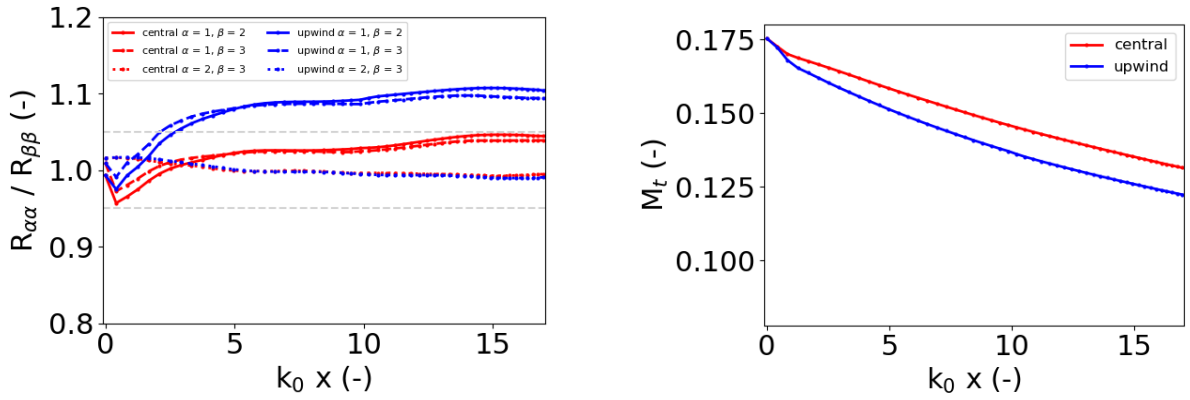

4-4 Effect of the spatial discretization on the Reynolds stress' anisotropy (left) and M_t (right) evolution using Taylor's hypothesis. Domain size of $(2\pi)^3$, grid with 104×64^2 cells and k_0 = 6.

In order to further investigate the underlying reasons for the above observed anisotropy growth, the temporal DHIT was again considered. A developed turbulent field with $M_t \approx 0.2$ and Re_λ = 15.15 was selected as an initial condition. For each flux treatment, three simulations were run superimposing a uniform convective velocity in all three directions corresponding to Mach = 0.3, 0.8 and 1.2. In addition, the standard temporal DHIT is also simulated which is equivalent to not-superimposing any velocity (Mach = 0.0). The resulting decay of M_t is shown in Figure 4-5. Adding a convective velocity will logically increase the dissipation with respect to the standard decay. However, the influence is extremely pronounced in case of the upwind flux. The dependency on the value of the superimposed velocity is stronger with a much quicker decay rate for a higher value. The difference with the central flux treatment indicates some issue with the upwind scheme which appears to be related to Thornber's modification [114]. More specifically, the activation of the low Mach number modification in TAU depends on the local Mach number. For the cases in Figure 4-5 with superimposed velocities, the local Mach number is high such that the correction is not considered, hence yielding the more rapid decay of the turbulence with initial incompressible character. It does also explains the problems encountered previously in the application of Taylor's hypothesis where in the transverse directions (zero mean velocities) the correction will be considered while it will not be in the streamwise direction (supersonic velocity). *In conclusion, this investigation*

indicates that the upwind scheme, in its currently implemented form, is not suitable for STI studies. Therefore, the central scheme has been considered in subsequent simulations.

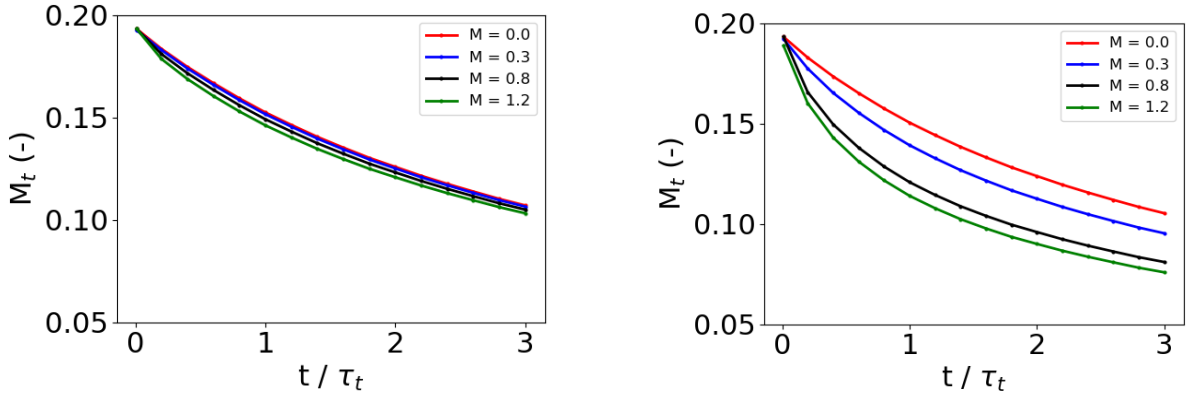

4-5 Effect of inviscid flux treatment with superimposed velocities on M_t in the temporal DHIT with initial turbulence field characterised by $M_{t,0} \approx 0.2$, $Re_{\lambda,0}$ = 15.15. Left = central (LD2), right = upwind (AUSMDV). Grid with 64^3 cells, $\tau_t \approx 0.36$

4.1.3. Shock treatment

An upwind scheme has inherent shock capturing behavior (information on the flow direction) which a central scheme does not have and is therefore more commonly adopted in supersonic flow simulations. However, it was shown in Section 4.1.2 that the current implementation of the uwpind scheme (AUSMDV) does introduce anisotropies when convecting turbulence. The central scheme (LD2) was therefore further considered in this work. It is therefore of interest to evaluate how to adequately apply a central scheme to problems involving shock waves.

4.1.3.1. Standard shock-related settings of the LD2 scheme

Details on TAU's low-dissipation low-dispersion or LD2 central scheme can be found in [70, 85]. The skew-symmetric form of Kok [48] is adopted and low dispersion properties can be optionally deactivated. The standard settings considered for the LD2 scheme are a scaling factor for the second-order artificial dissipation set to 0.5 and a scaling factor for the fourth-order artificial dissipation set at 1/1024 [70]. In the presence of shocks, the second-order dissipation term will be dominant which ensures that the scheme becomes locally first-order accurate. The latter behavior is valid for both, the scalar-valued and the matrix-valued [70, 85] dissipation options. In practice, a blend of the scalar- and matrix-valued dissipation approaches will be enabled. This occurs through two additional parameters which are, presently, set to the same value. We will call them the artificial dissipation switches. By default they will be set to 0.05 which implies a blend of 5 % scalar dissipation and 95 % matrix dissipation. The matrix dissipation has in addition another user defined constant: the pressure switch weighting factor with default value of 1. In the implementation of the matrix dissipation, a sensor is embedded which will be dominant in regions with high pressure gradients (such as shocks). Through this sensor, the dominance of the second-order dissipation term can be retrieved as well as a the evolution toward a first order Roe scheme. The sensitivity of this

"pressure" sensor can be controlled through the pressure switch weighting factor.

4.1.3.2. Mach 1.2 STI with 32 x 32^2 cells

Some test were run with the central scheme on a coarse grid, with 32^3 cells uniformly spaced ($(2\pi)^3$ domain) targeting the Mach 1.2 conditions of Garnier *et al.* [25] (see Subsection 5.2.2). The turbulence flow field convected through is characterised by $M_{t,res}$ = 0.136 and Re_λ = 11.67. Time step size (dual time stepping scheme) was set accordingly to 1/5th of the time to pass through one cell in the original uniform box (= time to change inflow BC) following the study of its effect in 4.2.2.2. A shock has been placed originally at the centre of the domain. Fixed pressure outflow is prescribed with a value obtained from the laminar jump conditions. The inflow is provided periodically and averaging performed after two flow through times for two flow through times (flow length based on mean convective speed of inflow).

Figure 4-6 presents the effect of the central's scheme dissipation / dispersion setting as well as the pressure switch weighting factor (set to 1 and 10 and indicated in the legend with prefix p) on the Favre-averaged temperature. A more detailed view on the pre- and post-shock region is given in Figure 4-7. The legend is as follow: L = low, H = high and N = no. The first D refers to the dissipation, the second to the dispersion. E.g. LDND indicates a simulation with low dissipation setting, and no dispersion extension activated while LDLD indicate low dissipation setting with low dispersion activated. Simulations with "H" indicate a 4th order artificial dissipation coefficient set to 1/64 instead of 1/1024 which is the "L" setting. Moreover, the artificial dissipation switches are set to 0.2 which implies 20 % scalar- and 80 % matrix dissipation.

It is interesting to see that the requirement to avoid spurious oscillations before and after the shock are different. It would however be imprudent to state that the pre-and post-shock behavior could be uncoupled. In the pre-shock region the low dispersion setting should not be considered as it leads to strong oscillations (see LDLD and HDLD). Without low dispersion setting, the pressure switch does not have much effect except slightly stronger post-shock oscillations for the lower value (LDND p1). In the post-shock region, only the LD2 scheme appears to provide a smooth profile with pressure switch set to 1. The pressure switch of 10 results in strong oscillations in this same region. The evolution of M_t is also shown in Figure 4-8 and confirms the above observations for the pre-shock region. Post-shock, the results differ and the same pressure switch weighting factor yields similar behavior whether low dispersion is activated or not. This could be the result of investigating M_t, a parameter obtained from more than one quantity.

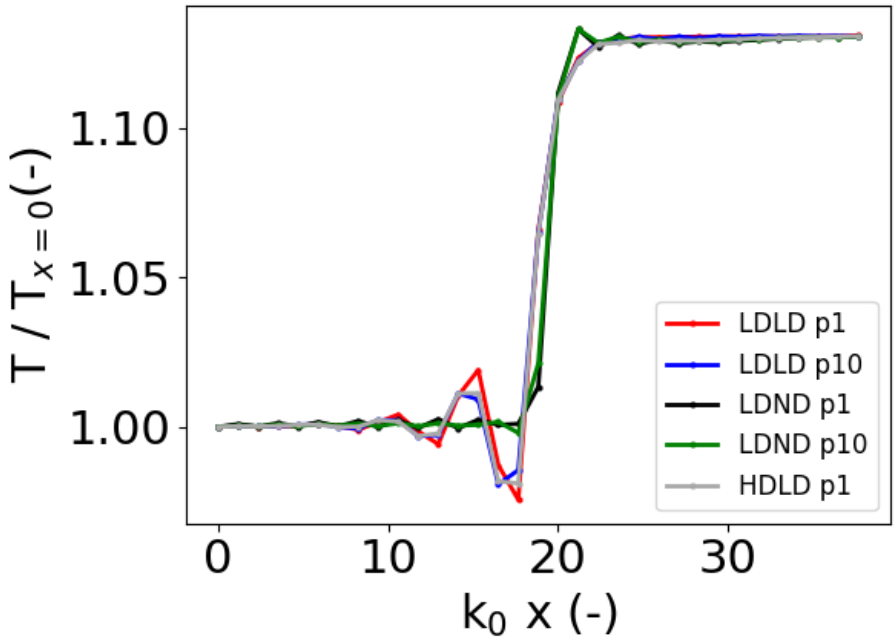

4-6 T decay in STI with central scheme. Effect of dispersion and pressure switch weighting factor. 32^3 cells, k_0 = 6.

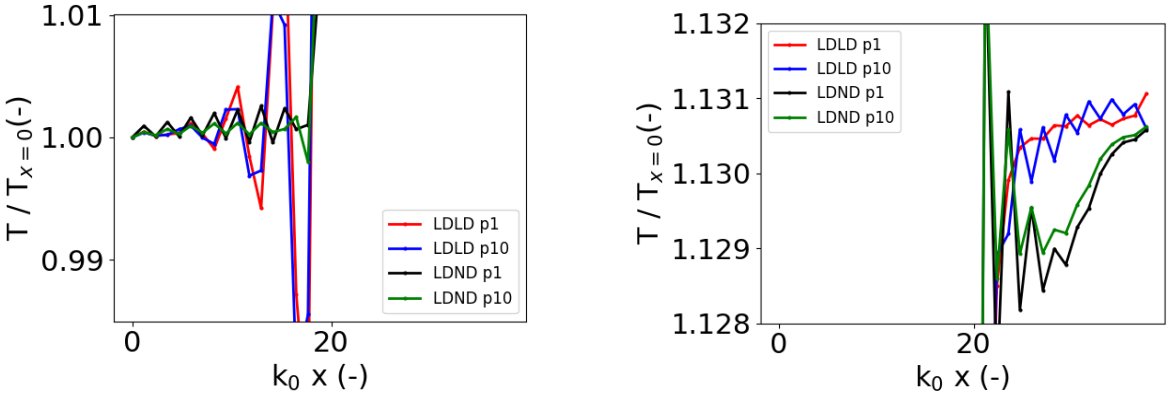

4-7 Zoomed in T decay in STI with central scheme. Effect of dispersion and pressure switch weighting factor. 32^3 cells.

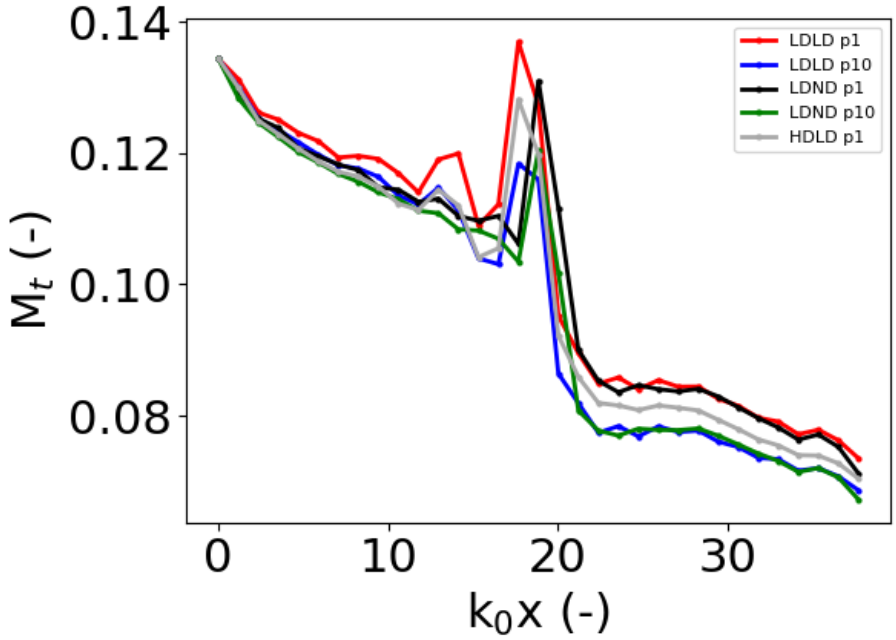

4-8 M_t decay in STI with central scheme. Effect of dispersion and pressure switch weighting factor. 32^3 cells, k_0 = 6.

4.1.3.3. Mach 1.2 STI with 64 x 32^2 cells

As in a more realistic STI situation, the grid spacing in the x-direction would be finer (see also Section 3.1), simulations to evaluate the shock with the central scheme were also performed with a uniform grid 64×32^2. The results are given in Figures 4-9 and 4-10. The inadequacy of the low dispersion setting is confirmed and the effect of the pressure switch weighting factor is observed to be minimal. In comparison to the 32^3 cells domain, the post-shock region is more smoothly represented without low dispersion. Regarding M_t, the behavior is pretty similar to Figure 4-8.

A comparison between the number of cells in the x-direction is given for the same quantity in Figure 4-12 for the setting LDND. The finer mesh does not suffer as much from an influence of the pressure switch. The pre-shock decay is also less steep for the finer grid. A comparison of the streamwise Reynolds stress amplification of the fine mesh yields values of 0.986 and 0.980 for p1 and p10, respectively and is less than 1 %. Therefore, it does not seem to be play an important role. It will, however, be shown in Subsection 5.2.3 that this parameter has a stronger impact at higher Mach numbers. The presence of a shock does not appear to affect the pre-shock decay of M_t (see Figure 4-13) and the difference between LDND and LDLD is less than 1 % in the upstream part. Figure 4-14 compares the Reynolds stress anisotropies with and without shock with LDND setting. No effect of the shock movement is observed which is a positive outcome. The effect of activating or deactivating the dispersion properties on the Reynolds stress' and vorticity anisotropies, in the absence of a shock, is shown in Figure 4-15. The higher dissipative behavior when not active (LDND) is especially visible in the vorticity. Refer to the legend in, for instance, Figure 4-3 for the details about which anistropy is represented by which curve line style.

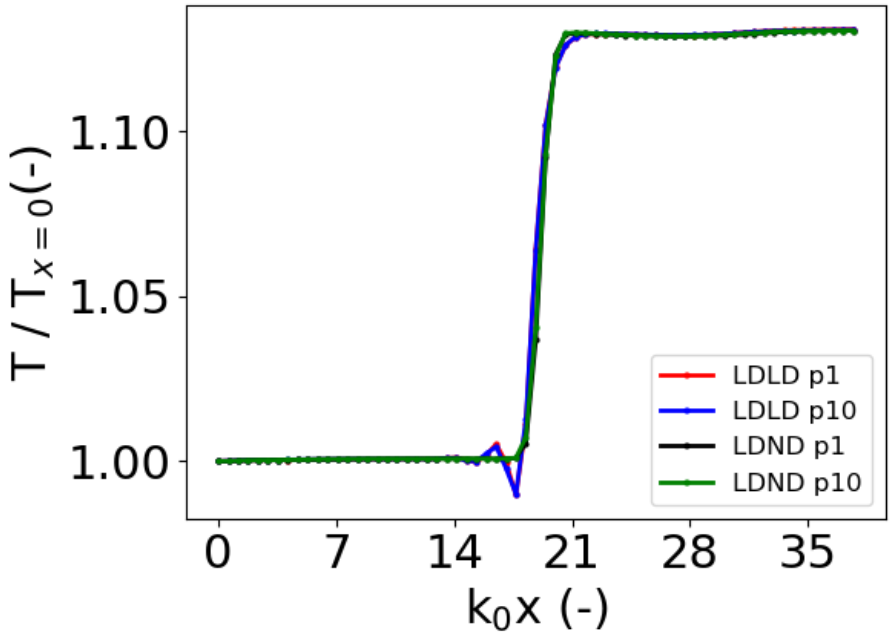

4-9 T decay in STI with central scheme. Effect of dispersion and pressure switch weighting factor. 64 $\times 32^2$ cells, k_0 = 6.

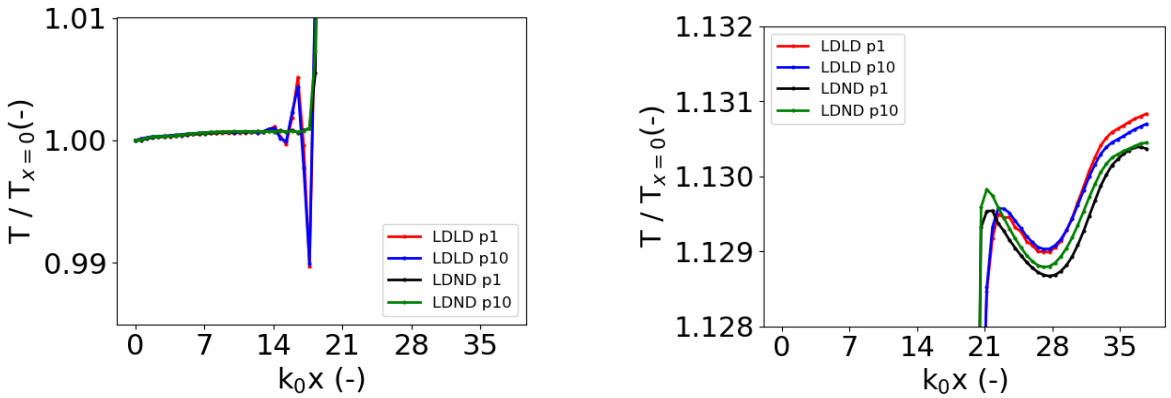

4-10 Zoomed in T decay in STI with central scheme. Effect of dispersion and pressure switch weighting factor. 64 $\times 32^2$ cells, k_0 = 6.

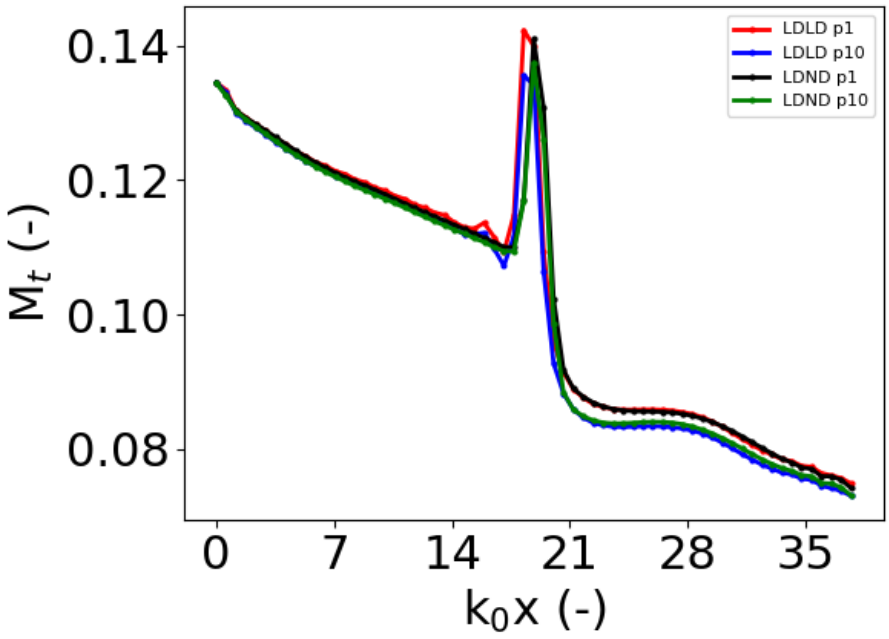

4-11 M_t decay in STI with central scheme. Effect of dispersion and pressure switch weighting factor. 64 $\times 32^2$ cells, k_0 = 6.

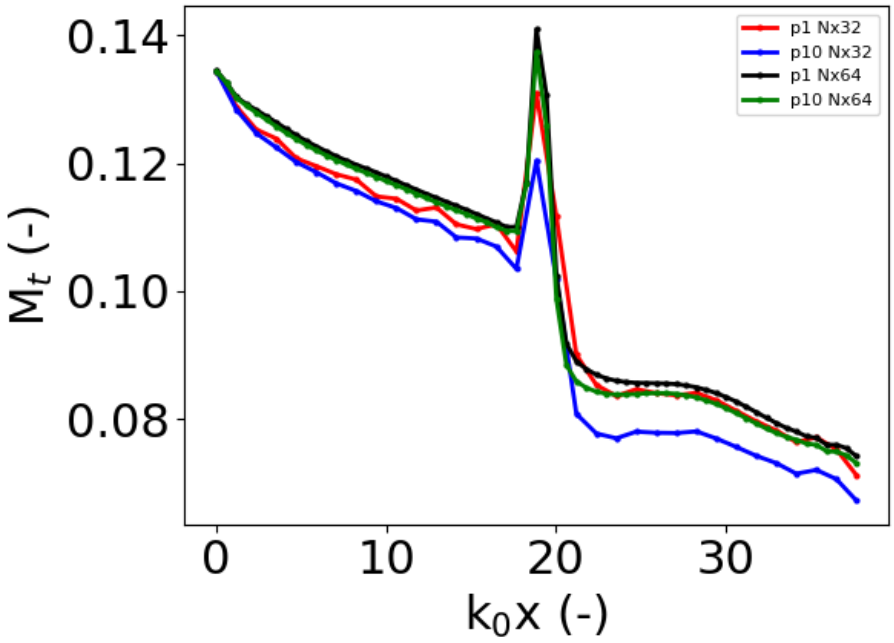

4-12 M_t decay in STI with central scheme LDND setting. Effect of pressure switch weighting factor and Nx.

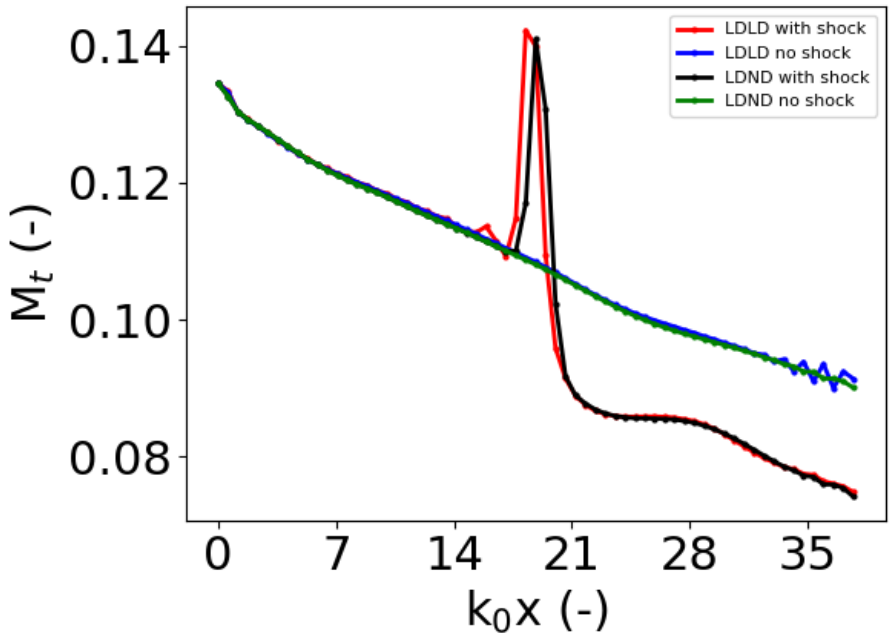

4-13 M_t decay in STI with central scheme. Effect of shock and dispersion. 64 $\times 32^2$ cells and p-switch = 1, k_0 = 6.

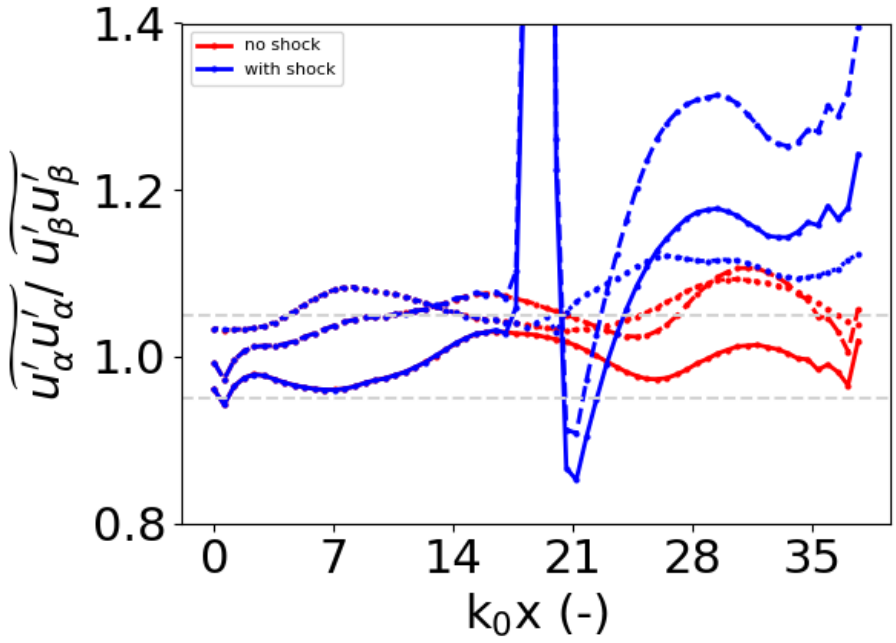

4-14 Effect of shock on Reynolds stress anisotropies with central scheme LDND. 64 $\times 32^2$ cells and p-switch = 1, k_0 = 6.

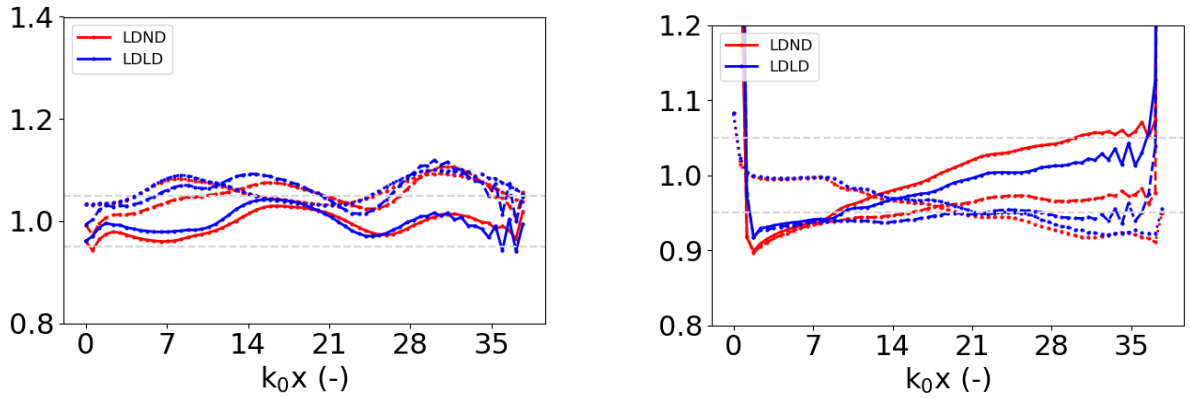

4-15 Effect of dispersion on Reynolds stress' (left) and vorticity fluctuations variance's (right) anisotropies with central scheme without shock. 64 $\times 32^2$ cells and p-switch = 1, k_0 = 6.

4.1.3.4. Mach 1.2 STI with N_x x 32^2 cells

Simulations were also performed with increasing N_x (64,128,194) to evaluate it's influence on the amplification, the anisotropy growth, etc. The different cell numbers yield uniform cell spacings of 0.0982, 0.0491 and 0.0324 respectively. The same inflow field obtained on a 32^2 cells box, as in previous studies is considered. Based on the reference conditions of Garnier *et al.* [25] and Lee *et al.* [59], an ideal near shock cell spacing should be 0.0445 and 0.0312 respectively. Based on the pre-shock resolved (or total) M_t and Re_λ obtained in the simulations, the ideal spacing (see Equation 3-4) should be 0.0362 (or 0.0389). From this, the finest considered grid should yield the desired amplification.

The impact on the anisotropies are given in Figure 4-16 and are only mildly affecting the Reynolds stresses but more strongly the vorticity. There seem to be a convergence toward a fixed behavior with similar evolutions for the 128 and 194 case. This is also shown in the streamwise velocity derivative skewness and M_t in Figure 4-17. However, the skewness also shows some other issue one have to be aware of: the aspect ratio. Too high aspect ratio's become problematic for the central scheme. Around k_0x = 11, the profile shows some oscillatory behavior as well as near the inflow plane. In terms of amplifications, Table 4-1 shows that 128 cells in the x-direction are sufficient for this case which is somewhat coarser than the 0.0362 (or 0.0389) computed with Equation 3-4.

4-1 Streamwise cell number effect on Garnier (32^3 cells) condition 1 with shock. LDND, p-switch = 1

Nx	$\mathbf{R}_{11,post}$ / $\mathbf{R}_{11,pre}$	$\omega'^2_{2,post}$ / $\omega'^2_{2,pre}$	δ/η **(res)**	δ/η
64	0.986	1.425	1.43	1.53
128	0.997	1.444	1.45	1.55
194	0.996	1.443	1.45	1.55

It must be noted that the convected field's anisotropies, i.e. the injected turbulence, are below 5 % as made visible in Figure 4-18 (see τ_t = 2.6). In order to ensure it was not caused by the low dispersion setting, a simulation starting from the same time was performed without low dispersion. It does not have a large impact (in terms of the box averages) as shown in Figure 4-18. Somehow, in the vorticity's evolution of Figure 4-16, the original levels appear to be lost. A constant observation throughout all spatial simulations is this increase of vorticity anisotropies, whatever may the grid or conditions be.

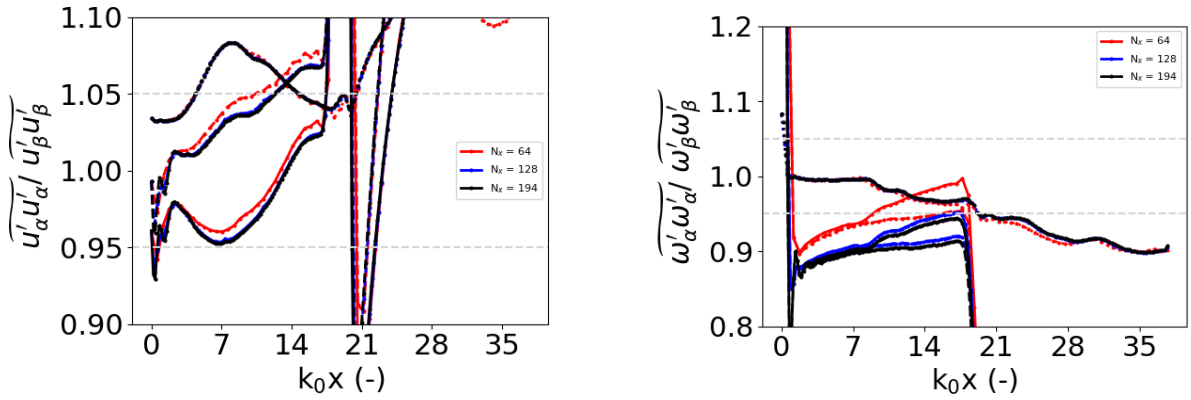

4-16 Effect of streamwise cell number on Reynolds stress' (left) and vorticity fluctuations variance's (right) anisotropies with central scheme (LDND). $N_x \times 32^2$ and p-switch = 1, k_0 = 6.

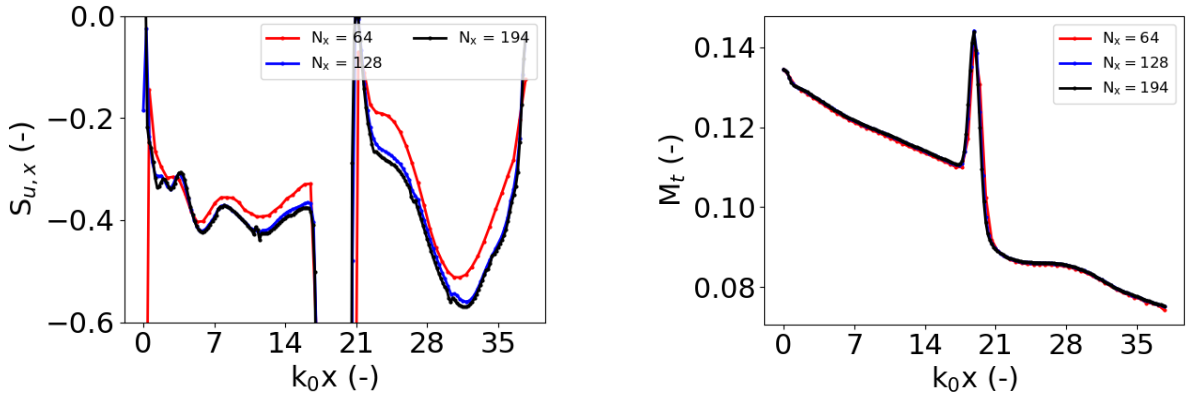

4-17 Effect of streamwise cell number on $S_{u,x}$ (left) and M_t (right) with central scheme (LDND). $N_x \times 32^2$ and p-switch = 1, k_0 = 6.

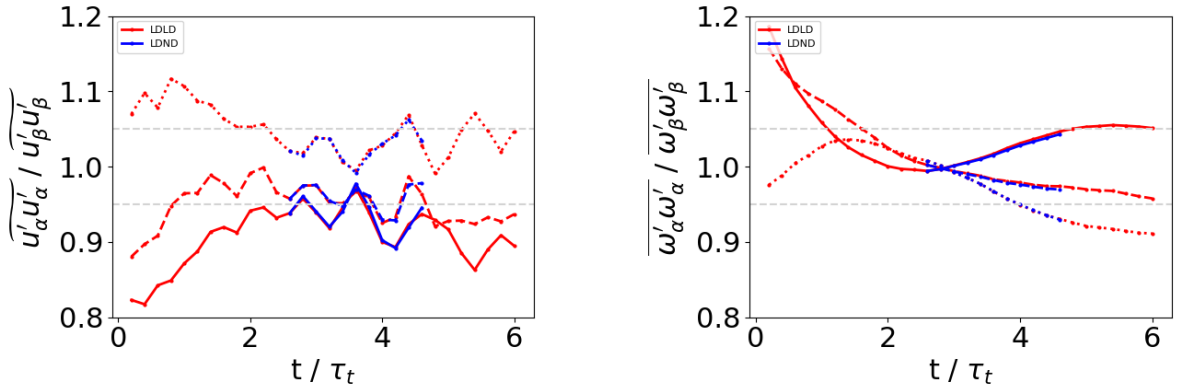

4-18 Reynolds stress' (left) and vorticity fluctuations variance's (right) anisotropies in temporal decay with central scheme. 32^2 cells and p-switch = 10, $\tau_t \approx 0.572$

4.1.4. Central scheme: Dissipation and Dispersion settings

Continuing on the 32^3 cells (2π domain) Mach 1.2 conditions of Garnier *et al.* [25]. Part of the investigation considered the settings of the central scheme itself and does not contain any shock, i.e. we purely convect a turbulent field, periodically, through a box with a supersonic outflow. The dual time stepping scheme is considered with a reduced time step (Δt_{cell} / 5) following a temporal discretization study in 4.2.2.2.

Figures 4-19 to 4-21 show the dissipation and dispersion settings' effects. Recall that the high dissipation setting implies artificial dissipation switches set to 0.2 (20% scalar and 80 % matrix-valued dissipation evaluation) and the fourth-order artificial dissipation coefficient set to 1/64. Not considering the low dispersion (LDND) has already a profound effect on the M_t decay and appears to be equivalent to a high dissipation setting (HDLD), at least for higher M_t values. The Taylor microscale (L_λ), Figure 4-21, increases more for the high dissipation case without dispersion (HDND). The non monotone evolution appears to be amplified with respect to the low dispersion simulations. This is even more pronounced for Re_λ in Figure 4-20. Note that the non monotone behavior in Figures 4-20 and 4-21 is caused by the coarse grid used here which impacts the derivatives. Finer grid studies show a more linear evolution.

The low dispersion impact is clearly shown in the x-velocity derivative skewness' evolution in Figure 4-22: regardless of the dissipation setting, the skewness levels remain pretty low. It is only by deactivating it that the skewness increases to higher levels. A previous study with shocks (see 4.1.3) has demonstrated the need to deactivate the low dispersion scheme.

The anisotropies are shown in Figure 4-23 for the LD2 scheme, which was previously identified to be an issue on coarser grids. However, the time step used was not low enough as will be shown in 4.2.2.2. The max velocity fluctuations anisotropy of the original field is $\approx$ 7 % but does grow further in the temporal decay. Vorticity fluctuations anisotropy remains below 5%.

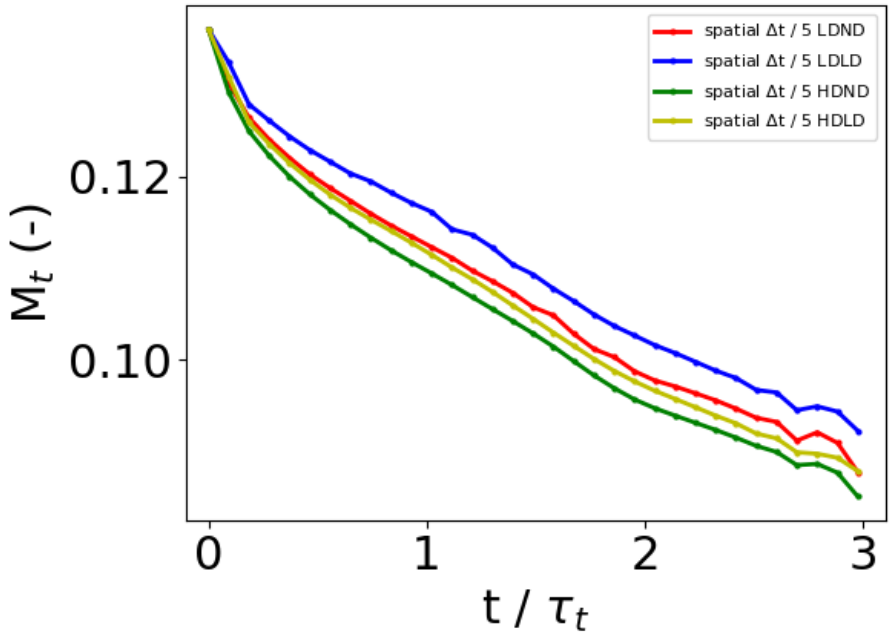

4-19 M_t decay with central scheme and different settings. L= low, H=high, N = no. 32^3 cells

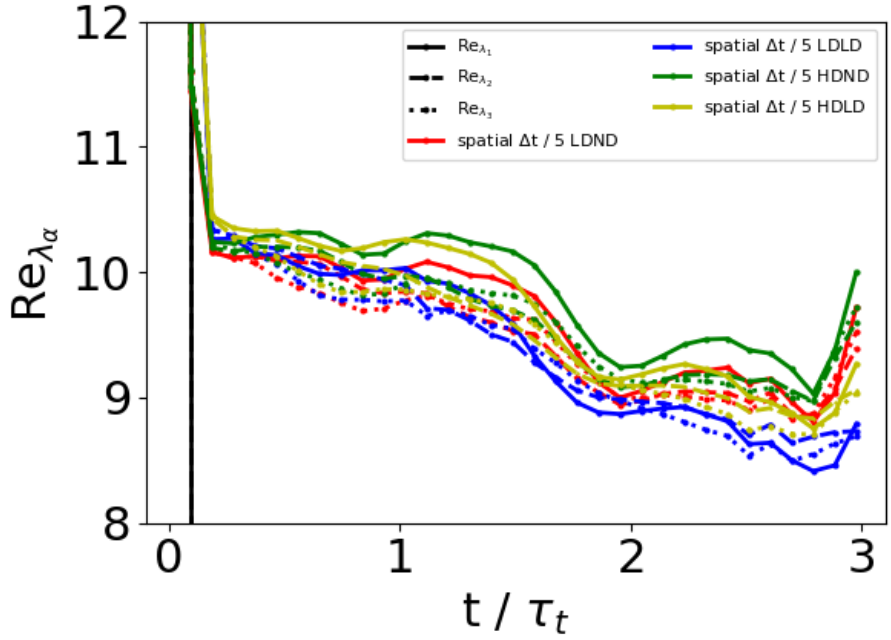

4-20 Re_λ decay with central scheme and different settings. L= low, H=high, N = no. 32^3 cells

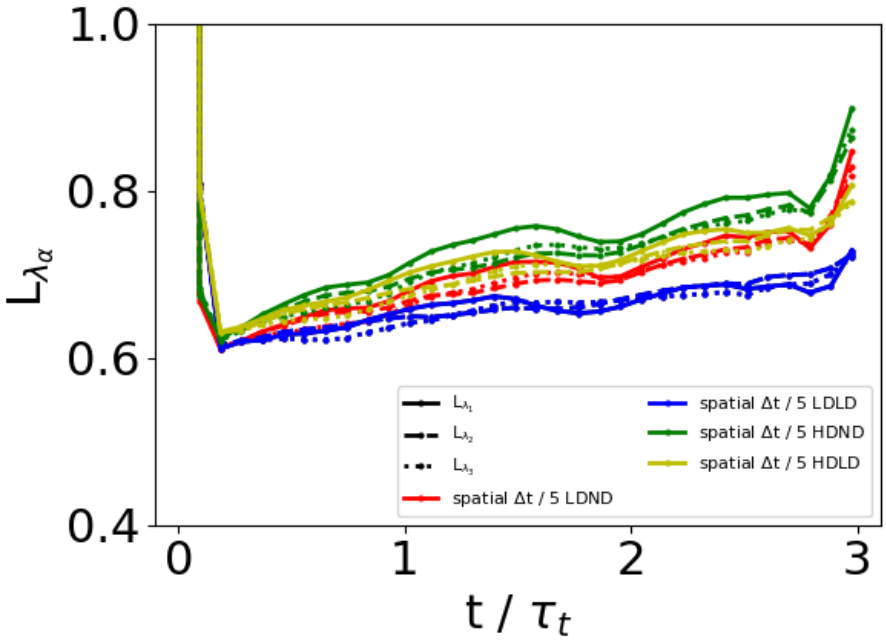

4-21 L_λ decay with central scheme and different settings. L= low, H=high, N = no. 32^3 cells

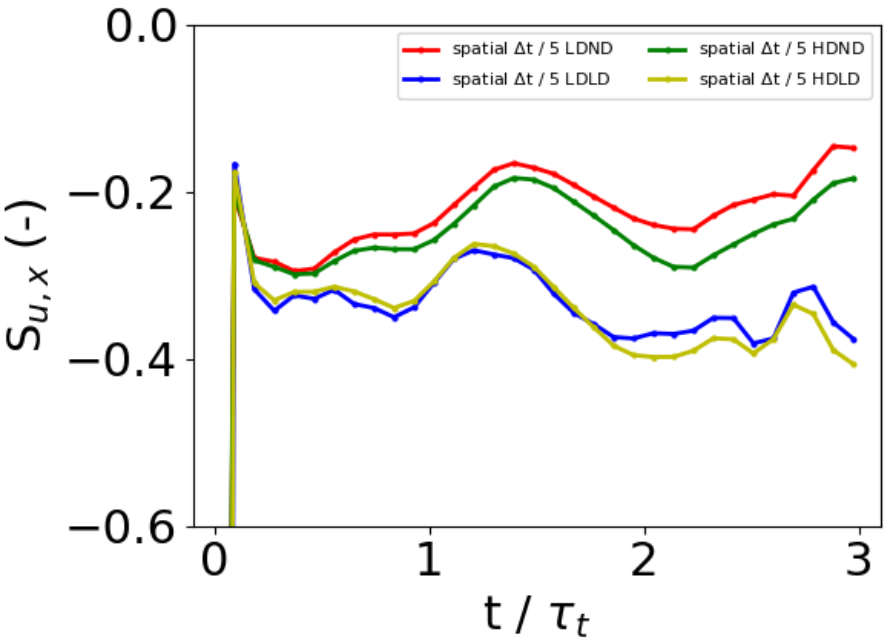

4-22 $S_{u,x}$ decay with central scheme and different settings. L= low, H=high, N = no. 32^3 cells

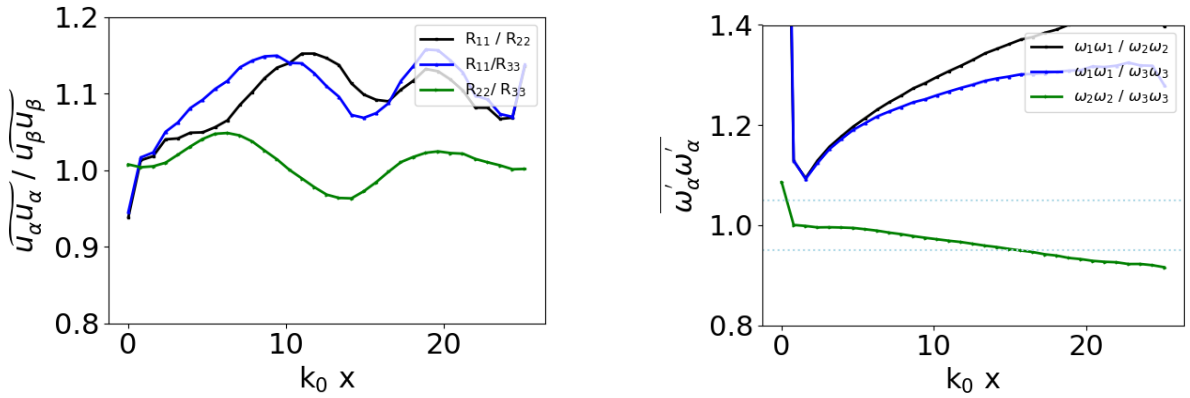

4-23 Velocity and vorticity anisotropies for the LD2 scheme. 32^3 cells, k_0 = 4.

4.2. Temporal discretization

In this Section, the temporal numerics are investigated. Commonly adopted in TAU simulations is the "dual" time stepping scheme (see e.g. [45, 84, 37, 105, 118]) and was originally considered in the STI studies. However, as it will be shown, the time step size requirements in such setting renders its use too computationally intensive and a "global" time stepping would be the obvious choice instead. Discussions will be placed in the context of the final STI setup we wish to study which is achieved through different steps including the generation of the turbulence (see 4.2.1) and its subsequent convection (see 4.2.2).

4.2.1. Temporally Decaying Homogeneous Isotropic Turbulence (DHIT)

The temporal DHIT simulations were performed with the dual time stepping scheme of Jameson [39]. Time step sizes were set to 1/100th of the eddy turnover time of the initial flow field, $\tau_t = L_\lambda/u_{rms}$ where L_λ is as defined as the average of the Taylor microscales in each direction. The settings were shown to be adequate in the different DHIT simulations with different turbulent conditions (see e.g. 4.1.1).

4.2.2. Convecting the turbulence through Taylor's hypothesis

In the situation when a turbulence flow field is generated with a temporal DHIT simulation it has to be convected to interact with a shock wave. This is done by relying on Taylor's hypothesis but is limited to conditions with relatively low compressibility effects. If higher turbulence intensities are of interest, the turbulence should be generated in a spatial way (see e.g. Lee et al. [58] or Grube et al. [31]). In applying Taylor's hypothesis, several aspects should be considered and are discussed below.

4.2.2.1. Periodic push

In order to study the STI problem, statistical averaging must be performed on the quantities of interest. This would require a minimum amount of simulation time which in term requires the turbulence fed in by the inflow to be sustained for a long enough time. Moreover, averaging would only be initiated after the initial transients are gone. With regard to the temporally generated turbulence, this would imply some sort of blending of multiple DHIT domains to provide a sufficient amount of inflow planes. See e.g. Xiong *et al.* [126] or Larsson *et al.* [51] for details on such blending procedure which requires solving a Poisson equation to a posteriori remove errors in the dilatational field introduced by the procedure itself. The method relies also on an overlapping region between the different DHIT boxes which sets another constraint on the number of individual DHIT needed to obtain an inflow turbulence signal of a given length.

A simplified method would be to consider a single DHIT turbulence realization and periodically send it through the STI domain. It has for instance been considered by Tian et al. [116]. From a statistical point of view, a longer inflow signal obtained through the blending procedure would provide a more realistic representation of a turbulence flow field. However, what are the implication of such

a simplification on the evolution of second order statistics? Would the different amplifications be strongly affected? These questions have been investigated in conditions relevant for the reproduction of the STI study of Garnier et al. [25].

Several DHIT boxes ($(2\pi)^3$ domain, 64^3 cells) with random initial turbulence (Gaussian, k_0 = 6, no thermodynamic fluctuations) were generated and rescaled such as to obtain initial values $Re_{\lambda,0}$ = 28 and $M_{t,0}$ = 0.36. The quantities are based on the resolved portion of the turbulence. The different boxes were allowed to decay with result shown in Figure 4-24 for M_t and Re_{λ_1} (based on x-direction). Maximum differences between the simulations in these quantities are 3 % and 5 %, respectively. The turbulent realization after 2.2 eddy turnover time ($\tau_{t,0}$) was selected to generate the STI inflow. To obtain a larger inflow database, the different boxes were blended following the procedure described by Larsson [51]. This was performed by Dr. Yogesh Prasaad Madras Sethuraman (currently: Postdoctoral Researcher at International Centre for Theoretical Sciences, Bengaluru, India) whose help is gratefully acknowledged. The overlap between the DHIT boxes was set to 1 L_λ and for the Poisson correction to 2 L_λ. The Taylor microscale (L_λ) $\approx$ 0.38. The resulting signal will be referred to as "non-periodic" in subsequent discussions. DHIT1 is selected as the single turbulence realization for periodic inflow use. The solutions at t = 2.2 $\tau_{t,0}$ and t = 2.6 $\tau_{t,0}$ are considered for two different simulations and are referred to as "periodic 1" and "periodic 2". Turbulence is characterised by M_t = 0.176, $Re_\lambda \approx$ 15 and M_t = 0.160, $Re_\lambda \approx$ 14 at t = 2.2 $\tau_{t,0}$ and t = 2.6 $\tau_{t,0}$, respectively. The inflow turbulence is convected at Mach 1.2 and the STI domain is set to the same size as the DHIT domain. It comprises 104 cells in the x-direction with a grading towards the initial shock position ($x = k_0\pi$) such that Equation 3-4 is satisfied at the shock. The grading was performed with the so-called Roberts cluster function which is detailed in [13] or [2].

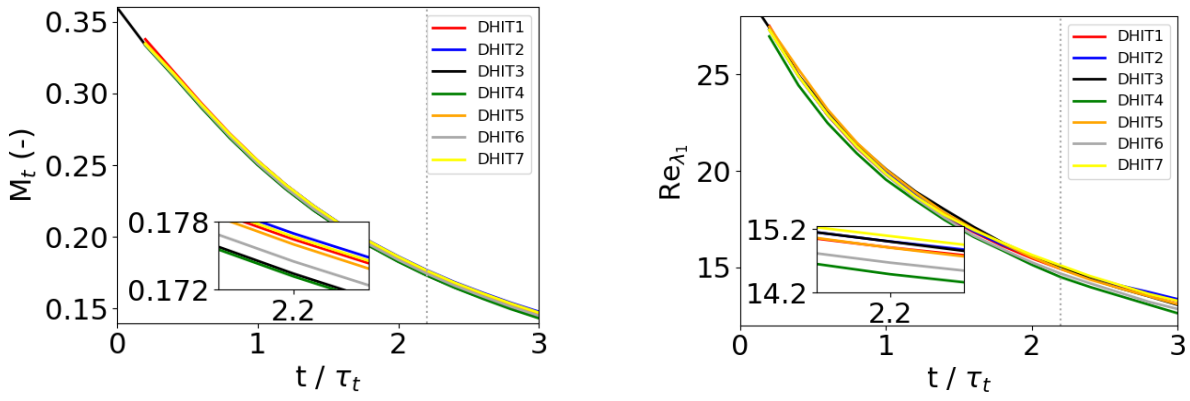

4-24 Temporal DHIT for several runs with initial turbulence field $Re_{\lambda,0}$ = 28 and $M_{t,0}$ = 0.36, $\tau_t \approx$ 0.36

The results of the STI are presented in Figures 4-25 to 4-28. The quantities are averaged over space and time for two flow lengths (based on supersonic convective velocity) after initial transients have disappeared (also two flow lengths based on supersonic convective velocity). The non-periodic signal has a different pre-shock decay, and therefore also pre-shock quantities, compared to the single DHIT realisation taken at the same time in the temporal decay (periodic 1). This is expected

given the influence of multiple realizations with different levels of anisotropies, skewness and other parameters. Therefore, to allow some other reference for comparison, the periodic 2 simulation was performed. Note that for variables computed based on gradients (Re_λ, $\omega_i'^2$, $S_{u,x}$), the extreme values near the inflow plane are purely a numerical artefact from the post processing. Pre-shock quantities are summarised in Table 4-2 as well as the amplifications of streamwise Reynolds stress and transverse vorticity variance. Provided amplifications are based on the peak post-shock values (see e.g. Figure 4-26 for R_{11}). The estimate for the ratio of shock thickness to Kolmogorov length scale (δ/η) given in Equation 1-8 is also given just before the shock. It was computed based on the resolved M_t. The pre-shock anisotropy levels in Reynolds stresses and vorticity variances (Figure 4-27) are slightly higher for the non-periodic signal but remain below 6 %. Another noticeable difference between the periodic and non-periodic cases is the higher levels in pre-shock streamwise velocity derivative skewness for the latter as shown in Figure 4-28. $S_{u,x}$ of the individual DHIT boxes used on the blending varies between -0.32 and -0.42 at t = 2.2 $\tau_{t,0}$. This explains the observations. Note that such levels of $S_{u,x}$ are not unheard of in LES [121, 25], especially for lower order accurate discretization schemes.

In terms of amplifications, the ratio δ/η is a useful parameter to compare different simulations. The lower its value, the less pronounced the viscous effects and the closer the amplifications are to LIA predictions [97]. In this regard, periodic 2, with a lower δ/η, results in stronger amplifications of R_{11} and $\omega_2'^2$ than periodic 1 which is consistent with the expectations. The non-periodic case has a δ/η ratio very similar to periodic 1, but with different pre-shock turbulence. Nevertheless, the amplifications are in close agreement with differences smaller than 1 % for R_{11} and smaller than 2% for $\omega_2'^2$. Similarly, the non-periodic simulation's amplifications are smaller than periodic 2.

Lastly, the evolution of the polytropic coefficients, computed according to Equations 4-1 and 4-2 are shown in Figure 4-28. It is noted that the pre-shock thermodynamic fluctuations are not as isentropic ($n_{p\rho} = n_\rho T = \gamma = 1.4$) as reported in e.g. [59]. Nevertheless, at t = 2.2 $\tau_{t,0}$, the rms to mean ratio's for pressure, density, temperature are 0.015, 0.013 and 0.006, respectively. Such values are similar to the vortical turbulence cases of Jamme *et al.* [41] (see Table II) and not comparable to the cases where acoustic or entropy modes are as well considered. The same observation is valid for the velocity temperature correlation (Equation 4-3) which is presently 0.033 and positive. In spite of the non perfectly isentropic character, the present comparison in inflow BC remains possible. The evolution of polytropic coefficients shows little influence of the different inflow cases.

In conclusion, with regard to the quantities described above, the use of a single turbulent DHIT flow field, and sending it periodically through the STI domain for the desired simulation time, appears to be an acceptable choice. It will therefore be considered in the different STI simulations.

$$n_{p\rho} = \frac{\sqrt{\overline{p'^2}/\bar{p}}}{\sqrt{\overline{\rho'^2}/\bar{\rho}}} \tag{4-1}$$

$$n_{\rho T} = 1 + \frac{\sqrt{\overline{T'^2}/\bar{T}}}{\sqrt{\overline{\rho'^2}/\bar{\rho}}} \tag{4-2}$$

$$\frac{\overline{u_1' T'}}{u_{1,rms}' T_{rms}'} \tag{4-3}$$

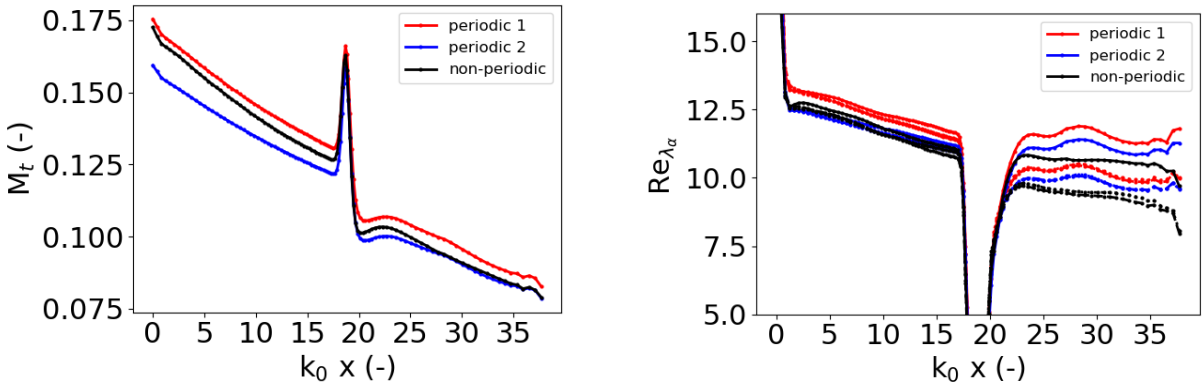

4-25 Effect of inflow BC on the spatial evolution of M_t (left) and Re_λ (right) in the STI. k_0 = 6

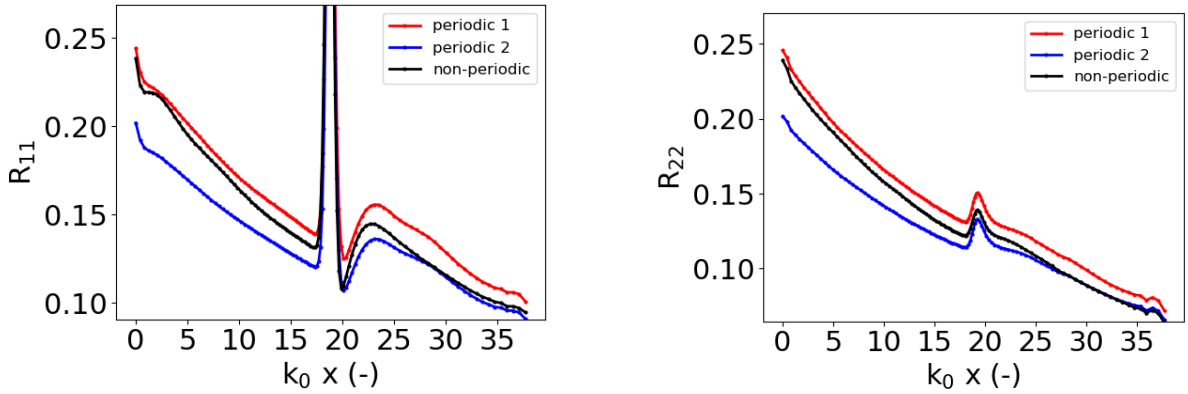

4-26 Effect of inflow BC on the spatial evolution of the streamwise (left) and transverse (right) Reynolds stresses in the STI. k_0 = 6

4.2.2.2. Time step selection

The time step influence was investigated for the same test case as in 4.1.3.1 with results shown in Figures 4-29 and 4-30. The inflow turbulence (M_t = 0.136, Re_λ = 11.67) is periodically convected at Mach 1.2 through a $(2\pi)^3$ domain discretized by 32^3 cells without any shock. A supersonic outflow is prescribed. Simulations are performed with the LD2 central scheme and the dual time-stepping method. The explicit time step is based on the temporal DHIT turbulence that is convected through

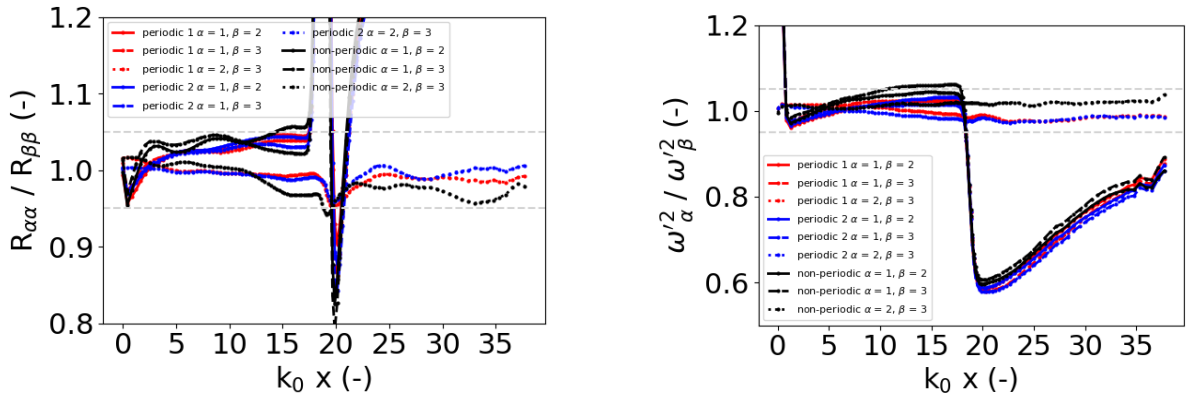

4-27 Effect of inflow BC on the spatial evolution of the anisotropies in Reynolds stresses (left) and vorticity variances (right) in the STI. $k_0 = 6$

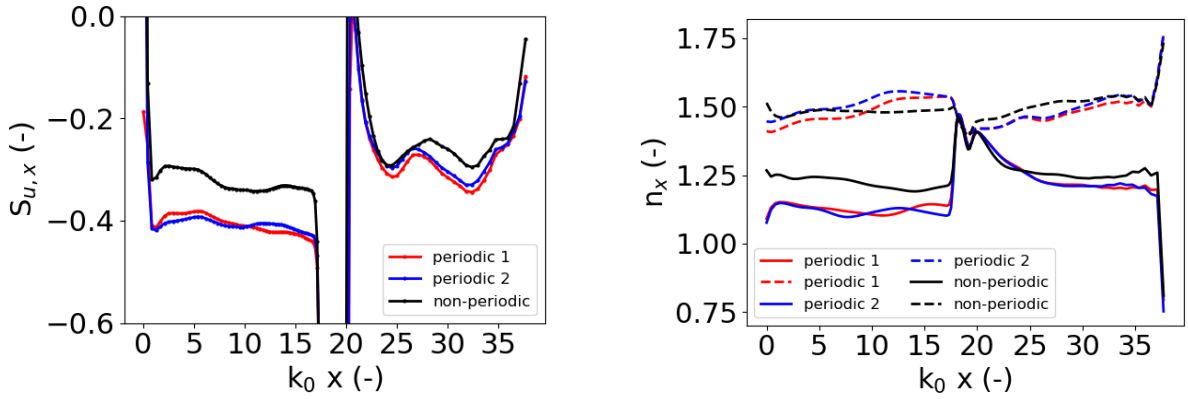

4-28 Effect of inflow BC on the spatial evolution of $S_{u,x}$ (left) and polytropic coefficients (right) in the STI. Full lines = $n_{p\rho}$, dotted lines = $n_{\rho T}$, $k_0 = 6$

4-2 Effect of inflow BC on the pre-shock quantities and amplifications in a Mach 1.2 STI.

	periodic 1	**periodic 2**	**non-periodic**
$\mathbf{M}_{t,res}$	0.131	0.127	0.122
$\overline{Re_\lambda}$	11.34	10.93	10.72
$\mathbf{R}_{11,d}$/ $\mathbf{R}_{11,u}$	1.115	1.101	1.126
$\omega'^2_{2,d}$/ $\omega'^2_{2,u}$	1.520	1.555	1.522
δ/η **(res)**	1.50	1.42	1.49

the domain and is set to the time it will take to move from one transverse plane to another at the desired convective speed:

$$\Delta t_{cell} = \Delta t = \frac{(L_x/N_x)}{U_{conv}} \tag{4-4}$$

where L_x and N_x are, respectively, the length and cell number in the x-direction of the DHIT box. Two other simulations were performed where the time step is set to a fraction of Δt_{cell}. The temporal decay is also shown for reference. The resulting decays of M_t, L_λ and Re_λ demonstrate the need for a smaller time step than given by Equation 4-4. Only then does the spatial decay coincide with the temporal decay. For the specific mesh considered, a time step size of Δt_{cell} / 5 appeared to be sufficient. In terms of skewness (Figure 4-30), there is some discrepancy with respect to the temporal decay, even with an appropriate time step size. The levels do, however, remain within known ranges typical of an LES simulation. Simulations with Δt_{cell} did also show a strong growth in the anisotropy levels of Reynolds stresses and vorticity variances (not shown here). The streamwise velocity fluctuations dissipate at a faster rate than the transverse.

The important result of this study is that in terms of computational cost the dual time stepping scheme becomes extremely disadvantageous. A global time stepping approach would be much faster. Note that in the latter case, the CFL criteria will be a decisive parameter to set and control the time step size, so that the inflow planes get changed a desired times. Consequently, for the remainder of this work, the STI simulations are performed with an explicit three-stage Runge-Kutta scheme [40] available in TAU [36].

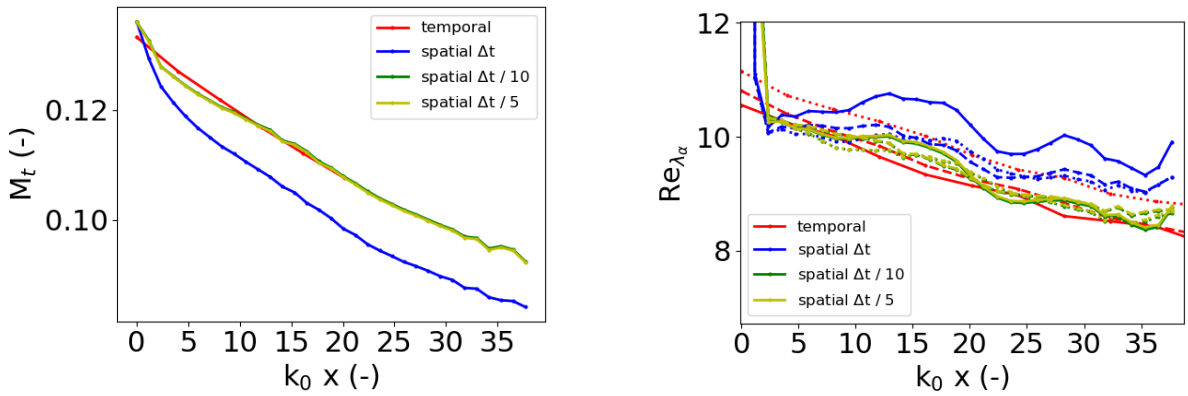

4-29 Spatial decay at Mach 1.2 of M_t (left) and Re_λ (right) with central scheme (LD2) and different time step sizes. Full lines = Re_{λ_1}, dashed lines = Re_{λ_2}, dotted lines = Re_{λ_3}. k_0 = 6, 32^3 cells

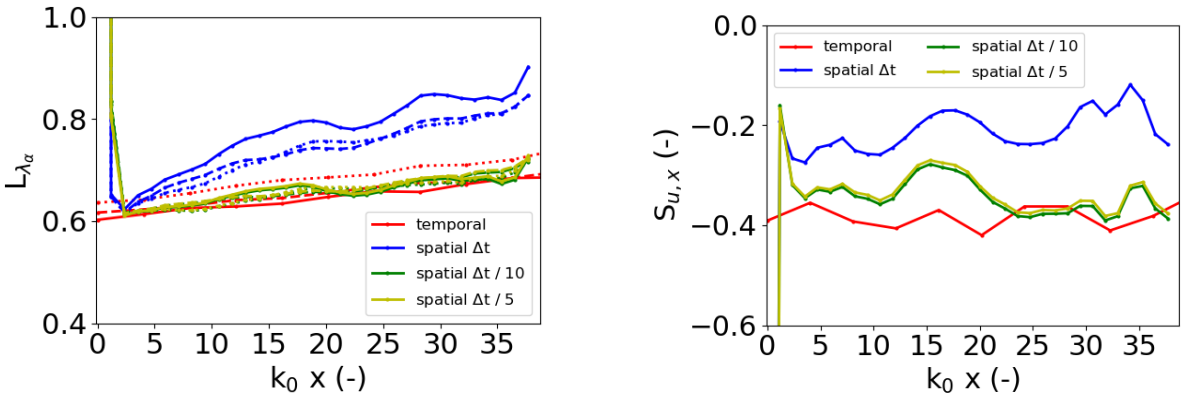

4-30 L_λ (left) and $S_{u,x}$ (right) decay with central scheme and different time step sizes. Full lines = L_{λ_1}, dashed lines = L_{λ_2}, dotted lines = L_{λ_3}. k_0 = 6, 32^3 cells

4.2.2.3. Time step size vs. sampling planes

The different investigations on the time stepping scheme and time step size led to the selection of an (explicit) global time stepping scheme to study the STI. A related requirement / issue is the need for much smaller time steps than the time it would take to travel with uniform supersonic convective velocity between two sampled planes. This would result in a step wise change of the inflow BC where each inflow plane would be kept the same for a number of time steps (e.g. 100). In order to investigate the influence of this procedure a simulation was performed with an increased number of sampling planes as follow:

1. Create uniform grid with double the amount of cell numbers in the x-direction as the original box. Double is important because of the adopted interpolation methodology which is based on a neighbouring search. If more new points are located between the original set of points, the interpolation will yield unexpected results.
2. Interpolate the solution of the original Nx^3 box onto the new grid
3. Extract the planes with same superimposed convective velocity as before
4. The above can be performed iteratively to obtain more and more sampling planes.

The procedure was applied twice to the test case of Garnier with conditions in Table 5-3 and with 64×64 cells in the transverse direction. The result for different quantities are given in Figure 4-31 to 4-33. The impact of doubling the number of sampling planes from 64 to 128 is very limited and the difference is even smaller between 128 and 256 (black and blue curves mostly overlap). The differences between the 64 and 128/256 case could easily be attributed to the interpolation procedure yielding small changes in the flow field that is convected through the domain. In terms of R_{11} (resolved) amplification the difference is less than 1 %. Note that in all simulations 100 subiterations were used which is probably an overkill when increasing the number of sampling planes.

In conclusion, using a number of sampling planes based on an isotropic uniform grid with a number of subiterations (time steps between the change of inflow BC) is an acceptable procedure.

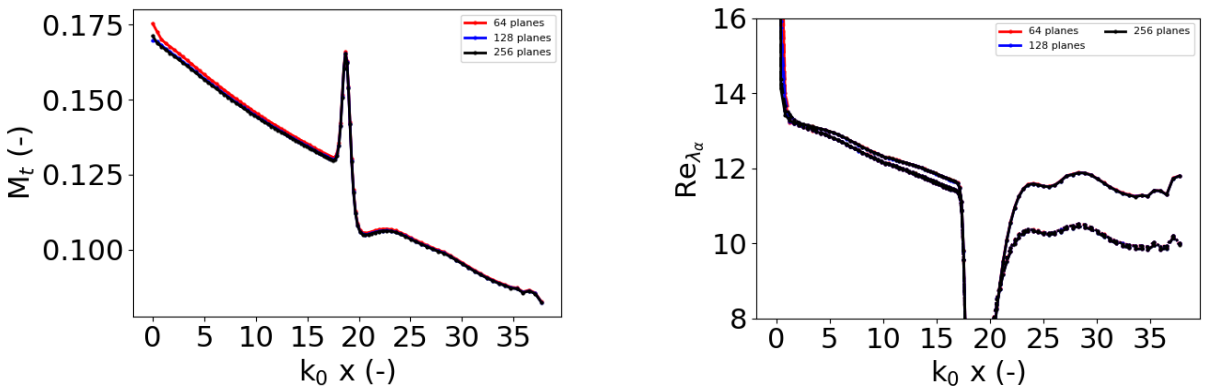

4-31 Number of sampling planes effect on M_t (left) and Re_λ (right) with central scheme LDND. 104 $\times 64^2$ cells and p-switch = 10, k_0 = 6

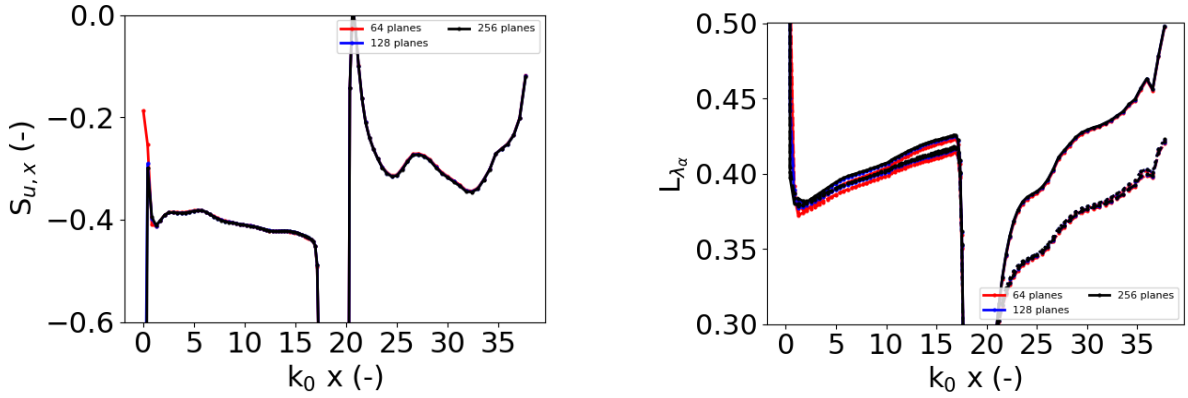

4-32 Number of sampling planes effect on $S_{u,x}$ (left) and L_λ (right) with central scheme LDND. 104 $\times 64^2$ cells and p-switch = 10, k_0 = 6

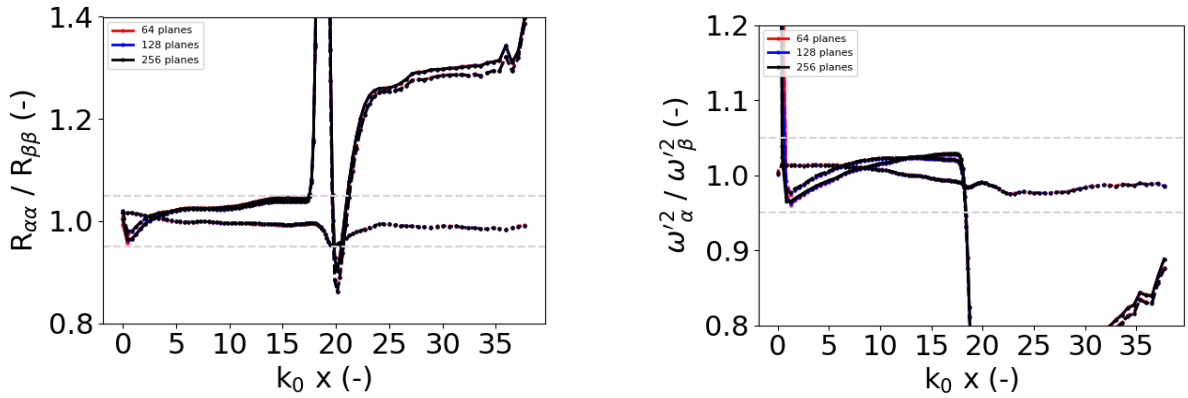

4-33 Number of sampling planes effect on Reynolds stress' (left) and vorticity fluctuations variance's (right) anisotropies with central scheme LDND. 104 $\times 64^2$ cells and p-switch = 10, k_0 = 6

5. The canonical STI problem

The previous chapters have explored the diverse numerical settings to different aspects relating to the canonical shock-turbulence interaction problem: turbulence generation, spatial and temporal discretization. With this knowledge, the current aim is to focus on the capabilities of the CFD solver to accurately study the STI. This is done by selecting a few conditions documented in the literature with varying levels of complexity in terms of computational requirements (Reynolds number and associated grids) and shock strength. The test cases are limited to solenoidal turbulence and low levels of fluctuations (turbulent Mach number). In a first part, the STI setup is introduced (5.1), followed by detailed discussions on the simulation results (5.2).

5.1. The General Setup

The computational domain considered in this work is shown in Figure 5-1. It consists of a rectangular box of size $L_x \times (2\pi)^2$ with a shock located initially at x = π. The (2π) size is convenient as it results in wavenumbers starting from 1 as discussed in 2.2. Turbulence is introduced supersonically at the inflow plane (see 5.1.2) and interacts with the shock. The numerical settings to study the problem are briefly discussed in 5.1.1 and the initialization in 5.1.3.

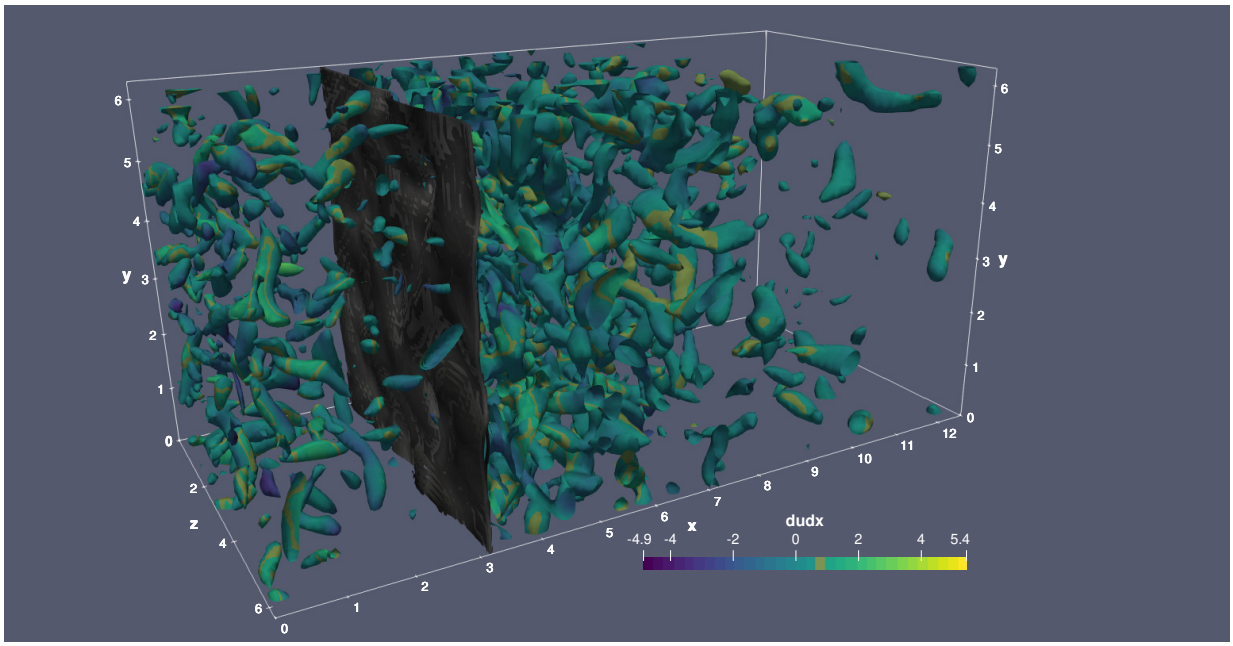

5-1 Setup of the canonical STI problem.

5.1.1. Numerics

Following extensive investigations in Chapter 4, the canonical STI problem is studied with the second-order accurate LD2 central scheme. However, given the hurdles encountered in dealing

with the shock wave (see 4.1.3), the low dispersion properties have been deactivated, reducing the approach to a low dissipation central scheme (see also [105]). The pressure switch weighting factor is set to 10 by default but does not influence simulation results for low supersonic Mach numbers (see 4.1.3). Time stepping is ensured through an explicit three-stage Runge-Kutta scheme [40] following the observations in 4.2.2.2. The time step was fixed at $\Delta t_{cell}/100$ where Δt_{cell} is given by Equation 4-4. LES filtering is implicitly performed through the finite volume approach with filter width set by the grid size (Equation 3-7). The subgrid scale contribution is obtained through Smagorinsky's model (Equation 3-6).

5.1.2. Boundary conditions

5.1.2.1. Inflow

Turbulence, obtained from separate DHIT simulations is convected through the domain by changing the inflow boundary plane. The inflow is defined as a Dirichlet boundary condition where fluctuations, from the sampled plane, are superimposed on the uniform mean pre-shock quantities. The DHIT is obtained through the procedure detailed in 2.2 and realistic turbulence carefully evaluated (see 2.2.2). A dual-time stepping scheme was adopted in the DHIT simulations as well as the LD2 scheme with low dispersion properties activated. The DHIT turbulence is convected periodically through the domain and was shown to be an acceptable methodology 4.2.2.1.

5.1.2.2. Transverse planes

Periodic boundaries are imposed on the transverse directions.

5.1.2.3. Outflow

In order to avoid acoustic reflections from the outflow boundary, the procedure typically adopted in the literature consists of implementing a non-reflective BC with references to Thompson [112] or Poinsot *et al.* [82] for the specifics. In spite of such a boundary condition, some authors [59, 41] have experienced non-physical oscillations in their second order statistics (Reynolds stresses) near the exit plane. The authors state, however, that the statistics are only affected in vicinity of the exit plane.

An additional procedure in avoiding downstream BC influence is the use of a so-called "sponge layer" [72] in addition to a non-reflective BC. The methodology essentially artificially dampens the fluctuations to a reference solution, which in the case of a STI are the Rankine-Hugoniot jump conditions of a laminar shock. The sponge layer is located before the outflow. In an LES, it is also possible to play with the grid stretching [25] downstream the shock wave to mimic the sponge layer's behavior. This methodology is based on the additional SGS dissipation linked to the grid stretching. The filter width in a classical Smagorinsky model can, for instance, be defined based on the maximum edge length of a cell (see Equation 3-7). In this case, an increased streamwise cell length which becomes larger than the transverse edge lengths will results in increased SGS dissipation. In case a sponge-like methodology is introduced, it is important to not consider this region in the STI analysis.

In this work, a subsonic outflow is prescribed with reference pressure obtained from the Rankine-Hugoniot jump conditions. It's effect on the second order statistics was investigated by considering several domain lengths, streamwise number of cells and stretching. A Mach 1.2 STI is selected with turbulence conditions of interest in the reproduction of the results of Garnier *et al.* [25]. The domain sizes are $2\pi \times (2\pi)^2$, $2\pi + 1 \times (2\pi)^2$ and $4\pi \times (2\pi)^2$ with initial shock located at x = π. The transverse planes contain 64×64 cells. Table 5-1 summarizes the different domains and cells considered. Figures 5-2 and Figure 5-3 shows the resulting Reynolds stress amplifications. Recall the definition of the Reynolds' stress components in terms of the following Favre average

$$R_{ij} = \widetilde{u_i'' u_j''} = \frac{\overline{\rho u_i'' u_j''}}{\bar{\rho}} \tag{5-1}$$

The first and second vertical lines, located respectively at k_0 1.5π and k_0 2π, indicate the positions from where the grid spacings are altered in the different cases (see also Table 5-1). The pre-shock spacing and cell count is the same for all simulations. The peak post-shock R_{11} and R_{22} positions and magnitudes differ minimally between the different cases. This indicate that the exit BC does not influence their values. For cases 2π, $2\pi + 1C$ and 4π, the maximum $\Delta x < \Delta y$ which implies that the LES filter width is set to $\Delta y = \Delta z$. Moreover, care is taken to enable a smooth transition between the different regions of cells. In the other cases, the streamwise cell spacing towards the end of the domain is such that $\Delta x > \Delta y$ which would result in larger filter widths towards the exit BC. However, it appears that these different cases lead to an unstable behavior. The vorticity variances in Figure 5-4 show similar results with no impact of the outflow on the amplification. The effect of increased grid spacing (filter width) is also more clearly visible.

In conclusion, the fixed pressure outflow in combination with a shorter domain length, does not impact the amplifications in second order statistics. In addition, no change in filter width is needed through an increased streamwise cell spacing.

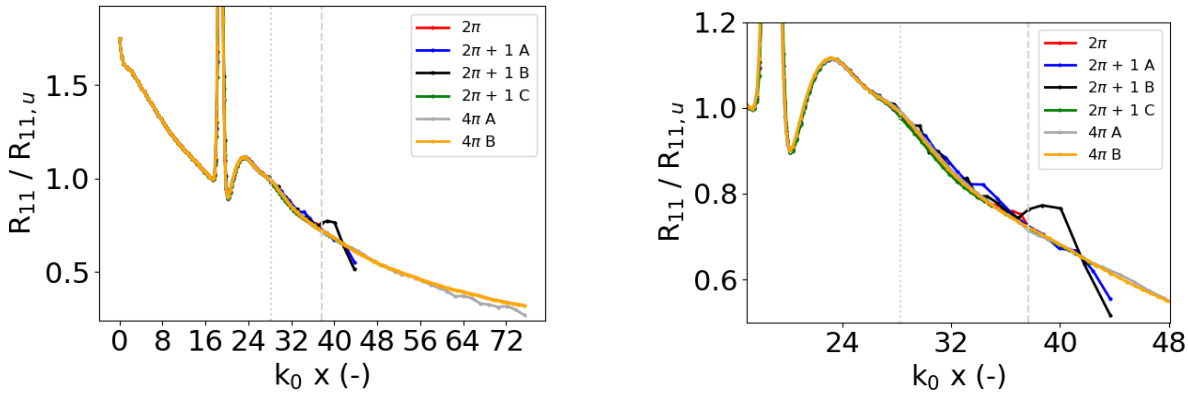

5-2 Effect of streamwise domain length and outflow on the streamwise Reynolds stress amplification. $N_x \times 64^2$ cells and p-switch = 10, k_0 = 6

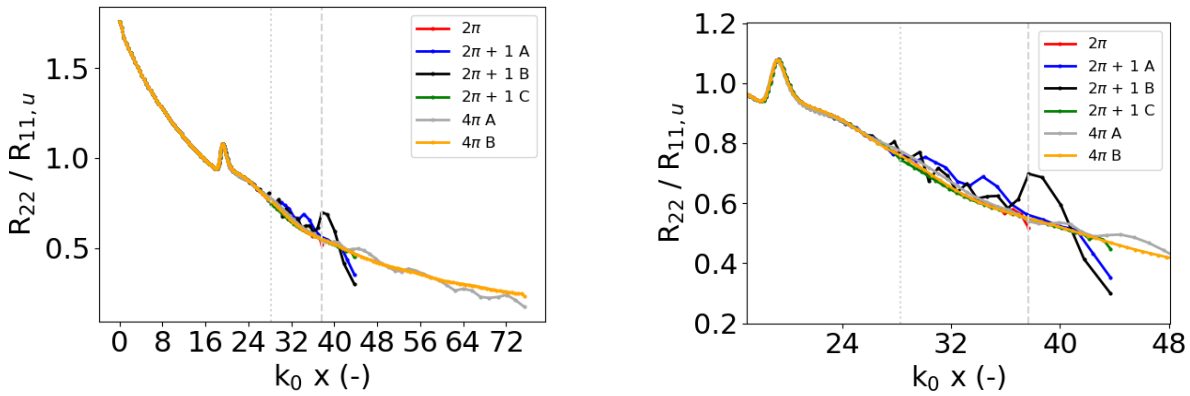

5-3 Effect of streamwise domain length and outflow on the spanwise Reynolds stress amplification. $N_x \times 64^2$ cells and p-switch = 10, k_0 = 6

5-1 Cell and domain details in the study of the effect of streamwise domain length and outflow on the amplifications for Garnier et al. [25], $N_y = N_z = 64$.

	N_x				$N_{x,tot}$
Domain size	**0–π**	**π–1.5π**	**π–2π**	**… – end**	
2π	62	26		16	104
2π + 1 A	62	26		16	104
2π + 1 B	62		42	4	108
2π + 1 C	62	26		28	116
4π A	62		42	30	134
4π B	62	26		82	170

5.1.3. Initialization and shock drift

A shock is initially placed at x = π inside the domain of Figure 5-1. The pre-shock and post-shock are prescribed through the Rankine-Hugoniot (laminar) jump conditions. Some authors (e.g. [52]) document the presence of a shock drift, i.e. when the incoming turbulence enters the domain and starts interacting with the shock wave, the latter starts moving out of place towards the inflow or outflow plane. It is explained by the fact that the Rankine-Hugoniot relations are valid for an instantaneous flow field but not on average [53]. The phenomenon could especially be problematic at higher M_t [51] and M_s [97]. A solution for this problem consists of evaluating the shock drift speed and adapting the back pressure (outflow BC) accordingly in a sort of response loop [53]. In present work, the shock drift was observed to be minimal and not an issue for the statistics' computations. Similar observations, in the context of the canonical STI, were reported in the literature [97, 116]. A plausible reason for the lack of shock drift in the present work is the low-order of the spatial discretization scheme.

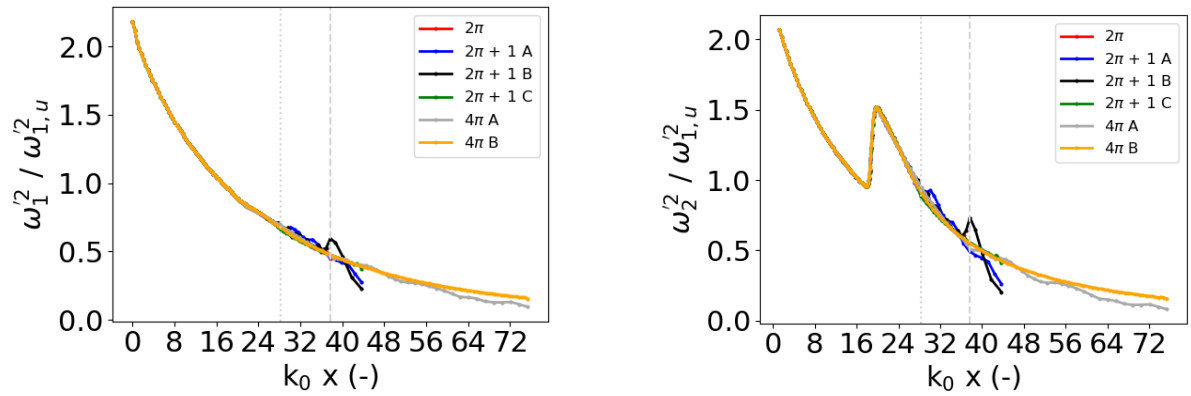

5-4 Effect of streamwise domain length and outflow on the streamwise (left) and spanwise (right) vorticity variances. $N_x \times 64^2$ cells and p-switch = 10, k_0 = 6

5.1.4. Statistics collection

Statistics were collected after the initial transients induced by injecting the turbulence through the inflow plane and starting with the initial field specified through the Rankine-Hugoniot relations. For domain sizes of $2\pi \times (2\pi)^2$, transients were allowed to settle for two flow through times based on the incoming supersonic convective speed. In the case of larger domain sizes, i.e. $4\pi \times (2\pi)^2$, four flow through times were imposed for the flow to settle. Statistics (space and then time averaged) were collected for four flow through times.

5.2. STI results

Detailed investigation of several shock-turbulence interaction studies are now presented. A first discussion introduces the challenge of comparing canonical STI results performed by different authors with different codes. Then, the STI results obtained with TAU are compared with available literature.

5.2.1. How to compare to the literature?

In the majority of LES studies of canonical STI from the literature [25, 19, 28, 27, 5, 35], a DNS reference simulation is also performed which can be filtered to the LES grids for comparison purposes. Such an approach is however only possible for moderate Re_λ at which the computational cost of DNS remains within acceptable limits. Other LES studies [54, 8, 9] use available DNS simulation data from the literature to assess their predictive capability. This type of comparison should be seen in a more indicative manner if the exact same grids are not used. Part of the reason is the grid dependence of the pre-shock turbulence characterization parameters (Re_λ, M_t) and will be discussed further below. Moreover, the SGS contribution to the different terms must also be accounted for, which is circumvented when a reference DNS solution is filtered to the LES grids. Another possible point of comparison is Linear Interaction Analysis (LIA) which represents an inviscid behavior (infinite Re_λ) and which was, for instance, considered in early LES studies of the canonical STI [20]. An additional difficulty in using LIA is the finite (low) Re_λ dependency of simulations resulting in viscous and non-linear effects on the amplifications of e.g. second order statistics. Consequently, LIA is perceived as an asymptotic reference for CFD simulations. Within this context, Ryu and Livescu [97] have reconciled DNS and LIA for $M_s < 2.2$ by suggesting the ratio of shock thickness to the Kolmogorov length scale δ/η as a guiding parameter and where the limit $\delta/\eta \to 0$ represents LIA. This ratio can be estimated from Equation 1-8 (rewritten for clarity as Equation 5-2 below) and is especially useful in the comparison of numerical studies between different authors. Moreover, it can also be used in indicating the STI regime (broken, wrinkled, borderline [52]).

$$\frac{\delta}{\eta} \approx \frac{7.69 M_t}{Re_\lambda^{0.5}(M_s - 1)} \tag{5-2}$$

An associated issue with the above ratio, specific to LES, is a grid dependence of M_t and Re_λ. The latter parameters characterize the turbulence state prior to the shock, and together with M_s, the canonical STI setup under investigation. In reproducing reference DNS results, a specific combination of M_t and Re_λ just before the shock is targeted. In an LES, M_t requires the contribution of the modeled (SGS) TKE which, in most cases, has to be estimated somehow [90]. This specific topic is discussed in 3.3 and is highly dependent on the CFD solver (numerics) and grids. Re_λ (Equation 1-2) relies on the computation of L_λ (Equation 1-3) which in turn requires velocity gradients to be computed. The latter has shown to be strongly grid dependent (see Table 3-1 and 3.2). Therefore, the computation of M_t and Re_λ on an LES grid yielding the same value of these parameters as a reference DNS might in fact differ. This would lead to a somewhat different δ/η. The problem vanishes when the LES grids tend towards the resolution required for DNS but loses the whole purpose of a LES simulation.

The above discussion remains valid in the comparison of different LES simulations, even if performed with the same solver but on different grids. This is illustrated with the canonical STI at Mach 1.2 with pre-shock turbulent conditions of Garnier *et al.* (see 5.2.2 for a detailed description of the setup). Two grids are selected for comparison: $104 \times (64)^2$ (Grid 1) and $138 \times (96)^2$ (Grid 2) cells with minimum grid spacing set as discussed in 5.2.2 which includes a transverse cell spacing dependency (and therefore a grid dependency). The reference DNS of Garnier *et al.* [25] was performed on a $138 \times (64)^2$ grid (see Table 5-4) yielding δ/η of 1.52 (see Table 5-3). The same value for this ratio was targeted for both grids with results shown in Table 5-2. This was, however, never achieved through the same combination of pre-shock M_t and Re_λ values. All quantities in the presented table are computed based on the resolved part of the flow field, i.e. the SGS contribution is not added, and is not an issue for the sake of the present discussion. Re_λ is taken as the average in each direction. Maximum pre-shock Reynolds stress anisotropies are 5% and 4% on the first and second (finest) grids, respectively.

The results for both grids are consistent with the expectations that the streamwise Reynolds stress amplification is higher for lower δ/η. Note that, in this discussion, the amplification is based on the peak post-shock value (see e.g. Figure 5-2). Comparing the amplifications between both grids, differences are already visible. E.g. Grid 2 - Case 1's δ/η ratio lies between Grid 1 - Case 1 and Case 2 but has an R_{11} amplification outside the latter cases' range. However, the differences are smaller than 2 %. As mentioned previously, the reason for the differences can be found in the grid dependency of the turbulent parameters which was discussed in Section 3.2. Based on Table 3-1, filtering a finer grid turbulence field onto a coarser one ($96^3 \rightarrow 64^3$) resulted in an 8 % difference (increase) in value of Re_λ. Note that the latter observation cannot be generalised but is solely used as an indicator in this discussion. Therefore, the δ/η ratio's of Grid 1 are not easily comparable to Grid 2. This statement is especially valid when the selected grid resolutions are far from that required for DNS. A comparison between Grid 2 - Case 1 and the filtered DNS of Garnier *et al.* [25] on grid A, which has the same δ/η ratio, indicates a difference in R_{11} amplification less than 2 %.

In conclusion, while the parameter δ/η demonstrates some grid dependence, it remains a useful parameter to analyze simulations, observe trends and discuss different settings on a similar grid. In comparing results between different grids or different solvers it should be seen as a more indicative parameter.

5.2.2. Mach 1.2 STI of Garnier

Garnier *et al.* [25] were one of the first to report LES results of the canonical STI problem. They considered high-order accurate numerical discretization methods. Inviscid fluxes are treated with a fourth-order centred scheme except in the vicinity of the shock wave (pre-defined zone) where a fourth-order accurate ENO scheme is applied. Viscous fluxes are treated with a second-order centred scheme and time advancement is achieved with a third-order Runge-Kutta Total Variation Diminishing (TVD) scheme. Several SGS models were considered for study: Smagorinsky, Mixed Scale Model (MSM), dynamic Smagorinsky (DSM) and Dynamic Mixed Scale Model (DMM). A Mach 1.2 and Mach 2 case with pre-shock Re_λ of 11.9 and 19, respectively was simulated on a $2\pi + 1 \times (2\pi)^2$

5-2 Comparison of δ/η effect on R_{11} amplification in the STI conditions of Garnier *et al.* [25] at Mach 1.2.

Case ID	$\mathbf{M}_{t,res}$	$\mathbf{Re}_\lambda$	δ/η **(res)**	$\mathbf{R}_{11,d}$ / $\mathbf{R}_{11,u}$ **(res)**
Grid 1 : 104×64^2				
Case 1	0.142	12.83	1.59	1.105
Case 2	0.131	11.32	1.50	1.115
Case 3	0.122	10.53	1.42	1.126
Grid 2 : 138×96^2				
Case 1	0.137	12.06	1.52	1.102
Case 2	0.131	12.15	1.44	1.113

domain. Note that the latter values are also documented in the DNS of Lee *et al.* [59, 56, 60] which was part of the author's motivation to allow some reference for comparison. The Mach 1.2 case, with pre-shock details listed in Table 5-3, is presently considered for reproduction. Based on the separate analyses of Larsson *et al.* [52] and Donzis *et al.* [18], the condition should result in the broken shock regime (see Equation 1-6) This is also confirmed visually in Figure 1 of [97].

5-3 Mach 1.2 STI conditions of Garnier *et al.* [25].

$\mathbf{M}_s$	$\mathbf{M}_t$	$\mathbf{Re}_\lambda$	δ/η	$\mathbf{M}_t$**/ (**$\mathbf{M}_s$**-1)**
1.2	0.136	11.9	1.52	0.68

Garnier *et al.* [25] also performed a DNS simulation of the test case which they used as a reference for their LES results. Relevant to the Mach 1.2 case, Table 5-4 summarizes the grid information documented by the authors. The low Re_λ considered allows DNS, with their choice of numerical discretization schemes, to be performed on a relatively coarse grid. This renders this specific set of conditions interesting from the point of view of reproducing different aspects of the canonical STI problem and fine tune the numerical setup needed in TAU. The LES grid (A1), has a streamwise stretching towards the initial shock position (x = π) ensuring $\Delta x = 2\sqrt{3} i_t \Delta y$ (see also Section 3.1) at the shock, where $\Delta y = 2\pi/N_y$. The turbulence intensity i_t is 0.07 and the maximum Δx considered is equal to the uniform transverse grid spacing Δy. The filter length used by Garnier *et al.* [25] is based on the local cell volumes $\Delta = (\Delta x \Delta y \Delta z)^{1/3}$. The LES inflow is provided by filtering the DNS onto the LES grids. Therefore, as discussed previously in 5.2.1, the pre-shock conditions of Table 5-3 which are assumed to be based on the DNS, might differ somewhat in their actual LES.

5.2.2.1. Optimal setup description for Mach 1.2 STI of Garnier

In present work, a $(2\pi)^3$ STI domain is selected as it was shown in 5.1.2.3 to be adequate in reproducing the amplifications of interest. Results are presented for a grid with 104×64^2 cells (Grid 1) for which the pre-shock conditions are listed in Table 5-5 and the amplifications in Table 5-6. The

5-4 Grid and amplification detail of the Mach 1.2 STI study by Garnier *et al.* [25]. SGS model = Smagorinsky.

Case	$\mathbf{N}_\mathrm{x}$	$\mathbf{N}_\mathrm{y}$ = $\mathbf{N}_\mathrm{z}$	$\mathbf{R}_{11,d}$ / $\mathbf{R}_{11,u}$	$\mathbf{R}_{22,d}$ / $\mathbf{R}_{11,u}$	$\omega'^2_{2,d}/\omega'^2_{2,u}$
DNS (A)	138	64	1.149	1.127	1.683
Filtered DNS (A1)	69	32	1.106	1.308	No info
LES Smagorinsky (A1)	69	32	1.122	1.252	No info

streamwise cell grading was set according to Equation 3-4 relying on the conditions of Lee *et al.* [59] yielding a turbulence intensity of 5 % which is more conservative than the 7% for Garnier *et al.* [25] based on the conditions of Table 5-3. Pre-shock anisotropies are below 5 % for the Reynolds stresses and below 4 % for vorticity variances. Note that the presented simulations were ran with a pressure switch weighting factor set to 10. It's impact was discussed in 4.1.3 and for the present shock strength it does not strongly affect the predictions. A separate investigation for Case 2 was performed with resulting differences in pre-shock turbulence state and amplifications that differ less than 1% by considering a pressure switch weighthing factor of 1.

5.2.2.2. Pre-shock conditions

Results for 4 cases are summarised. Three of them consider the Smagorinsky SGS model (Cases 1 to 3) and one (Case 4) without SGS model with same inflow as Case 2. In analogy to Garnier *et al.* [25] the latter could be named "coarse DNS". The ratio of shock thickness to Kolmogorov length (δ/η) scale just before the shock wave (mean shock position obtained from $|d\bar{u}_1/dx|$=0), obtained from Equation 5-2, is listed in Table 5-5. It was computed based on the resolved part ($_{res}$) of the turbulence as well as with $\mathrm{M_t}$ accounting for $\mathrm{TKE_{SGS}}$ through Equation 3-9 with both values of $\mathrm{C_k}$ = 0.07 and 0.17 following a discussion on estimating the SGS contribution in Section 3.3 . The former and latter value of the constant $\mathrm{C_k}$ are denoted by subscripts $_1$ and $_2$, respectively. It must be noted that the SGS contribution assumes local isotropy of the smallest modeled scales (see Equation 3-8). However, in the early post-shock region, this assumption does not hold [53]. The vorticity variances, which are related to the small scale motions, are anisotropic and take some time for a return to isotropy. Nevertheless, the Smagorinsky SGS model assumes local isotropy of the modeled scales by construction. Therefore, the use of Equation 3-9 is correct from the point of view of the LES implementation. The reference DNS of Garnier *et al.* [25] has δ/η = 1.52 as shown in Table 5-3 which lies between Case 1 and Case 2 if only considering the resolved part.

5.2.2.3. Reynolds stress amplifications

Recall that presently the $\mathrm{R_{11}}$ amplifications are based on the post-shock peak value and no extrapolation back to the mean shock position is performed or other methodology considered which would limit non-linear effects on this quantity as much as possible. The streamwise Reynolds stress amplifications are listed in Table 5-6 with and without SGS contribution. In all present cases, the latter contribution to the $\mathrm{R_{11}}$ amplification is less than 1.5 %. Filtering of the reference DNS to LES

5-5 Pre-shock turbulence state in the STI reproducing the conditions of Garnier *et al.* [25] at Mach 1.2.

Case ID	$\mathbf{M}_{\mathrm{t,res}}$	$\mathbf{M}_{\mathrm{t,tot}_1}$	$\mathbf{M}_{\mathrm{t,tot}_2}$	$\mathbf{Re}_\lambda$	$\delta/\eta\|_{res}$	$\delta/\eta\|_1$	$\delta/\eta\|_2$
Grid 1 : 104×64^2							
Case 1	0.142	0.150	0.143	12.83	1.59	1.67	1.59
Case 2	0.131	0.138	0.132	11.34	1.50	1.57	1.52
Case 3	0.122	0.128	0.123	10.93	1.42	1.49	1.43
Case 4 (no SGS)	0.133	/	/	11.06	1.54	/	/
Grid 2 : 138×96^2							
Case 1	0.137	0.142	0.138	12.06	1.52	1.57	1.53
Case 2	0.131	0.135	0.131	12.15	1.44	1.49	1.45

5-6 Amplifications in the STI reproducing the conditions of Garnier *et al.* [25] at Mach 1.2.

Case ID	$\delta/\eta\|_{res}$	$\mathbf{R}_{11,d}$ / $\mathbf{R}_{11,u}\|_{res}$	$\mathbf{R}_{11,d}$ / $\mathbf{R}_{11,u}\|_1$	$\mathbf{R}_{11,d}$ / $\mathbf{R}_{11,u}\|_2$	$\omega'^2_{2,d}$/ $\omega'^2_{2,u}\|_{res}$
Grid 1 : 104×64^2					
Case 1	1.59	1.105	1.116	1.109	1.500
Case 2	1.50	1.115	1.129	1.120	1.520
Case 3	1.42	1.126	1.140	1.130	1.555
Case 4 (no SGS)	1.54	1.136	/	/	1.577
Grid 2 : 138×96^2					
Case 1	1.52	1.102	1.110	1.104	1.560
Case 2	1.44	1.115	1.122	1.116	1.588

resolution (grid A1), suggests that the SGS contribution to the R_{11} amplification should be about 3.8 % (see Table 5-4). The LES of Garnier *et al.* [25], with Smagorinsky's SGS model, results in 2.4 % SGS contribution to the amplification on a grid with transverse planes cell numbers of 32×32. In comparison, presently, 64×64 cells are considered in the transverse planes which is consistent with the smaller levels of SGS contribution observed.

The reference results of Table 5-4 do also confirm the difficulty in comparing LES and DNS, even by filtering the DNS to the desired grids with the same CFD solver (see A1 filtered DNS and LES). The issue does relate again to the turbulent decay which is more rapid in the pre-shock region for the LES (with adequate LES grids, i.e. coarser than DNS) compared to the (filtered) DNS (see Figure 6 in [25]). This in turn results in lower pre-shock M_t which in turn, assuming similar pre-shock Re_λ, results in a smaller value of δ/η. The latter could explain the increased amplification in Table 5-4 for

the LES compared to the filtered DNS. Note that it is believed that the LES results of Garnier *et al.* [25] do not account for the SGS contribution which is based upon the fact that the filtered DNS is taken as the reference point for their discussions.

In terms of present R_{11} amplifications in Table 5-6, Case 3 coincide (difference < 1 %) with the reference LES when not accounting for the SGS contribution. In comparison to the reference (unfiltered) DNS, Case 3 with SGS contribution does come closest in terms of amplification with differences below 1% and 2% for the different SGS coefficients. Considering the ratio δ/η = 1.52 of the reference DNS, with the different SGS contributions, Case 3 $\delta/\eta|_1$ and Case2 $\delta/\eta|_2$ are closest. The differences in magnitide are 0.8 % and 2.5 % respectively which is very satisfactory. Case 4, which does not use any SGS model, yields as expected a higher amplification compared to the same set up with SGS model (Case 2). It does, however, differ only by 1.8 % ($|_{res}$). A similar comparison by Garnier *et al.* [25] yields a difference of 2.7 %. Figure 5-5 shows the streamwise evolution of R_{11} (resolved part) without and with scaling by the respective pre-shock magnitude. The pre-and post-shock decay occur faster when the turbulent Mach number is higher (see decay Case 1 $>$ Case 2 $>$ Case 3).

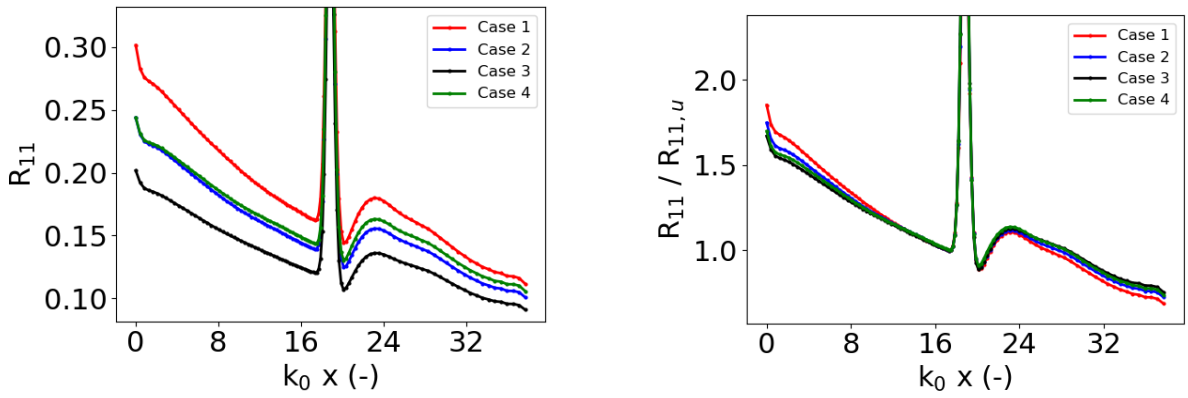

5-5 R_{11} amplifications in the STI of Garnier without (left) and with (right) scaling by pre-shock value. 104×64^2 cells and p-switch = 10, k_0 = 6

The transverse Reynolds stress R_{22} (resolved part) is presented in Figure 5-6. The related amplifications are listed in Table 5-7. Note that the peak R_{22} values (located within the shock identified through $|d\bar{u}_1/dx| = 0$) are scaled by the pre-shock R_{11} value. By doing so, the effect of pre-shock Reynolds stress anisotropies is removed and enables a better comparison with possible reference DNS or LES data from the literature where different levels of anisotropies than in present simulations could possibly be observed. Similarly to the R_{11} behavior, a decrease in δ/η ratio results in an increased amplification of R_{22} (see also Figure 4 of [97]).

The SGS contribution to the total R_{22} amplification reach up to 55% and 16 %, depending on the value of C_k, which is much more significant than for the R_{11} amplifications. The current range of results yield a maximum difference of 15 % with respect to the LES results of Garnier, not account-

ing for any SGS contribution. The amplifications with SGS contribution tend to overestimate the reference DNS. For the cases with δ/η closest to 1.52 of the reference DNS, present predictions differ 115% and 11 % for Case 3 ($\delta/\eta|_1$) and Case2 ($\delta/\eta|_2$), respectively. The reference LES differs only 4.3 % to the filtered DNS.

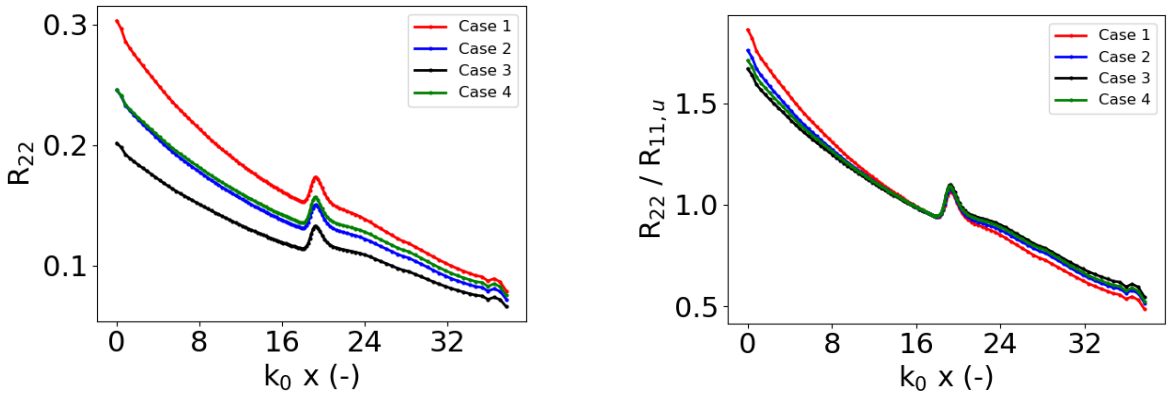

5-6 R_{22} amplifications in the STI of Garnier without (left) and with (right) scaling by pre-shock value. 104×64^2 cells and p-switch = 10, k_0 = 6.

5-7 Amplifications of R_{22} in the STI reproducing the conditions of Garnier *et al.* [25] at Mach 1.2.

Case ID	$\delta/\eta\|_{res}$	$\mathbf{R}_{22,d}$ / $\mathbf{R}_{11,u}\|_{res}$	$\mathbf{R}_{22,d}$ / $\mathbf{R}_{11,u}\|_1$	$\mathbf{R}_{22,d}$ / $\mathbf{R}_{11,u}\|_2$
Grid 1 : 104×64^2				
Case 1	1.59	1.067	1.942	1.206
Case 2	1.50	1.079	2.181	1.253
Case 3	1.42	1.100	2.424	1.305
Case 4 (no SGS)	1.52	1.090	/	/
Grid 2 : 138×96^2				
Case 1	1.52	1.137	1.741	1.215
Case 2	1.44	1.152	1.902	1.253

The high SGS contributions to the total R_{22} are further investigated. Figure 5-7 and shows the evolution of the resolved and total portions of the streamwise and transverse Reynolds stresses for Grid 1 - Case 2. The total quantities are estimated with Equation 3-10 and C_k = 0.17. The representation does indicate a clear difference in the curves for R_{22} in the shock region. Whilst the peak of the latter quantity is located in this region, it is not for the peak R_{11} considered in previous discussions. Therefore, the observations with regard to the high SGS contribution were not brought to light earlier. Outside the shock region, no unexpected behavior is visible. The percentages of resolved

to total Reynolds stress components are given by Figure 5-8 which confirm the adequacy of the selected LES grids.

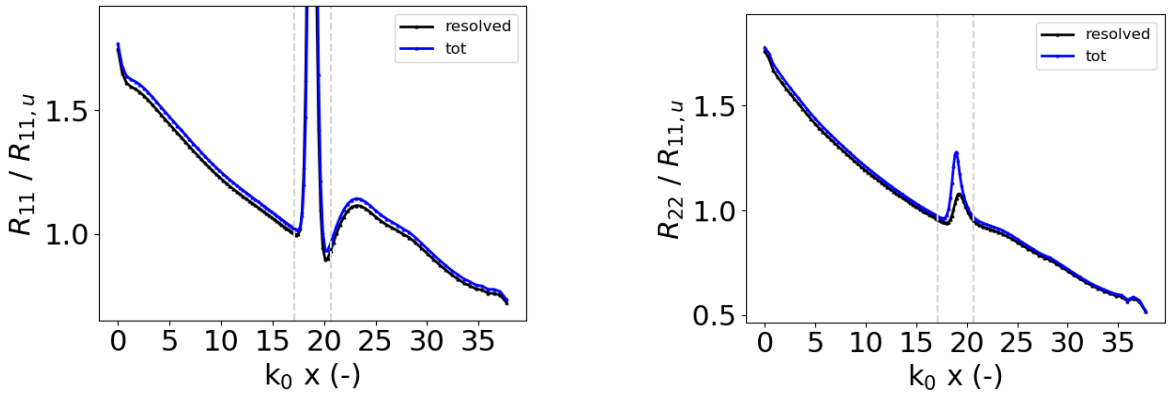

5-7 Resolved and total portion of R_{11} (left) and R_{22} (right) in the STI of Garnier. C_k=0.17, 104×64^2 cells, p-switch = 10, k_0 = 6. Grid 1 - Case 2.

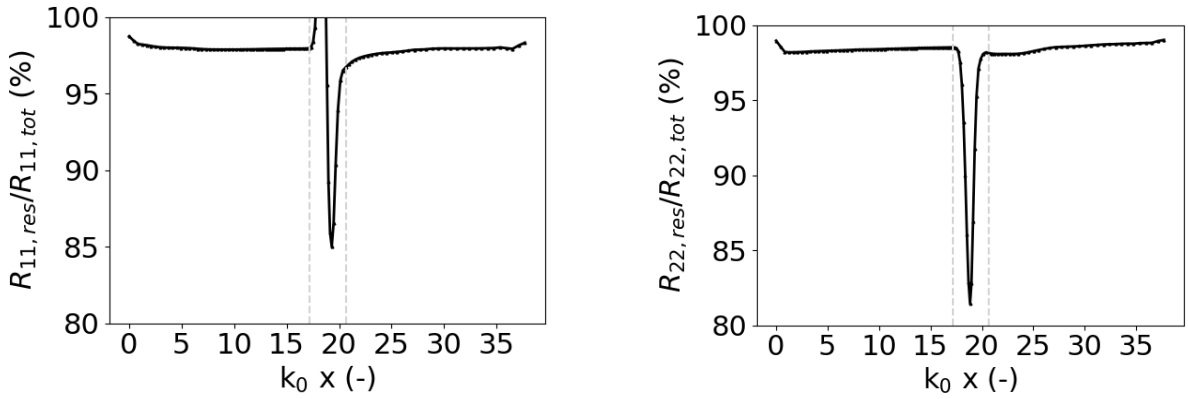

5-8 Ratio of resolved to total portion of R_{11} (left) and R_{22} (right) in the STI of Garnier. C_k=0.17, 104×64^2 cells, p-switch = 10, k_0 = 6. Grid 1 - Case 2.

Simulations were also performed with a finer grid consisting of 138×96^2 cells (Grid 2). Similarly to the coarser grid, the grading criteria of Equation 3-4 is applied. Note that such a refinement is somewhat contradictory to the idea of an LES as a larger portion of the turbulence is resolved closing in to DNS resolutions. The previous grid had shown to be already adequate ($>$ 80 %) from the point of view of Equation 3-10 as presented in Figure 3-1. The advantage of LES lies in the reduced computational cost by modeling as much as possible the SGS contribution which would translate in closing in on the reference of 80 % resolved TKE. It is however not confirmed that it would suffice in order to obtain reasonable amplifications in the canonical STI problem. Reynolds stress anisotropies remain below 4 % for the different results discussed with this grid.

With this finer grid, the SGS contribution to the R_{11} amplifications remain below 1 % for both C_k

coefficients. With respect to the reference DNS, the amplification based on the resolved portion of the LES yields differences of 4 and 3 % for Case 1 and 2, respectively. The ratio $\delta/\eta|_{res}$ of Case 1 coincides with the reference DNS and the relative difference in $R_{11,d}$ / $R_{11,u}|_{res}$ remaining below 5 % is an indicator of the capability of the present setup in TAU (with a DNS-like grid) to tackle the canonical STI problem, at least in terms of R_{11}. With the SGS contribution, $\delta/\eta|_2$ of Case 1 and $\delta/\eta|_1$ of Case 2 are closest to the 1.52 reference. The respective amplifications differ 4 and 2 % relative to the reference DNS. Note that the amplifications (resolved only) for Grid 2 - Case 2 and Grid 1 - Case 2 are the same despite differences (4%) in $\delta/\eta|_{res}$ ratios. This observation does again point toward the difficulty in comparing amplifications between different grids (see also 5.2.1 and 3.2) even within the same CFD solver.

In terms of R_{22} (Table 5-7), $R_{22,d}$ / $R_{11,u}|_{res}$ for Case 1 is in close agreement to the reference DNS of Table 5-4 (overestimation $<$ 1 %). SGS contributions to this amplifications are below 40 % for $\delta/\eta|_1$ and below 9 % for $\delta/\eta|_2$. Specifically, for the cases closest to $\delta/\eta|$ = 1.52, the contributions are 6.4 % ($\delta/\eta|_2$ Case 1) and 39.4 % ($\delta/\eta|_1$ Case 2). In comparison to Grid 1 (see previous discussion), the R_{22} amplification overestimation with SGS are significantly smaller: 40 % ($\delta/\eta|_1$ Case 2) and 7 % ($\delta/\eta|_2$ Case 1) relative error with respect to DNS.

In conclusion, the present solver can reproduce the reference DNS data within 5 % for R_{11} amplifications. For both grids considered, the SGS contribution to this amplification remains below 2 %, whichever C_k coefficient is used in the estimate given by Equation 3-9. However, the study of R_{22} amplifications demonstrate strong differences in the SGS contribution to its total value. With C_k = 0.07 the contribution can go higher than 50 % on the coarser grid and up to 40 % on the finer grid. A value of 0.17 for C_k yields maximum contributions below 16 and 9 % for these respective grids. Based on the cell count, the finest grid would be close to a DNS like resolution. The elevated SGS contributions to the R_{22} amplification of the smaller C_k coefficient would indicate that its value is not appropriate to estimate the SGS contribution. Moreover, the R_{22} study would suggest that it could be a decisive parameter in selecting the final grid size, even in an LES, i.e. solely basing a mesh strategy on R_{11} does not suffice. This statement is in line with the discussion of Larsson *et al.* [53] about the necessity to refine the grids in both stream-wise and transverse directions. A grid effect comparison in an LES of the canonical STI was also presented by Braun *et al.* [9] in which the resolved and total portions of the stream-wise and transverse Reynolds stresses is shown (M_s = 1.5, Re_λ = 75, M_t = 0.16). It (Figure 5 of [9]) does demonstrate a similar observation as discussed above, i.e. the SGS contribution is larger for R_{22} and is strongly dependent on the transverse grid spacing.

Note that slight errors in the digitalization of the reference data from Garnier *et al.* [25] might be present. It does, however, not impact the different conclusions drawn about the predictions with TAU.

5.2.2.4. Vorticity fluctuations variances

The evolution of the streamwise and transverse vorticity variance fluctuations is presented for the 64× 64 transverse cell count in Figures 5-9 and 5-10, respectively. The quantities are computed solely based on the resolved fluctuations as obtaining a subgrid-scale contribution is not trivial. This would require gradients of the SGS fluctuating velocity component(s) which is not readily available. As expected (see e.g. [59, 25]) , the streamwise component is barely affected by the interaction with the shock wave and only the transverse components are amplified, *i.e.* turbulence becomes axisymmetric. Similarly to the observations of the Reynolds stresses (Figure 5-5 and 5-6), the pre- and post-shock decay rates are faster for a higher M_t case (Case 1 $>$ Case 2 $>$ Case 3).

The transverse component's amplification levels are provided in Table 5-6. The amplifications are consistent with those of the Reynolds stresses, that is, a higher amplification for lower δ/η ratio. A maximum difference ratio of 3.7 % is observed between Case 1 and Case 3. Unfortunately, the reference only provides this quantity for the DNS result as shown in Table 5-4. The vorticity fluctuations are strongly dependent on the smallest scales [52]. Therefore, a DNS cannot directly be compared with an LES result. The smallest relative difference with respect to the DNS amplification of ≈ 1.683 (from digitized graph) is 7.6 % for Case 3.

Considering a finer grid with increased transverse cell spacing (Grid 2) results in higher $\omega_2'^2$ amplifications (Table 5-6) and is in line with the R_{22} behaviour. A difference of 7.3 % and 5.6 % is now observed between compared to the reference DNS for, respectively, Grid 2 - Case 1 and Grid 2 - Case 2. Even in a DNS, the strong grid dependence of the transverse vorticity variance's STI evolution is documented. See, for instance, Sethuraman *et al.* [102] (Figure 3 c). Note that in the latter work, the grid sizes impact the amplification and the near post-shock region but the downstream evolution behaves in a similar manner. In comparison, the Reynolds stress amplifications are shown to not depend as much on the transverse grid spacing.

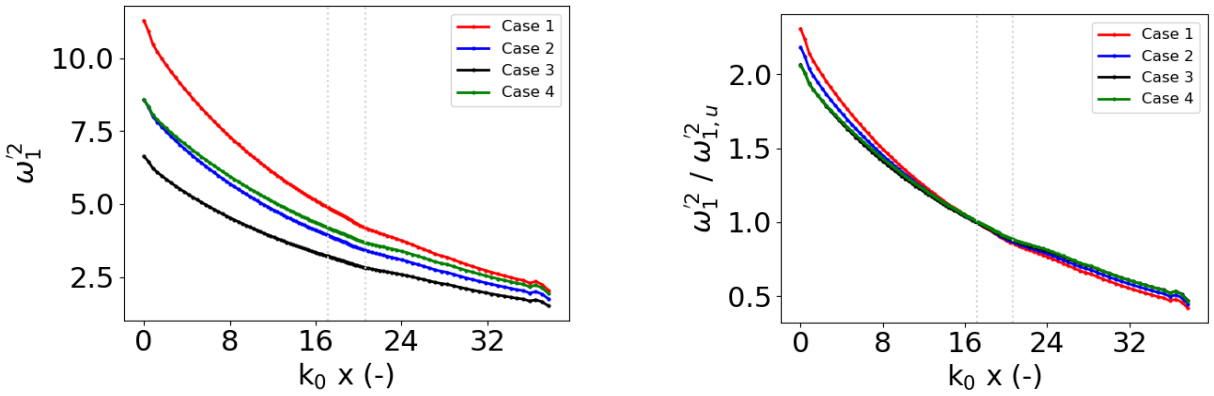

5-9 $\omega_1'^2$ amplifications in the STI of Garnier without (left) and with (right) scaling by pre-shock value. 104×64^2 cells and p-switch = 10, k_0 = 6.

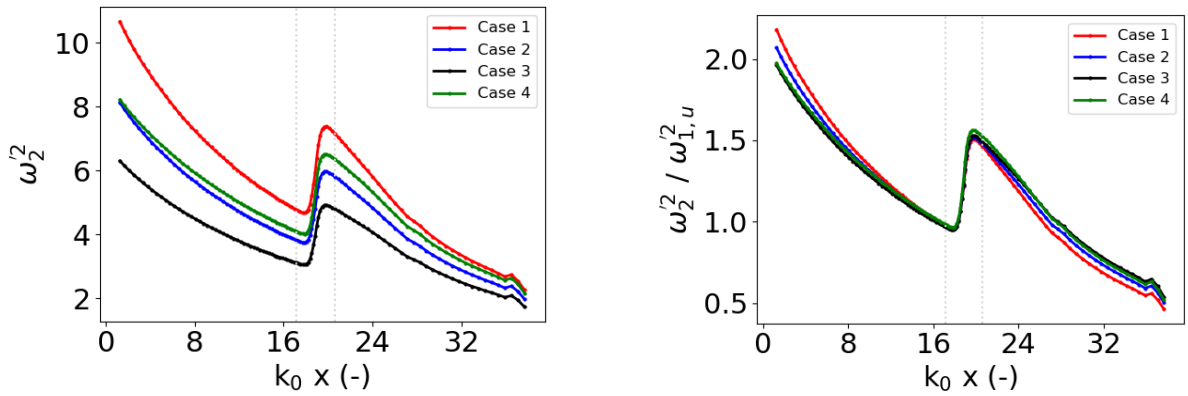

5-10 $\omega_2'^2$ amplifications in the STI of Garnier without (left) and with (right) scaling by pre-shock value. 104×64^2 cells and p-switch = 10, k_0 = 6.

5.2.2.5. Taylor microscales

The evolution of the Taylor microscales is shown in Figure 5-11 for the different cases on the domain discretized by 104×64^2 cells. After the rapid drop in the three components due to the interaction with the shock, the streamwise component becomes rapidly larger than the transverse ones. This behaviour is consistent with the expectations as indicated by Larsson *et al.* [53]. A constant offset between streamwise and transverse Taylor microscales appears to uphold further downstream. No return to isotropy is shown which was linked to the post-shock Reynolds stress anisotropies [53]. Capturing this behaviour gives a level of confidence in the grid resolution as an under-resolved post-shock grid would not consistently show this as discussed by [51] with reference to the work of Lee *et al.* [59, 60].

The post-shock streamwise component reaches relatively rapidly higher levels than the pre-shock which is not observed in other DNS. This is explained by the direct influence of the grid size, and the small scale fluctuations, on the computations of L_{λ_α} based on Equation 1-3. This was shown in Figure 3-6 and illustrated for the finer grid in Figure 5-12. In terms of post-shock evolution of the Taylor microscales, a finer grid seem to be required for the present LES with TAU.

Note the slight pre-shock increase in L_λ which is not observed in, for instance, the DNS of Lee *et al.* [59, 60] or Larsson *et al.* [53]. One reason for this is the deactivation of the low dispersion properties of the LD2 scheme as shown in Figure 4-21.

Also noteworthy is the steep drop for L_{λ_2} and L_{λ_3} which is not seen in other DNS work [59, 60, 53]. It raises the question whether the occurrence has anything to do with the less well-resolved shock region as shown in Figure 5-8. It does, however, also occur with the finer grid (Figure 5-12) and is perhaps an indication of the increased dissipation related to the central schemes' shock capturing behaviour. Specifically, the effective reduction toward a first-order accurate scheme is applied in all flux directions. Some authors e.g. [5] stipulate the application of the inviscid flux treatment in the

streamwise direction only. However, as this strategy was not adopted in the work of Larsson *et al.* [53] which still demonstrate much higher L_{λ_2} and L_{λ_3} in the shock region, it is not thought to be the explanation at hand. Another (obvious) possible reason would be the SGS effect which adds a dissipative contribution on top of the numerical dissipation due to shock capturing. As Case 4 (not shown here) without SGS did demonstrate a similar behaviour, it was discarded as a possible explanation. Another, speculative, explanation would be the viscous flux' treatment. In present work, a second-order accurate method is adopted while higher-order approaches are the common choice in the literature [59, 60, 53, 5, 52]

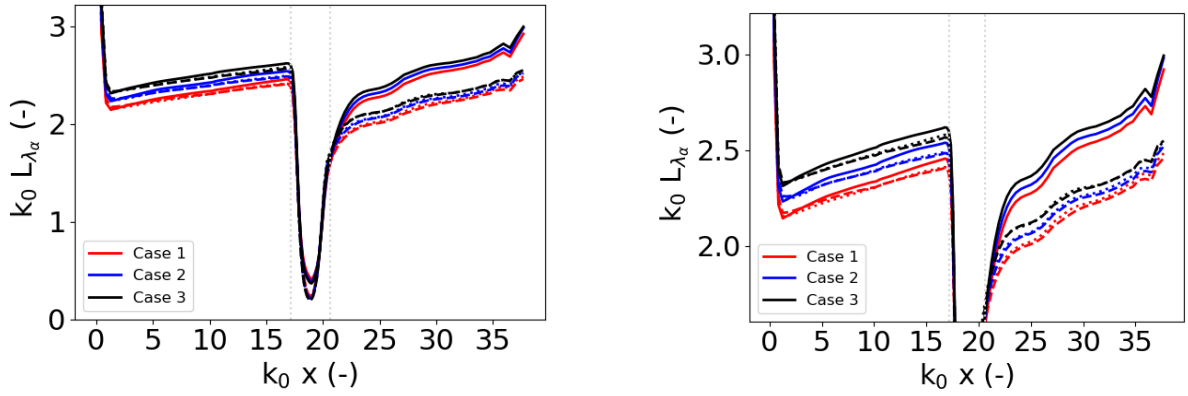

5-11 Evolution of L_{λ_α} in the STI of Garnier. Full line = L_{λ_1}, dashed line = L_{λ_2}, dotted line = L_{λ_3}. 104×64^2 cells and p-switch = 10, k_0 = 6.

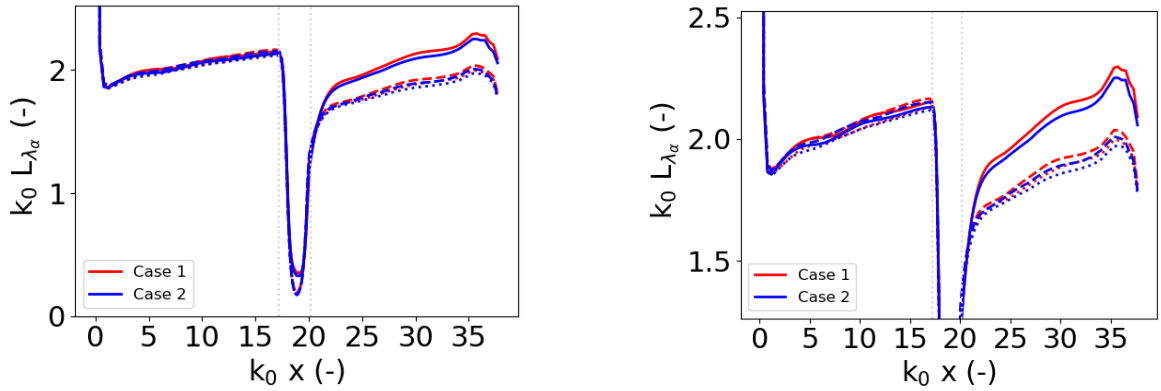

5-12 Evolution of L_{λ_α} in the STI of Garnier. Full line = L_{λ_1}, dashed line = L_{λ_2}, dotted line = L_{λ_3}. 138×96^2 cells and p-switch = 10, k_0 = 6.

5.2.2.6. Return to isotropy

In 5.2.2.5, failure in a return to isotropy of L_λ was observed which is explained by a similar behaviour of the Reynolds stresses [53]. However, the literature on the canonical STI problem report a return of isotropy of the small scales (see e.g. [53, 52]) which can be observed in the evolution of the vorticity variance fluctuating components. Anisotropies of both quantities are presented in Figure 5-13 for

Grid 1 - Case 2 of Table 5-5. The growth in post-shock Reynolds stress anisotropies (between streamwise and transverse components) for the resolved portion of the flow is steep but gradual, typical of a low M_t case (see Figure 4 c of [53]). The local maxima, just behind the shock, is at ≈ 1.26. The vorticity variance does not show a return to isotropy within the considered computational domain. Larsson *et al.* [52] indicate a general return to isotropy of this quantity within 10 convected Kolmogorov time scales for the different conditions considered. Lower M_t flows are coupled with a slower return to isotropy as shown in Figure 6 c of [53]. Failure in capturing the phenomenon could indicate that the post-shock turbulence is under-resolved [53]. However, in the extended domain of size $4\pi \times (2\pi)^2$, corresponding to "4 π B" in Table 5-1, the return to isotropy is visible around k_0x = 55. In comparison to Larsson *et al.* [53] (Figure 6 c Mach 1.5, M_t = 0.18, Re_λ = 40), the observation is somewhat slower. This could be due to the lack of grid refinement in the region paired with the use of second-order accurate LES. However, the ability of predicting a return to isotropy is an encouraging result.

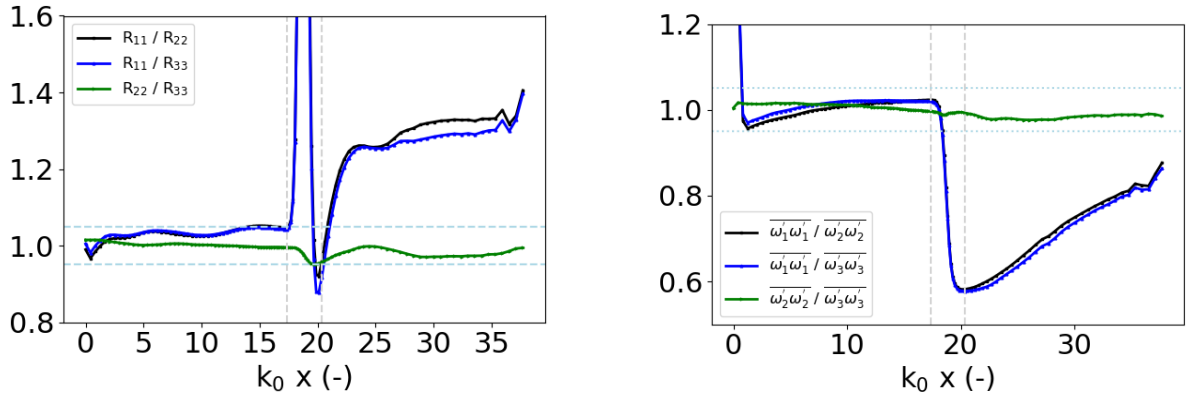

5-13 Resolved Reynolds stress' (left) and vorticity variances (right) anisotropies in the STI of Garnier. Case 2, 104×64^2 cells and p-switch = 10, k_0 = 6.

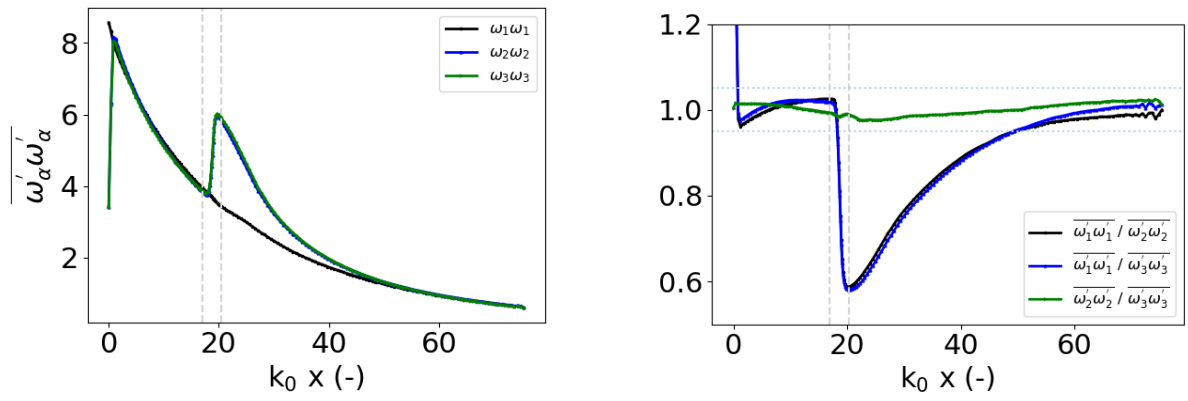

5-14 Vorticity variances (left) and their anisotropies (right) in the STI of Garnier. $4\pi \times (2\pi)^2$ domain with 170×64^2 cells and same inflow as Grid1 - Case 2, p-switch = 10, k_0 = 6.

5.2.3. Mach 2 STI of Garnier

Another condition of Garnier *et al.* [25] was considered for study with TAU. It is a Mach 2 case with similarly low M_t and Re_λ as in the previous case of 5.2.2. The δ/η ratio indicate that the condition is very close to an inviscid STI [97], i.e. close to the LIA limit. The interaction is of the wrinkled shock regime type according to Equation 1-6 (see also Figure 1 of [97]). The higher Mach number will challenge the shock capturing capability of TAU. Table 5-9 summarizes the amplifications for these conditions that could be extracted from the reference paper. It must be noted that while the R_{11} amplification is very similar for the filtered DNS and LES, the pre-shock decay does differ which result in different post-shock levels and subsequent decay in spite of the same amplifications across the shock.

5-8 Mach 2 STI conditions of Garnier *et al.* [25].

M_s	M_t	Re_λ	δ/η	$M_t/(M_s-1)$
2	0.108	19	0.19	0.11

5-9 Grid and amplification detail of the Mach 2.0 STI study by Garnier *et al.* [25]. SGS model = Smagorinsky.

Case	N_x	$N_y = N_z$	$R_{11,d}/R_{11,u}$	$R_{22,d}/R_{11,u}$	$\omega'^2_{2,d}/\omega'^2_{2,u}$
DNS (B)	220	64	1.63	2.63	No info
Filtered DNS (B1)	110	32	1.57	No info	No info
LES Smagorinsky (B1)	110	32	1.56	No info	No info

5.2.3.1. Garnier Mach 2 STI setup description

The selected setup is similar to the one in 5.2.2. A $(2\pi)^3$ domain is simulated on a grid with 104×64^2 cells. The same cell spacing as before is kept and was obtained through Equation 3-4 with i_t = 5 %. The turbulence intensity corresponding to the conditions in Table 5-8 equals 3 %. The selected grid spacing near the shock is therefore on the larger side. Note that Garnier *et al.* adopted a more stringent condition for their cell spacing through Equation 3-5. It was presently chosen to not change the grid and observe what the LES could achieve.

5.2.3.2. Shock treatment

The shock strength in this setup has lead to careful consideration of the LD2 scheme's settings. Subsection 4.1.3 described the shock capturing mechanism and the requirements for a Mach 1.2 case. The low dispersion properties were deactivated and the pressure switch weighting factor (p-switch) had a negligible effect when comparing its setting to 1 and 10. The latter cannot be said any more in the present case.

Simulations have been performed with p-switch values of 1,5,10,20, 100 and 1000. Its impact on

the decay of M_t (and thus TKE) is presented in Figure 5-15. Recall that the parameter affects the sensitivity of the matrix-valued dissipation (see 4.1.3) and a higher value implied stronger sensitivity to pressure gradients. Specifically, the latter will result in more rapid use of the first-order scheme in the regions impacted. This is clearly shown by comparing the M_t evolution for p-switch values of 1000 and 100 with respect to lower values. The turbulent decay is completely off with such high values which does set a limit for these canonical STI setups. Regardless of the p-switch values, the pre-shock region is characterized by spurious oscillations in the statistics. Their upstream extend is limited for higher p-switch values which is an expected result (higher dissipation). Nonetheless, the result for p-switch = 20 presents higher oscillations than a value of 10.

The Reynolds stress anisotropies are also strongly negatively influenced by higher p-switch values as seen in Figure 5-16. The matrix dissipation allows a different numerical treatment for each direction (convective fluxes) which is responsible for the growth in anisotropy with higher values. In such case, while it behaves as expected in the actual shock-region, the region further upstream is more negatively impacted in the shock normal direction than in the transverse directions. This indicates that pressure fluctuations emanate from the shock to generate the observed anisotropy. A zonal p-switch application could be a more appropriate methodology for such simulations. From the sensitivity studies in Figures 5-15 and 5-16, a pressure swith weighthing factor of 10 seems appropriate for this specific setup.

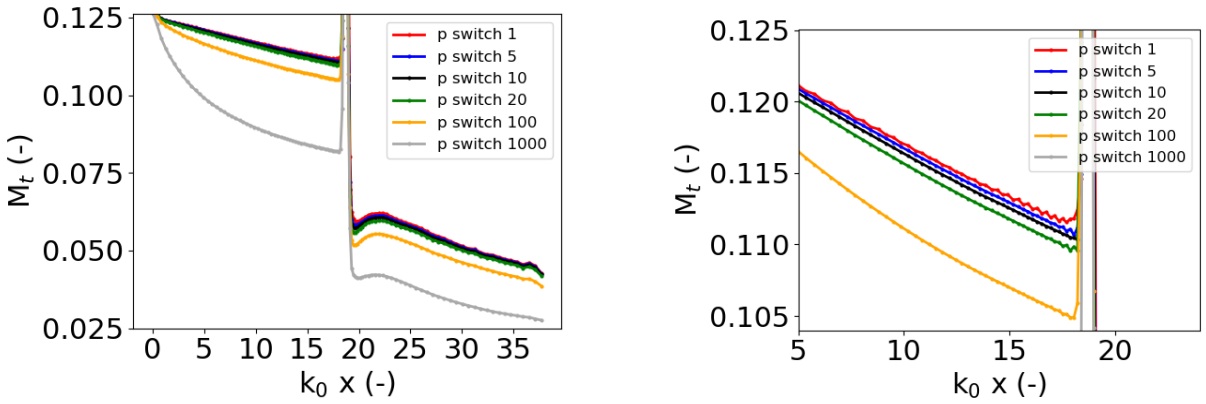

5-15 Effect of p-switch on the $M_{t,res}$ decay in the Mach 2 STI of Garnier. 104×64^2 cells, k_0 = 6.

5.2.3.3. Pre-shock conditions

For this condition, a single simulation has been performed with the 104 x 64^2 grid size. Resulting pre-shock conditions are summarized in Table 5-10. The present simulation was able to reproduce a δ/η ratio very close to the reference test case (see Table 5-8). The pre-shock Reynolds stress anisotropies are below 6 % and the anisotropies in vorticity variances below 2 %.

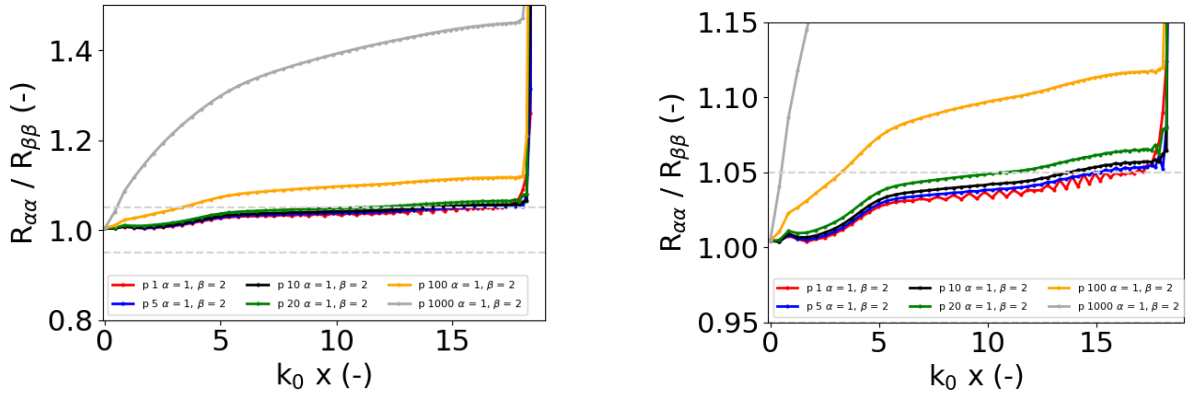

5-16 Effect of p-switch on the Reynolds stress anisotropy in the Mach 2 STI of Garnier. 104×64^2 cells, k_0 = 6.

5-10 Pre-shock turbulence state in the STI reproducing the conditions of Garnier *et al.* [25] at Mach 2.0.

Case ID	$\mathbf{M}_{t,res}$	$\mathbf{M}_{t,tot_1}$	$\mathbf{M}_{t,tot_2}$	$\mathbf{Re}_\lambda$	$\delta/\eta\|_{res}$	$\delta/\eta\|_1$	$\delta/\eta\|_2$
Grid 1 : 104×64^2							
Case 1	0.111	0.116	0.112	17.32	0.20	0.22	0.21

5.2.3.4. Evolution of Reynolds stresses and vorticity variances

The Reynolds stresses' evolution is presented in Figure 5-17 and the corresponding amplification values in Tables 5-11 and 5-12. Note that the horizontal axis is non-dimensionalised with k_0 = 6 instead of k_0 = 4 in Garnier *et al.* [25]. The reason for this being that in present work the inflow turbulence is generated with an initial spectrum with peak wavenumber 6 (see 2.2).

The SGS contributions to the streamwise Reynolds stress' amplification are 7.1 and 2.3 % for C_k = 0.07 and 0.17, respectively (Table 5-11). In comparison to the reference LES of Garnier *et al.* [25] in Table 5-9, a relative difference in R_{11} amplification (resolved) of 4.7 % is obtained. The reference LES differs, in turn, by 4.3 % with respect to the DNS. Present amplification result differs 8.8 % from the reference DNS.

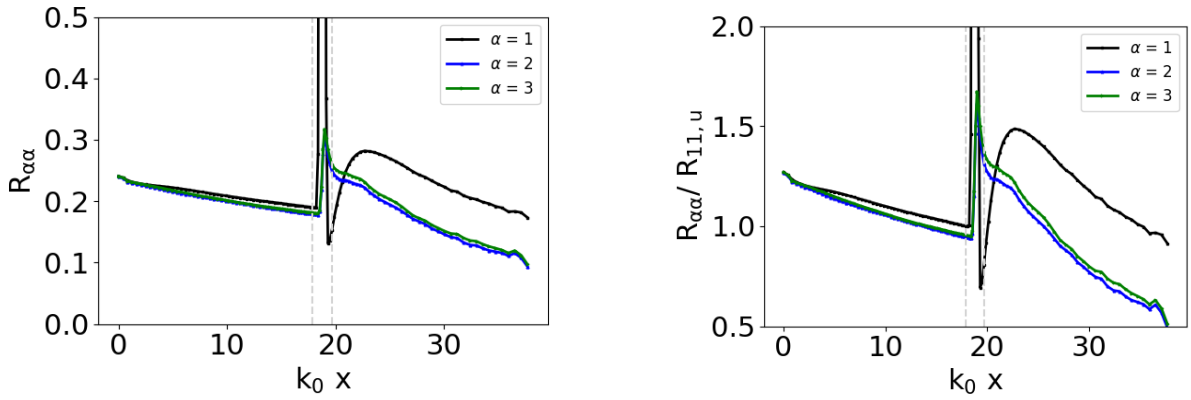

5-17 R_{11} amplifications in the Mach 2 STI of Garnier without (left) and with (right) scaling by pre-shock value. 104×64^2 cells and p-switch = 10, k_0 = 6

5-11 Amplifications of R_{11} in the STI reproducing the conditions of Garnier *et al.* [25] at Mach 2.0.

Case ID	$\delta/\eta\|_{res}$	$\mathbf{R}_{11,d}$ / $\mathbf{R}_{11,u}\|_{res}$	$\mathbf{R}_{11,d}$ / $\mathbf{R}_{11,u}\|_1$	$\mathbf{R}_{11,d}$ / $\mathbf{R}_{11,u}\|_2$	$\omega'^2_{2,d}$/ $\omega'^2_{2,u}\|_{res}$
Grid 1 : 104×64^2					
Case 1	0.20	1.486	1.592	1.510	4.525

The same SGS contribution to the transverse Reynolds stress' amplification (R_{22}) is however very high (Table 5-12). High SGS contributions to this variable were already observed in the Mach 1.2 case and discussed at length in 5.2.2.3. The estimated SGS contributions, obtained with Equation 3-8, relies on eddy viscosity (Equation 3-9) which is, in turn, provided by the SGS model (Equation 3-6). The ratio of turbulent to molecular viscosity for this Mach 2.0 STI case is shown in Figure 5-18. Its value is extremely high in the shock region. Compare to the Mach 1.2 case in Figure 3-8. Outside the shock region, the desired lower levels are retrieved. The high μ_t values cause high values for the estimated SGS contributions in the shock region which is where the amplification of the R_{22} (and R_{33}) components occur. The higher μ_t/μ ratios do hint at a lack of resolution in the shock region.

As discussed in 5.2.3.1, the near shock grid spacing is on the higher side and could therefore be a limiting factor in obtaining accurate results. It must also be evaluated whether the transverse grid spacing plays a major role. The discussion on the SGS contribution estimate to the R_{22} component in 5.2.2.3 indicate possible stringent requirements of transverse cell spacings. Recall that in the Mach 1.2 case the viscosity ratios are higher in the shock region but much lower than the present Mach 2 case. Nevertheless, in spite of the relatively low μ_t/μ values, the estimated shock zone SGS contributions were unrealistically high.

An a posteriori check on the streamwise velocity derivative skewness indicate some spurious oscillations in the near shock regions, similarly to those seen in Figure 5-15. Given that Equation 3-6 relies on velocity derivatives, it must be evaluated if this contributes in any way to the observations in Figure 5-18. A comparison between a p-switch factor of 1 (more spurious oscillations) and 10 (current) did not indicate a different behavior in the viscosity ratios.

A comparison of the resolved R_{22} amplification with respect to the reference DNS in Table 5-9 shows a relative error of 38.6 %. No reference LES information could be extracted from the reference paper. However, Figure 9. in [25] hints at an amplification with Smagorinsky model higher than 2.

5-12 Amplifications of R_{22} in the STI reproducing the conditions of Garnier *et al.* [25] at Mach 2.0.

Case ID	$\delta/\eta\|_{res}$	$\mathbf{R}_{22,d}$ / $\mathbf{R}_{11,u}\|_{res}$	$\mathbf{R}_{22,d}$ / $\mathbf{R}_{11,u}\|_1$	$\mathbf{R}_{22,d}$ / $\mathbf{R}_{11,u}\|_2$
Grid 1 : 104×64^2				
Case 1	0.20	1.614	17	85

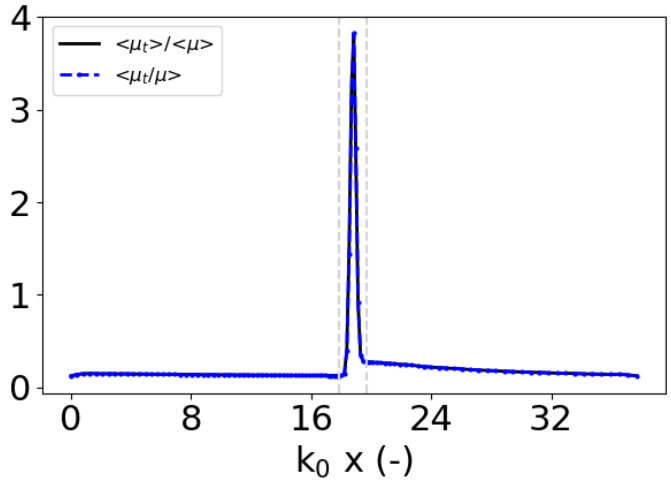

5-18 Ratio of modeled turbulent viscosity to molecular viscosity for Garnier Mach 2 STI.

Figures 5-19 and 5-20 present the portion of resolved Reynolds stress components in case of C_k=0.07 and C_k=0.17. The former of the two is the most conservative one. In both cases, outside

the shock region the turbulence is well resolved. Inside the shock (only relevant to transverse components) it is not any more. Compare present R_{22} to Figure 5-8. The C_k=0.07 case hints as well at a lack of resolution in the near post-shock region.

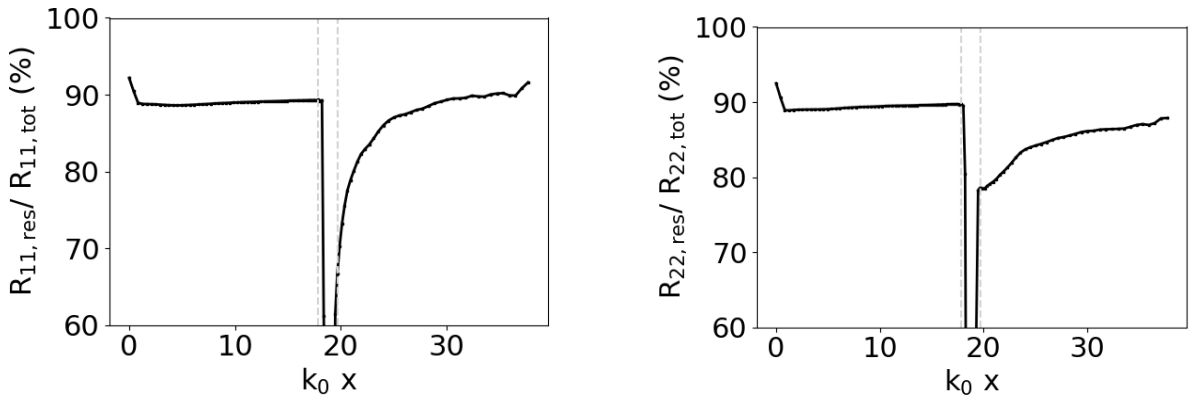

5-19 Ratio of resolved to total portion of R_{11} (left) and R_{22} (right) in the Mach 2 STI of Garnier. C_k=0.07, 104×64^2 cells, p-switch = 10, k_0 = 6.

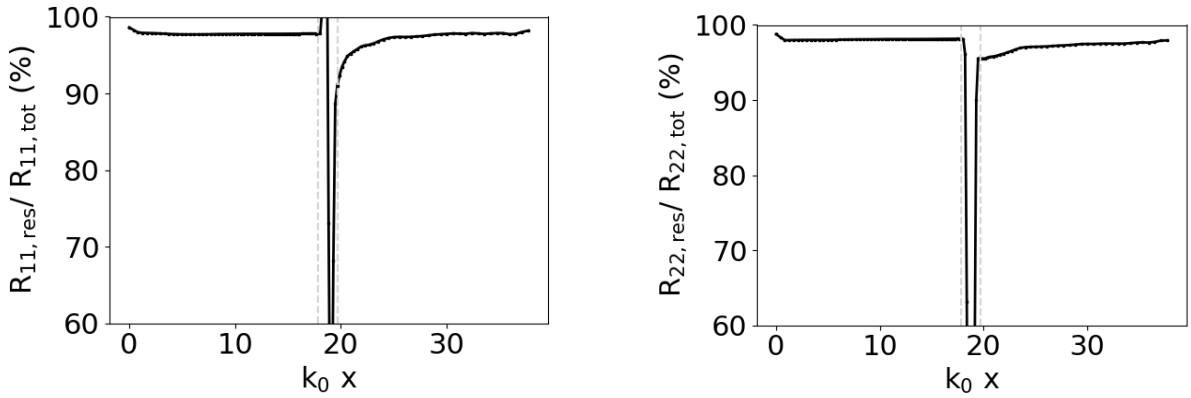

5-20 Ratio of resolved to total portion of R_{11} (left) and R_{22} (right) in the Mach 2 STI of Garnier. C_k=0.17, 104×64^2 cells, p-switch = 10, k_0 = 6.

The evolution of the vorticity fluctuations variance is shown in Figure 5-21. As expected, for a stronger shock Mach number, the amplification is higher (see Figure 6 of Larsson *et al.* [53]). While the Mach 1.2 amplifications of transverse components were of the order of 1.6, they are presently 4.525. No quantitative comparison with any reference can however by made.

5.2.3.5. Taylor microscales and return to isotropy

The evolution of the Taylor microscales in Figure 5-22 is similar to the Mach 1.2 case (see Figure 5-11). The steep drop in transverse components is not in line with reference literature [59, 60, 53] which is speculated to be due to the second-order accuracy of present CFD simulations. Unlike the Mach 1.2 case, the post-shock levels remain below the pre-shock ones which is the expected

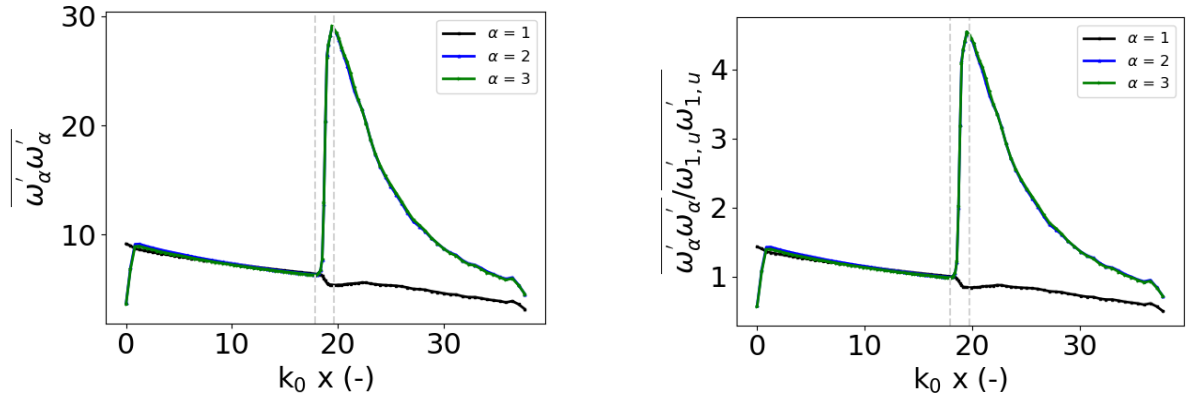

5-21 Evolution of vorticity fluctuations variance unscaled (left) and scaled (right) by pre-shock value in the Mach 2 STI of Garnier. 104×64^2 cells, p-switch = 10, k_0 = 6.

behavior documented in the literature (see e.g. Figure 8 in [53]). Moreover, an offset between streamwise and transverse is observed which is also shown in, for instance, Larsson*et al.* [53].

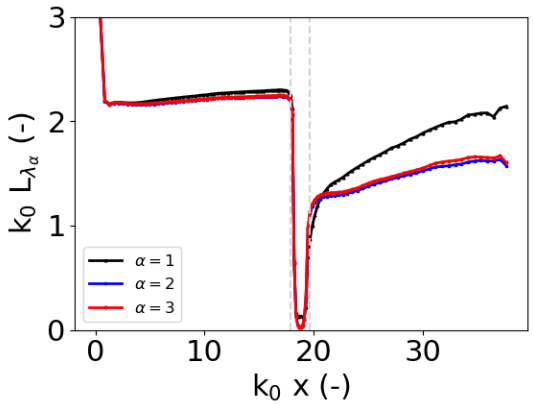

5-22 Evolution of L_{λ_α} in the Mach 2 STI of Garnier. k_0 = 6.

The Reynolds stresses in Figure 5-23 do not show any return to isotropy as expected. A return to isotropy on the smaller scales, represented by vorticity fluctuations variances, is however expected. Presently, just as in the Mach 1.2 case (Figure 5-13), a downstream isotropy is not achieved within the present computational domain. In this Mach 2 case, by the end of the domain, we are much farther from a return to isotropy in comparison to the Mach 1.2 STI. As shown in Figure 6 (c) of [53], a higher shock Mach number would result in a more rapid return to isotropy for a given M_t. However, for a given M_s, a lower M_t does result in a slower return to isotropy. The latter effect is more dominant than the former, hence explaining the current observations of the Mach 2 case at lower M_t than the Mach 1.2 case. The role of the grid size in a small scale return to isotropy was already discussed by Larsson *et al.* in [53]. However, the order of the numerics is also key as discussed in 5.2.2.6. In conclusion, the inability to return to isotropy on the smaller scale within a

short post-shock distance is a limitation of the second-order accurate LES presently considered.

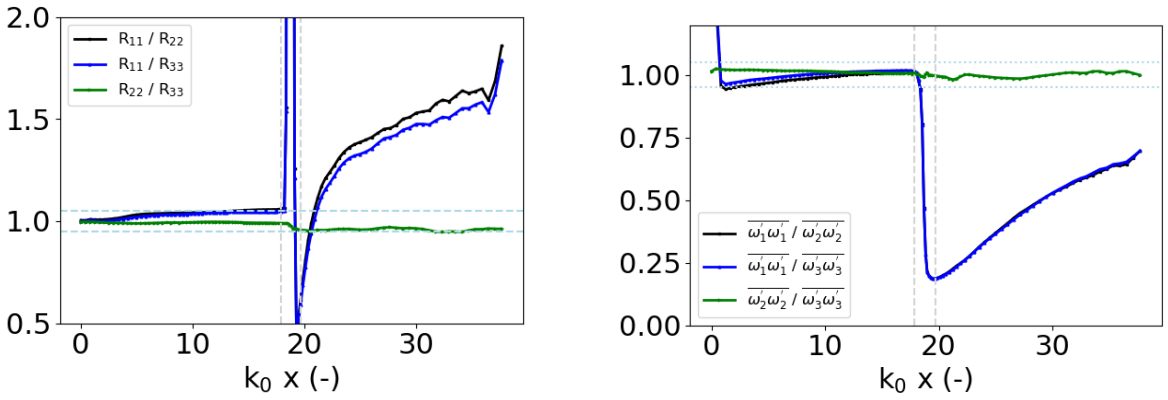

5-23 Resolved Reynolds stress' (left) and vorticity variances (right) anisotropies in the Mach 2 STI of Garnier. 104×64^2 cells and p-switch = 10, k_0 = 6.

5.2.4. Mach 1.5 STI of Jamme

Another canonical STI setup selected in this work is one of Jamme *et al.* [41]. The authors focused on the effect of the nature of the inflow turbulence on the STI problem as well as its anisotropy in a later work ([42]). DNS was performed for several conditions including two of pure solenoidal incoming turbulence. Moreover, second-order accurate discretization schemes were adopted by the authors. This reference work is herein considered as the conditions were charaterised by very low Re_λ (< 7) which does not require extremely fine grids. It is also of interest to compare present second-order accurate LES with the reference DNS of the same order. Among the investigated conditions, the Mach 1.5 case is selected with details listed in Table 5-13. According to Equation 1-6, the interaction is in the wrinkled shock regime.

5-13 Mach 1.5 STI conditions of Jamme *et al.* [41].

$\mathbf{M}_\mathrm{s}$	$\mathbf{M}_\mathrm{t}$	$\mathbf{Re}_\lambda$	δ/η	$\mathbf{M}_\mathrm{t}$**/ (**$\mathbf{M}_\mathrm{s}$**-1)**
1.5	0.133	5.5	0.87	0.266

Jamme *et al.* studied the STI on a $(2\pi)^3$ domain size discretized by 210x128x128 cells with stretching in the streamwise direction as to have 15 points in the shock region. The authors indicate that the shock is actually resolved due to the highly viscous character of the selected conditions (order of accuracy of the numerics does not drop). The resulting amplifications are summarized in Table 5-14. Note that for the transverse Reynolds stresses, there is a mismatch between its value when comparing Figure 2 and Figure 3 of [41]. Therefore, the value extracted from Figure 2 has been considered presently.

5-14 Grid and amplification detail of the Mach 1.5 STI DNS study by Jamme *et al.* [41].

Case	$\mathbf{N}_\mathrm{x}$	$\mathbf{N}_\mathrm{y}$ **=** $\mathbf{N}_\mathrm{z}$	$\mathbf{R}_{11,d}$ **/** $\mathbf{R}_{11,u}$	$\mathbf{R}_{22,d}$ **/** $\mathbf{R}_{11,u}$	$\omega'^2_{2,d}$**/**$\omega'^2_{2,u}$
DNS	210	128	1.293	1.46*	2.934

5.2.4.1. Numerical setup and pre-shock conditions for Mach 1.5 STI of Jamme

In present work, a $(2\pi)^3$ STI domain is selected similarily to the reference work. The same grid as in the Garnier studies previously presented is adopted with 104×64^2 cells. The grading ensured that Equation 3-4 holds based on a turbulence intensity of 5 % (see 5.2.2.1). The latter value is also true for the pre-shock conditions in the Mach 1.5 study of Jamme.

Two simulations have been run yielding the pre-shock conditions listed in Table 5-15 with $\delta/\eta|_{res}$ ratios above and below the target of 0.87 in Table 5-13. The pre-shock anisotropies in Reynolds stresses are below 4 % and for vorticity variances below 6 %.

5-15 Pre-shock turbulence state in the STI reproducing the conditions of Jamme *et al.* [41] at Mach 1.5.

Case ID	$\mathbf{M}_{t,res}$	$\mathbf{M}_{t,tot_1}$	$\mathbf{M}_{t,tot_2}$	$\mathbf{Re}_\lambda$	$\delta/\eta\|_{res}$	$\delta/\eta\|_1$	$\delta/\eta\|_2$
Grid 1 : 104×64^2							
Case 1	0.115	0.120	0.116	5.38	0.76	0.80	0.77
Case 2	0.138	0.144	0.139	5.63	0.89	0.94	0.90

5.2.4.2. Evolution of Reynolds stresses and vorticity variances

The evolution of the normal Reynolds stress components is shown in Figure 5-24 for Case 2. A generally smooth result is obtained. Amplification values are listed in Tables 5-16 and 5-17. The estimated SGS contribution to R_{11} remains below 2% (worst case with C_k = 0.07). The relative error with the reference DNS is 5 and 8 %, respectively for Case 1 and Case 2 based on the resolved portion. Case 2, which has a $\delta/\eta|_{res}$ closest to the reference DNS, demonstrate a worse prediction. Figure 5-25 does indicate that most of the energy is resolved in the pre-and post-shock regions. The grids seem therefore to be adequate. Note that the Figure presents the most conservative case with C_k = 0.07.

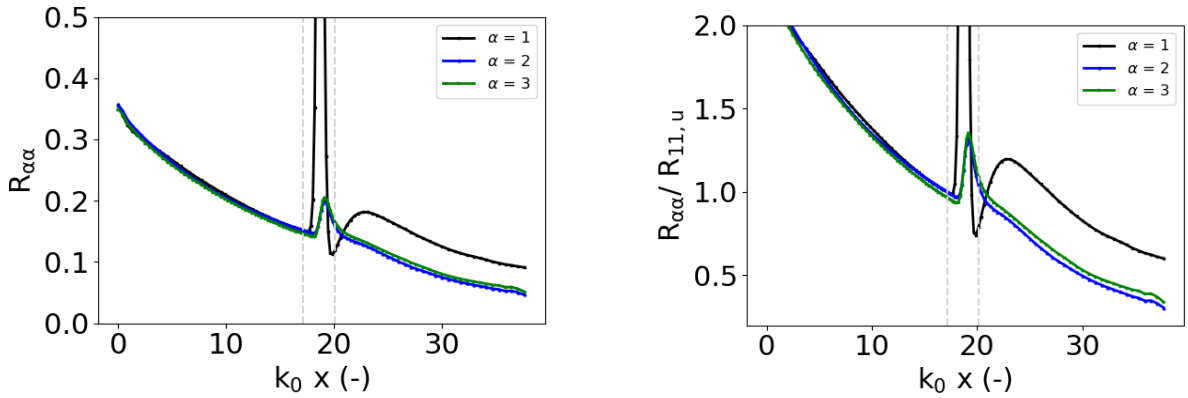

5-24 R_{11} amplifications in the Mach 1.5 STI of Jamme without (left) and with (right) scaling by pre-shock value. 104×64^2 cells and k_0 = 6

.

In terms of R_{22} prediction, relative errors of 6 and 10 % are obtained with Case 1 and Case 2 respecitvely based on the resolved contribution. Just like in the Mach 1.2 and Mach 2 studies of Garnier (5.2.2 and 5.2.3), the estimated SGS contributions in the shock region seem extremely unrealistic given the extremely high levels (up to 90 % SGS contributions). This consistent observation throughout the present work raises the question as whether a SGS estimate can be relied upon in the shock region. It will have to be seen if this persists in the following STI test cases. In the Mach 1.5 conditions of Jamme, the ratio of viscosities was already presented in Figure 3-9 and did not show levels much different than in the Mach 1.2 case of Garnier (Figure 3-8).

5-16 Amplifications of R_{11} in the STI reproducing the conditions of Jamme *et al.* [41] at Mach 1.5.

Case ID	$\delta/\eta\|_{res}$	$\mathbf{R}_{11,d}$ / $\mathbf{R}_{11,u}\|_{res}$	$\mathbf{R}_{11,d}$ / $\mathbf{R}_{11,u}\|_1$	$\mathbf{R}_{11,d}$ / $\mathbf{R}_{11,u}\|_2$	$\omega'^2_{2,d}$/ $\omega'^2_{2,u}\|_{res}$
Grid 1 : 104×64^2					
Case 1	0.76	1.231	1.252	1.236	2.499
Case 2	0.89	1.195	1.208	1.199	2.364

5-17 Amplifications of R_{22} in the STI reproducing the conditions of Jamme *et al.* [41] at Mach 1.5.

Case ID	$\delta/\eta\|_{res}$	$\mathbf{R}_{22,d}$ / $\mathbf{R}_{11,u}\|_{res}$	$\mathbf{R}_{22,d}$ / $\mathbf{R}_{11,u}\|_1$	$\mathbf{R}_{22,d}$ / $\mathbf{R}_{11,u}\|_2$
Grid 1 : 104×64^2				
Case 1	0.76	1.380	12.2	3.3
Case 2	0.89	1.318	7.7	2.4

The evolution of the vorticity fluctuations' variances is shown in Figure 5-26 with an evolution that is very similar to the reference work of Jamme *et al.* [41] (see Figure 6), including the offset between transverse and streamwise components near the end of the domain. Unlike the reference work, the post-shock region demonstrates a higher level of isotropy in the transverse directions. Note that present graphs are scaled horizontally by k_0 = 6 while the reference work uses k_0 = 4. In terms of transverse amplifications, relative errors of 15 and 19 % are obtained for Case 1 and Case 2. This result indicate, like before, the challenging nature of the STI which might require even finer grids and / or higher order numerical schemes.

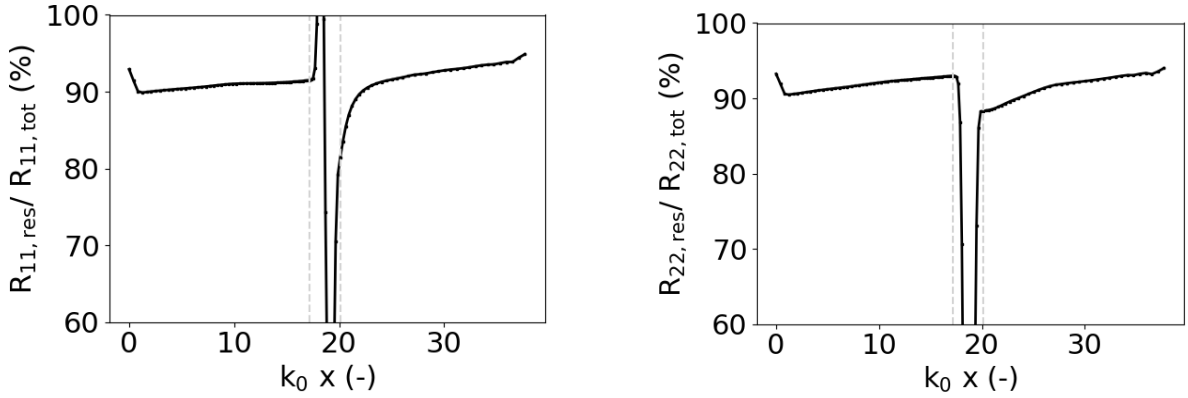

5-25 Ratio of resolved to total portion of R_{11} (left) and R_{22} (right) in the Mach 1.5 STI of Garnier. Case 2, C_k=0.07, 104×64^2 cells and k_0 = 6.

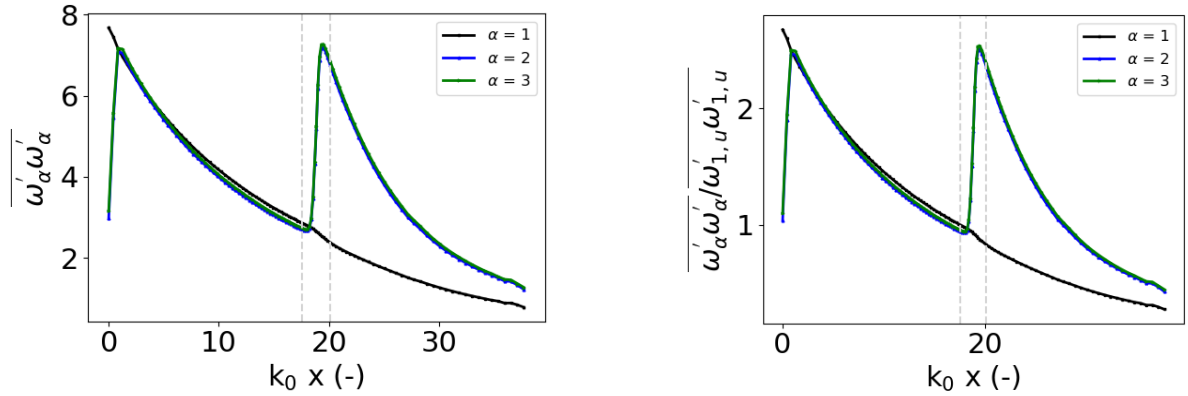

5-26 Evolution of vorticity fluctuations variance unscaled (left) and scaled (right) by pre-shock value in the Mach 1.5 STI of Jamme. Case 1 with 104×64^2 cells and k_0 = 6.

5.2.4.3. Taylor microscales and return to isotropy

The evolution of the Taylor microscales is presented in Figure 5-27 for both cases. The behavior is as previously observed and discussed in 5.2.3.5. In comparison with Figure 18 of [41], the post-shock growth in anisotropy is of the same qualitative nature. As previously commented on, the drop in transverse components is unexpectedly high. Jamme *et al.* do also report a small but gradual pre-shock increase in these values. Given that the numerics are of the same order of accuracy as presently adopted, the latter feature can be associated with it. Recall from 5.2.2.5 that such behavior is not reported in the literature.

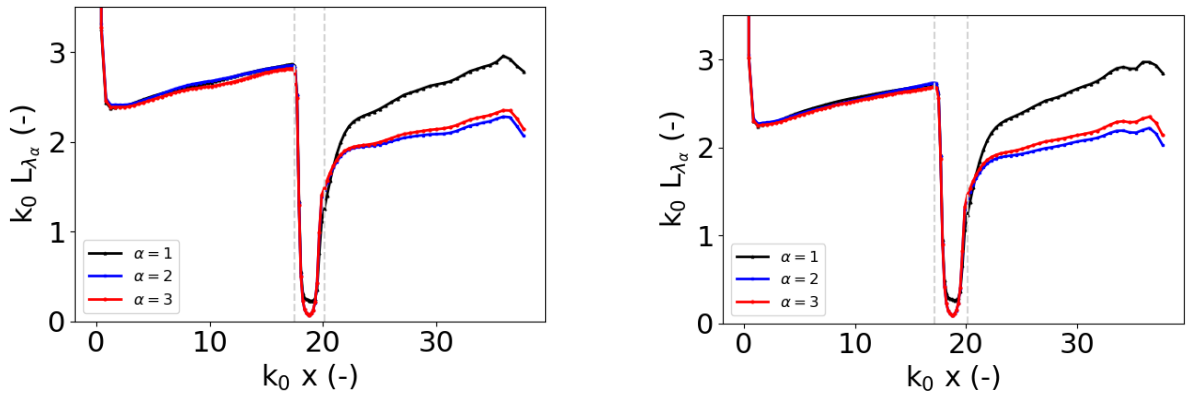

5-27 Evolution of Taylor microscales for Case 1 (left) and Case 2 (right) in the Mach 1.5 STI of Jamme. 104×64^2 cells and $k_0 = 6$.

Finally, the anisotropies in Reynolds stresses and vorticity fluctuations' variances are shown in Figure 5-28. In terms of Reynolds stresses, the post-shock transverse anisotropy levels (R_{22} / R_{33}) appear to grow which is not observed in other cases covered before. The small scale return to isotropy does as well appear to be far from happening. The turbulent Mach number is higher than in the previous cases which should result in a more rapid return to isotropy (neglecting the Mach number changes). However, the present behavior indicates that the Reynolds number (Re_λ) plays an important role. In this higher viscous case it is possible that no return to isotropy will ever be achieved downsteam the shock wave. In general, this low Re_λ test case has shown to be challenging from the perspective of second-order accurate LES. In order to improve the predictions, much finer grids might be needed. The aim of performing LES with ad hoc grids would therefore be lost.

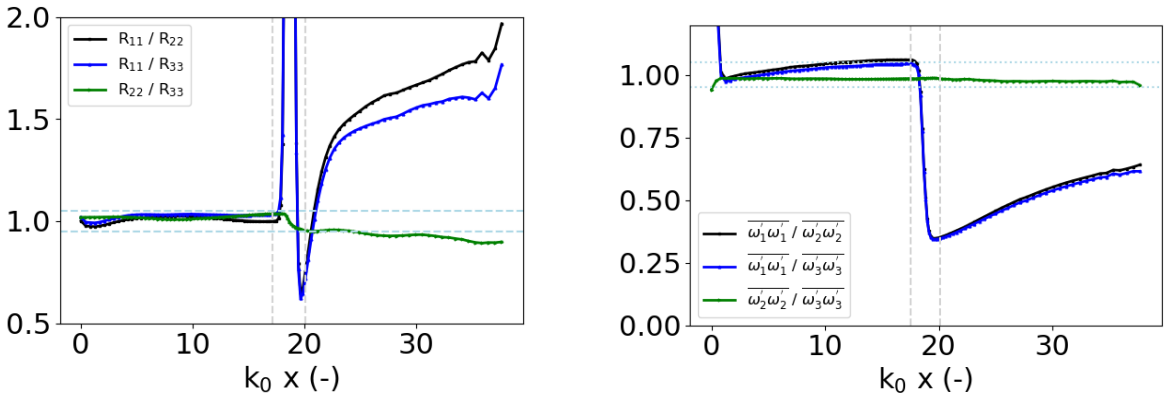

5-28 Anisotropies in resolved Reynolds stress' for Case 2 (left) and vorticity variances for Case 1 (right) in the Mach 1.5 STI of Jamme. 104×64^2 cells and k_0 = 6.

5.2.5. Mach 1.28 STI of Larsson

In the study of the canonical STI problem, Larsson has strongly furthered our understanding [53, 52] by performing a large number of DNS simulations at higher Reynolds numbers than previously considered ($Re_\lambda \approx 40$ and 70). One of the important findings was the fine grid requirements, in both streamwise and spanwise directions, to correctly capture the vorticity variance's behavior including its return to isotropy. In this work, two of Larsson's conditions [53] are considered. One with freestream Mach number of 1.28 (see Table 5-18) and one at Mach 1.5 (see Table 5-23). These conditions have been presently selected to evaluate the capability of a second-order accurate LES at a $Re_\lambda \approx 40$. The STI interaction regime for the Mach 1.28 setup is classified as borderline by Larsson *et al.* [53].

5-18 Mach 1.28 STI conditions of Larsson *et al.* [53].

$\mathbf{M_s}$	$\mathbf{M_t}$	$\mathbf{Re_\lambda}$	δ/η	$\mathbf{M_t/(M_s-1)}$
1.28	0.160	40	0.69	0.57

Larsson *et al.* [53] studied the interaction on a $4\pi \times (2\pi)^2$ domain size with high-order numerical methods. The grid spacing is not explicitly quantified but it ensures that pre-and post-shock spacings are three times finer than the in the transverse direction. A grid sensitivity study demonstrated the need to use very fine grids reaching 1040×384×384 grid points (>153M points). The computational constraint of such large grid sizes for DNS does make LES very attractive.

Table 5-19 summarizes the resulting amplifications obtained by Larsson *et al.* [53]. The values were extracted from Fig. 4 and Fig. 6. As the result for the exact condition of Table 5-18 was not displayed in the figures, some assumptions were made to obtain their value. For the R_{11} and $\omega_2'^2$ amplifications, the value is considered equivalent to the Mach 1.28, M_t = 0.22 case. This assumption can be justified given the very limited influence of M_t on these amplifications for the Mach 1.5 case as shown by the authors [53] (see case 0.16 and 0.22). For R_{22}, the latter statement does not hold and therefore, a range within which the amplification is expected is tabulated in Table Table 5-18. The lower bound is set by the amplification for Mach 1.28, M_t = 0.22 and the upper bound is by the Mach 1.5, M_t=0.16 case.

5-19 Grid and amplification detail of the Mach 1.28 STI DNS study by Larsson *et al.* [53].

Case	$\mathbf{N_x}$	$\mathbf{N_y = N_z}$	$\mathbf{R_{11,d}/R_{11,u}}$	$\mathbf{R_{22,d}/R_{11,u}}$	$\omega_{2,d}'^2/\omega_{2,u}'^2$
DNS	1040	384	1.269*	>1.246 and < 1.462	2.010*

5.2.5.1. Numerical setup and pre-shock conditions for Mach 1.28 STI of Larsson

In present work, a $(2\pi)^3$ STI domain is selected for study of these conditions. It is the same size considered in the afore-presented STI studies of Garnier and Jamme. Furthermore, the same number of cells has been selected, i.e. 104×64^2 cells. In terms of grading, Equation 3-4 was considered to specify the pre-shock streamwise to transverse cell ratio. The same turbulence intensity as in the case of Jamme and Garnier previously studied (5 %) is applied on the grid spacing allowing to re-use the grids. In comparison to the i_t of 7 % corresponding to the conditions in Table 5-18, the grid spacing is more conservative. For comparison purposes, a grid was also generated with a grid spacing set by i_t = 7 % (Case 1b).

The pre-shock conditions of the simulated cases are given by Table 5-20. Present pre-shock anisotropies in Reynolds stresses are below 7 % (except for Case 2b where it is 8.6 %) and for vorticity variances below 3 %. The $\delta/\eta|_{res}$ ratios are below the target condition which demonstrates the general difficulty in reproducing a given reference condition, requiring many trial and errors. Nevertheless, the simulated range remains useful for evaluation and comparison with Larsson whose results should be seen as a lower bound of what to be expected. Note as well that the resulting difference in amplification between current and reference conditions should remain limited as shown in Fig. 4 of Ryu and Livescu [97]'s work. By default a p-switch factor of 1 has been adopted which will be subsequently discussed.

5-20 Pre-shock turbulence state in the STI reproducing the M_t = 0.16 conditions of Larsson *et al.* [53] at Mach 1.28.

Case ID	$\mathbf{M}_{t,res}$	$\mathbf{M}_{t,tot_1}$	$\mathbf{M}_{t,tot_2}$	$\mathbf{Re}_\lambda$	$\delta/\eta\|_{res}$	$\delta/\eta\|_1$	$\delta/\eta\|_2$
Grid 1 : 104×64^2							
Case 1	0.136	0.146	0.138	38.86	0.60	0.64	0.61
Case 1b	0.137	0.146	0.139	38.10	0.61	0.65	0.62
Case 2	0.148	0.158	0.150	37.19	0.67	0.71	0.68
Case 2b	0.144	0.154	0.146	36.88	0.65	0.70	0.66

5.2.5.2. Evolution of Reynolds stresses and vorticity variances

The effect of near shock grid spacing on the amplifications is negligible as shown by Case 1 and Case 1b in Tables 5-21 and 5-22. On the streamwise Reynolds stress amplifications (resolved), the absolute error between both is 0.015 and for the transverse amplification (resolved) the same error is 0.036. From a relative error point of view the difference in amplifications remain below 1.2 and 3 %. These values are obtained by considering each of the Cases as a reference and considering the worst case scenario.

Throughout this work, the importance of the pressure-switch weighting factor (p-switch) in the LD2 scheme has been mentioned. In the Mach 2 STI of Garnier (in 5.2.3.2), a sensitivity study was performed leading to the conclusion that a value of 10 for the p-switch is appropriate. Unfortunately,

this previous guideline cannot be applied in the STI simulations of Larsson. The pre-shock Reynolds stress anisotropy levels become too important when adopting this setting of 10 (8.6%). Moreover, the influence on the amplifications and post-shock evolution are important as shown in Figure 5-29. Results for Case 2 and Case 2b are presented whose p-switch setting equals 1 and 10, respectively. While the influence on R_{11} can be considered limited, except for the post-shock peak (3% relative error), it is considerable on R_{22} (6 % relative error). The increased dissipation linked to a higher p-switch value has a very negative influence in post-shock decay of the latter quantity. Therefore, in present simulations, a p-switch setting of 1 should be considered. This requirement could be a consequence from the higher Re_λ conditions presently under study. This does in turn imply that stronger shocks (higher M_s) cannot be studied with the available numerics and associated settings as stability would only be ensured through higher p-switch settings.

5-21 Amplifications of R_{11} in the STI reproducing the M_t = 0.16 conditions of Larsson *et al.* [53] at Mach 1.28.

Case ID	$\delta/\eta\|_{res}$	$\mathbf{R}_{11,d}$ / $\mathbf{R}_{11,u}\|_{res}$	$\mathbf{R}_{11,d}$ / $\mathbf{R}_{11,u}\|_1$	$\mathbf{R}_{11,d}$ / $\mathbf{R}_{11,u}\|_2$	$\omega'^2_{2,d}$/ $\omega'^2_{2,u}\|_{res}$
Grid 1 : 104×64^2					
Case 1	0.60	1.315	1.376	1.328	2.096
Case 1b	0.61	1.300	1.348	1.312	2.050
Case 2	0.67	1.282	1.341	1.293	2.043
Case 2b	0.65	1.254	1.291	1.263	1.872

5-22 Amplifications of R_{22} in the STI reproducing the M_t = 0.16 conditions of Larsson *et al.* [53] at Mach 1.28.

Case ID	$\delta/\eta\|_{res}$	$\mathbf{R}_{22,d}$ / $\mathbf{R}_{11,u}\|_{res}$	$\mathbf{R}_{22,d}$ / $\mathbf{R}_{11,u}\|_1$	$\mathbf{R}_{22,d}$ / $\mathbf{R}_{11,u}\|_2$
Grid 1 : 104×64^2				
Case 1	0.60	1.213	5.103	1.909
Case 1b	0.61	1.249	4.750	1.860
Case 2	0.67	1.190	4.157	1.709
Case 2b	0.65	1.124	4.120	1.656

In comparison with the reference result of Larsson *et al.* [53] in Table 5-19, the R_{11} amplifications of Case 1 and Case 2, based on the resolved part of the energy, result in relative errors of 4.4 and 6.2 %. Recall however that the ratios of $\delta/\eta|_{res}$ are lower than in the reference condition. Therefore, higher amplifications should be expected (see [97]) and the reference case could be seen as a minimum target. The former statement holds for both cases, without accounting for unresolved contributions. Considering unresolved contributions, Case 2 comes closest to the 0.69 reference δ/η ratio. With C_k = 0.17, the actual δ/η ratio is estimated to be 0.68 with a relative error of only 2 %. With C_k = 0.07, the resulting relative error is 5.6 %. However, considering the required level

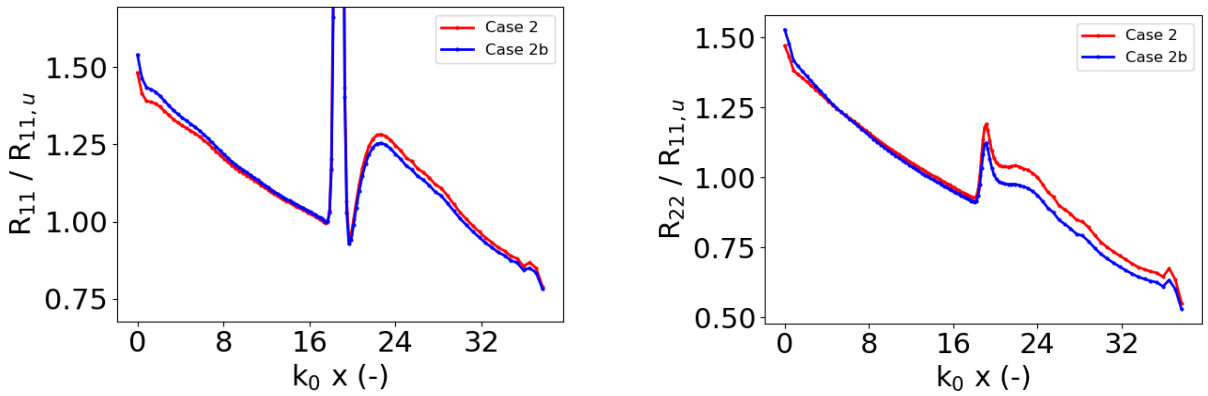

5-29 Effect of p-switch factor in the Mach 1.28 STI of Larsson for R_{11} (left) and R_{22} (right) with scaling by pre-shock value. 104×64^2 cells and k_0 = 6

.

of precision (grids) used in the reference DNS, it is unlikely that the present LES resolves $>$ 95 % of the flow as suggested by Figure 5-30. Therefore, the results with C_k = 0.07 would be more likely, Nevertheless, it appears that the second-order LES can reasonably well predict the streamwise Reynolds stress amplification in this higher Re_λ conditions.

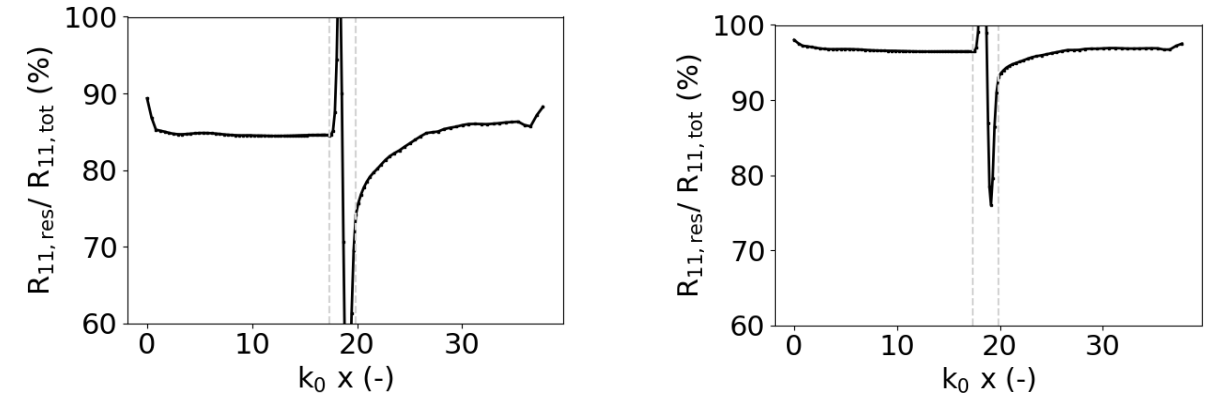

5-30 Ratio of resolved to unresolved R_{11} in the Mach 1.28 STI of Larsson for c_k = 0.07 (left) and c_k = 0.17 (right). Case 2, 104×64^2 cells and k_0 = 6.

In terms of transverse Reynolds stress amplification, relative errors of 2.6 and 4.5 % are obtained, for the resolved portion only considering the lower bound of the reference in Tablre 5-19. The amplifications are lower than what would be expected. In accordance with previous STI test cases, the estimated contribution of the unresolved SGS to this component appear to be strongly miscalculated. The present grid resolution is shown to be appropriate for both R_{11} and R_{22} (Figure 5-31) except for the shock region. This behavior is a constant throughout this work. Nevertheless, only considering the resolved part, encouraging results have been obtained.

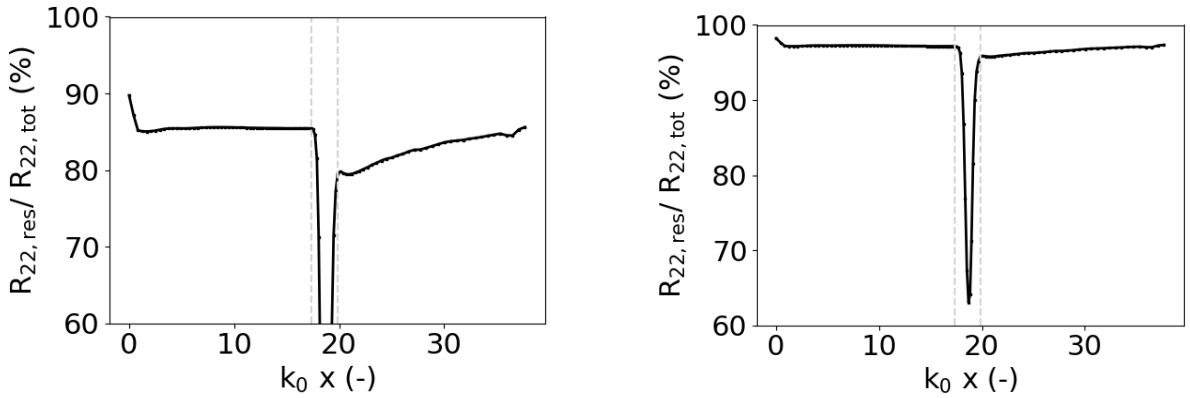

5-31 Ratio of resolved to unresolved R_{22} in the Mach 1.28 STI of Larsson for c_k = 0.07 (left) and c_k = 0.17 (right). Case 2, 104×64^2 cells and k_0 = 6.

The vorticity fluctuations variance's evolution is presented in Figure 5-32. Unlike the other cases considered in this work, the peak transverse component's amplification occurs outside the shock region. Furthermore, the peak itself is not as sharp as what should be expected. Both of the aforementioned observations are not in line with what is reported in the literature. This could indicate a lack of resolution in the shock and near post-shock region. Nonetheless, a decrease in sharpness is also visible in Fig 6. of the reference work [53] for lower M_s. The slight increase in streamwise component, just behind the shock, is in accordance with observations of Larsson *et al.* [53]. A general underestimation of peak amplification in transverse component is presently found (Table 5-21) with relative errors of respectively, 5 and 15 % for Case 1 and 2.

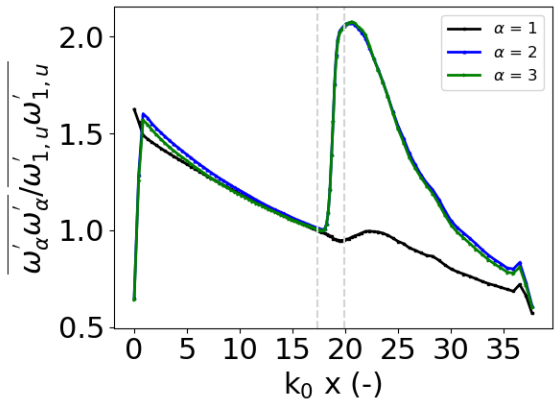

5-32 Evolution of vorticity fluctuations variance in the Mach 1.28 STI of Larsson. Case 2, k_0 = 6.

5.2.5.3. Taylor microscales and return to isotropy

The Taylor microscales' evolution in Figure 5-33 is as expected in the post-shock region where the streamwise component grows faster than the spanwise and evolves in an almost parallel manner from a given downstream location. However, in the shock region the transverse components are

not expected to drop as significantly as shown. This is, for instance, observed in Fig 8 by Larsson *et al.* [53] for a Mach 1.5 case with only a slight drop. Failing to retrive this behavior could again be related to a lack of transverse grid resolution.

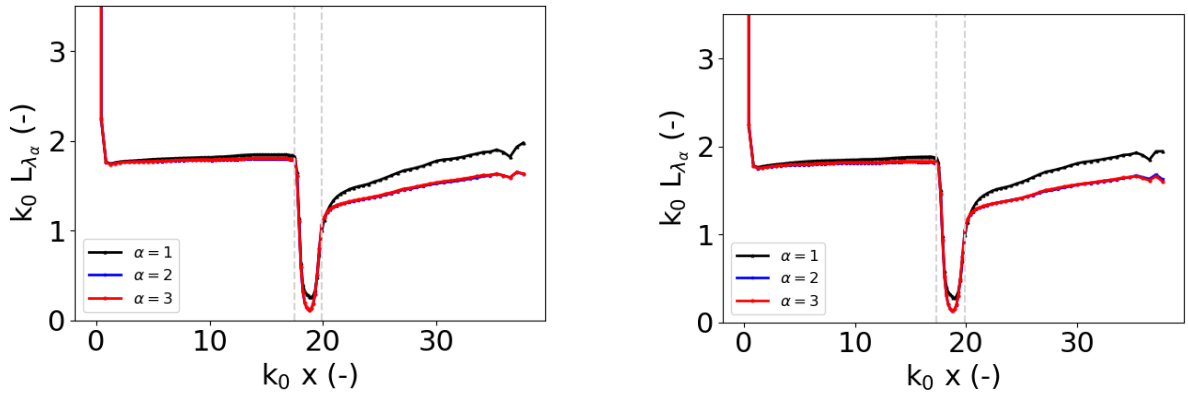

5-33 Evolution of Taylor microscales for Case 1 (left) and Case 2 (right) in the Mach 1.28 STI of Larsson. 104×64^2 cells and $k_0 = 6$.

The anisotropies in Reynolds stresses and vorticity fluctuations variances are presented in Figure 5-34. The streamwise to transverse Reynolds stress anisotropies demonstrate the tendency of reaching an asymptotic level. Note that the small oscillations are as well observed in the reference of Larsson *et al.* [53] (Fig 4 (c)). The vorticity variance hints at a return to isotropy at a short downstream distance from the current domain. In the reference work, for the Mach 1.28 case, a return to isotropy is retrieved (Fig 6. (c)). However, it is hard to extract the exact location. It could be inferred that it occurs within half of their computational domain. This is equivalent to the end of the present domain. A finer grid would be required to ensure such behavior. In general, a more rapid return to isotropy than any of the other lower Re_λ cases previously studied is obtained.

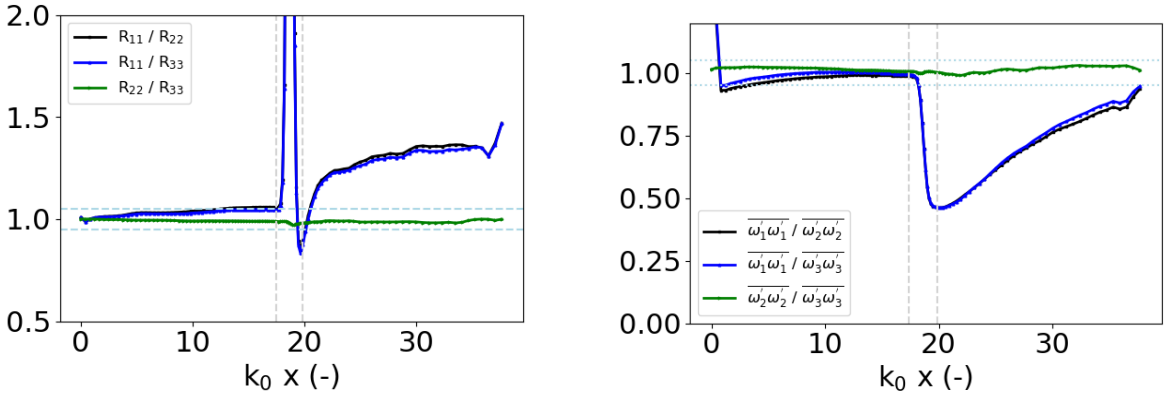

5-34 Anisotropies in resolved Reynolds stress' for Case 1 (left) and vorticity variances for Case 2 (right) in the Mach 1.28 STI of Larsson. 104×64^2 cells and $k_0 = 6$.

5.2.6. Mach 1.5 STI of Larsson

Another condition from Larsson *et al.* [53] is considered. It is a Mach 1.5 case but with the same pre-shock turbulent Mach number as in Subsection 5.2.5. A summary is given in Table 5-23. The interaction regime is of the wrinkled shock type in accordance with Equation 1-6. The corresponding reference amplifications are given in Table 5-24 which were extracted from Fig 4 and Fig 6 of [53]. The latter results were obtained on a similar grid size as the Mach 1.28 case (see Table 5-19).

5-23 Mach 1.5 STI conditions of Larsson *et al.* [53].

$\mathbf{M_s}$	$\mathbf{M_t}$	$\mathbf{Re_\lambda}$	δ/η	$\mathbf{M_t/(M_s-1)}$
1.5	0.160	40	0.39	0.32

5-24 Grid and amplification detail of the Mach 1.5 STI DNS study by Larsson *et al.* [53].

Case	$\mathbf{N_x}$	$\mathbf{N_y = N_z}$	$\mathbf{R_{11,d}/R_{11,u}}$	$\mathbf{R_{22,d}/R_{11,u}}$	$\omega'^2_{2,d}/\omega'^2_{2,u}$
DNS	1040	384	1.441	1.462	3.162

5.2.6.1. Numerical setup and pre-shock conditions for Mach 1.5 STI of Larsson

Exactly the same grid and domain setup as in 5.2.5.1 are considered. In terms of pre-shock grid spacing, this choice is also on the conservative side given that i_t = 6 in for the conditions in Table 5-23.

The simulated cases are listed in Table 5-25 with pre-shock anisotropies in Reynolds stresses and for vorticity variances lower than 6 % and 3 %, respectively. The $\delta/\eta|_{res}$ ratios are higher than the reference simulation of Larsson *et al.* [53]. The p-switch factor of the LD2 scheme was kept to 1 following the observations made in 5.2.5.2.

5-25 Pre-shock turbulence state in the STI reproducing the M_t = 0.16 conditions of Larsson *et al.* [53] at Mach 1.5.

Case ID	$\mathbf{M_{t,res}}$	$\mathbf{M_{t,tot_1}}$	$\mathbf{M_{t,tot_2}}$	$\mathbf{Re_\lambda}$	$\delta/\eta|_{res}$	$\delta/\eta|_1$	$\delta/\eta|_2$
Grid 1 : 104×64^2							
Case 1	0.139	0.149	0.141	39.17	0.34	0.37	0.35
Case 2	0.152	0.163	0.154	42.03	0.36	0.39	0.36

5.2.6.2. Evolution of Reynolds stresses and vorticity variances

Figure 5-35 presents the evolution of Reynolds stresses in this Mach 1.5 STI. The different amplifications are listed in Tables 5-26 and 5-27. Based on the resolved part only, both cases results in a relative error below 1 % for the R_{11} amplification. In accordance with the higher δ/η ratios, with respect to the reference case, the amplifications are lower. However, accounting for subgrid

scale estimates the situation is reversed and is not as what should be expected. The same comment regarding the grid resolution as in the Mach 1.28 can be made here. It is more probable that c_k = 0.07 should be used. Adopting the latter, R_{11} relative errors in amplification of 4.9 and 5.8 % are obtained for Case 1 and Case 2 respectively.

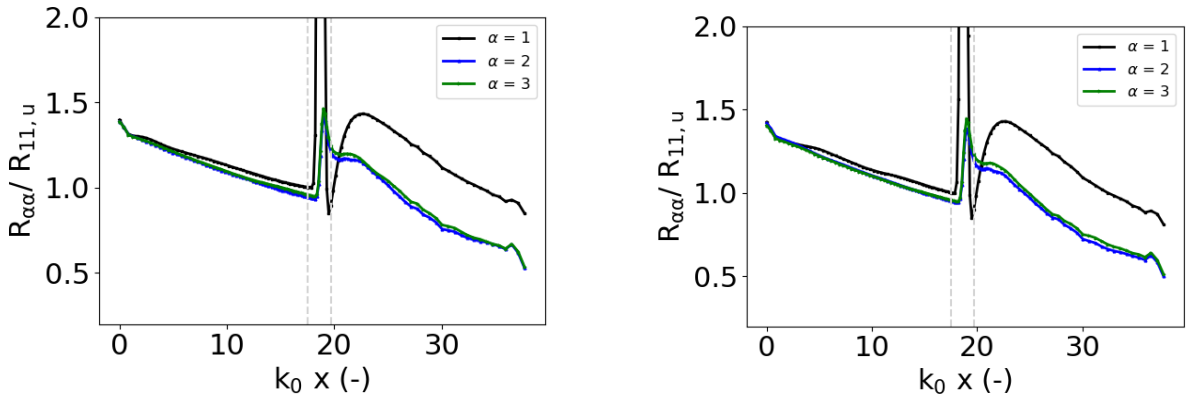

5-35 Evolution of Reynolds stresses in the Mach 1.5 STI of Larsson for Case 1 (left) and Case 2 (right) with scaling by pre-shock value. 104×64^2 cells and k_0 = 6

.

Looking at the transverse Reynolds stresses (R_{22}), relative errors below 5 % are found based on the resolved part only. Just as in the Mach 1.28 case, the estimates of SGS contributions are leading to very high values which are seemingly wrong.

Finally, the amplifications in transverse vorticity fluctuations variance by Case 1 and Case 2 lead to relative erros of 4.8 and 6.2 % with respect to the reference. The evolution of the different vorticity components are displayed in Figure 5-36.

5-26 Amplifications of R_{11} in the STI reproducing the M_t = 0.16 conditions of Larsson *et al.* [53] at Mach 1.5.

Case ID	$\delta/\eta\|_{res}$	$\mathbf{R}_{11,d}$ / $\mathbf{R}_{11,u}\|_{res}$	$\mathbf{R}_{11,d}$ / $\mathbf{R}_{11,u}\|_1$	$\mathbf{R}_{11,d}$ / $\mathbf{R}_{11,u}\|_2$	$\omega'^2_{2,d}$/ $\omega'^2_{2,u}\|_{res}$
Grid 1 : 104×64^2					
Case 1	0.34	1.432	1.524	1.449	3.011
Case 2	0.36	1.429	1.512	1.444	2.966

5.2.6.3. Taylor microscales and return to isotropy

In terms of Taylor microscale (Figure 5-37) and anisotropies (Figure 5-38) similar conclusions as in the Mach 1.28 case (see 5.2.5.3) can be drawn.

5-27 Amplifications of R_{22} in the STI reproducing the M_t = 0.16 conditions of Larsson *et al.* [53] at Mach 1.5.

Case ID	$\delta/\eta\|_{res}$	$\mathbf{R}_{22,d}$ / $\mathbf{R}_{11,u}\|_{res}$	$\mathbf{R}_{22,d}$ / $\mathbf{R}_{11,u}\|_1$	$\mathbf{R}_{22,d}$ / $\mathbf{R}_{11,u}\|_2$
Grid 1 : 104×64^2				
Case 1	0.34	1.412	14.410	3.786
Case 2	0.36	1.384	11.990	3.319

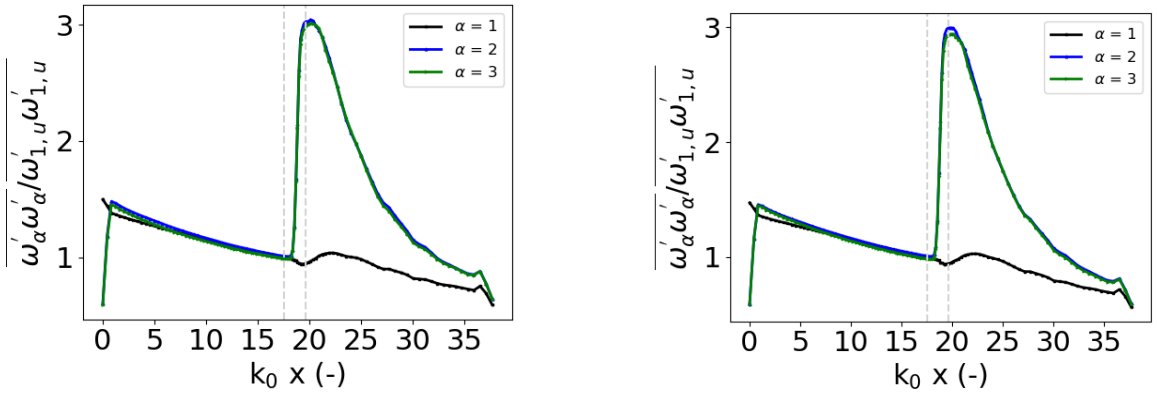

5-36 Evolution of vorticity fluctuations variances in the Mach 1.5 STI of Larsson for Case 1 (left) and Case 2 (right) with scaling by pre-shock value. 104×64^2 cells and k_0 = 6

.

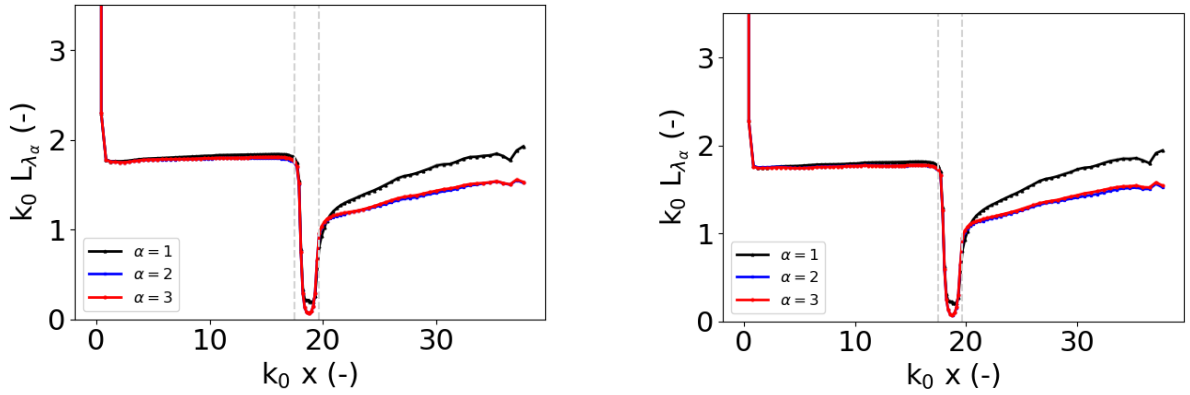

5-37 Evolution of Taylor microscales for Case 1 (left) and Case 2 (right) in the Mach 1.5 STI of Larsson. 104×64^2 cells and k_0 = 6.

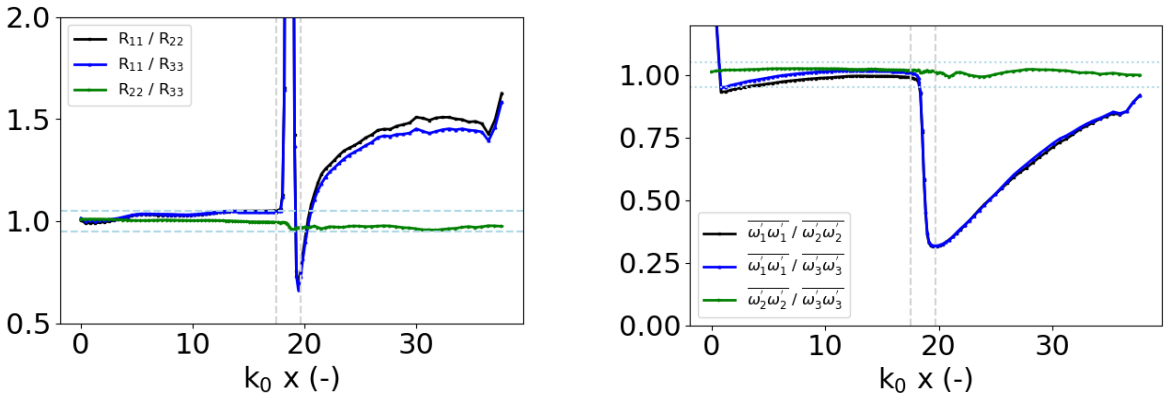

5-38 Anisotropies in resolved Reynolds stress' for Case 2 (left) and vorticity variances for Case 1 (right) in the Mach 1.5 STI of Larsson. 104×64^2 cells and $k_0 = 6$.

5.2.7. General discussion on present STI case studies

A comparative discussion between the five test cases detailed previously allows to take some perspective. The cases represent different shock turbulence interaction regimes as well as different conditions for freestream M_s, Re_λ and M_t. A convenient manner to compile the results is a comparison based on the scale separation δ/η which has been the subject of several discussions throughout this work. This is done for the amplifications of Reynolds stresses (resolved part only) and the vorticity fluctuations variances in Figures 5-39, 5-40 and 5-41. The points with transverse grids of 64×64 cells are plotted. In these Figures, wherever possible, the result of the reference work is also shown as black symbols.

From a qualitative perspective, the streamwise Reynolds stress amplifications in Figure 5-39 shows two considerable under-estimations of present simulations, i.e. for the Mach 2 case of Garnier and the Mach 1.5 case of Jamme. The other setups demonstrate appropriate trends and seemingly good matches with references, in spite of the quantitative mismatches discussed in previous sections. Nevertheless, this is an encouraging result. The Mach 2 case of Garnier has shown to be challenging for the LD2 central scheme and the p-switch factor setting. Moreover, it was pointed out (see 5.2.3), that the near shock grid spacing, as well as transverse grid spacing, is probably not fine enough to capture the correct amplification behavior. Regarding the Mach 1.5 of Jamme, current amplifications are in line with a Mach 1.2 LIA prediction instead of the targeted M_s. The adopted grid was shown to be appropriate for this study. The speculated reason for such an under-prediction is the low Re_λ (=5.5), and thus high viscosity, condition which is hard to simulate with only second-order accurate LES. The quantitatively good predictions for the Mach 1.5 of Larsson at much higher Re_λ corroborate this statement. Based on the other simulations, it could be inferred that a minimum Re_λ of ≈ 12 would be required to adopt the present numerical setup. Similar conclusions can be drawn for the transverse Reynolds' stresses in Figure 5-40 as well as for the vorticity variances in Figure 5-41.

It is also interesting to compare the TKE amplifications of the different setups (resolved part only). This will shed light on the behavior of a second-order accurate LES approach on a parameter with great importance in RANS modeling. Figure 5-42 presents the TKE amplifications across the shock as a function of the scale separation. The amplification is based on the peak post-shock value which coincides with the location of the peak in R_{11}. Reference values are extracted from digitzed images which does introduce a slight level of uncertainty. In general, similar observations as the streamwise Reynolds' stresses can be made. The strongest mismatch remains the Mach 2.0 case. However, in terms of TKE amplification, the case of Jamme is somewhat better reproduced than for R_{11} only. These results are encouraging and shows that the adopted numerics could be relied upon to devise modeling strategies for RANS. This statement is at least true for $M_s < 2$, as further investigations (grids) are required to conclude the same for higher Mach numbers. In the LES studies (higher order numerics) of Bermejo-Moreno *et al.* [5], it was indicated that amplifications predictions of TKE were better than the individual components which is explained by some leveling of under-and over-predictions in each component. Presently, such effect is not obvious. The budgets of TKE have as well been investigated and some of the results are presented below.

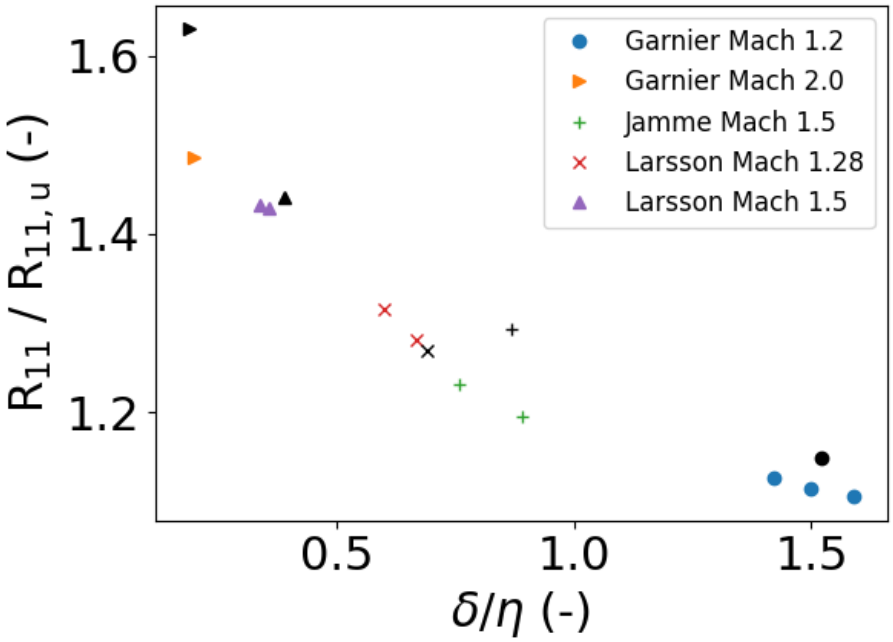

5-39 Amplifications of R_{11} as a function of the scale separation δ/η for the different STI case studied.

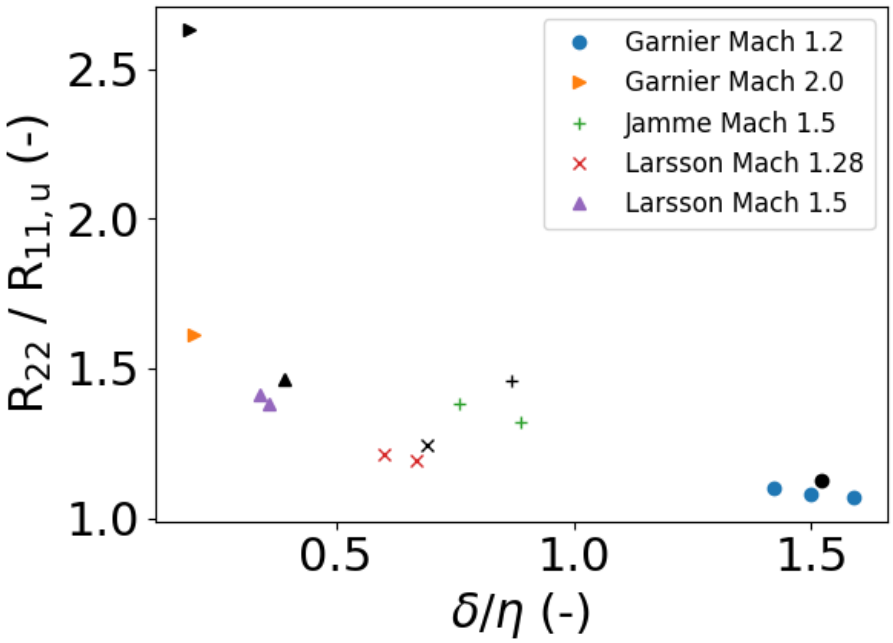

5-40 Amplifications of R_{22} as a function of the scale separation δ/η for the different STI case studied.

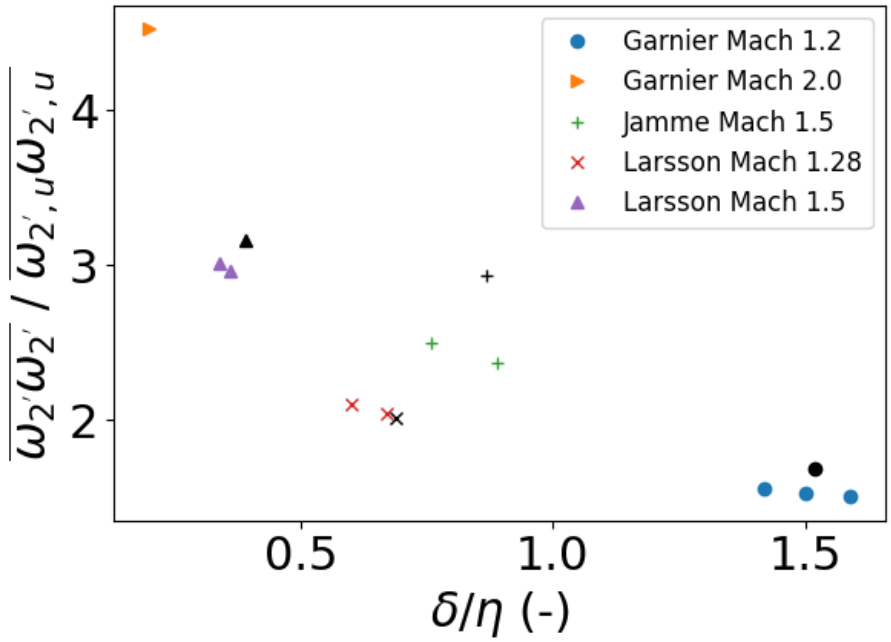

5-41 Amplifications of $\omega_2^{'2}$ as a function of the scale separation δ/η for the different STI case studied.

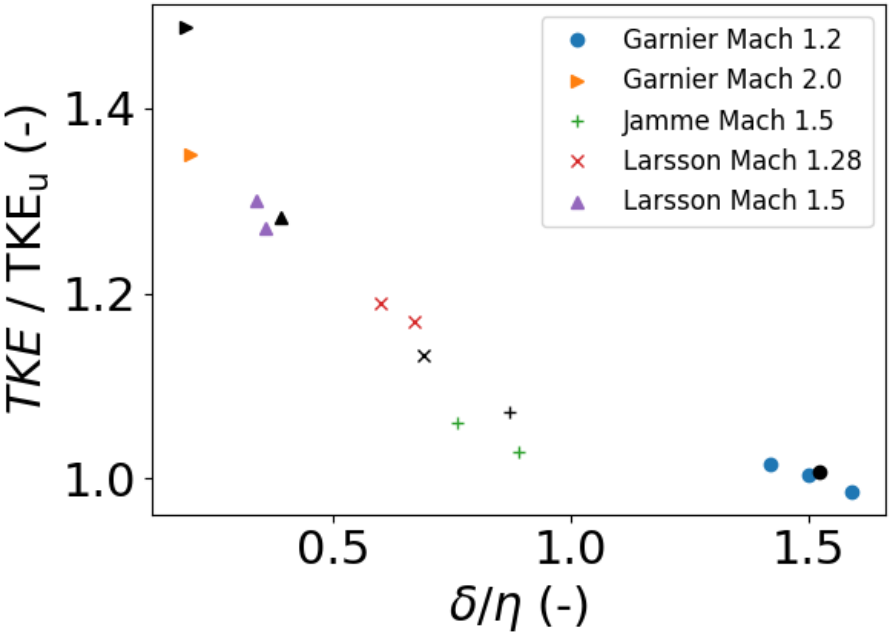

5-42 Amplifications of TKE as a function of the scale separation δ/η for the different STI case studied.

The budget of TKE is obtained by considering the trace of the Reynolds stress tensor transport equations which are detailed in [61]. This leads to the following equation [59]

$$\underbrace{\frac{1}{2}\bar{\rho}\tilde{u}_k R_{ii,k}}_{\text{I}} = \underbrace{-\bar{\rho}R_{ik}\tilde{u}_{i,k}}_{\text{II}}\underbrace{-\overline{u_i''\bar{p}_{,i}}}_{\text{III}}\underbrace{-\overline{u_i''p'_{,i}}}_{\text{IV}}\underbrace{-\overline{(0.5\rho u_i''u_i''u_k'')_{,k}}}_{\text{V}}\underbrace{+\overline{u_i''\tau_{ik,k}}}_{\text{VI}} \tag{5-3}$$

The different terms are in order; convection (I), production by mean strain (II), production by mass fluctuation (III), pressure work (IV), turbulent transport (V) and viscous dissipation and transport (VI). Note the use of Einstein's index notation in Equation 5-3 where a spatial derivative of a variable α in the direction k is denoted as $\alpha_{,k}$. Recall also that R_{ii} is a Favre-averaged quantity (Equation 5-1). Given the one-dimensional reduction of the statistics, several terms in Equation 5-3 will not be present, such as, for instance, the first term for k = 2 and 3. This is also shown in Jamme *et al.* [41] (their Equation 6). The exact mechanism of Reynolds stress (and TKE) amplifications are discussed at length in the literature, see e.g. [61, 59, 41, 31, 52]

Figure 5-43 shows the different terms of the above budget of TKE in the present Mach 1.2 STI study of Garnier for Case 1. Inside the shock region (denoted by the grey shaded area), the statistics are contaminated by the intermittent shock movement and can therefore not be relied upon (see also [59, 61]). The different terms are normalized by ($\bar{\rho}_{x=0}\ \bar{a}_{x=0}u_0^2k_0$) with the first two terms obtained from the space-and time averages at the start of the domain, u_0 is taken as 1.5 and k_0 as 6. Note that SGS contributions are not accounted for and that this study should therefore be seen in an indicative manner. Nevertheless, as most of the turbulent kinetic energy is resolved in LES, it remains useful to consider. As expected, the significant terms in the TKE transport are the pressure work (IV) and the viscous dissipation (VI).

A qualitative comparison with the results of Lee *et al.* [59] (their Figure 6 for conditions M_s = 1.2, M_t = 0.0953, Re_λ = 11.9) can be made. Consistent higher absolute levels of viscous dissipation are presently observed in the pre-shock region (term VI). Instead, the expectation would be a balance between this term and the convection (term I). This characteristic is recovered further downstream the shock region. It cannot be concluded if this is a result of the use of second-order accurate numerics, and thus an increased numerical dissipation, or the fact that SGS contributions (and thus dissipative scales) are not considered.

Regarding the pressure work (term IV), slight levels of oscillations are visible in the post-shock region which are to be expected (see also Figure 6 of Lee *et al.* [59]). A separate investigation of the streamwise and transverse Reynolds' stress contribution to the TKE budget is shown in Figure 5-44. The pressure work is responsible for the rapid changes in TKE through the STI, and therefore as well for the amplifications just downstream the shock. In general, under-predictions were observed throughout this work. The R_{11} pressure work' component ($\overline{-u_1''p'_{,1}}$) is the principal contributor to the amplifications as shown in Figure 5-45. This specific pressure work component is not as strong as it should be (see also Figure 4 of [41]). Moreover, according to Jamme *et al.* [41], the pressure work term acts as a source in the budget of R_{11} and a sink in the budget of R_{22} (R_{33}). The former is

indeed well captured but not the latter. Note that for this specific set of conditions, there is barely any amplification observed in TKE which is illustrated in Figure 5-46 (see also Figure 5-42).

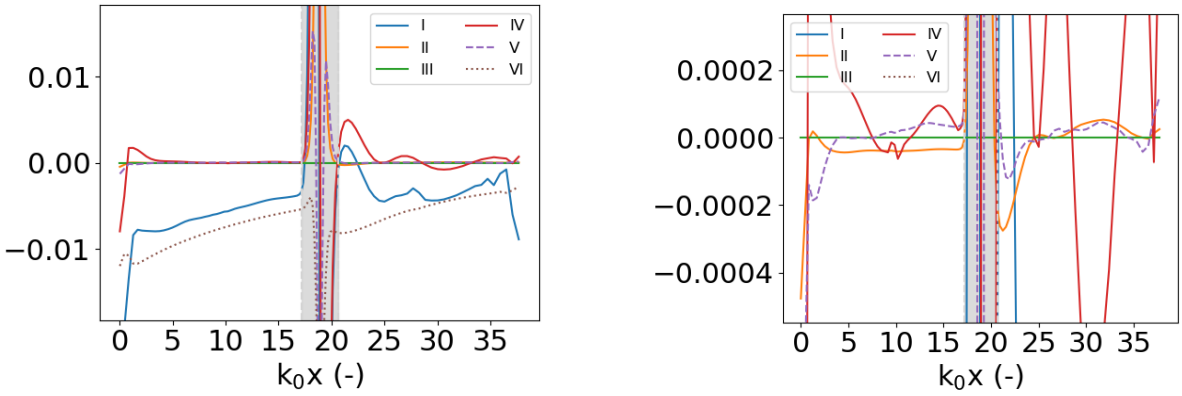

5-43 Budget of TKE for Mach 1.2 STI setup of Garnier, Case1. Values scaled by ($\bar{\rho}_{x=0}\ \bar{a}_{x=0}u_0^2k_0$). Right = close-up of Left.

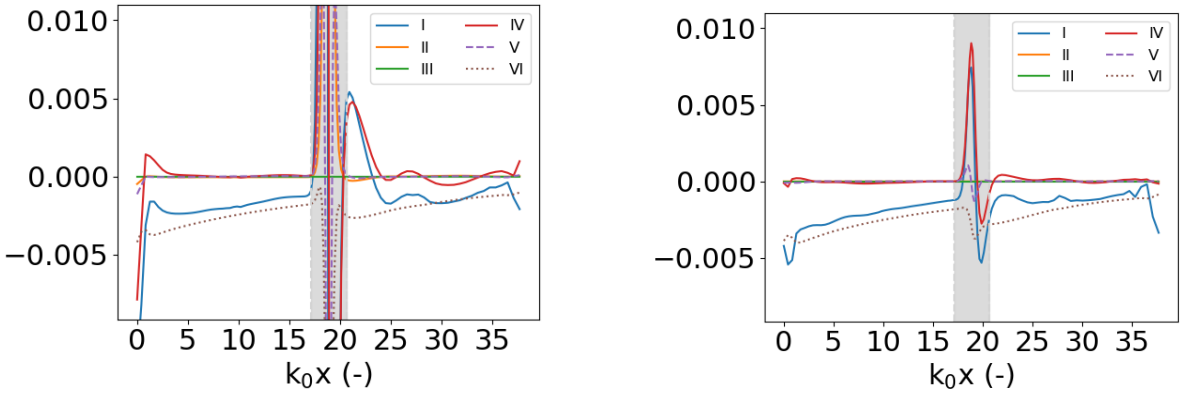

5-44 Transport of streamwise (left) and transverse (right) Reynolds' stresses in the Mach 1.2 STI of Garnier, Case 1.Values scaled by ($\bar{\rho}_{x=0}\ \bar{a}_{x=0}u_0^2k_0$).

To ensure that the above observations are not limited to this specific test case, the same quantities have been investigated for the Mach 1.28 Case 1 of Larsson. Some of the results are shown in Figures 5-47 and 5-48. In terms of TKE (and R_{11}) budget , the dissipation term (VI) is not as high, in absolute term, as in the previous test case. In general, the statistics are more oscillatory in the downstream region which could indicate some reflection from the exit boundary. This is as well observed in the Mach 1.5 case at similar Reynolds number. It could also be linked to the lower p-switch factor setting of the LD2 scheme. Further investigations would be needed to confirm this, including longer averaging times to discard to possibility of a lack of sampled instantaneous fields. Nonetheless, the results are in line with the previous test case and general expectations of these budgets.

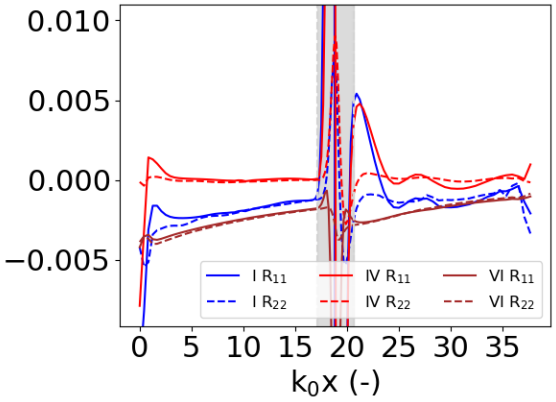

5-45 Most relevant terms in budget of R_{11} and R_{22} for Mach 1.2 STI setup of Garnier, Case1. Values scaled by ($\bar{\rho}_{x=0}$ $\bar{a}_{x=0}u_0^2k_0$).

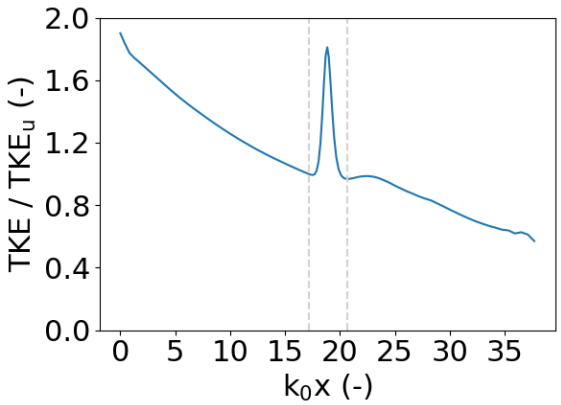

5-46 TKE evolution for Mach 1.2 STI setup of Garnier, Case1.

As a final investigations, the pressure-work term (IV in Equation 5-3) is further investigated. It can be decomposed in a pressure-dilatation and a pressure-transport term as follow.

$$\underbrace{-\overline{u_i'' p'_{,i}}}_{pressure\ work} = \underbrace{\overline{u''_{i,i} p'}}_{pressure\ dilatation} + \underbrace{-\overline{(u_i'' p')_{,i}}}_{pressure\ transport} \tag{5-4}$$

The pressure dilatation is the main contributor to the transfer between mean internal energy and the TKE just behind the shock. The pressure transport is responsible for the transport of this transformed TKE downstream. Such behavior can be observed in Figure 5-49 for two of the simulations presently performed. Whilst the decomposition provides very reasonable pressure-transport contributions, the pressure-dilatation is however underpredicted just behind the shock. Compare with Figure 5 of Jamme *et al.* [41] and Figure 12 of Larsson *et al.* [52] to support this observation. As shown in the latter work, the principal contribution to this term is provided by the streamwise Reynolds' stress of Equation 5-4. A lack of streamwise grid resolution just behind the shock could be the main responsible for this. Nonetheless, due to the rapid decay in pressure-work, the downstream

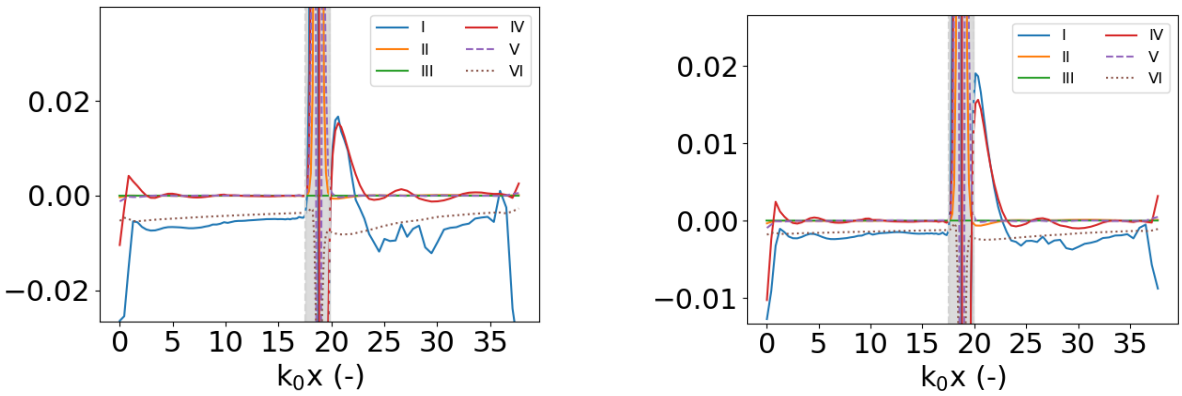

5-47 Budget of TKE (left) and R_{11} (right) for Mach 1.28 STI setup of Larsson, Case1. Values scaled by ($\bar{\rho}_{x=0}\ \bar{a}_{x=0} u_0^2 k_0$). Right = close-up of Left.

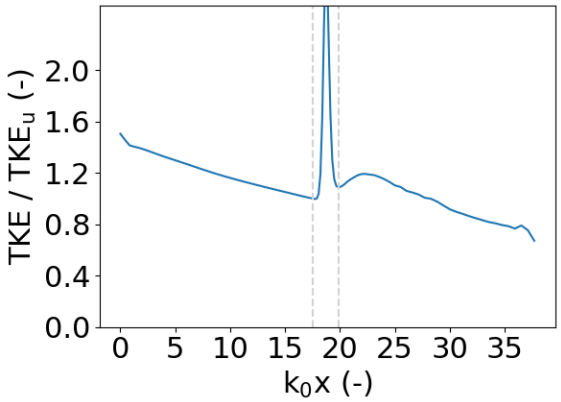

5-48 TKE evolution for Mach 1.28 STI setup of Larsson, Case1.

evolution is only mildly influenced by this. Once away from the shock, the pressure dilatation presently obtained is well within expectations. The inability to account for higher levels of pressure-dilatation just behind the shock can be identified as the main contributor to lower levels of R_{11} amplifications observed throughout this work. Furthermore, this would indicate that the transfer between thermodynamic fluctuations and TKE is a deficiency of the currently applied numerical framework. It was verified, on the Mach 1.2 STI of Garnier, whether or not the p-switch factor had any influence on the result. It was observed not to have any influence in a comparison between p-switch = 10 (default) and 1. Furthermore, for the same setup, the budget of TKE and pressure-work decomposition have been investigated for the simulations with $138 \times 96 \times 96$ cells on the same domain size, and thus increased post-shock grid resolution. The same conclusions can be drawn and no radically different behavior discerned. It is unclear how much the order of the numerics would play a role in here but based on the second-order DNS work of Jamme *et al.* [41], it can be inferred to not be the principal reason. This would leave the SGS model as a possible cause. The latter statement can, however, not be confirmed as none of the LES work in the literature, except for Genin [28] but for the TKE_{SGS}, present the budget of TKE in a similar manner as in this work.

Further investigations are thus required.

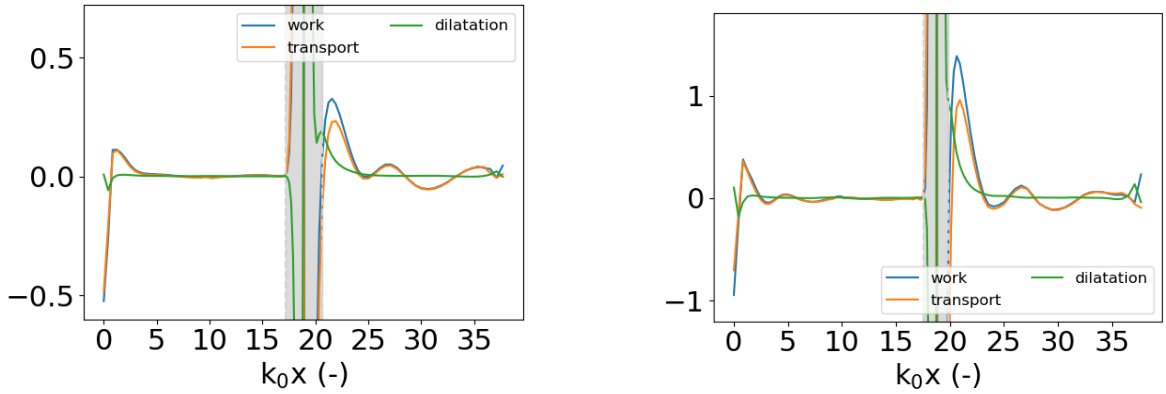

5-49 Pressure-work decomposition for Mach 1.2 STI of Garnier (left) and Mach 1.28 STI of Larsson (right). In both representations results for Case 1 are shown.

6. Conclusions

The conclusions are divided into two parts. A first part (6.1) is dedicated to the TAU code, its possibilities for study of the STI and the best approach to do so with its current capabilities. The second part (6.2) focuses on the canonical STI physics with the most adequate use of TAU.

6.1. On the status of TAU to study the STI

In terms of scale-resolving capability, TAU offers two possibilities. These are Detached Eddy Simulation (DES) and Large Eddy Simulation (LES). DES is very attractive from the practical application's perspective as it would allow for study of more complex geometries at a relatively affordable computational cost in comparison to a pure LES methodology in the presence of walls. This attractive feature motivated to firstly consider DES for possible study of the canonical STI. In order to generate turbulence fluctuations in the STI setup within a DES framework, a synthetic turbulence methods is required. In the context of DES, it is convenient to rely on methodologies specifically devised for this such as Shur's Synthetic Turbulence Generator (STG) and Jarrin's Synthetic Eddy Method (SEM). Both methods were considered for this task in a setup with three zones: a RANS zone, a STG / SEM zone and an LES / DES zone (see 2.1.2). Note that the synthetic turbulence generation methods can be used both in DES and LES, hence the relevance of its extensive study in this work. The RANS zone is used as a reference for the STG / SEM turbulence fluctuation's generation. The possibility of such a setup was investigated without a shock with the focus on obtaining the desired turbulence characteristics, i.e. (quasi-) vortical turbulence with target M_t and Re_λ, at a given point downstream the STG / SEM region. This task has proven to be impractical as it was impossible to easily control the desired turbulence at a given point in the domain. Several other aspects have led to halting the possibility of relying on the STG or SEM and more details on this are provided in 2.1.2.3. The main reason for abandoning the efforts to further investigate and / or develop the capabilities of these methods is the stringent requirement of (relatively) easily obtaining a turbulence state in order to allow comparison with canonical STI studies from the literature. If this was not required, the STG / SEM setup would be extremely attractive as it would provide a state with realistic turbulence at an affordable computational cost. It is, moreover, well suited for wall bounded flows. This would then allow to bridge the gap from an isolated canonical STI setup to more realistic geometries such as scramjet isolators or other shock dominated flow fields with turbulence interactions. It would be a logical follow up of this work to continue looking into this direction.

Due to the above mentioned hurdles, the canonical STI setup was studied in a more classical manner as done by many authors in the literature. A separate temporal Decaying Homogeneous Isotropic Turbulence (DHIT) LES simulation is used to obtain a priori the desired turbulence state. The DHIT result is subsequently convected through the domain containing the shock by relying on Taylor's hypothesis. The DHIT simulations have proven to be another challenge in the present work (see 2.2). The procedure required many trials in order to obtain a turbulence state with anisotropy levels below 5 %. Moreover, the choice of the initial spectrum, as described in 2.2.1, was only possible

with an initial peak wavenumber of 6. Another important point is the interdependence between grid size and order of numerics. Specifically, there is a minimum number of cells required to obtain isotropic turbulence with a second-order accurate LES method. These points were discussed at length in 2.3.

The LES method adopted in TAU relies on the classical Smagorinsky-Lilly formulation of the Subgrid-Scale (SGS) model with a static constant. An important complication in such an SGS model is the estimation of the SGS portion of the turbulent kinetic energy (TKE_{sgs}). Specifically, which is the SGS dissipation introduced by the SGS model and which is the one introduced by the combination of numerics and grid size? An in depth study of this problem has been performed by other authors with TAU leading to a rather inconclusive result. Therefore, a simple estimation described in 3.3, was presently considered which unfortunately still relies on a constant. Throughout this work, two values for this constant were considered in order to provide boundaries as to the level of TKE_{sgs} contributions. This estimation is also relevant to evaluate if sufficient TKE is resolved by the LES methods and helps in selecting appropriate grid sizes.

Another point of study was the choice between an upwind or central discretization scheme for the STI simulations, both second-order accurate. Upwind schemes are particularly well suited for shock capturing but are known to be more dissipative which is undesirable for accurately resolving turbulence structures. TAU deals with the latter disadvantage by relying on Thornber's low Mach number modification which allows the upwind scheme to act as a central scheme at small Mach numbers, and hence reducing the numerical dissipation. The DHIT simulations have been performed with both the upwind and central scheme (see A.2.2 and also 4.1.1) with satisfactory results. However, once the turbulence resulting from the DHIT was convected an unexpected increase in dissipation was consistently observed which led to a mismatch between temporal and spatial decay (see 4.1.2). The reason for this has been found to be the implementation of Thornber's low Mach modification. It does rely on the local Mach number and only acts at low values. When convecting the turbulence, a uniform supersonic Mach number is superimposed which results in the inactivity of the implemented low Mach modification. This in turn explains the increase in dissipative character. This behavior also explains observations made in the STG simulations. Therefore, furher consideration of the upwind scheme were not made. Additional developments should be undertaken in order to allow more accurate simulations of incompressible turbulence in supersonic flow fields with upwind schemes in TAU.

Following the inadequacy of an upwind spatial discretization scheme, the central type scheme was considered for the canonical STI studies in this work. The specific scheme implemented in TAU is a low-dispersion low dissipation, or LD2, type. Unlike upwind schemes, central schemes have more difficulties in handling shocks and need careful considerations in order to avoid spurious oscillations. They are, however, very well suited to handle turbulence with minimal dissipation. The LD2 scheme has many parameters that can be chosen. It was therefore required to study the best combination for these in order to simulate the STI problem, which was reported in 4.1.3 and 4.1.4. The low dispersion setting has shown to be problematic in the presence of shocks, introducing pre-shock

spurious oscillations. In the post-shock region, its use is however recommended, especially having evaluated its impact on the small scale turbulence (see velocity derivative skewness and vorticity variances). Unfortunately, the current framework of TAU does not allow zonal specification of numerical scheme parameters. It would however be a good point for future developments. The low dispersion characteristic of the LD2 has therefore been deactivated throughout this work. Another important parameter in the LD2 formulation with regard to shock capturing is a pressure sensor (or pressure switch or p-switch) which controls the dominance of the second-order dissipation term as a sensitivity to pressure gradients. Its influence has been mainly observed with stronger shocks (Mach > 1.5) and a value of 10 has been used as a default (see 5.2.3.2). Note that increasing the value of this parameter results in increased anisotropy of the incoming turbulence which is explained by strong differences in behavior of the flow in shock normal and transverse directions. The low dissipation setting has proven to be suitable and kept to its default setting. Further investigations would be required to devise even better strategies on the use of the LD2 scheme for shock turbulence interaction and could become beneficial when stronger shocks have to be dealt with. This could be in the form of smart strategies with scalar and matrix dissipation. It also entails the implementation of the numerics with potential separate formulation between shock normal and transverse directions, a topic discussed by several authors in the STI related literature.

The temporal discretization's choice has been the subject of another study (see 4.2). The attractive dual-time stepping approach has been shown to lose its advantage due to low time step requirements to accurately study the canonical STI setup. Therefore, a global time stepping approach with a three-stage Runge-Kutta method has been preferred instead.

A last point to mention are the thermodynamic fluctuations which have been the subject of very little investigations in the present work. A mismatch in pre-shock isentropic character of the incoming turbulence has been indicated in 4.2.2. It was however shown that the the rms levels of the thermodynamic fluctuations remain typical of (quasi-) vortical turbulence. It would be of general interest to dig deeper into the effects of the presently chosen numerics on the thermodynamic fluctuations, which plays a role during the STI.

6.2. On the STI with TAU

The canonical STI setup has been studied with the LES capability of TAU, using a simple Smagorinsky SGS model. The LD2 scheme was used for spatial discretization, without the low dispersion setting and a default p-switch of 10, and a global time stepping approach for the temporal discretization. The inflow turbulence, generated through a priori DHIT simulations, is convected periodically through the domain. A seperate study on the influence of such a periodic push (see 4.2.2.1) has been carefully studied and shown to be very limited, and hence appropriate for consideration. Initialization of the shock in the domain was done by relying on the laminar jump conditions. Initial transients were discarded from the statistics by allowing the incoming turbulence to go through the domain during two flow-through times before collecting statistic for another two flow-through times.

Five different reference conditions from the literature were reproduced, two from Garnier, one from Jamme and two from Larsson. The selection allowed to study the different regimes of shock interactions (borderline, broken and wrinkled). The pre-shock conditions implied variations in viscosity ($Re_\lambda \in [5.5,40]$), in turbulence intensity ($M_t \in [0.108,0.16]$) and shock Mach numbers (M_s) $\in [1.2,2]$. More importantly, the scale separation parameter, the ratio of laminar shock thickness to Kolmogorov length scale (δ/η), varied between 0.19 and 1.52. This parameter has been shown in the literature to be well suited in comparing different STI results. Its importance was discussed as part of this work (see 5.2.1) as it provides a way to evaluate the target conditions to be matched by the current LES, for a given shock Mach number. It was also pointed out that the δ/η ratio differs between an LES and a DNS due to the use of an SGS model. Specifically, Re_λ is mostly influenced as it relies on the evaluation of the Taylor microscale which in turn relies on velocity derivatives which are highly dependent on small scale fluctuations (see also 3.2). M_t is less influenced as the SGS contribution to the total TKE for an adequate LES should remain below 20 %. It is therefore almost impossible to achieve a perfect agreement in pre-shock conditions between a DNS and an LES. Moreover, in LES, evaluating the SGS contribution to quantities such as the TKE is not trivial as was seen throughout this work, adding another level of uncertainty. Nonetheless, good enough agreements can be obtained as is summarized in 5.2.7.

Regarding the appropriate setup to study the canonical STI, the grid spacing plays a major role. This was separately studied in 3.1 and the guidelines provided in the literature were thus followed which links the pre-shock ratio of streamwise to transverse cell spacing to the intensity of the turbulence under study. The requirement allows for adequate capture of the shock front corrugation. Another important point with respect to grid spacing is the transverse grid size. It has been shown in DNS studies to be extremely important, especially in the near post-shock region. These observations were linked to the small scale turbulence, which is modeled in an LES. A comparison between different grid sizes (see e.g. 5.2.2) did not indicate such a strong dependence on the different amplifications obtained with LES and the present numerical choices. Some of the simulations indicated instead that the transverse direction might be underresolved inside the shock region. Given these observations, most of the results were obtained on similar domain sizes with similar grid spacings. It must be noted that the STI setup still imposes stringent requirements for an LES in terms of time steps, grid spacings and grid sizes in order to adequately study the problem. This should be kept in mind when more complex problems are of interest with LES / DES methods, such as, for instance, a shock-train. Can there be an appropriate meshing strategy which relies on shock capturing to help in this and accounts for transverse grid spacing requirements? It also raises the question of how important the accuracy in representing the STI physics is in an actual configuration. Tackling this question is left to future work.

Amplifications of Reynolds stresses and vorticity fluctuations variances were studied for the different reference conditions. The general observations were relative errors with respect to reference DNS in Reynolds stress component amplifications below 10 % (except for transverse amplification in Mach 2 of Garnier discussed further below). This was based on the resolved part of the energy. Account-

ing for SGS contributions to these amplification has shown to yield diverse results. Typically, for the streamwise Reynolds stresses the estimates would seem reasonable with uncertainties remaining on the actual coefficient to be used to provide the most realistic view. Inferences can be made based on the grid requirements from the reference DNS but in the case where such reference wouldn't be available it would be impossible to make a choice. For the transverse amplifications, using the SGS estimates has shown to be extremely unreliable with estimated SGS contributions > 80 %. It could be inferred that this estimate does not work well inside the shock region, which is where the transverse Reynolds stresses are most amplified. The qualitative evolutions of the resolved Reynolds stresses do moreover not indicate extreme lacks of amplifications in the shock region that would confirm the possibility of very high SGS contributions. The role of the SGS model active inside the shock region in present work is however unknown. Based on other LES studies performed in the literature it is adviced to deactivate any SGS model insided the shock wave as the dissipation introduced by the spatial discretization scheme will act as an SGS model already. The possibility to deactivate the SGS model locally is currently not possible with TAU but should be considered in the future.

Transverse amplifications of vorticity fluctuations' variances could only be compared based on the resolved portion of the flow as an SGS estimate could not be provided. In the comparisons with available references, relative errors in amplifications below 10 % were also obtained except for the Mach 1.5 case of Jamme where they reached almost 20 %. This specific setup has been generally challenging with the present numerical choices. It is also the most viscous test case with Re_λ of 5.5. The STI setup of Jamme has indicated a possible limitation with the present LES framework. It is possible that higher Re_λ are needed in order for the second-order LES to be applicable. This statement is supported by the much better qualitative and quantitative comparisons with the other STI conditions, except for the Mach 2 test case. The Mach 2 test case, taken from the work of Garnier, has shown to be extremely challenging with significant underpredictions of transverse amplifications (both Reynolds stresses and vorticity) which occur inside the shock region. The reason for this is most probably linked to the central scheme and its difficulty in dealing with such high shock Mach numbers with the currently adopted settings. This indicates the need for further careful parametric study, and possibly new developments, of the LD2 scheme in TAU.

Compiling the information of the different amplifications on a single graph, by making use of the scale separation ratio δ/η, allowed to take some perspective on the results presently obtained. From this qualitative perspective, it is shown that the results presently obtained for the cases of Larsson and the Mach 1.2 of Garnier are in good agreement. From this, it can be suggested that appropriate trends can be obtained with the present numerical framework for shock Mach numbers below 2 and for Re_λ above 5.5. It has still to be demonstrated how TAU copes with higher turbulence intensities (higher M_t) and much higher Re_λ than presently considered.

Other quantities that were presently looked at for the different conditions are the anisotropies in Reynolds stresses and vorticity variances as well as the evolution of the Taylor microscales. Regarding the former, no return to isotropy of the small scales (vorticity variances) were observed by the end

of the domain but the evolution suggests this to happen at some point downstream the present computational domain. The observations are in agreement with most of the references except for the cases from Larsson. In the latter, the return to isotropy is expected within the computational domain, however it was shown by the authors to require very fine grids in the near post-shock region to accurately retrieve this behavior. It is most likely that a second-order accurate LES will never be able to correctly predict such a behavior.

In terms of the Taylor microscales, the different simulations show the same evolution with a very rapid post-shock increase in streamwise component which becomes larger than the transverse ones. However, throughout this work the simulations predict a strong drop in the shock region of the transverse components which is not in accordance with the literature. It is unclear what lays at the origin of this as the influence of grid spacing and SGS model has been discarded. Speculatively, it could be linked to the central scheme, and should be further investigated.

As a final point of interest, the TKE has been further investigated. In terms of amplifications, similar conclusions as in the individual Reynolds stress amplifications were made. It confirms that for the Mach and Reynolds number range identified as appropriate for study with TAU, the TKE amplifications can reasonably well be provided through simulations. The budget of TKE was subsequently discussed in order to shed light on the ability of the present numerical framework in correctly representing the expected physics. In accordance with reference expectations, the dominant term in the TKE transport equation were as well identified. The pressure-work, being the main responsible for the rapid evolution of the quantities, and amplifications, in the post-shock region has further been decomposed into contributions from the pressure-dilatation and the pressure-transport. The former is the key process which transforms internal energy, from thermodynamic fluctuations, into TKE, and therefore the term that has a direct link to the magnitude of the amplifications in TKE (and streamwise Reynolds stresses). The expected balance between pressure-dilatation and pressure-transport was observed. However, it was also shown that the pressure-dilatation just behind the shock is not as high in magnitude as reported by other authors in the literature. It could perhaps be the limiting factor of the current LES. It would also indicate a potential difficulty in appropriately describing thermodynamic fluctuations. At this point, it is, however, very difficult to comment on the latter given that no other LES work of the canonical STI setup in the literature has reported on the budget of TKE.

The aim of this work was to use TAU to the best of its abilities and study the challenging problem that is the canonical STI. Depending on the conditions of the setup, it was shown to be capable of simulating the interaction with a reasonable level of accuracy given a second-order accurate LES framework. Different points for improvement have been identified as well as some aspects for further study. These would enable the solver to be used for a broader range of conditions including stronger shocks.

A. Turbulence decay

Additional information is herein provided on the free decay equations from RANS (Section A.1) and the validation of TAU with a commonly adopted reference DHIT setup (Section A.2).

A.1. The free decay equations

This section presents the decay equations for turubulence in a flow free from walls or any other type of disturbances, referred herein as "free-decay". Firstly, the governing equations are detailed in A.1.1 followed by an example in A.1.2.

A.1.1. The formulation

As the RANS turbulence model of choice in TAU is Menter's k-ω SST [73, 74] (2003), the equations of interest have to be cast in terms of the TKE and its dissipation rate (ω). The procedure is similar to that of Spalart and Rumsey [109] and Lopes et al. [69], except for a compressible formulation used presently with respect to the latter work. The basic assumption is that only the destruction term of the equations are active and the flow is in the x-direction which leaves us with the following two equations for a given point in space:

$$(\rho U k)_{,x} = -\rho\beta^* \omega k \tag{A.1}$$

$$(\rho U \omega)_{,x} = -\rho\beta \omega^2 \tag{A.2}$$

where $\beta^* = 0.09$ and $\beta = 0.0828$ which is taken as the value β_2 in the SST model. Note that a similar procedure can be adopted to obtain the temporal formulation. Recall also the relation between TKE, ω and ϵ as

$$\epsilon = \beta^* k \omega \tag{A.3}$$

First solving the ODE for ω (Equation A.2) yields

$$\omega = \omega_0 \left(1 + \omega_0 \frac{\beta}{U}(x - x_0)\right)^{-1} \tag{A.4}$$

where the subscript 0 indicates the free-stream. Note that x_0 would be typically set to 0.

Making use of A.4 we can integrate equation A.1 which will eventually result in:

$$k = k_0 \left(1 + \omega_0 \frac{\beta}{U} x\right)^{-\beta^*/\beta} \tag{A.5}$$

Rewriting these equations in terms of free-stream turbulence quantities yields:

$$\omega_0 = \frac{\omega}{1 - \omega \frac{\beta}{U} x} \tag{A.6}$$

and

$$k_0 = k \left(1 + \omega_0 \frac{\beta}{U} x\right)^{\beta^*/\beta} \tag{A.7}$$

It is important to note that Equation A.6 has a singularity if

$$1 = \omega \frac{\beta}{U} x \;\; or \;\; x = \frac{U}{\omega \beta} \tag{A.8}$$

This will set a limit on the distance over which you can consider the decay in a situation where a target combination of TKE and ω is of interest and an upstream combination of $(TKE - \omega)_0$ is sought.

A.1.2. An example of spatially free decaying turbulence

Figures A.1.1 and A.1.2 exemplify the idea. A double periodic channel-like geometry with uniform grid spacing is simulated with TAU and the k-ω SST model. A supersonic inflow is prescribed at Mach 1.5 with T=300 K, p=1e5 Pa, R=287.1, γ = 1.4.

The target turbulence state we wish to achieve is $M_t = 0.14$, and Re_{L_ϵ} = 650 (Re_λ = 73) and corresponds to one of the pre-shock conditions of Larsson *et al.* [52] (see Table 1 in their work).

From the above target turbulence state and the ambient conditions we obtain pre-shock conditions: I_s =5.4 %, $(\mu_t/\mu)_s$ = 71.6, TKE_s = k_s=1181.7, ω_s =1047923 (1e6), where the index *s* indicate the pre-shock state. "I" is the turbulence intensity defined as

$$I = \frac{\sqrt{\frac{1}{3}(M_t \tilde{a})^2}}{\tilde{u}_{1,u}} \tag{A.9}$$

with $\tilde{u}_{1,u}$ is the upstream streamwise velocity component and M_t is given by Equation 1-1. The associated value of $L_{\epsilon,s}$ (Equation A.18) $\approx$ 0.36 mm.

Assuming a free decay over x=0.005 m gives us:
I_0=14.2%, $(\mu_t/\mu)_0$ = 83.7, k_0=8262.7, ω_0= 6271565 (6.2e6) or in terms of ratios: $\omega_s/\omega_0 = 0.167$, $k_s/k_0 = 0.143$. These conditions are prescribed at the superonsic inflow of our simulation.

Figures A.1.1 and A.1.2 show the resulting decay predicted by the TAU code sampled along a single horizontal line. The analytical curve corresponds to results with Equations A.5 and A.4. As expected, a very good match between both solutions are shown. Due to the singularity (Equation A.8), a maximum upstream distance that could be considered equals 6 mm. A distance of 5 mm $\approx$ 14 $L_{\epsilon,s}$.

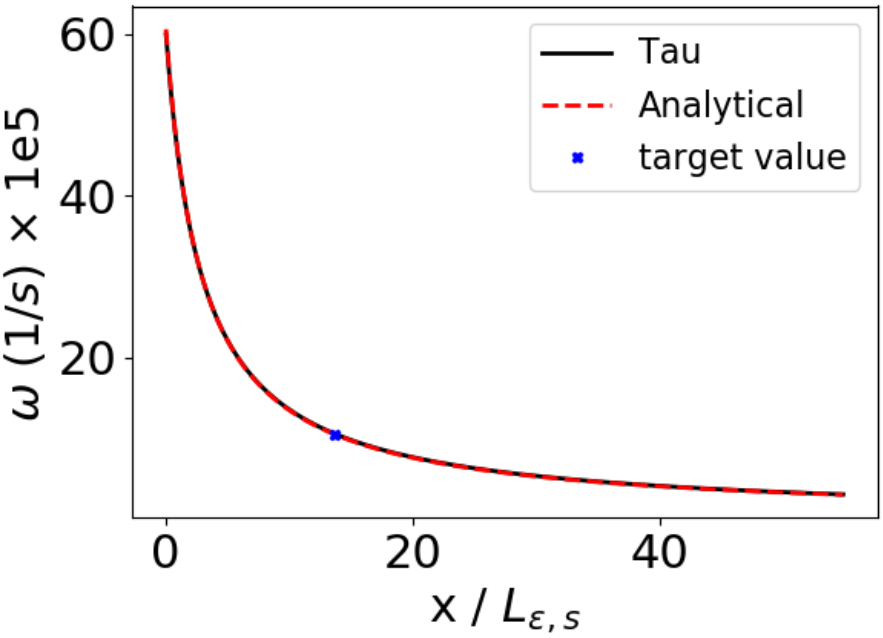

A.1.1 Decay of ω for targeted location 5 mm downstream the inlet. Non-dimensionalized by eddy dissipation length scale before shock.

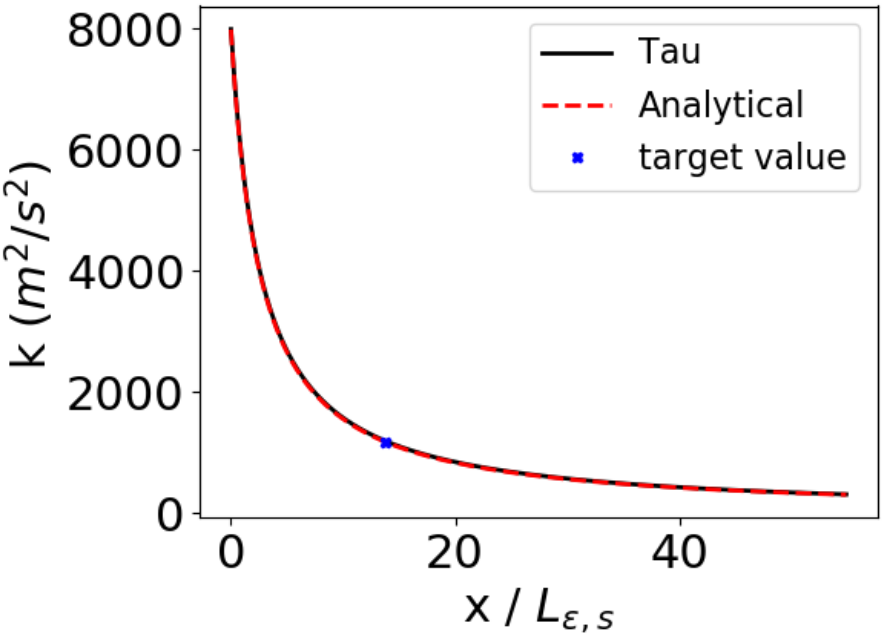

A.1.2 Decay of TKE for targeted location 5 mm downstream the inlet. Non-dimensionalized by eddy dissipation length scale before shock.

A.2. Decaying Homogenous Isotropic Turbulence (DHIT)

A DHIT setup is a typical first validation of a scale-resolving CFD code. In TAU, this has previously been done with the incompressible turbulence study of Comte-Bellot and Corrsin [11] by Knopp *et al.* [47]. Another widespread reference test case is the DNS of Wray which is presently considered. In a first step (Subsection A.2.1), the latter setup is described as well as the relevant parameters of interest. Then, the results with TAU are discussed (Subsection A.2.2). The author whishes to acknwoledge the contribution of Tim Horchler (DLR) in the validation simulations with TAU.

A.2.1. Wray DNS

Jimenez provides the temporal evolution of some integral quantities from their spectral code with 512x512x512 nodes as well as some turbulent energy spectra (see `https://torroja.dmt.upm.es/turbdata/agard/chapter3/HOM02/CB512.f_t`) . The initial turbulence field is Gaussian with a Taylor microscale Reynolds number (Re_λ) of 952. The website also provides a document (pdf format) with further details about different test cases and formulas used. We will now analyse this information and compare with what we can obtain from the provided DNS spectra.

A.2.1.1. TKE and ϵ

Figure A.2.3 shows the decay of TKE and its dissipation rate (ϵ). The TKE is referred to as "Total energy" in the provided data. The label "from ref file" indicates this data while the label "from spectrum" indicates our postprocessing from the energy spectrum that is given (E(k)) and contains data over 241 wavenumbers. Spectra are available at four different time instances. The total TKE is obtained by integrating a spectrum as

$$TKE = \frac{3}{2}u'^2 = \int_0^\infty E(k)dk \tag{A.10}$$

where u' is the rms velocity. For ϵ, the quantity is not directly given. We used two approaches based on the available data. The first one is the definition:

$$\epsilon = -\frac{d(TKE)}{dt} \tag{A.11}$$

which we simply compute based on the TKE and the time information. The second approach is by using the enstrophy provided by Jimenez defined in general as a function of spectral quantities (from appendix of Crespo [13]) :

$$\mathcal{E} = \left(\frac{2\pi}{L_b}\right)^2 \int_0^\infty k_i^2 E(k_i)dk_i \tag{A.12}$$

where L_b is the size of the box under consideration. In our case the box size is 2π which simplifies the formulation. Moreover, as our box side length is 2π, the wavenumbers k_i will held values of 1,

2, 3, etc. It is replaced by k in the following discussions. The simplification yields therefore:

$$\mathcal{E} = \int_0^\infty k^2 E(k) dk \tag{A.13}$$

For incompressible flow and low Mach number compressible flows a relation exists between ϵ and $\mathcal{E}$, specifically:

$$\epsilon = 2\nu\mathcal{E} \tag{A.14}$$

In order to get ϵ from the four spectra of Jimenez we used the relation

$$\epsilon = 2\nu \int_0^\infty k^2 E(k) dk \tag{A.15}$$

Very similar results are obtained with the different computations. The graphs also show the typical initial transients where dissipation has to build up and TKE remains almost constant before both quantities start to decay. When we initialize the field randomly with a given spectrum, we have uncorrelated phases. Such a field does not dissipate energy significantly until the velocity develops short term correlations [44]. Note that for the computation of ϵ (Equation A.14), the factor two was not accounted for as it exactly matched the other data provided. It could be that the "Total Enstrophy" in this reference has a somewhat different definition.

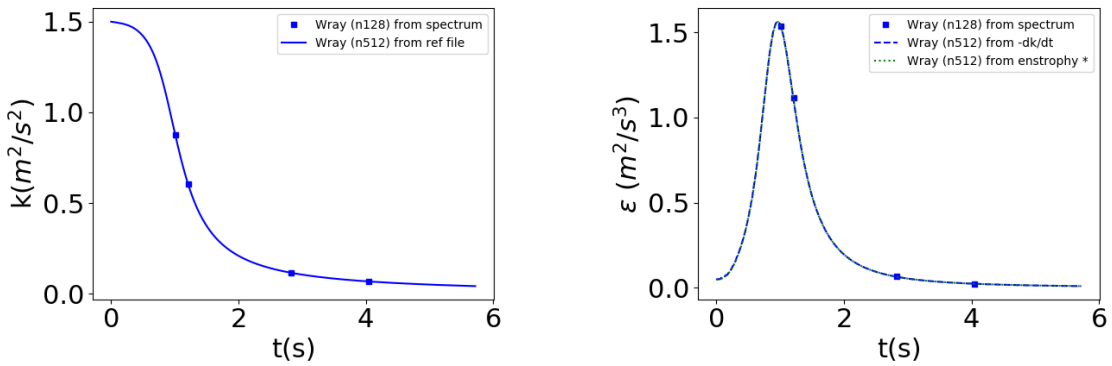

A.2.3 Turbulent kinetic energy and its dissipation rate (ϵ) for the DNS decay of Wray.

A.2.1.2. Charateristic turbulence parameters

Figure A.2.4 shows the integral length scale and the velocity derivative skewness defined as :

$$L_t = \frac{\pi}{2u'^2} \int_0^\infty k^{-1} E(k) dk = \frac{3\pi}{4} \frac{\int_0^\infty k^{-1} E(k) dk}{\int_0^\infty E(k) dk} \tag{A.16}$$

$$S = -\frac{\overline{\left(\frac{\partial u}{\partial x}\right)^3}}{\left[\overline{\left(\frac{\partial u}{\partial x}\right)^2}\right]^{3/2}} \tag{A.17}$$

where the average in Equation A.17 is performed over all grid points. The skewness is the scaled third moment of a quantity and describes the asymmetry of the PDF of the distribution of the quantity of interest. E.g., if $u_{,x}^3$ =0, then $S_{u_{,x}}$ = 0 and we have a symmetric PDF around the origin. Both of the graphs in Figure A.2.4 show some initial transient and a slight mismatch in the computations of the integral length scale can be seen. In a paper from Tavoularis et al. [110], observations show that in isotropic turbulence for moderate to small Reynolds numbers (Re_λ), S (as defined in Equation A.17), increases slowly with decreasing Re_λ. It reaches however a maximum value for Re_λ between 4 and 3 and then decreases rapidly. It can be seen that presently, at the first provided spectra ($Re_\lambda \approx 97$, see Figure A.2.5), the values for the former are below 150 and stay well above the value of ≈ 4. Based on the observations of Tavoularis et al. [110], we should have an increase in S which we can observe (except for the initial transients).

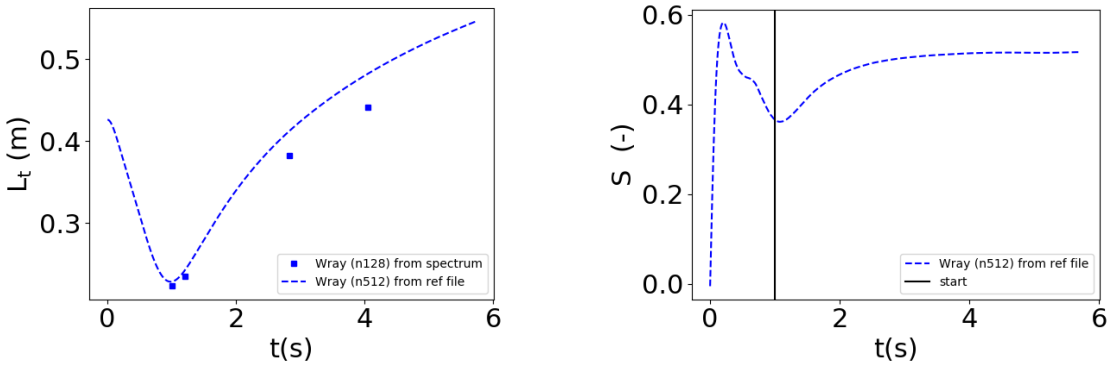

A.2.4 Integral length scale and skewness for the DNS decay of Wray

With regard to obtaining realistic / developed turbulence, both of the above quantities are closely monitored to evaluate this as mentioned by, e.g. Larsson *et al.* [52]. Note that in this latter paper an integral length scale L_ϵ is considered which is closely related to L_t: the dissipation length scale which is defined as

$$L_\epsilon = \frac{k^{3/2}}{\epsilon} = \frac{(R_{kk}/2)^{3/2}}{\epsilon} = \frac{(R_{kk}/2)^{1/2}}{\beta^* \omega} \tag{A.18}$$

The velocity derivative skewness is usually defined with an opposite sign to Equation A.17. For realistic turbulence, the skewness (with opposite sign) should settle around -0.5 and L_ϵ (or L_t) should grow in time. The latter is the more restrictive condition. Note that reaching velocity derivative skewness at levels around -0.5 is not always possible in LES as shown by Vreman et al. [121], even for high-order accurate methods as shown by Garnier et al. [25].

Figure A.2.5 shows the Reynolds number based on the (longitudinal) Taylor microscale and the (longitudinal) Taylor microscale. Normally three Taylor microscales (and thus Re_λ) can be defined based on each spatial direction. However, when the flow is isotropic these quantities should be the same yielding a single value appropriate to describe the flow. The (longitudinal) Taylor microscale is

defined (here) as:

$$L_\lambda = \lambda = \sqrt{\frac{15\nu u'^2}{\epsilon}} \tag{A.19}$$

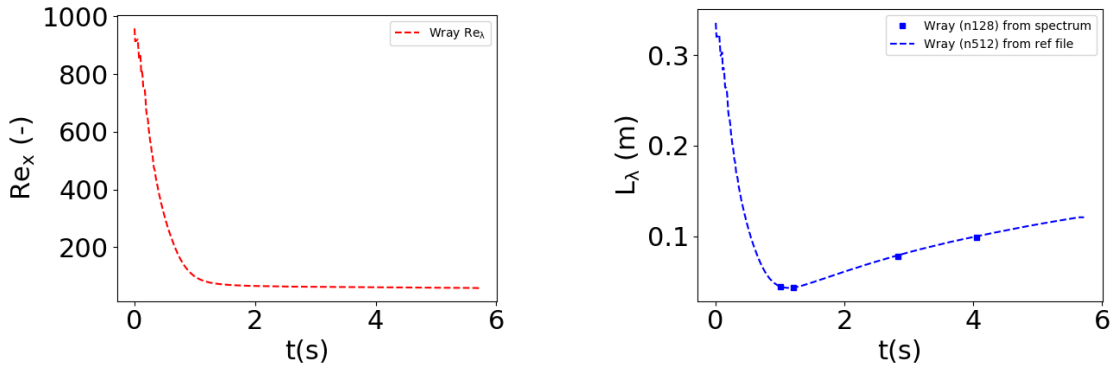

A.2.5 Taylor microscale Reynolds number and Taylor microscale for the DNS decay of Wray

Figure A.2.6 shows the temporal evolution of different turbulent length scales as well as the temporal evolution of large scale eddy turnover times. The dissipation length scale (L_ϵ) is computed in accordance with Equation A.18. The Kolmogorov length scale is estimated as follow

$$L_\eta = \left(\frac{\nu^3}{\epsilon}\right)^{\frac{1}{4}} \tag{A.20}$$

The time at which the first reference DNS spectrum is given, is also indicated. In terms of length scales, L_ϵ and L_t have the longest transients before increasing in time. The latter observation demonstrates the point made by Larsson *et al.* [52] that it should be carefully monitored in order to assess fully developed turbulence. The second representation shows the (longitudinal) large eddy turnover times defined as

$$T_x = \frac{L_x}{u'} \tag{A.21}$$

The ratio TKE/ϵ is also shown and can be relied on to select a time step for CFD simulations. This ratio appears to be located between T_t (based on L_t) and T_ϵ (based on L_ϵ). At the start of the asymptotic turbulence state the values are close to each other.

Figure A.2.7 shows the ratio of the integral and dissipation length scale to the Kolmogorov length scale during the decay. This ratio can be found in many papers.

Finally, Figure A.2.8 shows ϵ (integrand in equation A.15 with constants) as a function of the wavenumber. Note that the wavenumbers are given in a logarithmic scale. The length scales are presented in a single color. The time evolution in linestyle goes as : full, dashed, dahsdot and dotted. The peak in dissipation at the earlier times appear around the cutoff wavenumber (on a 128^3 cells grid).

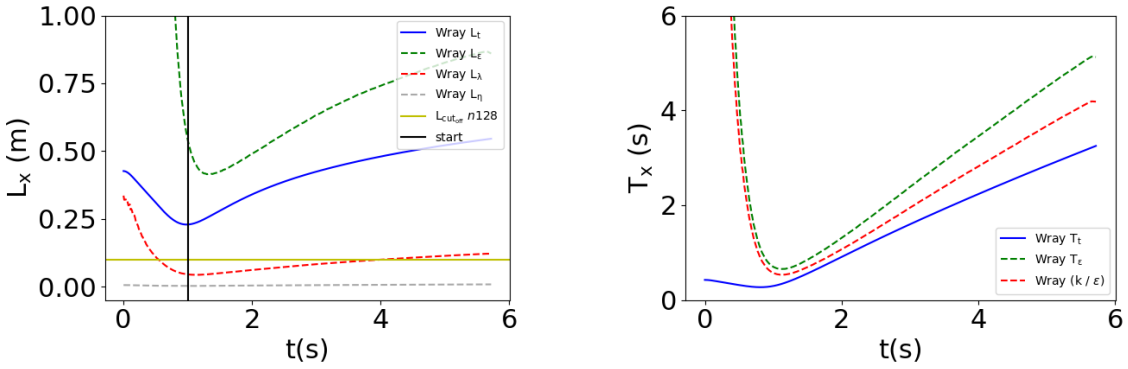

A.2.6 Turbulent length scales and eddy turnover time for the DNS decay of Wray

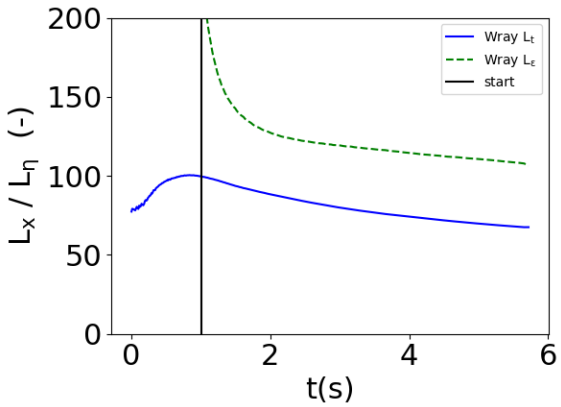

A.2.7 Ratio of turbulent length scale to Kolmogorov for the DNS decay of Wray.

As a general note: a more appropriate time x-axis selection for the different Figures would have been the non-dimensional ratio t/T_t (or another eddy turnover time).

A.2.1.3. Energy spectra

Figure A.2.9 shows the energy spectrum at different times in the decay with the indication of the different length scales, including the cut off with a given grid size (in this case 128^3 cells), $L_{cutoff} = 2\pi/(2\Delta)$ [14]. This grid size has proven to be sufficient for LES studies with second-order accurate spatial discretization schemes. Note that Jimenez reference data's grid size is much larger so that their cutoff is based on kmax = 241. The corresponding wavenumbers are simply obtained as $2\pi/L_x$. As time evolves, L_t and L_ϵ get slightly closer to each other. The Taylor based wavenumber equals the grid cutoff at the end of the decay. What the graph really show is that it's extremely difficult to get any of these length scales from a visual study of the spectrum.

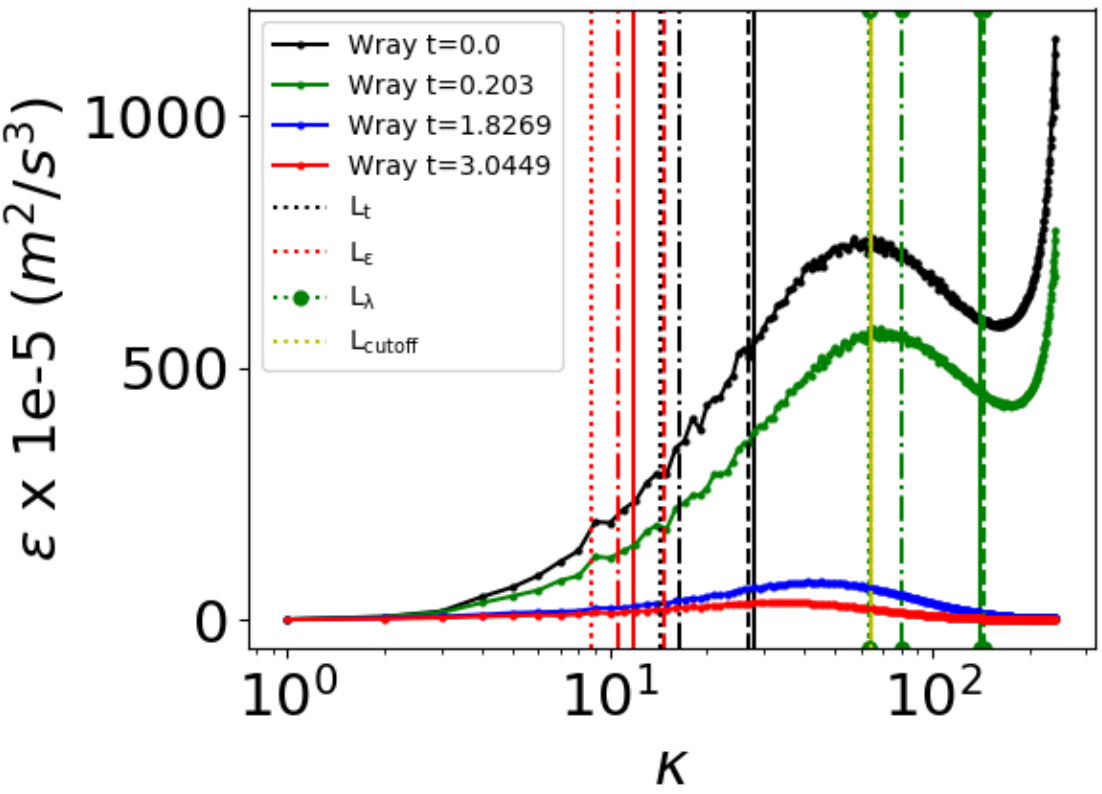

A.2.8 ϵ vs wavenumber at different time instants for the DNS decay of Wray.

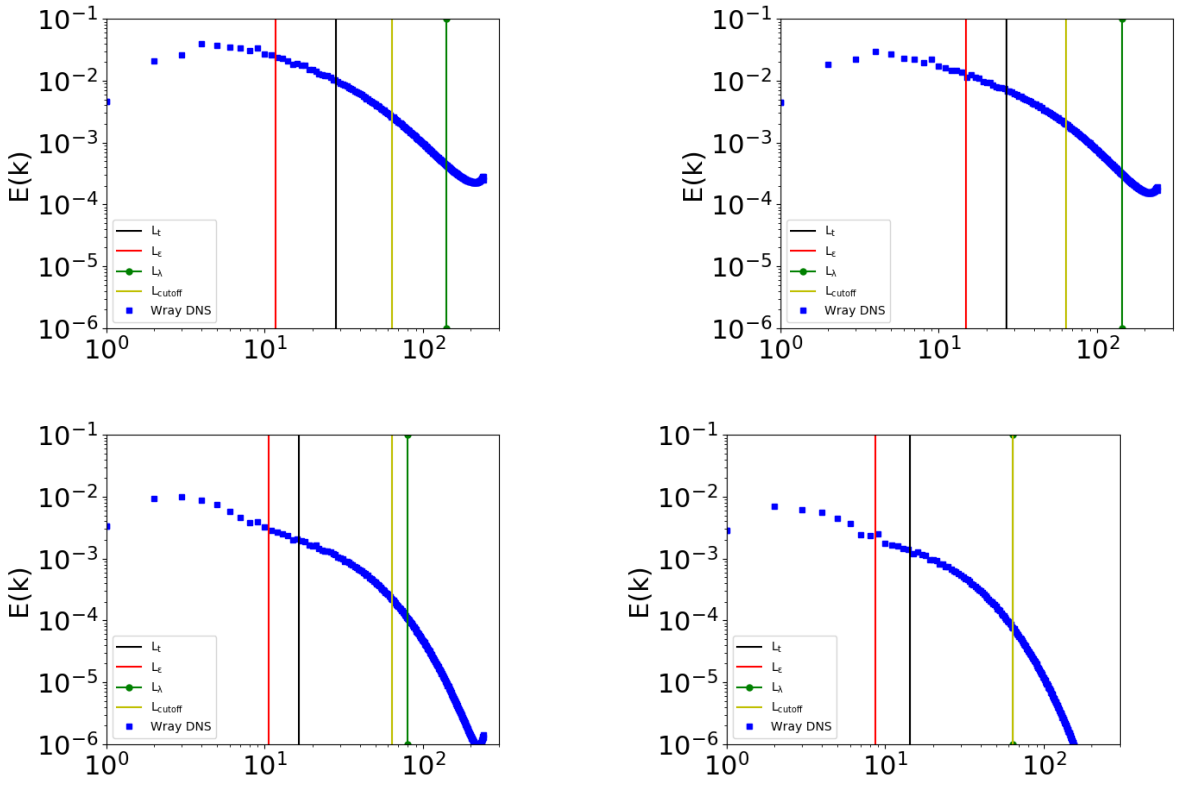

A.2.9 Turbulent length scales superimposed on the energy spectra at different times for the DNS decay of Wray

A.2.2. Wray LES with TAU

The Wray test case has also been studied with LES in TAU. In a first evaluation, simulations starting from an available DNS reference spectrum of Wray were performed (see A.2.2.1). In a second study, an initial field was constructed from which the decay was allowed to start (see A.2.2.2).

A.2.2.1. Starting from reference DNS

A spectrum of realistic turbulence is available and can be used to specify an initial velocity field corresponding to a $\mathrm{Re}_\lambda \approx 97$ and $\mathrm{M}_t \approx 0.0038$. A sharp cutoff filtering of the reference spectra to the desired grid size is applied. It was used in an LES simulation with the LD2 scheme on a $(2\pi)^3$ containing 128^3 cells and the resulting flow fields were kindly provided by Tim Horchler (AS-RFZ). Figure A.2.10 compares the LES (labelled LES n128 and referred to as LES128) with the available DNS energy spectra at different times. It shows a relatively good agreement. Figure A.2.11 looks at the evolution of the viscosity ratios (μ_t/μ) and indicates that a much finer grid would be required to reach DNS levels.

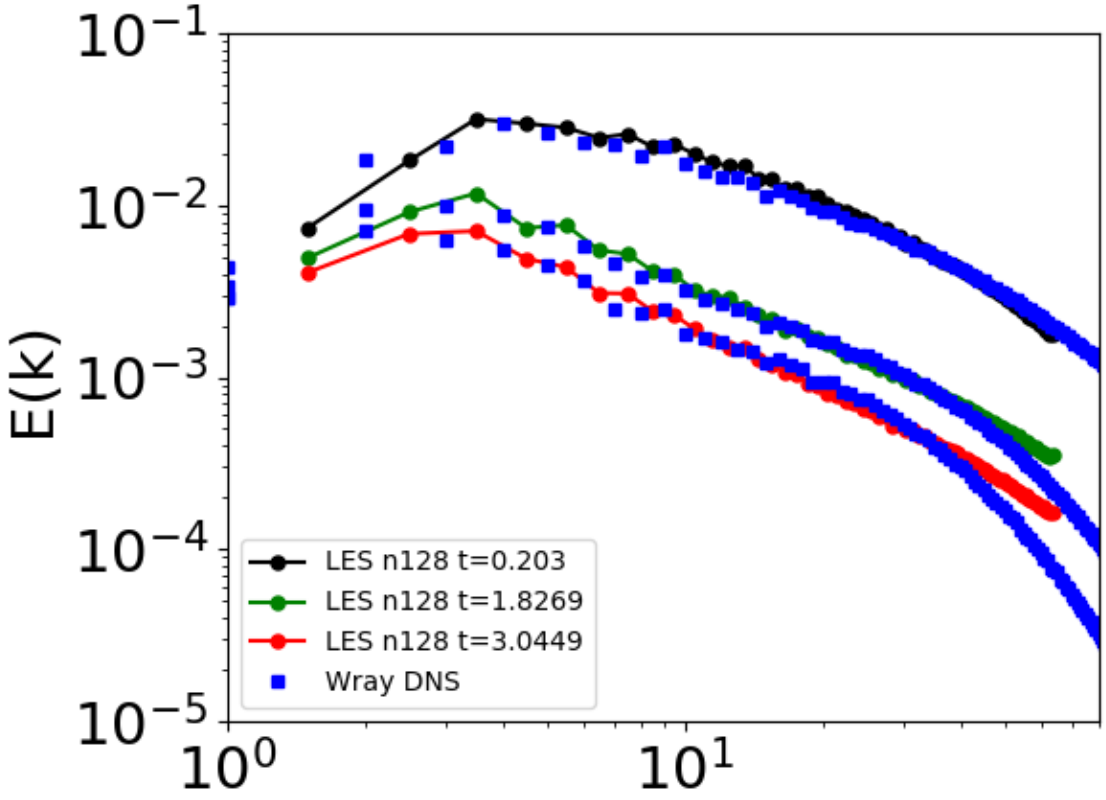

A.2.10 Energy spectra at different time steps obtained with LES128 and the LD2 central scheme for the decay of Wray.

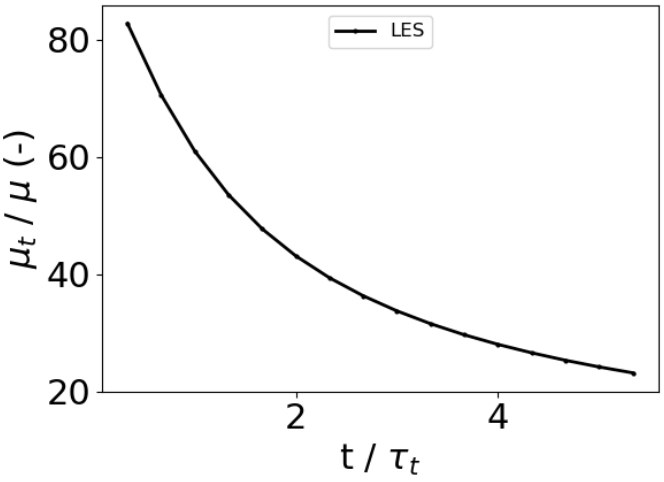

A.2.11 Ratio μ_t/μ obtained with LES128 and the LD2 central scheme for the decay of Wray. $\tau_t = 0.60897$

A.2.2.2. Starting from random initial field

Unlike in the majority of the STI studies in the literature, we cannot rely on DNS generated turbulence to send through a shock wave. Instead, LES has to be used to obtain our desired realistic turbulence which has firstly been tested on the DHIT of Wray.

The initial turbulence, of solenoidal (or vortical or divergence free) nature, is generated with a Gaussian spectrum (Equation 2-1) and peak wavenumber k_0=4 (see 2.2 for further details). The generation is performed with a generator provided by Johan Larsson from the University of Maryland. The DHIT is then run with LES128 for both the upwind scheme (AUSMDV) and the central scheme (LD2). Note that Thornber's low Mach number modification [114] has been enabled for the upwind scheme. It is a correction for compressible solvers which should render them able to appropriately resolve incompressible turbulence, which is presently the case given the very low M_t.

Figures A.2.12 to A.2.15 show the resulting spectra evolution during the decay. The evolution of the velocity derivative skewness ($S_{u_{,x}}$), a measure used to evaluate the development level of turbulence (see 2.2.2), is given in Figure A.2.16. It shows the difference between a high-resolution DNS and low-resolution LES: the second-order accurate LES fluctuates at higher levels than the DNS. Such observations regarding $S_{u_{,x}}$ were already made in the literature [121, 25]. It is explained by the fact that a quantity such as $S_{u_{,x}}$ is highly dependent on resolving the smallest scales (higher wavenumbers). It is difficult to assess from the LES128 whether the turbulence is realistic or not. The LES evolution indicate some initial transition ($t/\tau_t < 3$) but not a clear decrease as in the DNS. Nevertheless, the evolution show fluctuations around a fixed level.

Figure A.2.17 presents the spectra at different times as well as the initial DNS spectrum which was used in obtaining Figure A.2.10. At t/τ_t = 3.537, the overlap of the lower wavenumbers from LES matches best the DNS. The difference between a DNS and LES resolution is shown at the higher

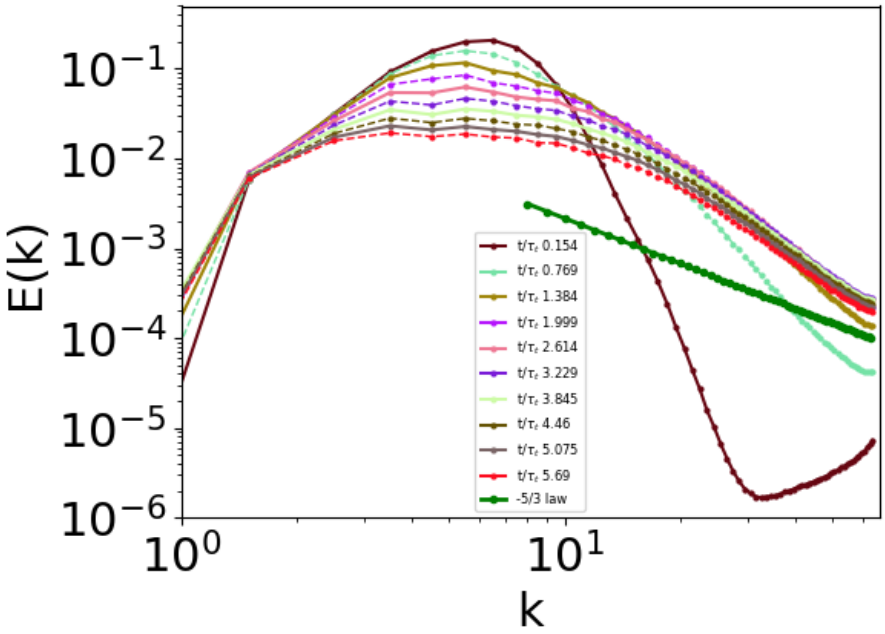

A.2.12 Evolution of E(k) for uwpind Wray LES128, τ_t = 0.33

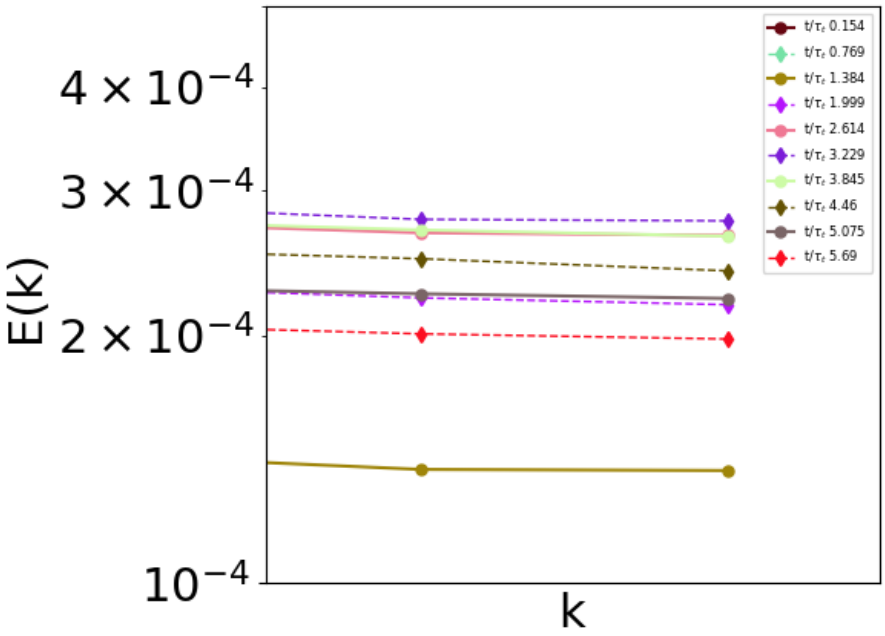

A.2.13 Evolution (tail) of E(k) for uwpind Wray LES128, τ_t = 0.33

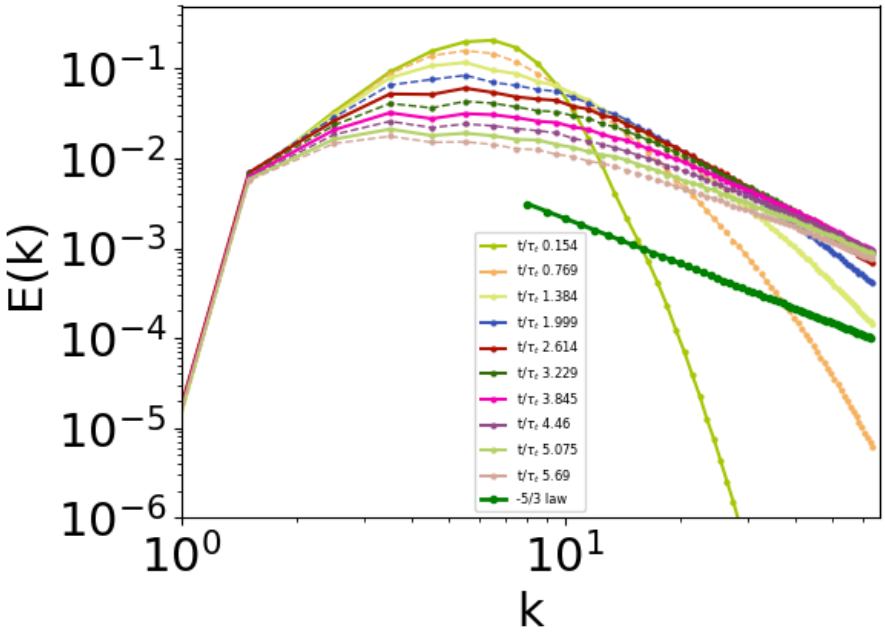

A.2.14 Evolution of E(k) for central Wray LES128, τ_t = 0.33

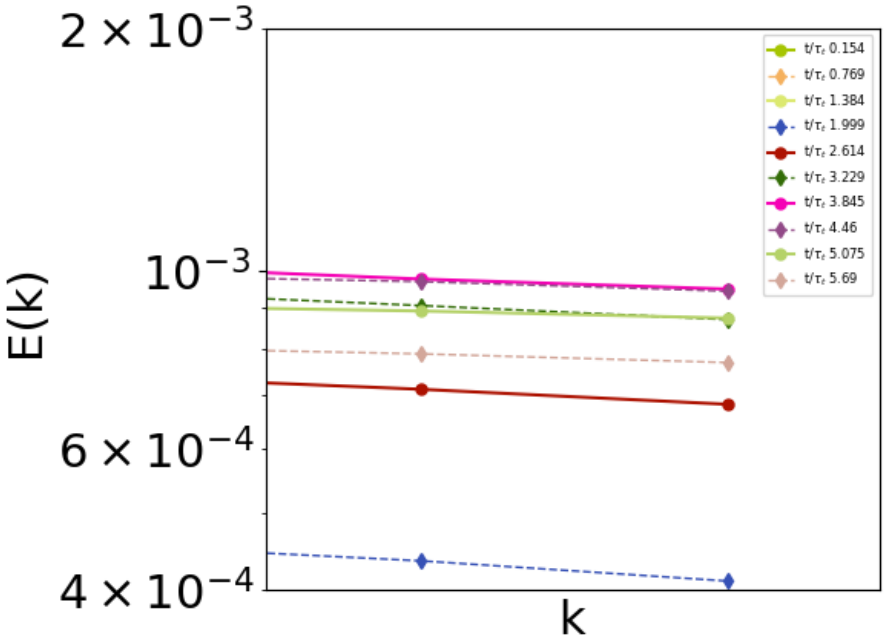

A.2.15 Evolution (tail) of E(k) for central Wray LES128, τ_t = 0.33

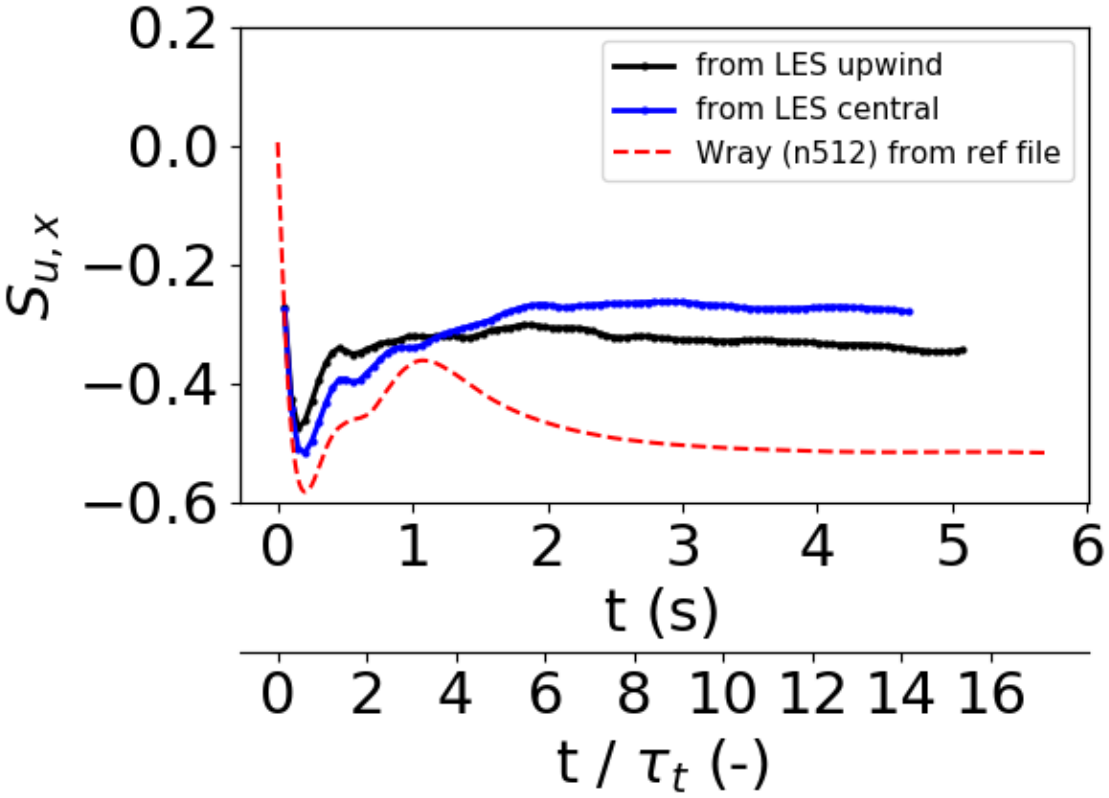

A.2.16 Evolution of the velocity derivative skewness ($S_{u,x}$) with LES started from the initial conditions, τ_t = 0.33

wavenumber range with increased dissipation of the LES128. This dissipation is even more pronounced for the upwind scheme than for the central scheme. In spite of this difference, the impact on the total TKE (or M_t) decay was minimal. This is expected given the major contribution from the lower wavenumber range on the latter quantity which is similarly predicted by both schemes.

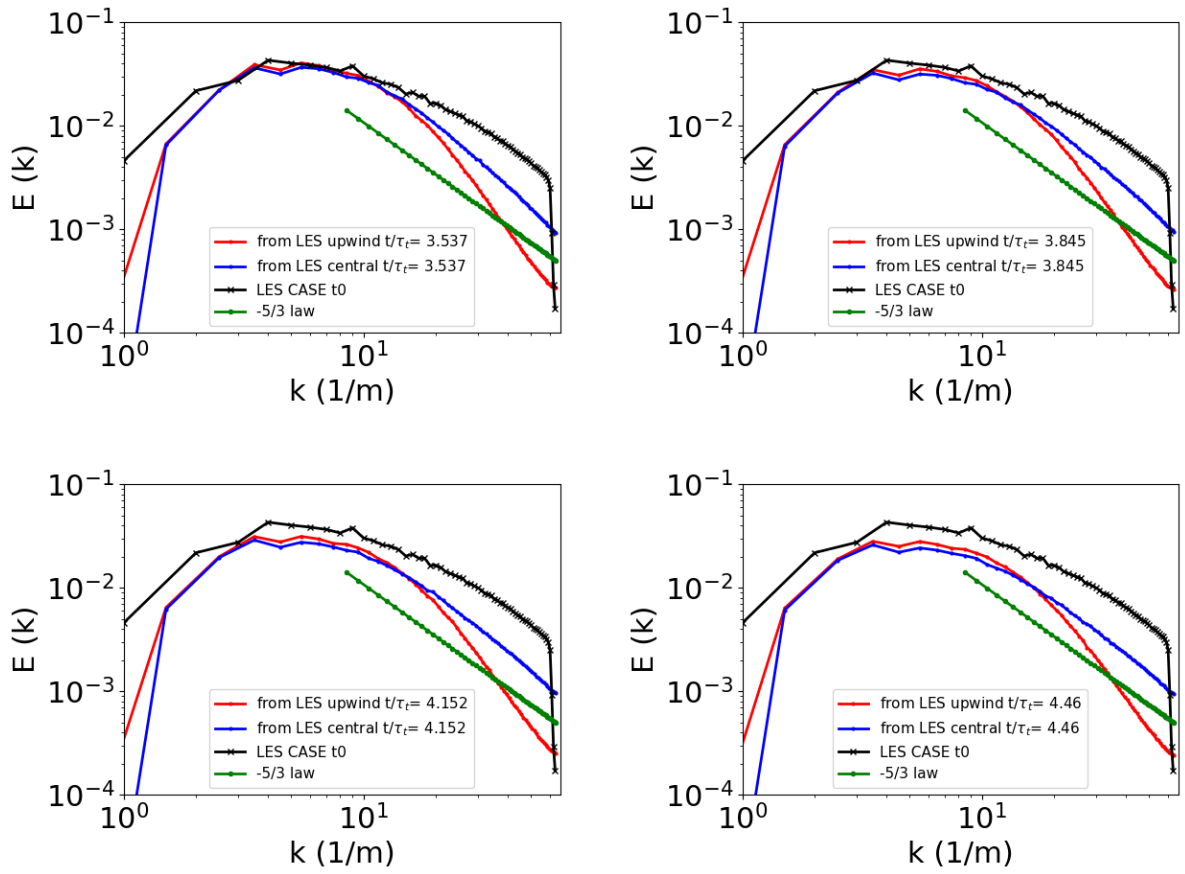

A.2.17 Energy spectrum from LES128 upwind and central at different times. τ_t = 0.33

B. Periodicity correction for the STG

In a first section (B.1) the parts of the STG that are required to understand the periodic correction are detailed. The implemented correction will then be discussed in B.2. A similar notation as in the different references will be adopted.

B.1. The STG formulation

The STG generates random fluctuations as defined in Equation B.1 [1] where q^n represents the normalized amplitude associated with wavenumber k^n sampled from the reference spectrum. The parameters $\mathbf{d}^n$, $\boldsymbol{\sigma}^n$, ϕ^n and s^n are random numbers sampled within given intervals and only defined once (see also [14] for more details on the first three as well as their visual representation). The latter parameter, s^n, is specific to Adamian and Travin's formulation [1, 22] and represents a non-dimensional frequency associated with the n-th mode. A divergence-free formulation is ensured by requiring the orthogonality between $\mathbf{d}^n$ and $\boldsymbol{\sigma}^n$. The periodicity correction entails modifications in the generation of the random numbers as is discussed in B.2.

$$\mathbf{v'}(\mathbf{r},t) = \sqrt{6}\sum_{n=1}^{N}\sqrt{q^n}\left[\boldsymbol{\sigma}^n cos\left(k^n\mathbf{d}^n.\,\mathbf{r}+\phi^n+s^n\frac{t}{\tau}\right)\right] \tag{B.1}$$

Note that the actual fluctuations synthetically introduced through source terms into the computational domain (STG zone of Figure 2-1) are not necessarily the same as given by Equation B.1 as the procedure is more involved and accounts for a mean value [22, 104, 1].

B.2. The periodicity correction

In a configuration with periodic boundaries, such as the STI setup (transverse directions), the periodicity would require the waves represented on a given grid to be consistent at these respective boundaries. An inconsistency in the STG formulation for such specific configurations was pointed out by Morsbach and Franke [78]. Subsequently, a methodology to resolve the above mentioned limitation has been devised by the latter authors and is the base of the present implementation.

In order to account for periodicity, all wavenumbers of a given target spectrum have to be wholly represented, without a sudden cut-off. In other words, an integer number of waves, associated with k^n, have to be represented. The waves with the smallest wavenumbers will be the limiting factor. Hence, this requirement translates into [78]:

$$k^n d_i^n L_i = 2\pi m_i^n, \qquad i \in [y,z] \tag{B.2}$$

where m_i^n is an integer number and the index "i" represents the periodic directions (y and z in the present case). The term on the LHS of Equation B.2 is the spatial term of the cosine in the synthetic

fluctuation definition (Equation B.1) for r = $L_{y/z}$. To achieve this we will redefine the random unit vectors $\mathbf{d}^n$ as follow.

For each wavenumber, k^n

1. Find $d^n_{y,new}$ so as to satisfy Equation B.2, i.e. find m^n_y. We do this by relying on the original random numbers which we will name $d^n_{y,old}$. We get

$$m^n_y = \frac{k^n d^n_{y,old} L_y}{2\pi} \tag{B.3}$$

   The result is cut-off to represent an integer for which $d^n_{y,new} < d^n_{y,old}$. Therefore the condition stated in Morsbach et al. [78], i.e. $d^n_{y,new} < 1$, will be satisfied.
2. Find $d^n_{z,new}$ so that Equation B.2 is satisfied, i.e. find m^n_z. We use exactly the same method as in the above step.
3. Recompute $d^n_{x,new} = \sqrt{1 - \left[(d^n_{y,new})^2 + (d^n_{z,new})^2\right]}$.
4. Ensure that $\mathbf{d}^n_{new} \perp \boldsymbol{\sigma}^n$ so that the divergence-free characteristic is retrieved. We achieved this by relying on the original random values $\boldsymbol{\sigma}^n_{old}$ with the following decomposition:

$$\boldsymbol{\sigma}^n_{new} = \boldsymbol{\sigma}^n_{old} - (\boldsymbol{\sigma}^n_{old} \cdot \mathbf{d}^n)\, \mathbf{d}^n \tag{B.4}$$

Note that the above steps differs slighlty from the original procedure of Morsbach and Franke [78]. Specifically, the notation of the third step, and more importantly the addition of a fourth step which ensures the divergence-free character of our turbulence and should be essential.

The above method has been applied in the generation of synthetic turbulence with a script following Davidson et al.'s strategy [14]. Reference conditions targeted the reproduction of the Mach 1.05 pre-shock state of Larsson et al. [52]. More specifically, the spectrum represents a more energetic state which could be found at an upstream location following the free decay equations (see also 2.1.2). This state has Re_λ=42 and M_t = 0.156. As adviced by Davidson et al. [14], 150 modes were selected. The domain size is assumed to be $2\pi L_\epsilon$ discretised with 64 cells (65 points) and with L_ϵ= 1.09e-4 m.

Figure B.2.1 shows the distribution of the random numbers ($\boldsymbol{\sigma}^n$ and $\mathbf{d}^n$) before and after correction. No apparent difference can be seen in these graphs. However, when plotting the Probability Density Function (PDF) of each component of $\mathbf{d}^n$, significant changes are observed as illustrated by Figure B.2.2. In order to enable direct comparison with [78], 21 bins are selected to generate the PDF. The expected probability should lie at 0.5 [78], which can be seen in the original formulation as well as in the periodic correction for most of the values, except in the vicinity of 0.0. The distribution is similar to Morsbach et al. [78], confirming the correct implementation of the approach. What happens around 0.0 is directly influenced by the smaller wavenumbers as mentioned by Morsbach et al. [78] and can be understood as follow. Equation B.3 yields for these specific conditions at

wavenumber 0 (we omit the subscript old)

$$\begin{aligned} m_y^0 &= \frac{k^0 d_y^0 2\pi L_\epsilon}{2\pi} \\ &< \frac{d_y^0 2\pi L_\epsilon}{L_\epsilon 2\pi} < 1 \\ &= 0 \end{aligned} \tag{B.5}$$

Where we used the fact that in Davidson et al. [14], $k^0 < 1/L_\epsilon$, that $\mathbf{d}_y^0$ is a unit vector, and that the integer rendering (cut-off) of d_y^0 will become zero . The above will be the case for the first few wavenumbers (the more modes we use, the more it occurs), and can as well occur at other random occasions in the original random number generation process.

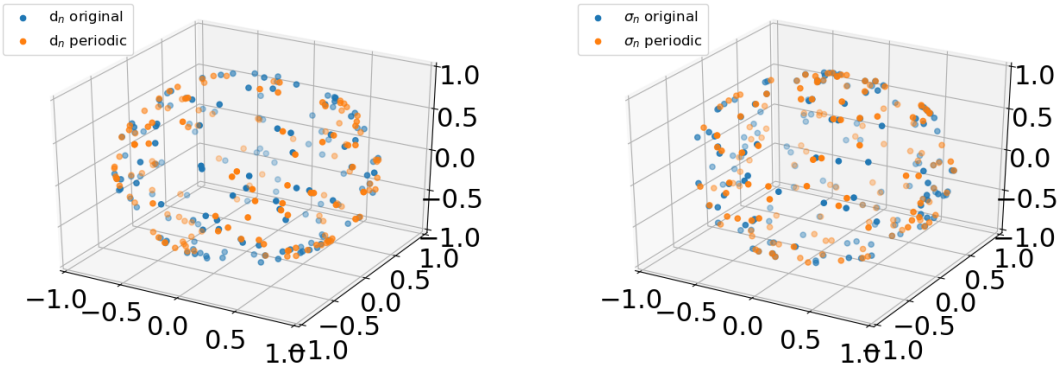

B.2.1 Distribution of $\mathbf{d}^n$ and $\boldsymbol{\sigma}^n$ before and after periodic correction.

B.2.1. Final comments on the periodic correction

In an unsteady simulation relying on the STG, $\mathbf{d}^n$ should be changed at every STG step because the wavenumber range (k^n) is based on quantities at reference locations in the upstream RANS region which will change over time. This could have repercussions on the temporal correlation. However, Morsbach et al. [78] demonstrated only small changes in two-point correlations at two downstream locations. The use of STG in the canonical STI setup would result in a steady RANS zone. Therefore, the potential aforementioned periodic correction related issue is not relevant and a single change of $\mathbf{d}^n$ would suffice.

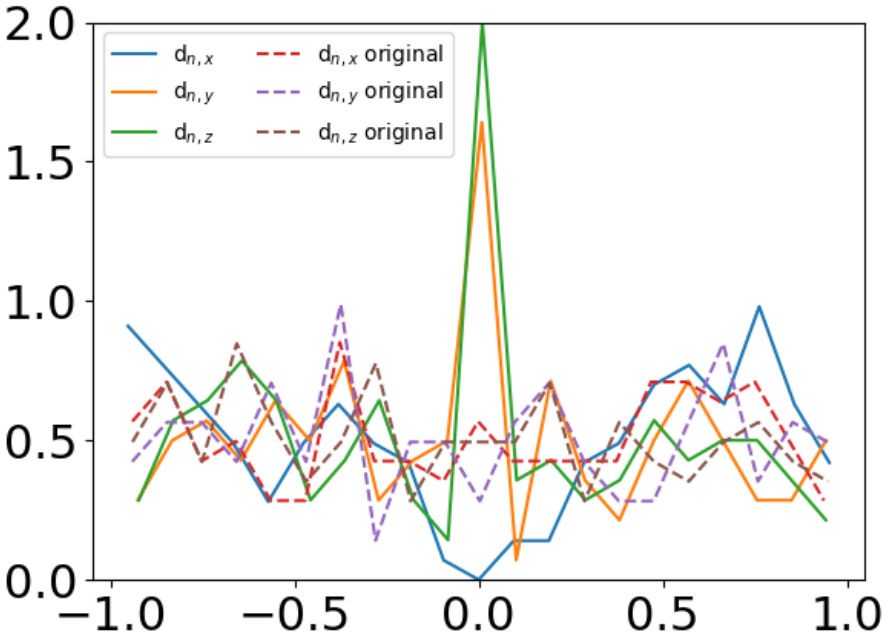

B.2.2 PDF of $\mathbf{d}^n$ before and after periodic correction, nbins = 21.

Register of illustrations

List of tables

Bibliography

[1] D Adamian and A Travin. An efficient generator of synthetic turbulence at rans–les interface in embedded les of wall-bounded and free shear flows. In *Computational Fluid Dynamics 2010*, pages 739–744. Springer, 2011.

[2] DA Anderson, JC Tannehill, and RH Pletcher. *Computational Fluid Mechanics and Heat Transfer.Computational Methods in Mechanics and Termal Sciences.* Mc Graw-Hill, 1984.

[3] I Bermejo-Moreno. Subgrid-scale modeling of shock-turbulence interaction for large-eddy simulations. *Annu. Res. Briefs, Center for Turbulence Research*, pages 247–259, 2009.

[4] I Bermejo-Moreno, J Bodart, J Larsson, BM Barney, JW Nichols, and S Jones. Solving the compressible navier-stokes equations on up to 1.97 million cores and 4.1 trillion grid points. In *SC'13: Proceedings of the International Conference on High Performance Computing, Networking, Storage and Analysis*, pages 1–10. IEEE, 2013.

[5] I Bermejo-Moreno, J Larsson, and SK Lele. Les of canonical shock-turbulence interaction. *Annual Research Briefs*, pages 209–222, 2010.

[6] R Boukharfane, Z Bouali, and A Mura. Evolution of scalar and velocity dynamics in planar shock-turbulence interaction. *Shock Waves*, 28(6):1117–1141, 2018.

[7] NO Braun. *An LES and RANS Study of the Canonical Shock-Turbulence Interaction*. PhD thesis, California Institute of Technology, 2018.

[8] NO Braun, DI Pullin, and Daniel I Meiron. Regularization method for large eddy simulations of shock-turbulence interactions. *Journal of Computational Physics*, 361:231–246, 2018.

[9] NO Braun, DI Pullin, and DI Meiron. Large eddy simulation investigation of the canonical shock–turbulence interaction. *Journal of Fluid Mechanics*, 858:500–535, 2019.

[10] CH Chen and DA Donzis. Shock–turbulence interactions at high turbulence intensities. *Journal of Fluid Mechanics*, 870:813–847, 2019.

[11] G Comte-Bellot and S Corrsin. Simple eulerian time correlation of full-and narrow-band velocity signals in grid-generated, isotropic turbulence. *Journal of Fluid Mechanics*, 48(2):273–337, 1971.

[12] M Crespo. *Etude de l'Interaction entre une Onde de Choc et une Turbulence Cisaillée en Presence de Gradients Moyens de Temperature et de Masse Volumique*. PhD thesis, Institut National Polytechnique de Toulouse, 2009.

[13] M Crespo. *Etude de l'Interaction entre une Onde de Choc et une Turbulence Cisaillée en Presence de Gradients Moyens de Temperature et de Masse Volumique: Annexes*. PhD thesis, Institut National Polytechnique de Toulouse, 2009.

[14] L Davidson and M Billson. Hybrid les-rans using synthesized turbulent fluctuations for forcing in the interface region. *International journal of heat and fluid flow*, 27(6):1028–1042, 2006.

[15] PE Dimotakis. The mixing transition in turbulent flows. *Journal of Fluid Mechanics*, 409:69–98, 2000.

[16] D Donzis. Similarity scaling in shock-turbulence interactions. In *APS Division of Fluid Dynamics Meeting Abstracts*, 2010.

[17] D Donzis. Amplification factors in shock-turbulence interactions: Effect of shock thickness. *Physics of Fluids*, 24(1):011705, 2012.

[18] DA Donzis. Shock structure in shock-turbulence interactions. *Physics of Fluids*, 24(12):126101, 2012.

[19] T Dubois, JA Domaradzki, and A Honein. The subgrid-scale estimation model applied to large eddy simulations of compressible turbulence. *Physics of Fluids*, 14(5):1781–1801, 2002.

[20] F Ducros, V Ferrand, F Nicoud, C Weber, D Darracq, C Gacherieu, and T Poinsot. Large-eddy simulation of the shock/turbulence interaction. *Journal of Computational Physics*, 152(2):517–549, 1999.

[21] G Erlebacher, MY Hussaini, HO Kreiss, and S Sarkar. The analysis and simulation of compressible turbulence. *Theoretical and Computational Fluid Dynamics*, 2(2):73–95, 1990.

[22] DG Francois, R Radespiel, S Reuß, and A Probst. Computations of separated flows with a hybrid rans/les approach. In *Advances in Simulation of Wing and Nacelle Stall*, pages 23–39. Springer, 2016.

[23] X Gao, I Bermejo-Moreno, and J Larsson. Parametric numerical study of passive scalar mixing in shock turbulence interaction. *Journal of Fluid Mechanics*, 895, 2020.

[24] X Gao, I Bermejo-Moreno, J Larsson, L Fu, and SK Lele. Scalar mixing under shock/turbulence interaction: Dns, statistical and geometric analyses. *Proceedings of the 2018 Summer Program*, page 165, 2018.

[25] E Garnier, P Sagaut, and M Deville. Large eddy simulation of shock/homogeneous turbulence interaction. *Computers & fluids*, 31(2):245–268, 2002.

[26] RM Gehre. *The flow physics of inlet-fueled, low-compression scramjets*. PhD thesis, The University of Queensland, 2015.

[27] F Génin and S Menon. Studies of shock/turbulent shear layer interaction using large-eddy simulation. *Computers & Fluids*, 39(5):800–819, 2010.

[28] FM Genin. *Study of compressible turbulent flows in supersonic environment by large-eddy simulation*. PhD thesis, Georgia Institute of Technology, 2009.

[29] N. Gibbons. *Simulation and dynamics of hypersonic turbulent combustion*. PhD thesis, PhD Thesis, The University of Queensland, Australia.

[30] N Grube, E Taylor, and P Martin. Direct numerical simulation of shock-wave/isotropic turbulence interaction. In *39th AIAA Fluid Dynamics Conference*, page 4165, 2009.

[31] N Grube, E Taylor, and P Martin. Numerical investigation of shock-wave/isotropic turbulence interaction. In *49th AIAA Aerospace Sciences Meeting including the New Horizons Forum and Aerospace Exposition*, page 480, 2011.

[32] R Hannappel and R Friedrich. Interaction of isotropic turbulence with a normal shock wave. *Applied Scientific Research*, 51(1-2):507–512, 1993.

[33] R Hannappel and R Friedrich. DNS of a M= 2 shock interacting with isotropic turbulence. In *Direct and Large-Eddy Simulation I*, pages 359–373. Springer, 1994.

[34] R Hannappel and R Friedrich. Direct numerical simulation of a mach 2 shock interacting with isotropic turbulence. *Applied scientific research*, 54(3):205–221, 1995.

[35] S Hickel, CP Egerer, and J Larsson. Subgrid-scale modeling for implicit large eddy simulation of compressible flows and shock-turbulence interaction. *Physics of Fluids*, 26(10):106101, 2014.

[36] T Horchler, J Armbruster, Wand Hardi, S Karl, K Hannemann, A Gernoth, and M De Rosa. Modeling combustion chamber acoustics using the dlr tau code. In *Space Propulsion 2018*, 2018.

[37] T Horchler, K Oßwald, V Hannemann, and K Hannemann. Hybrid rans-les study of transonic flow in the wake of a generic space launch vehicle. In *Symposium on Hybrid RANS-LES Methods*, pages 291–300. Springer, 2016.

[38] SH Huang, QS Li, and JR Wu. A general inflow turbulence generator for large eddy simulation. *Journal of Wind Engineering and Industrial Aerodynamics*, 98(10-11):600–617, 2010.

[39] A Jameson. Time dependent calculations using multigrid, with applications to unsteady flows past airfoils and wings. In *10th Computational Fluid Dynamics Conference*, page 1596, 1991.

[40] A Jameson, W Schmidt, and E Turkel. Numerical solution of the euler equations by finite volume methods using runge kutta time stepping schemes. In *14th fluid and plasma dynamics conference*, page 1259, 1981.

[41] S Jamme, J-B Cazalbou, F Torres, and P Chassaing. Direct numerical simulation of the interaction between a shock wave and various types of isotropic turbulence. *Flow, Turbulence and Combustion*, 68(3):227–268, 2002.

[42] S Jamme, M Crespo, and P Chassaing. Direct numerical simulation of the interaction between a shock wave and anisotropic turbulence. In *35th AIAA Fluid Dynamics Conference and Exhibit*, page 4886, 2005.

[43] N Jarrin, S Benhamadouche, D Laurence, and R Prosser. A synthetic-eddy-method for generating inflow conditions for large-eddy simulations. *International Journal of Heat and Fluid Flow*, 27(4):585–593, 2006.

[44] J. et al. Jimenez. A selection of test cases for the validation of large-eddy simulations of turbulent flows. Technical report.

[45] S Karl. *Numerical investigation of a generic scramjet configuration*. PhD thesis, Saechsische Landesbibliothek-Staats-und Universitaetsbibliothek Dresden, 2011.

[46] S Karl, JP Hickey, and F Lacombe. Reynolds stress models for shock-turbulence interaction. In *International Symposium on Shock Waves*, pages 511–517. Springer, 2017.

[47] T Knopp, X Zhang, R Kessler, and G Lube. Enhancement of an industrial finite-volume code for large-eddy-type simulation of incompressible high reynolds number flow using near-wall modelling. *Computer methods in applied mechanics and engineering*, 199(13-16):890–902, 2010.

[48] JC Kok. A high-order low-dispersion symmetry-preserving finite-volume method for compressible flow on curvilinear grids. *Journal of Computational Physics*, 228(18):6811–6832, 2009.

[49] LSG Kovasznay. Turbulence in supersonic flow. *Journal of the Aeronautical Sciences*, 20(10):657–674, 1953.

[50] F Lacombe, S Roy, K Sinha, S Karl, and JP Hickey. Characteristic scales in shock–turbulence interaction. *AIAA Journal*, 59(2):526–532, 2021.

[51] J Larsson. Blending technique for compressible inflow turbulence: algorithm localization and accuracy assessment. *Journal of computational physics (Print)*, 228(4):933–937, 2009.

[52] J Larsson, I Bermejo-Moreno, and SK Lele. Reynolds-and mach-number effects in canonical shock–turbulence interaction. *Journal of Fluid Mechanics*, 717:293–321, 2013.

[53] J Larsson and SK Lele. Direct numerical simulation of canonical shock/turbulence interaction. *Physics of fluids*, 21(12):126101, 2009.

[54] S Lee. Large eddy simulation of shock turbulence interaction. 1993.

[55] S Lee, S Lele, and P Moin. Direct numerical simulation and analysis of shock turbulence interaction. In *29th Aerospace Sciences Meeting*, page 523, 1991.

[56] S Lee, S Lele, and P Moin. Interaction of isotropic turbulence with a strong shock wave. In *32nd Aerospace Sciences Meeting and Exhibit*, page 311, 1994.

[57] S Lee, SK Lele, and P Moin. Eddy shocklets in decaying compressible turbulence. *Physics of Fluids A: Fluid Dynamics*, 3(4):657–664, 1991.

[58] S Lee, SK Lele, and P Moin. Simulation of spatially evolving turbulence and the applicability of taylor‚Äôs hypothesis in compressible flow. *Physics of Fluids A: Fluid Dynamics*, 4(7):1521–1530, 1992.

[59] S Lee, SK Lele, and P Moin. Direct numerical simulation of isotropic turbulence interacting with a weak shock wave. *Journal of Fluid Mechanics*, 251:533–562, 1993.

[60] S Lee, SK Lele, and P Moin. Interaction of isotropic turbulence with shock waves: effect of shock strength. *Journal of Fluid Mechanics*, 340:225–247, 1997.

[61] S Lee, P Moin, and SK Lele. Interaction of isotropic turbulence with a shock wave. Technical report, STANFORD UNIV CA DEPT OF MECHANICAL ENGINEERING, 1992.

[62] SK Lele. Shock-jump relations in a turbulent flow. *Physics of Fluids A: Fluid Dynamics*, 4(12):2900–2905, 1992.

[63] SK Lele and J Larsson. Shock-turbulence interaction: what we know and what we can learn from peta-scale simulations. In *Journal of Physics: Conference Series*, volume 180, page 012032. IOP Publishing, 2009.

[64] Douglas Keith Lilly. On the application of the eddy viscosity concept in the inertial sub-range of turbulence. *NCAR manuscript*, 123, 1966.

[65] M-S Liou. Ten years in the making - AUSM-family. *AIAA Paper*, pages 2001–2521, 2001.

[66] D Livescu. Turbulence with large thermal and compositional density variations. *Annual Review of Fluid Mechanics*, 52:309–341, 2020.

[67] D Livescu and Z Li. Subgrid-scale backscatter after the shock-turbulence interaction. In *AIP Conference Proceedings*, volume 1793, page 150009. AIP Publishing LLC, 2017.

[68] D Livescu and J Ryu. Vorticity dynamics after the shock–turbulence interaction. *Shock Waves*, 26(3):241–251, 2016.

[69] R Lopes, L Eça, and G Vaz. On the decay of free-stream turbulence predicted by two-equation eddy-viscosity models. In *20th Numerical Towing Tank Symposium*, pages 133–138, 2017.

[70] J Löwe, A Probst, T Knopp, and R Kessler. Low-dissipation low-dispersion second-order scheme for unstructured finite volume flow solvers. *AIAA Journal*, 54(10):2961–2971, 2016.

[71] K Mahesh, S Lee, SK Lele, and P Moin. The interaction of an isotropic field of acoustic waves with a shock wave. *Journal of Fluid Mechanics*, 300:383–407, 1995.

[72] K Mahesh, SK Lele, and P Moin. The influence of entropy fluctuations on the interaction of turbulence with a shock wave. *Journal of Fluid Mechanics*, 334:353–379, 1997.

[73] FR Menter. Two-equation eddy-viscosity turbulence models for engineering applications. *AIAA journal*, 32(8):1598–1605, 1994.

[74] FR Menter, M Kuntz, and R Langtry. Ten years of industrial experience with the sst turbulence model. *Turbulence, heat and mass transfer*, 4(1):625–632, 2003.

[75] P Moin and K Mahesh. Direct numerical simulation: a tool in turbulence research. *Annual review of fluid mechanics*, 30(1):539–578, 1998.

[76] P Moin, K Squires, W Cabot, and S Lee. A dynamic subgrid-scale model for compressible turbulence and scalar transport. *Physics of Fluids A: Fluid Dynamics*, 3(11):2746–2757, 1991.

[77] FK Moore. *Unsteady oblique interaction of a shock wave with a plane disturbance*, volume 1165. National Advisory Committee for Aeronautics, 1953.

[78] C Morsbach and M Franke. Analysis of a synthetic turbulence generation method for periodic configurations. In *Direct and Large-Eddy Simulation XI*, pages 169–174. Springer, 2019.

[79] MR Overholt and SB Pope. A deterministic forcing scheme for direct numerical simulations of turbulence. *Computers & Fluids*, 27(1):11–28, 1998.

[80] T Passot and A Pouquet. Numerical simulation of compressible homogeneous flows in the turbulent regime. *Journal of Fluid Mechanics*, 181:441–466, 1987.

[81] S Pirozzoli and F Grasso. Direct numerical simulations of isotropic compressible turbulence: influence of compressibility on dynamics and structures. *Physics of Fluids*, 16(12):4386–4407, 2004.

[82] TJ Poinsot and SK Lele. Boundary conditions for direct simulations of compressible viscous flows. *Journal of computational physics*, 101(1):104–129, 1992.

[83] SB Pope. *Turbulent Flows*. Cambridge University Press, 2000.

[84] A Probst. Implementation and assessment of the synthetic-eddy method in an unstructured compressible flow solver. In *Symposium on Hybrid RANS-LES Methods*, pages 91–101. Springer, 2016.

[85] A Probst, J Löwe, S Reuß, T Knopp, and R Kessler. Scale-resolving simulations with a low-dissipation low-dispersion second-order scheme for unstructured flow solvers. *AIAA Journal*, 54(10):2972–2987, 2016.

[86] R Quadros and K Sinha. Modelling of turbulent energy flux in canonical shock-turbulence interaction. *International Journal of Heat and Fluid Flow*, 61:626–635, 2016.

[87] R Quadros, K Sinha, and J Larsson. Turbulent energy flux generated by shock/homogeneous-turbulence interaction. *J. Fluid Mech*, 796:113–157, 2016.

[88] P Rawat and X Zhong. Numerical simulation of shock-turbulence interactions using high-order shock-fitting algorithms. In *48th AIAA Aerospace Sciences Meeting Including the New Horizons Forum and Aerospace Exposition*, page 114, 2010.

[89] P Rawat and X Zhong. Direct numerical simulations of turbulent flow interactions with strong shocks using shock-fitting method. In *49th AIAA Aerospace Sciences Meeting including the New Horizons Forum and Aerospace Exposition*, page 649, 2011.

[90] Reuß, T Knopp, A Probst, and M Orlt. Assessment of local les-resolution sensors for hybrid rans/les simulations. In *Progress in Hybrid RANS-LES Modelling*, pages 93–103. Springer, 2015.

[91] HS Ribner. Convection of a pattern of vorticity through a shock wave. 1954.

[92] HS Ribner. Shock-turbulence interaction and the generation of noise. Technical report, NASA Lewis, Cleveland, OH, 1955.

[93] JR Ristorcelli and GA Blaisdell. Consistent initial conditions for the dns of compressible turbulence. *Physics of Fluids*, 9(1):4–6, 1997.

[94] S Roy, U Pathak, and K Sinha. Variable turbulent prandtl number model for shock/boundary-layer interaction. *AIAA Journal*, 56(1):342–355, 2018.

[95] S Roy and K Sinha. Turbulent heat flux model for hypersonic shock–boundary layer interaction. *AIAA Journal*, 57(8):3624–3629, 2019.

[96] C.L. Rumsey. Compressibility Considerations for k-ω Turbulence Models in Hypersonic Boundary-Layer Applications. *Journal of Spacecraft and Rockets*, 47(1):11–20, 2010.

[97] J Ryu and D Livescu. Turbulence structure behind the shock in canonical shock–vortical turbulence interaction. *Journal of Fluid Mechanics*, 756, 2014.

[98] J Sesterhenn, JF Dohogne, and R Friedrich. Direct numerical simulation of the interaction of isotropic turbulence with a shock wave using shock-fitting. *Comptes Rendus Mécanique*, 333(1):87–94, 2005.

[99] YPM Sethuraman. *Analysis and modeling of thermodynamic fluctuations in canonical shock-turbulence interaction*. PhD thesis, Indian Institute of Technology Bombay, 2019.

[100] YPM Sethuraman and K Sinha. Effect of turbulent mach number on the thermodynamic fluctuations in canonical shock-turbulence interaction. *Computers & Fluids*, 197:104354, 2020.

[101] YPM Sethuraman and K Sinha. Modeling of thermodynamic fluctuations in canonical shock–turbulence interaction. *AIAA Journal*, 58(7):3076–3089, 2020.

[102] YPM Sethuraman, K Sinha, and J Larsson. Thermodynamic fluctuations in canonical shock–turbulence interaction: effect of shock strength. *Theoretical and Computational Fluid Dynamics*, 32(5):629–654, 2018.

[103] FS Sherman. A low-density wind-tunnel study op shock-wave structure and relaxation phenomena in gases. NASA TN-3298, University of California, 1955.

[104] ML Shur, PR Spalart, MK Strelets, and AK Travin. Synthetic turbulence generators for rans-les interfaces in zonal simulations of aerodynamic and aeroacoustic problems. *Flow, turbulence and combustion*, 93(1):63–92, 2014.

[105] ML Shur, M Strelets, A Travin, A Probst, S Probst, D Schwamborn, S Deck, A Skillen, J Holgate, and A Revell. Improved embedded approaches. In *Go4Hybrid: Grey Area Mitigation for Hybrid RANS-LES Methods*, pages 51–87. Springer, 2018.

[106] K Sinha. Evolution of enstrophy in shock/homogeneous turbulence interaction. *Journal of fluid mechanics*, 707:74, 2012.

[107] J Smagorinsky. General circulation experiments with the primitive equations: I. the basic experiment. *Monthly weather review*, 91(3):99–164, 1963.

[108] PR Spalart. Young-person's guide to detached-eddy simulation grids. NASA CR-2001–211032, Beoing Commercial Airplanes, Seattle, Washington, 2001.

[109] PR Spalart and CL Rumsey. Effective inflow conditions for turbulence models in aerodynamic calculations. *AIAA journal*, 45(10):2544–2553, 2007.

[110] S Tavoularis, JC Bennett, and S Corrsin. Velocity-derivative skewness in small reynolds number, nearly isotropic turbulence. *Journal of Fluid Mechanics*, 88(1):63–69, 1978.

[111] GI Taylor. The spectrum of turbulence. *Proceedings of the Royal Society of London. Series A-Mathematical and Physical Sciences*, 164(919):476–490, 1938.

[112] KW Thompson. Time dependent boundary conditions for hyperbolic systems. *Journal of computational physics*, 68(1):1–24, 1987.

[113] B Thornber and D Drikakis. Large-eddy simulation of isotropic homogeneous decaying turbulence. In *ECCOMAS CFD, TU Delft, The Netherlands*, 2006.

[114] B Thornber, A Mosedale, D Drikakis, D Youngs, and RJR Williams. An improved reconstruction method for compressible flows with low mach number features. *Journal of computational Physics*, 227(10):4873–4894, 2008.

[115] Y Tian, F Jaberi, D Livescu, and Z Li. Numerical simulation of multi-fluid shock-turbulence interaction. In *AIP Conference Proceedings*, volume 1793, page 150010. AIP Publishing LLC, 2017.

[116] Y Tian, FA Jaberi, Z Li, and D Livescu. Numerical study of variable density turbulence interaction with a normal shock wave. *Journal of Fluid Mechanics*, 829:551–588, 2017.

[117] Y Tian, FA Jaberi, and D Livescu. Density effects on post-shock turbulence structure and dynamics. *Journal of Fluid Mechanics*, 880:935–968, 2019.

[118] F Tonti, J Hardi, T Horchler, S Fechter, and M Oschwald. Influence of numerical model setup on the response of acoustically forced lox/h2 flames. In *Proceedings of the 8th European Conference for Aeronautics and Space Sciences*, 2019.

[119] JB Vemula and K Sinha. Reynolds stress models applied to canonical shock-turbulence interaction. *Journal of Turbulence*, 18(7):653–687, 2017.

[120] JB Vemula and K Sinha. Explicit algebraic reynolds stress model for shock-dominated flows. *International Journal of Heat and Fluid Flow*, 85:108680, 2020.

[121] AW Vreman, BJ Geurts, JGM Kuerten, and PJ Zandbergen. A finite volume approach to large eddy simulation of compressible, homogeneous, isotropic, decaying turbulence. *International journal for numerical methods in fluids*, 15(7):799–816, 1992.

[122] Y Wada and M-S Liou. An accurate and robust flux splitting scheme for shock and contact discontinuities. *SIAM Journal on Scientific Computing*, 18(3):633–657, 1997.

[123] X Wang and X Zhong. Effect of compressibility on strong shock and turbulence interactions. In *50th AIAA Aerospace Sciences Meeting including the New Horizons Forum and Aerospace Exposition*, page 1243, 2012.

[124] X Wang and X Zhong. A high-order shock-fitting non-equilibrium flow solver for DNS of strong shock and turbulence interactions. In *Seventh International Conference on Computational Fluid Dynamics*, 2012.

[125] X Wu. Inflow turbulence generation methods. *Annual Review of Fluid Mechanics*, 49:23–49, 2017.

[126] Z Xiong, S Nagarajan, and SK Lele. Simple method for generating inflow turbulence. *AIAA journal*, 42(10):2164–2166, 2004.